A General Model for the Analysis of the Transient Radiation Damage Environment from Pulsed Thermonuclear Radiation

Thomas O. Hunter

July 1978

UWFDM-238

Ph.D. thesis.

A General Model for the Analysis of the Transient Radiation Damage Environment from Pulsed Thermonuclear Radiation

Thomas O. Hunter

Fusion Technology Institute
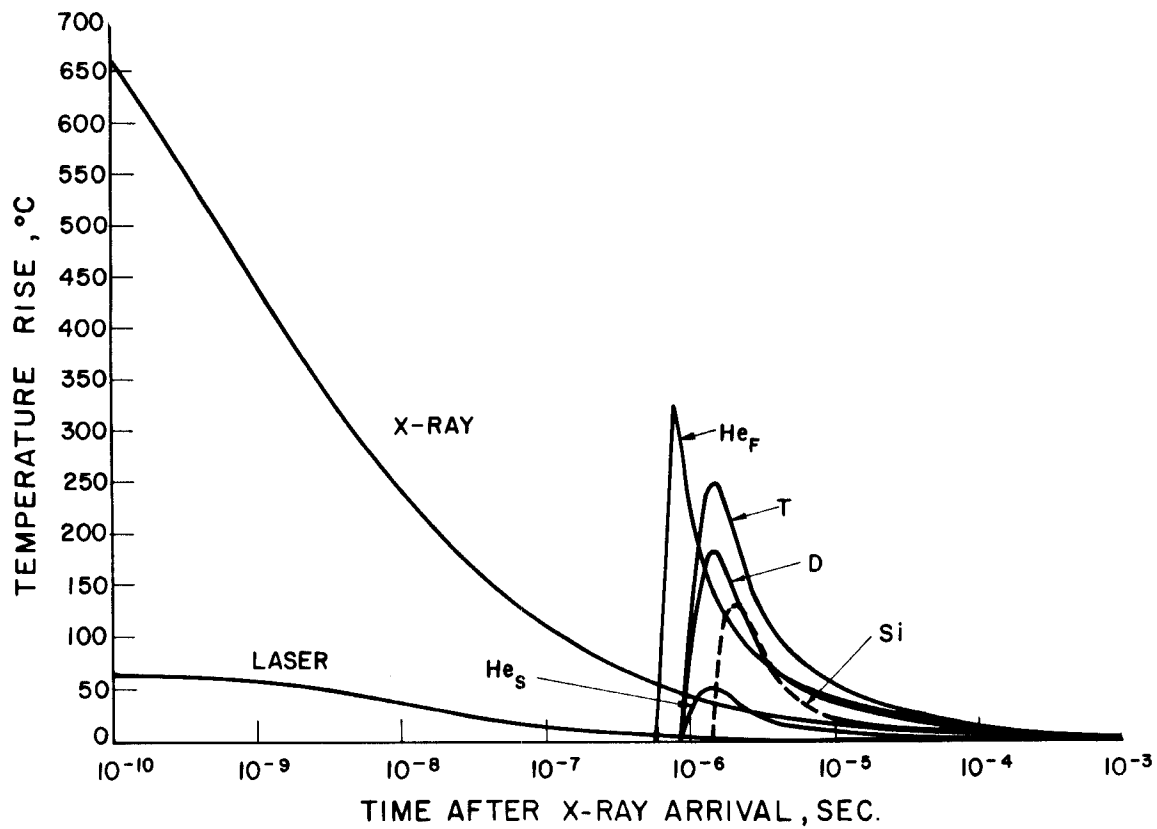University of Wisconsin
1500 Engineering Drive
Madison, WI 53706

http://fti.neep.wisc.edu

July 1978

UWFDM-238

Ph.D. thesis.

A GENERAL MODEL FOR THE ANALYSIS
OF THE TRANSIENT RADIATION DAMAGE ENVIRONMENT
FROM PULSED THERMONUCLEAR RADIATION

BY

THOMAS O. HUNTER

UNIVERSITY OF WISCONSIN

JULY 1978

A GENERAL MODEL FOR THE ANALYSIS

OF THE TRANSIENT RADIATION DAMAGE ENVIRONMENT

FROM PULSED THERMONUCLEAR RADIATION

by

THOMAS OLIVER HUNTER

A thesis submitted in partial fulfillment of the
requirements for the degree of

DOCTOR OF PHILOSOPHY
(Nuclear Engineering)

at the

University of Wisconsin-Madison

1978

ABSTRACT

A GENERAL MODEL FOR THE ANALYSIS OF
THE TRANSIENT RADIATION DAMAGE ENVIRONMENT FROM
PULSED THERMONUCLEAR RADIATION

Thomas Oliver Hunter

Under the Supervision of Professor Gerald L. Kulcinski

This research consisted of the development and application of
analytical techniques which can be used to assess the radiation damage
environment produced by irradiation in pulsed fusion devices. The
emphasis was to develop efficient models for simultaneously determining
the energy deposition, temperature, stress, and displacement irradia-
tion responses from both photons and ions characterized by spectra with
wide energy distributions.

A general method for ion interaction in materials was developed
based on characteristic functions which were analogous to cross sec-
tions in neutronics calculations. The "deposition" functions can be
used to determine the spatial distribution of energy into either
nuclear or electronic processes and can be used to develop the dis-
placement production from arbitrary ion spectra.

Temperature response was formulated into general Green's func-
tions, incorporating these ion depositions and those associated with
photons, which can be applied to half-space and slab geometries.
Similar functions are used for solution to the thermoelastic wave
equation.

The models are applicable to any situation in which transient irradiation occurs but have specific application to first walls and other components in inertial confinement fusion devices.

A solution based on a diffusion approximation of the transport of ions in isotropic, homogenous materials was developed to predict the modification of ion flux and spectra by gases which may be used in protective schemes.

All models were incorporated into a general computer code (T-DAMEN) which included a data handling and graphics package. This code was used to assess the response of carbon, copper and molybdenum to photon and ion spectra which included a) parametric variations in characteristic spectral parameters and b) general reference spectra typical of laser fusion systems.

Results of these analyses were used to assess the synergism of the irradiation on subsequent effects. Ion sputtering, for example, was found to by significantly enhanced by surface temperature excursions. Evaporation was also shown to produce serious erosion in low Z materials but was found to be negligible for higher Z metals in the spectra analyzed. Conditions for blistering were examined by comparing the damage production and thermal transients in the regions of helium implantation.

July 6, 1975

Signed:

Gerald L. Kulcinski
Professor of
Nuclear Engineering

ACKNOWLEDGEMENTS

It is on this page that tradition requires homage to those who have played a role in my program of graduate study. To associate this work with the abettors could add little credit to already illustrious credentials while to identify any detractors would accomplish even less.

I must however express my sincere appreciation to Professor G. L. Kulcinski whose dedication, encouragement, and support made this work possible. His example and friendship will forever remain among the most notable of my memories.

I am also indebted to Professor W. Wolfer, who was able to demonstrate the utility of the esoteric, for many valuable discussions; and to Professor R. Conn with whom any association can only lead to enrichment.

My fellow graduates also provided additional insight and support, specifically the association of N. Ghoniem, H. Attaya, and Fred Beranek. The aid of T. McCarville, E. Anderson and M. Shuy in portions of the computer programming and data analysis is also gratefully acknowledged.

No amount of prose could give proper credit to my most ardent supporter, my wife Miriam. Her patience, love, and understanding have provided endurance during a period of tribulation. My daughters, Tammy, Tracy, and Theresa are also to be credited for tolerating periods of regrettable negligence.

The financial support for this work was provided by the U. S.

TABLE OF CONTENTS

LIST OF TABLES

LIST OF FIGURES

Chapter I

INTRODUCTION

The prospects for controlled thermonuclear fusion have become quite optimistic, and numerous alternative approaches to a useful reactor[1-2] have been formulated. All such concepts,[3-6] whether they rely on magnetic or inertial confinement, have many varied technological problems, but they do share in one basic dilemma: the energy released from the fusion reaction must be altered before it is useful. A necessary consequence of this alteration to practical reactor designs, therefore, is that the radiation from the thermo-nuclear reaction will interact with materials of which the reactor is constructed. One principle distinction between various fusion concepts is the time scale over which the thermonuclear energy is released; consequently, the response of materials will be determined by the duration and magnitude of this energy release.

This research is concerned with the "transient" response of materials; i.e., the cases in which radiation is produced over short enough time scales that the dynamics of the response must be con-sidered. In order to provide a complete analysis of these transient conditions, this document will:

- describe current work in fusion reactor design in which these phenomena are important.

- outline the phenomenology associated with transient ra-diation response.

- present the theories on which the radiation interaction processes are based.

- describe a general analysis methodology which will allow a self-consistent evaluation of the response of materials.

- compare the methods of this analysis with those used by previous work for analysis of specific effects.

- develop general mathematical models which can be used to quantitatively determine the radiation damage conditions in an arbitrary thermonuclear spectrum.

- describe a general computer code (T-DAMEN) in which these models are incorporated.

- present results of the application of these techniques to selected materials and various radiation spectra.

A complete description of the transient analysis of radiation damage includes both the initial response due to the primary interaction of radiation with materials and the longer term response (e.g., swelling, creep, change in yield properties, etc.) when equilibrium is approached. An outline of this more general problem is included here, but only the analyses and results pertinent to the energy deposition, thermal, stress, and displacement damage response will be presented in detail. The synergism of these related effects can then be assessed as a basis for determining the implications for longer term effects.

The most apparent application for this work is the response of materials directly exposed to the radiation from inertial confinement fusion reactors (ICFR's). These systems are described in more detail in Chapter II. In these systems numerous components including first walls, mirrors, liners and diagnostic equipment can be exposed to the various combinations of photon, ion, and neutron

radiation which are produced in nanosecond, or less, pulses. As a result of this most obvious application, discussion will be based on, but not limited to, the phenomena associated within these environments.

The work presented here has been actively documented and published during its development. As a result of this process much of the information is contained in documents written by the author. In addition, the methods and results developed have been used by others with the consent and aid of the author for the analysis of components in the conceptual design of laser fusion reactors. A summary of the related publications by the author is presented in Table I.1.

I. A. Pulsed Fusion Systems

With the possible exceptions of mirrors, most confinement systems for thermonuclear fusion operate in a pulsed mode. Tokamak systems operate in a pseudo steady manner, but are limited in pulse duration by impurity buildup in the plasma and the available magnetic flux for plasma current. Theta pinches utilize pulsed magnetic fields for implosion heating and adiabatic compression of a toroidal plasma. These fields are programmed so that the ignited plasma will expand against the field but are not allowed to reach the first wall. Pulse durations are consequently on the order of 0.1 second.

TABLE I.1

SUMMARY OF AUTHOR'S RELATED PUBLICATIONS

Reference	Date	Authors	Title
86	March 1977	Thomas O. Hunter Gerald L. Kulcinski	(UW FDM-196) Description of the Response of Reactor First Walls to Pulsed Thermonuclear Radiation (Part I)
80	July 1977[a,b]	S.I. Abdel-Khalik Thomas O. Hunter	(UW FDM-197) Assessment of Surface-Heating Problems in Laser Fusion Reactors
100	October 1977	Thomas O. Hunter Gerald L. Kulcinski	(UW FDM-217) Description of the Response of Materials to Pulsed Thermonuclear Radiation (Part II). Transient Energy Deposition, Temperatures and Displacement Rates
28	October 1977[c,d]	Thomas O. Hunter S.I. Abdel-Khalik Gerald L. Kulcinski	(UWFDM-221) Response of First Walls in Inertial Confinement Reactors to Thermonuclear Radiation
128	November 1977[e]	Thomas O. Hunter Gerald L. Kulcinski	Temperature and Displacement Transients in Inertial Confinement Fusion First Walls
83	January 1978[f]	James E. Howard Thomas O. Hunter	(UW FDM-230) Mirror Damage Thresholds for Laser Fusion Pulse Shapes

4

TABLE I.1 (cont'd.)
SUMMARY OF AUTHOR'S RELATED PUBLICATIONS

Reference	Date	Authors	Title
107	April 1978	Thomas O. Hunter G. L. Kulcinski	(UW FDM-232) Description of the Response of Materials to Pulsed Thermonuclear Radiation (Part III)
113	April 1978(g,h)	Thomas O. Hunter G. L. Kulcinski	(UW FDM-233) Surface Damage and Thermal Effects from Transient Thermonuclear Radiation in Inertial Confinement Fusion Reactors
47	May 1978	Thomas O. Hunter G. L. Kulcinski	(UW FDM-247) The T-DAMEN Computer Code

a) Presented at AICHE-ASME Heat Transfer Conference, Salt Lake City, August 15, 1977.

b) To be published in Journal of Heat Transfer.

c) Presented at International Atomic Energy Agency Conference and Workshop on Fusion Reactor Design, October 10, 1977, Madison, Wisconsin.

d) To be published in Nuclear Fusion.

e) Presented at American Nuclear Society, Winter Meeting, San Francisco, California, November, 1977.

f) To be published in Journal of Applied Physics.

g) Presented at 3rd International Conference on Plasma Surface Interaction in Controlled Fusion Devices, UKAEA CULHAM Laboratory, Oxfordshire, United Kingdom, April 3, 1978.

h) To be published in Journal of Nuclear Materials.

Inertial confinement systems, which include lasers, electron beams, and ion beams, rely on the rapid deposition of energy in the periphery of a small fuel pellet. This energy will cause the pellet to be compressed and heated to thermonuclear conditions. The duration of the power pulse is determined by the time necessary for hydrodynamic expansion to a state where temperatures and densities are insufficient for further energy production.

Conceptual design studies have been performed for each of the above confinement schemes.[3-6] A general comparison of the burn characteristics and neutron wall loading is shown in Table I. 2, and it reveals the relative time scales over which the systems operate. Comparisons of different inertial confinement schemes will be made in Chapter II.

The dynamic response of a first wall to pulsed radiation sources can only be significantly different from steady state response if the duration of the loading pulse is smaller or the same order as the response time of interest. Consequently, the systems most likely to have a significant dynamic response contribution will be the inertial confinement approaches. The remainder of the discussion will address the phenomenology associated with these systems.

In inertial confinement systems, only about 75% of the thermonuclear energy is released from the source in the form of high energy neutrons. The remainder of the energy will be distributed between the pellet debris, the reaction products, and attendant electromagnetic radiation. In addition, a portion of the energy from

the compression source can be redirected towards the walls. As a result, reflected laser light, scattered electrons, and ions can also contribute to the environment which a first wall encounters. This partitioning of energy between various forms is discussed in Chapter II.

In addition to normal operating radiation environments, abnormal situations can also occur in magnetic confinement systems (e.g., transient plasma disruptions or pulses to limiters and divertors) which will require transient methods for proper analysis.

Table I. 2

PULSED FUSION SOURCE CHARACTERISTICS FROM
TYPICAL FUSION REACTOR DESIGNS

	Tokamak[2]	Theta[3] Pinch	Laser[4]
Thermonuclear Burn Time (sec)	1800	0.07	10^{-11}-10^{-10}
Thermonuclear Energy/pulse (GJ)	7300	30	0.10
Wall area (m^2)	1300	1100	310
14 MeV Fluence/ pulse (n/cm^2)	2×10^{17}	8.9×10^{14}	1.1×10^{13}
Peak wall current (n/cm^2 - sec)	1.1×10^{14}	1.1×10^{16}	1.0×10^{21}
Time Between Burns (sec)	100	10	.01-.1
Average 14 MeV Neutron Wall Loading (MW/m^2)	2.5	2.0	2.5

I.B. Phenomenology and Spectral Sensitivity

The phenomenology associated with transient irradiation in
a fusion environment is outlined in Figure I.1. The information re-
quired to determine the multitude of associated response modes in-
cludes a description of the irradiation source and a description of
a material exposed.

The source of pulsed thermonuclear radiation can be de-
scribed by the spectra of neutron, charged particles, or photons
produced in each pulse. The neutron spectrum will be determined by
the fusion nuclei, the source density, and any non-fusing nuclei
present in the source. The neutron energy in most fusion reactions
is limited to about 15 MeV.

The charged particle spectra from a thermonuclear source
will consist of the fusion nuclei, product nuclei, and non-fusing
species. The range of energies will be limited to approximately
the maximum kinetic energy given to a product nucleus in a fusion
reaction.

The photon spectra will be determined by the confinement
mechanism, source temperature, and the species present. For typical
short pulse duration systems, the energy range for photons is up to
about 100 keV. However, there will be higher energy photons, prin-
cipally due to secondary radiation such as neutron capture, and
these will also interact with the first wall.

To establish a qualitative understanding of the response
of materials, the relative mean free paths in carbon (range in the
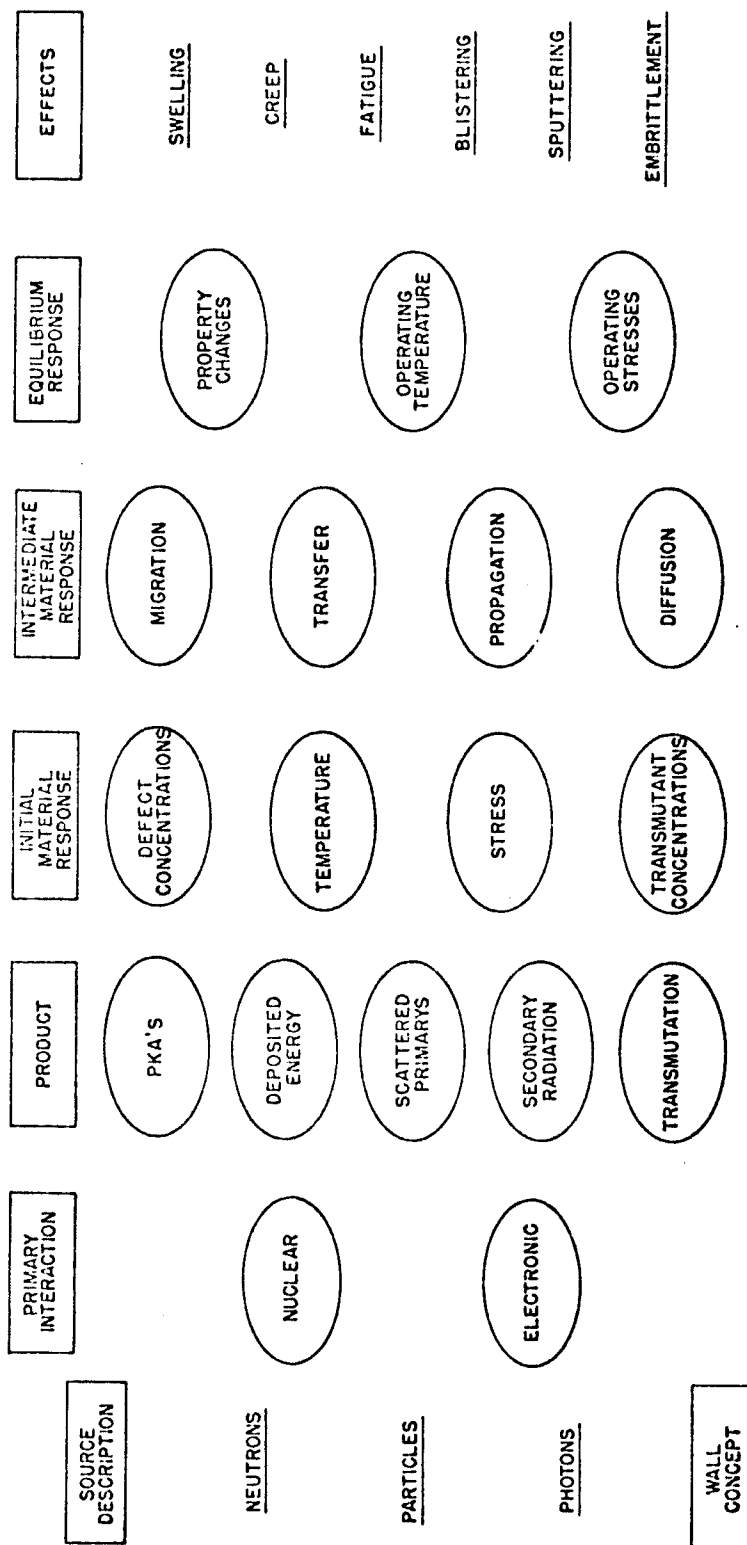
Fig. I. 1. Transient Irradiation Phenomenology

case of charged particles) for various energy radiations is shown in
Figure I.2. First walls for most fusion systems are on the order of
a few mm in thickness, hence, from the data in Figure I.2., it is
clear that the incident neutron current will be only slightly af-
fected by the first wall regardless of the initial neutron spectrum.
The ion flux on the first wall will be absorbed in the first 10 μm for
all reasonable ion energies. The mean free path of the energetic pho-
tons, however, can vary by a factor 10^7 over the energy range of int-
erest. Consequently, the spectral sensitivity of material response
to the primary radiation can be summarized as:

<div style="text-align:center">

neutrons -- relatively insensitive

ions -- sensitive

photons -- extremely sensitive

</div>

I.C. Interaction Chronology

The primary interaction of the source neutrons is with the
target nuclei, while the photon interaction is with target electrons,
and ions interact with both electrons and nuclei. The partitioning
of interaction energy between nuclei and electrons is crucial to the
ultimate response of the material, since only the nuclear energy
losses will result in damage to the metallic structure in the form
of atomic displacements, while the electronic energy will produce
ionization and local deposition of energy (heat).

The damage energy is given first to primary-knock-ons (PKA)
which then produce subsequent displacements as they travel through
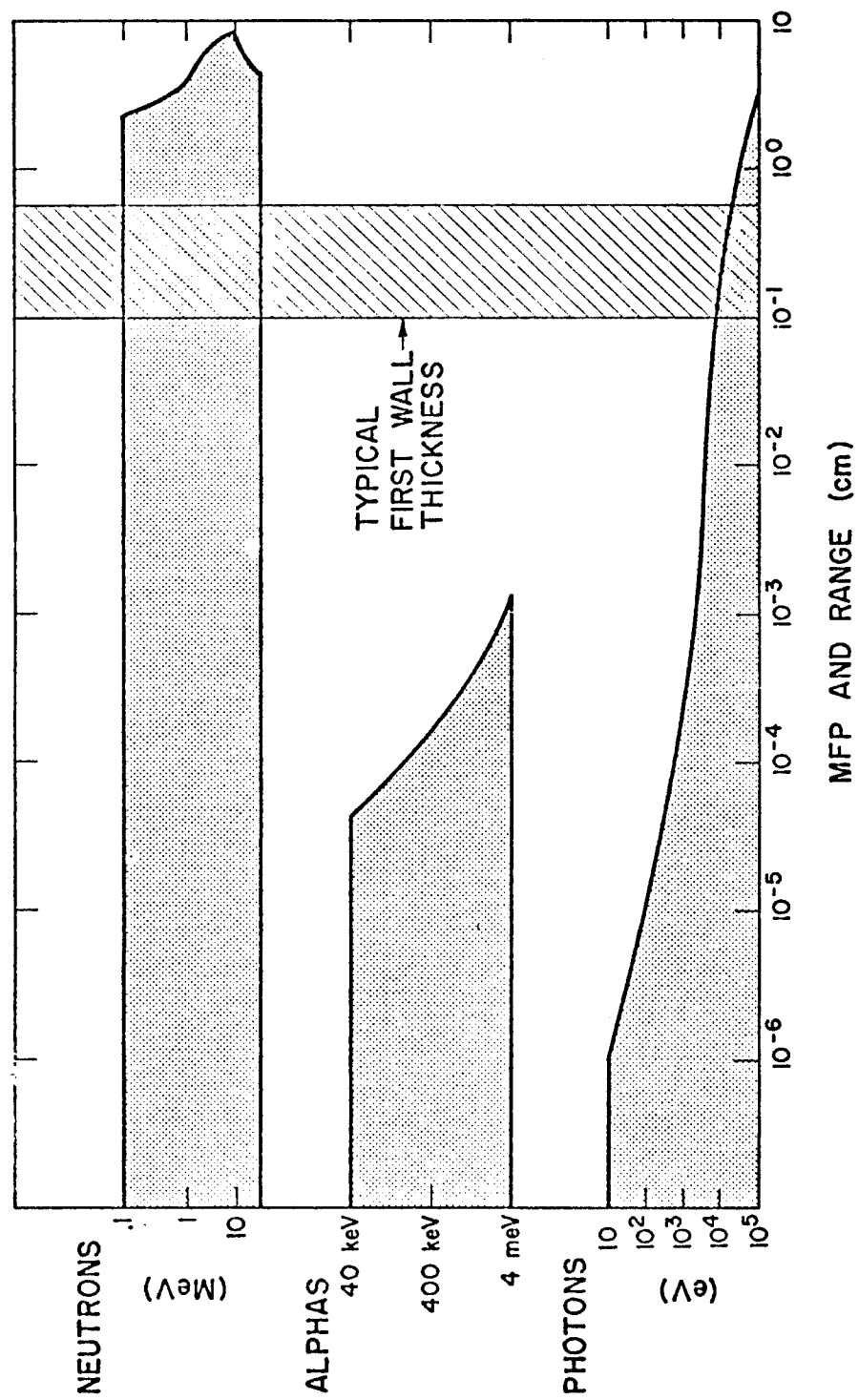
Fig. I. 2. Mean Free Path and Range of Fusion Irradiation
in Carbon

the material. The resulting concentration of point defects will
undergo recombination, migration, and agglomeration depending upon
the microstructure of the material. The accumulation of single and
clustered defects can result in macroscopic effects such as swell-
ing, creep, etc.[8], which will determine the ultimate life of the
first wall material.

The above processes also depend on the thermodynamic state of
the material since the destiny of the original defects is strongly in-
fluenced by the local temperature and stress state. That portion of
the incident radiation energy which is deposited as internal energy
in the first wall can give rise to both temperature and stress ex-
cursions. The magnitude of the temperature excursion will depend on
the rate of energy deposition at a given location versus the rate
at which energy is lost by heat transfer from that point. It will
be shown in subsequent sections that energy deposition from neutron
and photons in inertial confinement systems may be sufficiently fast
that it may be approximated by impulse sources. On the other hand,
significant heat conduction can take place over the long durations of
ion irradiation.

Stress transients can be induced in the first wall due to either
of two manifestations of the same basic phenomenon. The first is a
thermoelastic response to the deposition of energy. If the material
is heated faster than its characteristic thermal expansion time,
local stresses will develop which are then relieved as stress waves
propagate throughout the material. The second is the creation of

stress waves in response to an ablation of the surface due to energy deposition in excess of that required for incipient vaporization. This material will "blow off" and there will be an impulse imparted to the remaining solid surface equal to the momentum in the ablated material.

This study addressed the response of dry first walls in which ablation is not a consideration. It will be shown in section V.D. that, while photons can be deposited in sufficiently short times for production of thermoelastic stress waves, it is unlikely that ion spectra will be sufficiently narrow (and hence ion pulse duration sufficiently short) to produce significant stress waves. As a consequence of this analysis to derive the conditions for stress wave creation by ion irradiation, further quantification of the stress waves produced by various ion spectra was not emphasized in this investigation.

I.D.   Pulsed Radiation Damage

Transient irradiation of materials produces unique damage not only because of the synergisms of the various effects but also because of the rate of damage production. Traditionally, radiation damage has been associated with those phenomena which arise from neutron irradiation of materials at relatively low (10^{-7} to 10^{-6} dpa/sec) displacement rates and the materials are in a uniform stress and temperature state. Such conditions are encountered in a fission reactor and in a pseudo steady state fusion reactor. The primary responses to such irradiation are displacement damage and transmuta-

tion reactions. These primary interactions lead to the subsequent phenomena, as outlined in Figure I. 1, of sputtering, swelling, electrical resistivity changes, embrittlement, creep, and compositional charge.

Some of the phenomena are considered to be rate dependent[9] and such dependence is usually characterized by the displacement rate or the rate of primary interaction. To a first approximation the displacement rate is proportional to the instantaneous flux in a material; however, the neutron spectrum can cause significant modification to the displacement rate (as measured by surviving defects) especially as more energetic neutrons are present. A qualitative comparison of displacement rates for metals in various environments in which displacement damage has been observed or is anticipated is given by Table I. 3.

The effect of these various damage rates on specific phenomena such as swelling has been investigated by Johnson, et al[12] and more recently by Whitley.[13] Significantly different responses are observed. For example, there is a significant shift in the swelling vs. temperature behavior as the displacement rate is increased for the same total number of displacements.

An aspect of damage production which is more pertinent to inertial confinement systems is the pulsed nature of the radiation. Damage is produced at very high rates for a short interval of time followed by a quiescent phase in which the material is free to respond with no new defects being produced. Both the duration of the

pulse and the interval between pulses can be of the same order as
the lifetimes of the interstitials and vacancies whose migration
ultimately determines the swelling of an irradiated material. In
addition, the defect migration is occurring at the same time that
the temperature is oscillating with the frequency of the radiation
pulses. A comparison of interstitial and vacancy life times with
the pulse durations and pulse interval for various temperatures in
a typical metal (Cu) is shown in Figure I. 3. From this comparison
it can be noted that neutron pulse durations are on the order of the
interstitial lifetimes, while subsequent pulses occur on the order
of the vacancy lifetimes. In addition, fluctuations in tempera-
ture have a slight effect on interstitial response and a significant
effect on vacancy response. This effect is directly attributable to
a factor of 20 difference in free energy of migration between the
two species.[14]

The effect of short pulses of high displacement rates on
swelling has been investigated by Ghoniem[15] under conditions of
constant temperature and stress. That study, based on a dynamic
solution of the rate theory equations for point defect behavior,
indicated that significant modification to swelling behavior can be
expected if pulses are short (10^{-8} sec) and pulse intervals are on
the order of 10^{-1} seconds at high temperatures. The emphasis of
the investigation in this more general analysis was to develop
methods to predict the transient energy deposition, temperature,
stress, and displacement production associated with the pulses of

16
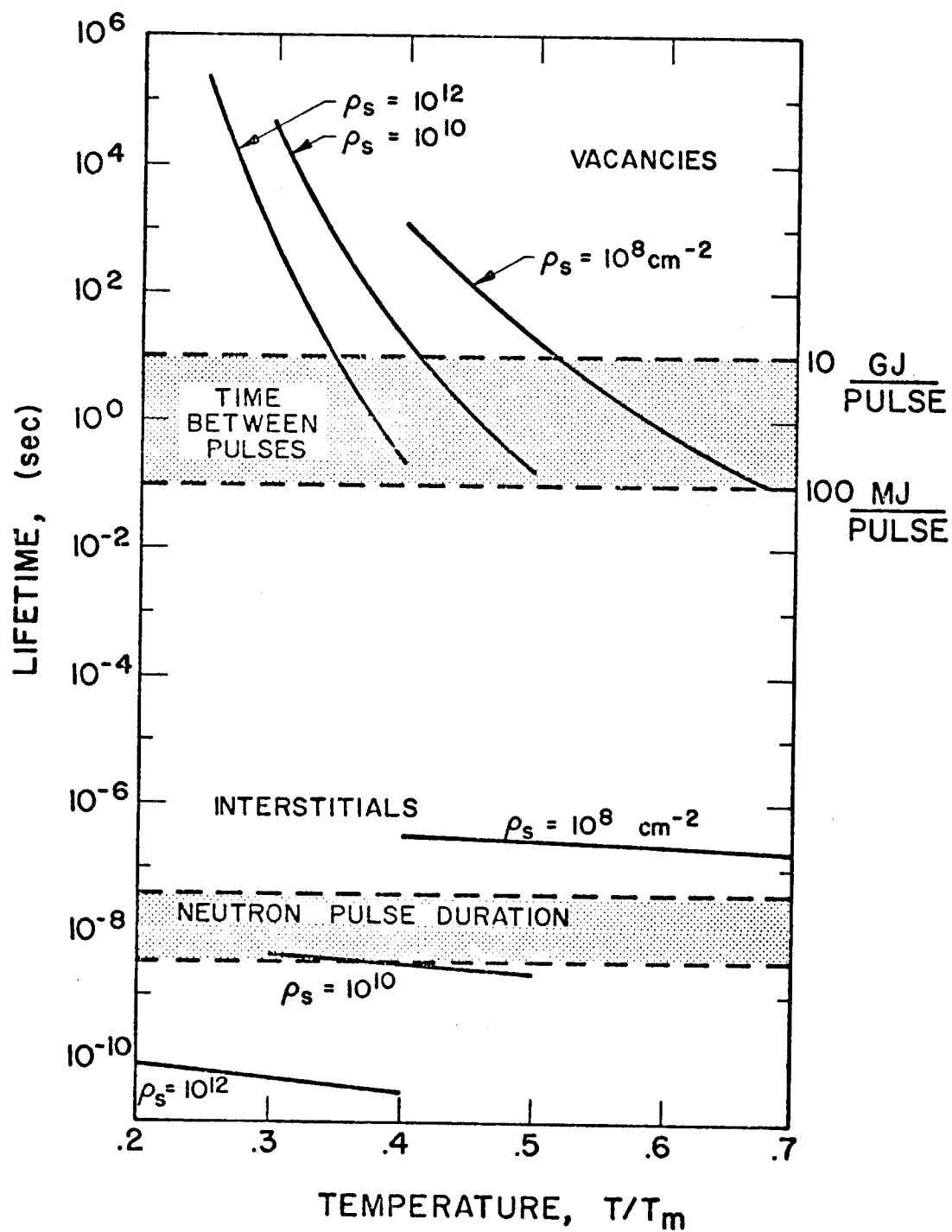
Fig. I. 3. Comparison of Point Defect Lifetime and
Characteristic Radiation Times

TABLE I.3

COMPARISON OF INSTANTANEOUS DISPLACEMENT RATES IN
SOLID COMPONENTS OF NUCLEAR SYSTEMS

	dpa/sec
Tokamak Fusion First Wall	3×10^{-7}
Thermal Fission cladding	10^{-7}
Fast Fission-cladding	10^{-6}
Θ-pinch*	3×10^{-5}
HV Electron Microscope	10^{-3}
Heavy Ion Bombardment	$10^{-4} - 10^{-1}$
Laser Fusion First Wall*	1-10

*Neutrons only.

thermonuclear radiation. The models are constructed so as to encompass a broad variation in both types and spectra of radiation.

One result of this study was the development of a computer code which incorporates all these general models so that a quantitative prediction of the response of a material exposed to any mixture of photons or ions spectra can be made. This code incorporates features which allow assessment of combination of effects which were not possible with previous methods of analysis. In addition, the nature of the solution allowed sufficient numerical efficiency so that wide variations in characteristic parameters (e.g., spectra, ion types, material properties, etc.) could be accomodated.

Chapter II

INERTIAL CONFINEMENT REACTOR DESIGNS

The production of thermonuclear fusion energy by inertial confinement has received considerable attention in recent years and experimental programs using both lasers and electron beams have produced encouraging achievements in terms of neutron yield. Recent results and anticipated results from nearterm drivers were reported at a workshop on fusion reactor design[16] and were summarized in Reference 17 and reproduced here as Tables II. 1 and II. 2. As a result of these developments several groups have proposed reactor concepts with laser drivers receiving the most emphasis. In addition to central power generation using pure fusion, numerous other applications for laser fusion have been proposed, including fusion-fission hybrid, actinide burning, synthetic fuel production and propulsion systems.[17a] Although the various concepts differ in design details, certain basic principles are noted in all designs. This chapter will outline these recent design studies with particular attention given to the output spectra assumed. In many of the designs, a protective method is utilized to modify or eliminate the radiation which strikes the first wall. These methods and the materials chosen for the wall will be noted in this section. A summary of the generic classes of cavity designs has been made by Booth and Frank.[18]

TABLE II.1

NEUTRON PRODUCTION MILESTONES IN INERTIAL

CONFINEMENT FUSION RESEARCH

LABORATORY	DRIVER	POWER (TW)	NEUTRON YIELD	DATE
KMS[1]	Nd: GLASS	0.2	10^7 (DT FUEL)	1974
LLL	Nd: GLASS (JANUS I)	0.2	10^6 (DT FUEL)	1974
LLL[2]	Nd: GLASS (JANUS II)	0.4	10^7 (DT FUEL)	1975
LLL[3]	Nd: GLASS (ARGUS)	4.6	10^9 (DT FUEL)	1976
KURCHATOV[5]	e-BEAM (TRITON)	0.06	10^6 (D_2 FUEL)	1976
LASL[4]	CO_2	0.4	10^6 (DT FUEL)	1977
SLA[6]	e-BEAM (HYDRA)	0.1	10^6 (D_2 FUEL)	1977

TABLE II.2

NEAR TERM EXPERIMENTAL DRIVERS FOR

INERTIAL CONFINEMENT FUSION EXPERIMENTS

LABORATORY	DRIVER	POWER, TW	COMPLETION DATE	ANTICIPATED EXPERIMENTAL RESULTS
SANDIA-A	e-BEAM (PROTO-II)	7	1977	$10^7 - 10^9$ NEUTRONS
LLL	Nd: GLASS LASER (SHIVA)	10-40	1977	~10^{13} NEUTRONS
LASL	8-BEAM CO$_2$ LASER	10-20	1978	$10^{10} - 10^{12}$ NEUTRONS
LLE-UR	Nd: GLASS LASER (OMEGA-10)	3-30	1979-80	USER FACILITY
SANDIA-A	e-BEAM (EBFA-I)	30 (1 MJ, 40 ns)	1980	$10^{10} - 10^{13}$ NEUTRONS
KURCHATOV	e-BEAM (ANGARA V)	80 (5 MJ, 85 ns)	1982	G ~ 100
LLL	Nd: GLASS LASER (NOVA)	100-300	1983	$10^{16} - 10^{19}$ NEUTRONS, G ~ 1 - 100
LASL	CO$_2$ LASER (ANTARES)	100-200	1983	$10^{16} - 10^{17}$ NEUTRONS, G ~ 1 - 10
SANDIA-A	e-BEAM (EBFA-II)	60-80	1983-85	$10^{15} - 10^{17}$ NEUTRONS, G ~ 0.1 - 10

In each of these systems, fuel pellets will be injected into a reactor cavity and a short duration (<10 ns) pulse of energy will be deposited in the periphery of this pellet by: (1) multiple laser beams, (2) a focused relativistic electron beam, or (3) a heavy ion beam. The response to this energy deposition in the pellet will be an outward ablation of the surface and an inward compression of the fuel core. When densities and temperatures in the core are sufficiently high, a short duration thermonuclear energy pulse (<1 ns) will occur and proceed until the pellet disassembles. The thermonuclear radiation and the pellet products are then blasted out towards the walls of the cavity. A recent review of the technology to achieve fusion conditions by laser implosion is given by Brueckner.[19]

The response of the first wall to this radiation will be determined by the energy partitioning between these products. Several different first wall designs have been proposed to safely withstand these irradiations.

One of the earliest laser fusion designs was proposed by Williams, et al.,[20] in which a 1 MJ laser ignited a pellet which produced 100 MJ. A possible first wall consisted of a layer of liquid lithium covering a niobium structure. The function of the liquid lithium is to absorb the ion and photon energy from the micro-explosion and ablate, leaving the first wall undamaged. An alternate design for protecting the first wall is magnetic protection as outlined by Frank,[21] et al., which serves to divert the charged particles

away from the first wall. An example of the energy partitioning

from the pellet explosion for these designs is given in Table II. 3.

This liquid wall protection is similar in concept to the original

"Blascon" by Fraas,[22] which envisioned a laser initiated explosion

in the center of a liquid lithium vortex. Another design was pro-

posed by Hovingh, et al.,[23] which utilized a smaller yield pellet

(7 MJ) and lower power laser (.1 MJ). This approach was used to

suppress the ablation of a wetted wall by improved pellet design,

increased first wall area (through pyramidal first wall topography

and increased wall radius), and by reducing the blast energy.

Elimination of the ablation removed the "blow-off" stress imparted

to the first wall in previous designs. Information is also con-

tained in this reference about the typical photon and neutron

spectra from 1 MJ DT fusion microexplosion. These spectra are pre-

sented in Figures II. 1 and II. 2.

A study by Maniscalco[24] describes a low yield laser fusion

reactor which employs a fissile (hybrid) blanket to get energy and

fuel multiplication. This concept employs a graphite liner over a

stainless steel first wall. The total pellet yield is 10.5 MJ, with

a laser input to the pellet of 500 KJ.

The first wall response to the microexplosion for this hybrid

reactor is described by Hovingh.[25] In addition to x-rays, alphas,

neutrons, and pellet debris, this analysis considers the laser light

which is reflected from the pellet and strikes the first wall. The

arrival times for energy from the pellet and hence the energy deposi-

tion time in the first wall is given in Figure II. 3.

Table II. 3

TYPICAL ENERGY RELEASE SPECTRA FOR A 99 MJ
PELLET MICROEXPLOSION

	Release Fraction	Particles Per Pulse	Average Energy Per Particle
X-rays	0.01		4 keV peak
α particles (that escape plasma)	0.07	2.2×10^{19}	2 Mev
Plasma kinetic Energy	0.15		
α Particles		1.3×10^{19}	0.6 Mev
Deuterons		1.2×10^{20}	0.3 Mev
Tritons		1.2×10^{20}	0.4 Mev
Neutrons	0.77	1.3×10^{19}	14.1 Mev
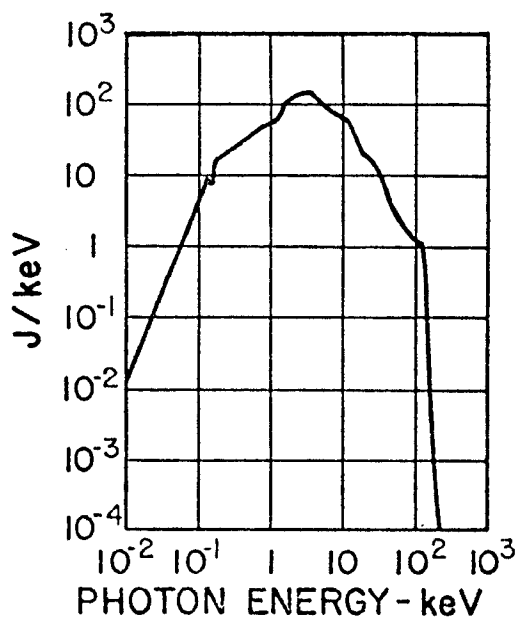
Fig. II.1. X-ray Pulse Spectrum of a Megajoule DT Fusion Microexplosion. (Ref. 23)
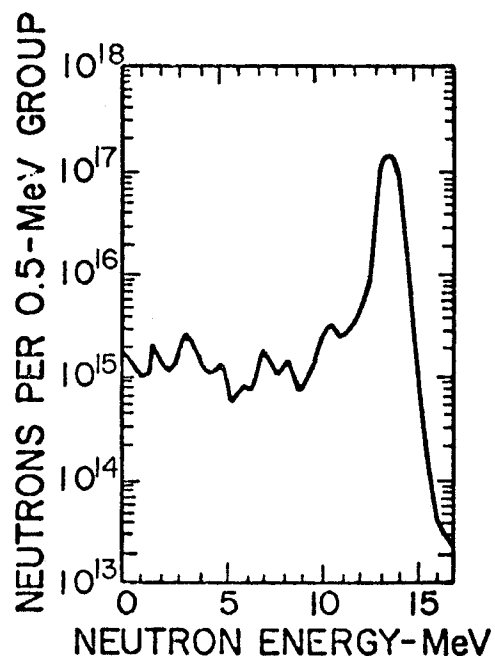
Fig. II. 2. Neutron Pulse Spectrum of a Megajoule DT Fusion Microexplosion. (Ref. 23)
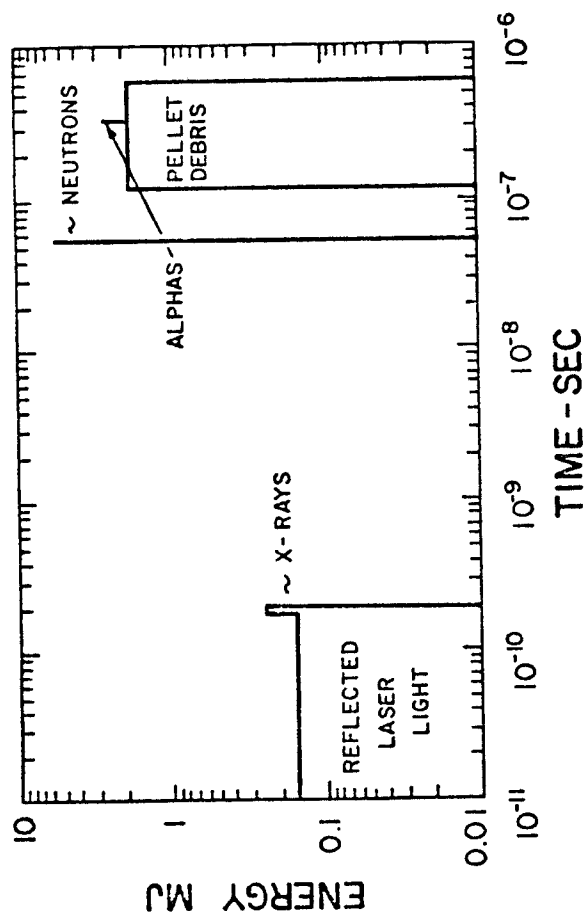
Fig. II. 3.   Time of Arrival of Microexplosion Energy at First
             Wall Radius of 3.5 m (Ref. 25)

A general design by the Lawrence Livemore Laboratory,[26] which relies on high gain targets and reduced laser system requirements, employs a thick falling region of lithium for protection of the reactor structure from the products of the microexplosion. This design not only allows all the photon and ion energy to be deposited in this lithium, but also produces significant modification of the neutron spectrum as well. Energy partitioning and neutronics calculations[27] for high ρR pellet designs associated with this design reveal that a significant amount (30-40%) of the neutron energy can be deposited in the pellet itself.

A detailed conceptual design of a laser fusion reactor has been performed by the University of Wisconsin fusion design team.[17] This design employed a moderate gain pellet and used gaseous protection to absorb the low energy photon and ion energy from the pellet. A carbon first wall with a carbon-lithium oxide blanket was used in this design. Two output spectra were developed for this design with a parametric analysis of pellet performance. The partition of energy in these spectra are shown in Table II. 4.[28] This design study also utilized the methods of this research to assess the performance of first wall and final mirror response to variation in output spectra and to determine the effect of gas protection on the modification of this response. As a consequence, some of the results in this document will in part be similar to those developed in the above conceptual design.

An alternate approach to inertial confinement fusion would utilize relativistic electron beams (REB). Some design considerations for a reactor using REB's are outlined by Varnado and Carlson.[29] Pellets for REB fusion are typically larger and more structured than in laser fusion,[30] due to the difficulty in slowing down 1 MeV electrons in short distances. As a result the output spectra are expected to be significantly different. The most significant difference is the large percentage of the energy in x-rays. These x-rays are also quite low in energy which results in an extremely short deposition depth. The x-ray spectrum for a 85 MJ microexplosion in a REB fusion system was calculated to be approximately equivalent to a 350 eV Blackbody which has peak intensity at 980 eV. A comparison of the relative energy partitioning for all the systems discussed above is given in Table II. 5.

Table II.4
(Ref. 28)

CHARACTERISTIC PELLET SPECTRA (150 MJ)

	Bare Pellet		Structured Pellet	
	ENERGY (MJ)	SPECTRUM	ENERGY (MJ)	SPECTRUM
LASER	0.15	10.6μ	0.15	10.6μ
X-RAY	1.5	2 keV-BB	14	20 keV-BB
D	9.5	340 keV-M	0.13	15 ± 9 keV-G
T	12.5	465 keV-M	0.19	20 ± 9 keV-G
He (SLOW)	1.9	240 keV-M	0.25	30 ± 10 keV-G
HE (FAST)	6.6	2.4 ± 0.6 MeV-G	---	---
MERCURY	---	---	14.8	3 ± 1 MeV-G
NEUTRONS	120	14 ± 1 MeV-G	120	14 ± 1 MeV-G

BB = Black Body; M = Mexwellian; G = Gaussian

Table II. 5

Reactor Type	E_{in} (MJ)	E_{out} (MJ)	First Wall Material	Energy Percentage			
				Neutron	Charged Particle	X-ray	Laser
Laser (Liquid Wall) Ref. 20	1	100	Li/Nb	77	22	1	--
Laser (suppressed ablation) Ref. 23	.1	7	Li/Nb	76	23	1	--
Laser (Hybrid) Ref. 24	.5	10.5	C/SS	73.5	24	1	1.5
E-Beam (Ref. 29)	10.8	96	C	71	12	17	--
Laser (Ref. 26)	-	-	Li	60	12	(balance)	--
Laser (Ref. 17)	1	150	C	80	11	9	--

Chapter III

ANALYSIS METHODOLOGY

This chapter will address the methodology on which the general

analysis for the response of materials to an arbitrary thermonuclear

spectrum is based. The basic steps in a self-consistent analysis

will be outlined and discussed. Since various analytical techniques

for certain phases of the analysis had been previously developed,

this chapter will also discuss the limitations of these methods to

the general problem. The differences between previous methods and

the ones developed in this research will be highlighted. Finally,

comments will be made about the applicability and utility of the

methods developed here.

III. A. Outline

A self-consistent analysis of the energy deposition, tempera-

ture, and displacement production due to thermonuclear spectra must

systematically consider the entire response of a material. The

process chosen in this study follows the flow diagram shown in

Figure III. 1. The statement of the problem begins with a descrip-

tion of the ion, photon, or neutron spectrum from thermonuclear

source and the location and characteristics of the material exposed.

Each radiation component will transit the reactor chamber and

impact the surface of the exposed material at different times and

with different energies. In cases where protective mechanisms, such

28

THERMONUCLEAR SPECTRA
PHOTONS IONS NEUTRONS

$N_i(E)$

TRANSPORT THROUGH
CHAMBER ENVIRONMENT

$N_i(E,t)$
gas
$\left(\dfrac{dE}{dX}\right)_i(X,t)$

ENERGY DEPOSITION IN TARGET
NUCLEAR, ELECTRONIC

$\left(\dfrac{dE}{dX}\right)_i(X,t)$

TEMPERATURE

$T_i(X,t)$

DISPLACEMENTS

$DPA_i(X,t)$

EFFECTS
SPUTTERING
EVAPORATION
SWELLING
BLISTERING

$S_i(t)$
$\eta(t)$
$\Delta V(X,t)$
-
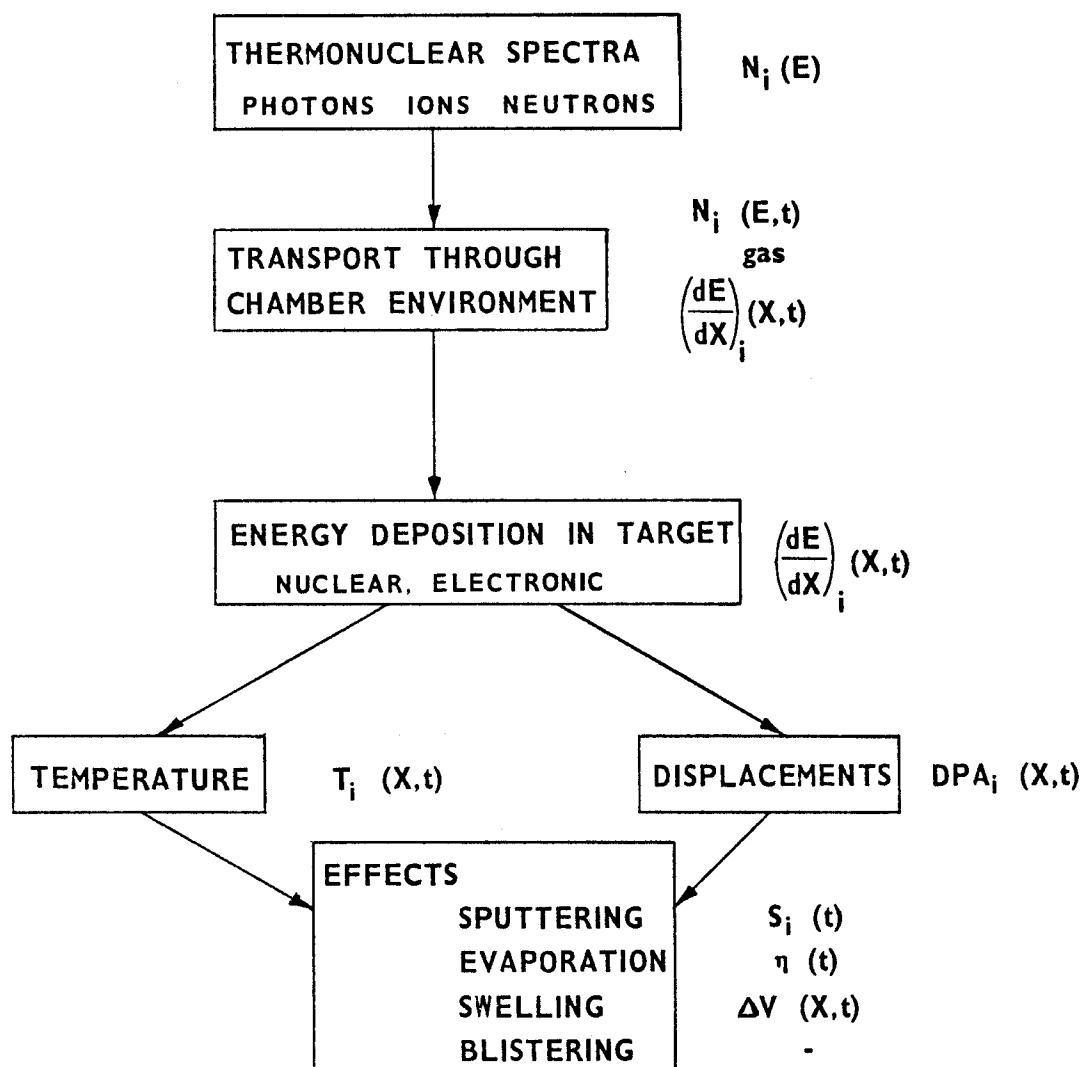
Fig. III. 1. Transient Radiation Damage Analysis Methodology

as magnetic fields or gas layers are employed, the spectra and flux
will be altered upon arrival at the exposed surface. In a gas
filled cavity, a significant portion of the energy can be deposited
in the gas, thereby initiating a shock wave and causing a much
different spectra to be incident on the wall than was found near the
surface of the pellet.

Upon determination of the flux, spectra, and impact time of the
various species at the exposed surface, the spatial distribution of
deposited energy must be determined. These distributions are par-
titioned into nuclear or electronic deposition rates commensurate
with each component of the spectrum.

All of the energy depositions will constitute driving forces
for large temperature excursions. For finite deposition times these
forces will compete with energy loss from the deposition region by
heat conduction. The nuclear energy deposition determines the amount
of energy which initially goes into lattice distortion and hence the
production of atomic displacements.

All the effects can occur simultaneously, especially near the
surface of the material. The synergism of the phenomena can result
in significant modification to the damage rates in fusion devices,
e.g., sputtering, blistering, evaporation and swelling.

III. B. Previous Work Related to Energy Deposition and Response

III. B. 1. Photon Energy Deposition and Response

Methods for determining the deposition of photons must, in

general, account for absorption and transport of scattered radiation. Computational techniques have been developed for this purpose which rely on a cross section library based on photon energies. (Such a library will be discussed in Chapter IV.) Examples of computer codes which can perform deposition calculations based on these cross-sections are ANISN[31] and BUCKL.[32] The former is a transport theory code used for both neutrons and photons, while the latter is a diffusion approximation developed specifically for x-rays.

If time-dependent energy deposition can be developed for a given radiation condition, the response in terms of stress and temperature can be determined (on sufficiently large computer systems) by the use of what have been referred to as "hydrocodes." Examples of two of these are WONDY[33] and CHART-D.[34] The codes are finite-difference solutions to the equation of motion and energy, and, especially in the case of CHART-D, include comprehensive equations-of-state and energy transfer techniques by radiation and conduction.

The BUCKL and CHART-D codes have been integrated to incorporate both deposition and response. It is this combination that has been in the published work on the response of initial confinement fusion first walls, specifically the work of Hovingh[25] at Lawrence Livermore Laboratories and Carlson[29] at Sandia Laboratories - Albuquerque.

Although such combinations of computer codes can perform analysis of radiation response with great accuracy, a great penalty in computer time and complexity can result if used for parameter studies in which numerous successive calculations are performed. In addition,

since their solutions are based on finite-differences techniques, considerable difficulty is encountered[35] when the response to various components is required, (e.g., ion and photons, which are characterized by different spatial depositions and time scales), since the calculation is confined to specific steps and zoning requirements.

III. B. 2. Ion Energy Deposition

The interaction of energetic ions with matter is based on various theories of primary interaction of the ion with the electrons and nuclei of the target material.

Although uncertainty exists in the exact nature of both of these interaction processes, several techniques have been developed to derive the implantation distributions (ranges and other moments) and the energy deposition distributions. The most notable methods are:

- Manning and Mueller code EDEP-1[36]

- The codes of Brice[37]

- The methods of Winterborn[38]

- Monte Carlo Calculation[39]

- Transport Theory Direct Solutions[40]

The first three of these approaches form a set which are based on a "moments" solution of the transport equation. They are the most widely used techniques for problems of ion implantation. Each of these methods rely on the generation of the moments of the

implantation distributions by a Legendre polynomial expansion solution of the integro-differential transport equation. They differ however on the method for producing the deposition distribution.

The Manning and Mueller method develops the implantation moments based on techniques developed by Gibbons and Johnson.[41] It is the simplest of the techniques and the deposition distributions are based on a variation technique using the first and second moments of the implantation distributions.

The methods of Brice are incorporated in the general computer codes: COREL, RASE4, and DAMG2. Brice's solution for the range distributions contains a general electronic energy loss formulation which is valid over both low and high velocity ranges.[42] The unique feature of this method is that it is a "direct" solution in that it uses an approximation for determination of the energy deposition distribution. The procedure consists basically of determining the range distribution (ion density as a function of position in the target) at intermediate energies between the impact value and end-of-range.[43] These distributions are considered gaussian in shape. The damage at any point can then be established by evaluating the deposition produced by each intermediate energy and integrating over all intermediate energies. This process allows for the redistribution of energy by PKA recoil which is not included in the method of Manning and Mueller.

A complete calculation for the range distribution, the energy deposited into nuclear damage, and the energy deposited into elec-

tronic process consists of successive use of the COREL code for the PKA range distributions, RASE4 for the intermediate energy implantation distributions, and DAMG2 for the energy deposition distributions. Such calculations, while extensive in the phenomena incorporated, can require large amounts of computer time even for a few incident ion energies. The direct application of these methods, therefore, to a wide range of ion spectra was not considered appropriate for this research, especially when parameter studies on ion spectra were anticipated.

The method of Winterborn is considered a general "moments" solution; i.e., the first four moments are generated by solution of the transport equation for all the following: the range distribution, the nuclear energy deposition distribution, and the electronic energy deposition distribution. These moments, however, are not extremely useful unless the distribution can easily be created from a limited number of moments. Winterborn[44] suggests several methods for recreation of the distributions from the moment including an inverse Fourier transform technique.

A comparison of these three methods, all of which are used in ion implantation studies, yields an understanding of the "state of the art" on energy deposition distributions. Figure III. 2 shows the nuclear energy deposition distributions for a 5 MeV Ta ion onto aluminum. Data are taken from references 44 and 45 and calculations on the EDEP1 code. Each distribution is normalized to the same peak height. One concludes from this comparison that uncertainty
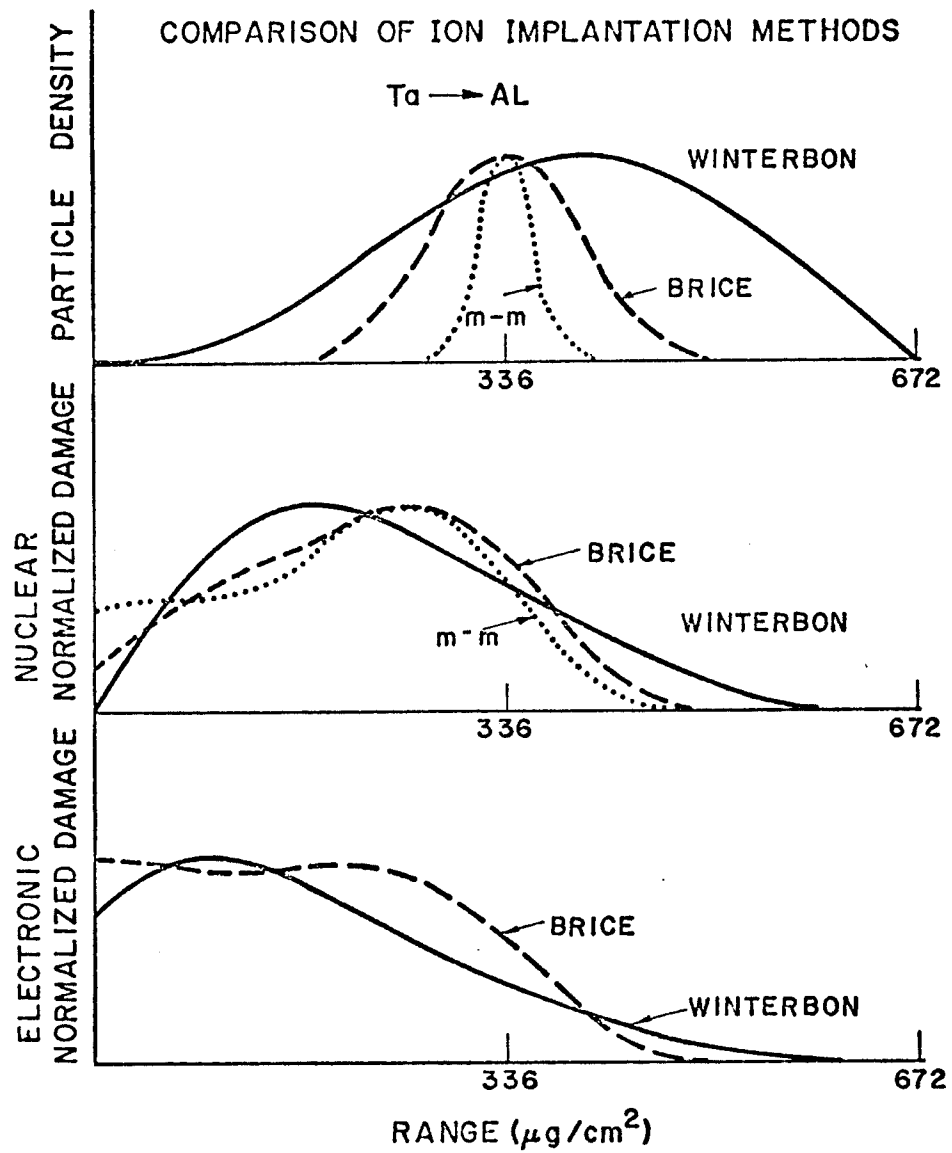
Fig. III. 2. Comparison of Ion Implantation Methods

in energy deposition distributions clearly exists and approximate solutions which simplify the calculational procedure can easily fall within the range of accepted values. In Chapter V, methods will be developed which can determine the above distribution but which are applicable to wide spectral ranges with minimum computing time.

III.C. Comparison with Methods of this Research

In general all the techniques discussed above were developed as solutions to a single interaction problem: e.g., photon response of a material. In this more general study, methods were necessary which could be efficiently used to generate the simultaneous response to several radiation components, each of which could have a wide spectral range. Furthermore, the form of each of the spectra should be arbitrary so that parametric variations could be assessed.

This research, therefore, centered on developing solutions which could be evaluated efficiently and which could be linearized to allow superposition of responses. The procedure for each phenomena will be discussed in Chapter V. The general approach was to develop analytic solutions for the problems of energy deposition, stress, temperature, and displacement production. These solutions were based on energy dependent parameters which specified the temporal or spatial characteristics of each phenomena. Upon generation of a parameter set for the spectrum of a particular radiation component, a solution could be developed at arbitrarily specified time and position coordinates. Results for several components could then be superimposed due to the linearity of the response models.

The photon interactions were based on the x-ray cross section models of Biggs[46] and were restricted to exponential spatial depositions due to the low energy spectra typically encountered in inertial confinement systems which restricted the interactions to photoelectric absorption, thereby eliminating the necessity for scattering interaction and transport.

Energy deposition for ions are based on stopping power correlations which have closed form integrals for spatial profiles and on the creation of general deposition functions whose spatial forms are polynomials whose coefficients are energy dependent.

Depositions of such form can then used as forcing functions for the heat conduction equation and stress wave equation. Solutions were developed based on a Green's function technique in which the spatial dependence was analytically evaluated, and the time dependence solved by numerical integration to allow arbitrary specification of photon and ion spectra.

Displacements were calculated by transforming all interactions into effective displacement cross-sections for ion interactions. Methods were based on either a binary collision model and the expressions for local ion energy as the ion slows down, or on transformation of the nuclear energy deposition functions with a secondary defect production model.

All models were incorporated into the T-DAMEN computer code[47] whose form allows multiple responses to be evaluated and all data to be placed in forms compatible with assessment of subsequent synergistic responses.

III. D. Application and Utility

The techniques developed in this research provide a self-consistent correlation between the primary responses of materials exposed to the various ion and photon spectra from a thermonuclear radiation pulse. In addition these methods can be applied to the following specific areas in fusion reactor design:

1) Assess performance of candidate fusion first walls and other components.

Within the limitations of single phase response models, various first wall, mirror, insulator or liner materials can be examined to determine optimum choices for a specific pulsed fusion reactor concept. In addition, allowable wall radii or radiation fluxes can be determined upon the imposition of acceptable performance criteria.

2) Examine response of material to variation in output spectra.

The flexibility of arbitrary specification of radiation spectra and the efficiency of the computational techniques allow complete response assessment to be determined for a wide range of output spectral parameters. From their studies allowable yields, energy partitioning, and spectral tolerances for both ions and photons can be developed for specific designs.

3) Evaluate effectiveness of wall protection schemes.

Protection schemes which stop or alter the radiation from the source can be evaluated in terms of modification of first wall response. Response can be determined for any case in which the

flux and spectra can be specified. Specific models are included for modification of photon and ion spectra by gaseous layers.

4) <u>Evaluate the effectiveness of simulation schemes.</u>

Simulation schemes, which are proposed to test materials prior to implementation in fusion reactors, can be evaluated in terms of the response provided relative to the total synergistic response in an actual reactor exposure. In addition, structural materials for simulation devices can be evaluated.

5) <u>Evaluate rate effects on specific phenomena.</u>

Information on the transient temperature, stress, and displacement histories in a material will allow specification of the conditions which can enhance other effects such as swelling, sputtering, blistering.

6) <u>Evaluate transient gas diffusion histories.</u>

The transport of injected gas (He, T, D) and transmutation products (He, H, etc.) can be more accurately determined since the transient conditions which influence the diffusivity can be specified.

7) <u>Evaluation of transients in magnetically confined systems.</u>

Rapid energy releases in normally steady state devices such as plasma dumps in Tokamaks can be evaluated in terms of effect on the first wall or on limiters.

Chapter IV

BASIC PRINCIPLES

This chapter will briefly review the theory available for the primary interaction of photons, ions, and neutrons in materials. Discussion will be restricted to the energy ranges of interest in pulsed fusion applications. The emphasis will be on those models which can be used to reproduce cross sections in efficient numerical form. These data are then used to develop the response of materials in Chapter V, VI and VII.

IV. A. Photon Interactions

The first walls of inertially confined fusion reactors can encounter photon radiation which ranges from a few electron volts to a few million electron volts. The general relationship of these radiations to the electromagnetic spectrum is shown in Figure IV. 1.

The primary interaction of photons with materials in these energy ranges are:

- photoelectric effect

- coherent scattering

- incoherent scattering

- pair production

Cross sections for each of these reactions have been tabulated in various forms[48-50] and are available for numerical calculations.
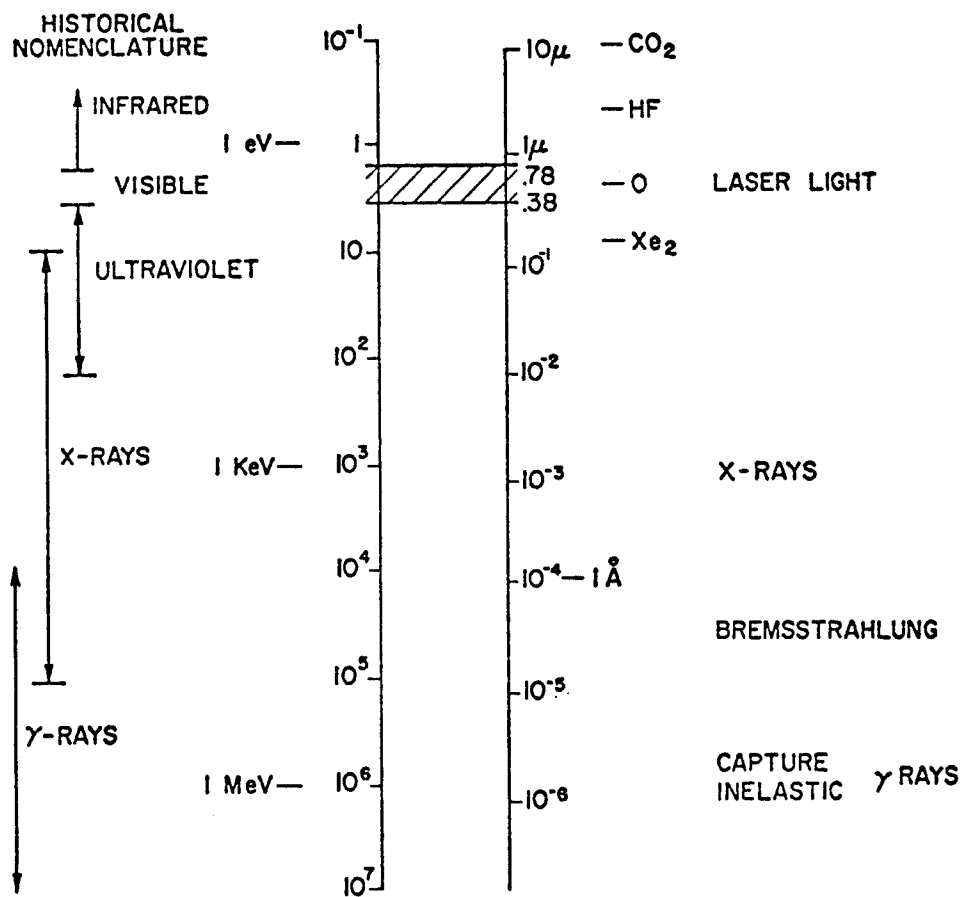
Fig. IV. 1. Electromagnetic Spectrum

A brief discussion of the material and spectral dependence of the cross sections is, however, appropriate before development of material response from the radiation.

IV. A. 1. Pair Production

At the high energy end of the spectrum pair production will be the dominant contributor to the total cross section. The pair production process is a photon-matter reaction which occurs when the electric field of the photon interacts with the electric field of an atomic nucleus. The incident photon is destroyed and a positron-negatron electron pair is created. Mathematically,[51] the theory is similar to the bremsstrahlung process in which an electron undergoes a transition in which a photon is emitted. In pair production, the photon is absorbed and an electron undergoes a transition out of a negative energy state into a positive energy state leaving a hole in the negative state or a positron. The reaction necessarily has a threshold energy of $2\ m_o c^2$ (1.02 MeV).

The interaction rate is dependent on the nuclear cross section and is therefore proportional to Z^2 of the absorbing material. Both the differential cross section in relation to the energy shared by the positron and the total cross section, obtained by integrating over all positron energies, have analytic expressions[46] and accurate approximations.[52] Since the process is a nuclear interaction, the cross-section is simply proportional to the nuclei density and Z^2 as above. A reasonable approximation (except for minor screening correction at high energies) for the total cross-section can be deter-

mined as a function of a standard cross-section for a material such a lead as:[51]

1) $$\mu_{pp} = \frac{\rho}{11.35} \frac{207.2}{A} (\frac{Z}{82})^2 \mu_{PP}^{Pb}$$

where μ_{pp} = pair production attenuation coefficient (cm^{-1})

ρ = material density (g/cm^3)

A = atomic weight (amu)

Z = atomic number

and μ_{pp}^{Pb} is given by Figure IV. 2.

The energy absorbed is normally taken as the kinetic energy of the electron-positron pair as:

2) $$\mu_a^{PP} = \mu(1 - \frac{2m_o c}{E})$$

where μ_a^{PP} = pair production energy absorption coefficient

E = photon energy

However, the energy lost by the photon is not the local energy deposition, since both the electron and positron have finite ranges in solid materials.
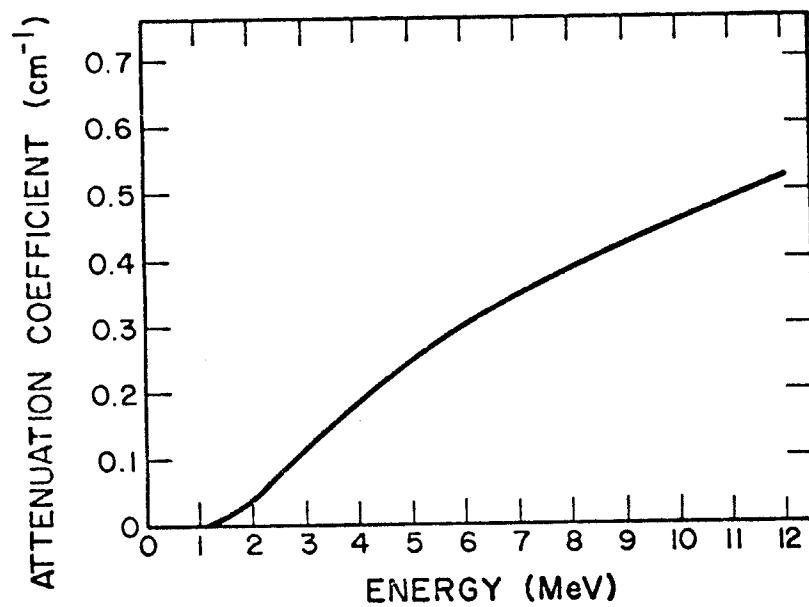
Fig. IV. 2.   Pair Production Cross Section of Lead

IV. A. 2. Incoherent Scattering

At intermediate energies the principle photon interaction can be incoherent (or Compton) scattering. In this process, energy is given by an incident photon to an electron and results in a scattered photon. The incoherent scattering cross-section can be derived using quantum electrodynamics and is given by the Klein-Nishina formula for unpolarized incident radiation as:[51]

$$3) \quad \frac{d\sigma}{d\Omega} = \frac{r_o^2}{2} [1+\chi(1-\cos\Theta)]^{-3} [1+\cos^2\Theta + \frac{\chi^2 (1-\cos\Theta)^2}{1+\chi (1-\cos\Theta)}]$$

$$\frac{d\sigma}{d\Omega} = \text{differential cross section, } (cm^2/\text{electron})$$

where $\quad \chi = E/m_o c^2$

r_o = classical electron radius = 2.818×10^{-13} cm

Θ = scattering angle

E = photon incident energy

This is the cross section for one electron and, since Compton scattering implies incoherent field superposition, each electron adds independently. Thus, for a given material, the above formula is multiplied by Z to get the differential cross section per atom. Equation 3 can be integrated to give the total cross section as in Evans [15] in a form which is difficult to evaluate numerically. However, Biggs[53] gives a useful approximation as:

4) $\sigma^{kn}_{tot} = 0.4006 \dfrac{Z}{A} \left[\dfrac{1 + 1.148 + 0.6141X^2}{1 + 3.171X+0.9328X^2 +0.02572X^3}\right](\dfrac{cm^2}{gm})$

Both Equation 3 and 4 are for free electrons and must be corrected for electron binding effects. These corrections are made in reference[52] and will not be repeated here since the effect is most important for low photon energies where the incoherent cross section is a small contribution to the total cross section.

The portion of the incident photon energy which is deposited as kinetic energy of the electrons can be expressed in terms of an energy absorption cross section. The energy absorption cross section may be derived from Equation 3 by multiplying by the energy fraction given to the electron and integrating over all angles. Again the exact analytical expression is not convenient for numerical approximation and Biggs[53] proposes the following approximation:

5) $\sigma^{kn}_a = 0.4006 \dfrac{Z}{A} \left[\dfrac{X + 0.825X^2 + 0.0323X^3}{1+5.393X +5.212X^2 +0.878X^3 +0.01599X^4}\right]$

units $= cm^2/gm$

As before, an alternate energy absorption cross section can be derived which accounts for electron binding. Commensurate approximation of these results are also available for efficient numerical evaluation.

IV. A. 3. Coherent Scattering

As the energy of the incident photon is reduced to low enough frequencies where the momentum can be ignored, Equation 3 approaches the classical formula for Thompson scattering for isolated electrons as:[54]

$$6) \qquad \frac{d\sigma}{d\Omega} = \frac{r_o^2}{a} \quad (1 + \cos^2\theta)$$

If Equation 6 is integrated over all directions, the total Thompson scattering cross section is obtained:

$$7) \qquad \sigma_c = \frac{8\pi}{3} \; r_o^2 = 0.665 \text{ barns/electron}$$

If Equation 6 is to be applied to a population of electrons it is necessary to account for the coherent effect of all the particles. This approach gives an intensity proportional to Z^2 and is limited to small scattering angles whose magnitudes are inversely proportional to the incident photon energies. Consequently, when this angular distribution and the effects of electron binding are accounted for, the total coherent cross section falls off with increasing energy.

Since coherent scattering is elastic, it does not result in any net loss of photon energy, and there is no significant local deposition of energy.

IV. A. 4. Photoelectric Effect

At low photon energies the total photon cross section is dominated by the photoelectric cross section in which a photon transfers all its energy to an electron in the vicinity of a nucleus. The electron is emitted (Auger electron) with the photon energy minus its binding energy.

A universal theoretical treatment does not exist for the photoelectric effect; consequently empirical data are used in determining cross section values. A convenient form for fitting photoelectric cross section has been proposed by Biggs and Lighthill as:[46]

$$8) \qquad \sigma_j = \sum_{k=1}^{4} C_{jk} \, e^{-k} \qquad cm^2/gm$$

where a set of four parameters, C_{jk}, are used for fitting the data within discrete energy intervals characterized by the parameter j. It is necessary to break the spectrum into different intervals in order to properly account for absorption edges.

The local energy absorption is usually determined by discounting the energy associated with the K shell fluorescence. This is essentially the same as deducting the binding energy from the photon energy and it reduces the total photoelectric cross section somewhat.

In general, the photoelectric cross section shows a very strong material and spectral dependence. Useful approximations for these dependencies are given by Evans[51] for energies away from absoprtion edges as:

9) $$\sigma_{pe} \propto (Z/E)^{3 \text{ to } 4}$$

IV. A. 5. Low Energy Photon Attenuation

Electromagnetic radiation in the near visible range (e.g., from reflected lower light) cannot be adequately described by the cross sections previously presented. Hovingh[25] has proposed a simple relation based on the propagation of electromagnetic radiation in homogeneous, isotropic, conducting media. This relation can be developed from basic electrodynamics[55] in the following manner:

The combination of Maxwell's equations and the relation of current density to the electric field in a conducting material,

10) $$J = \sigma E$$

yields the following relation for the electric vector:

11) $$\nabla^2 E = \frac{4\pi\sigma\mu}{c^2} \frac{\partial E}{\partial t} + \frac{\mu}{c} \frac{\partial^2 \xi E}{\partial t^2}$$

where J = current density

σ = specific conductivity

E = electric vector

c = velocity of light

μ = magnetic permeability

ξ = dielectric constant

Taking a Fourier transform in time and space gives the complex wave number as:

12)
$$k^2 = \frac{\omega^2 \xi \mu}{c^2} \left(1 + i \frac{4\pi\sigma}{\omega\xi}\right)$$

Since the electric vector goes as $e^{i(kx-\omega t)}$ and the energy goes as E^2, the imaginary part of the wave number, multiplied by 2, gives the energy attenuation. Thus

13)
$$k'' = \left[\frac{\sqrt{1 + \left(\frac{4\pi\sigma}{\omega\xi}\right)^2}}{2} - 1\right]^{1/2} \sqrt{\xi\mu} \quad \frac{\omega}{c}$$

for a conductor $\dfrac{\pi\sigma}{\omega\xi} \gg 1$ and

14) $\Sigma = 2k'' = \sqrt{\dfrac{8\pi\mu\omega\sigma}{c^2}} = 4\pi \sqrt{\dfrac{\mu\sigma}{\lambda c}}$

where Σ = attenuation coefficient

ω = frequency

λ = wavelength

k = wave number, k'' = imaginary part

The absorbed energy can be determined by determining the reflectivity at the surface

15) $$R = \left| \frac{n-1}{n+1} \right|^2 \qquad n = \text{complex refractive index}$$

which for metals becomes

16) $$R = 1 - 2\sqrt{\frac{c}{\sigma\lambda}}$$

The absorptivity is then

17) $$\alpha = 1 - R = 2\sqrt{c/\sigma\lambda}$$

If the assumption is made that the surface is a black body $\alpha = 1$ and by multiplying Equation 14 by Equation 17, the attenuation coefficient can be found as

18) $$\Sigma = \frac{8\pi}{\lambda} \qquad (\text{cm}^{-1})$$

This development is based on principles which are derived for low frequency radiation and do not take into account the numerous phenomena which should be considered for photons with approximately 1 eV energy. Values from this relation are nevertheless plotted with the other cross sections in Figure IV. 3 for comparison. Further investigation is necessary to obtain realistic values for laser irradiation. It is likely that only empirically determined values will be available.
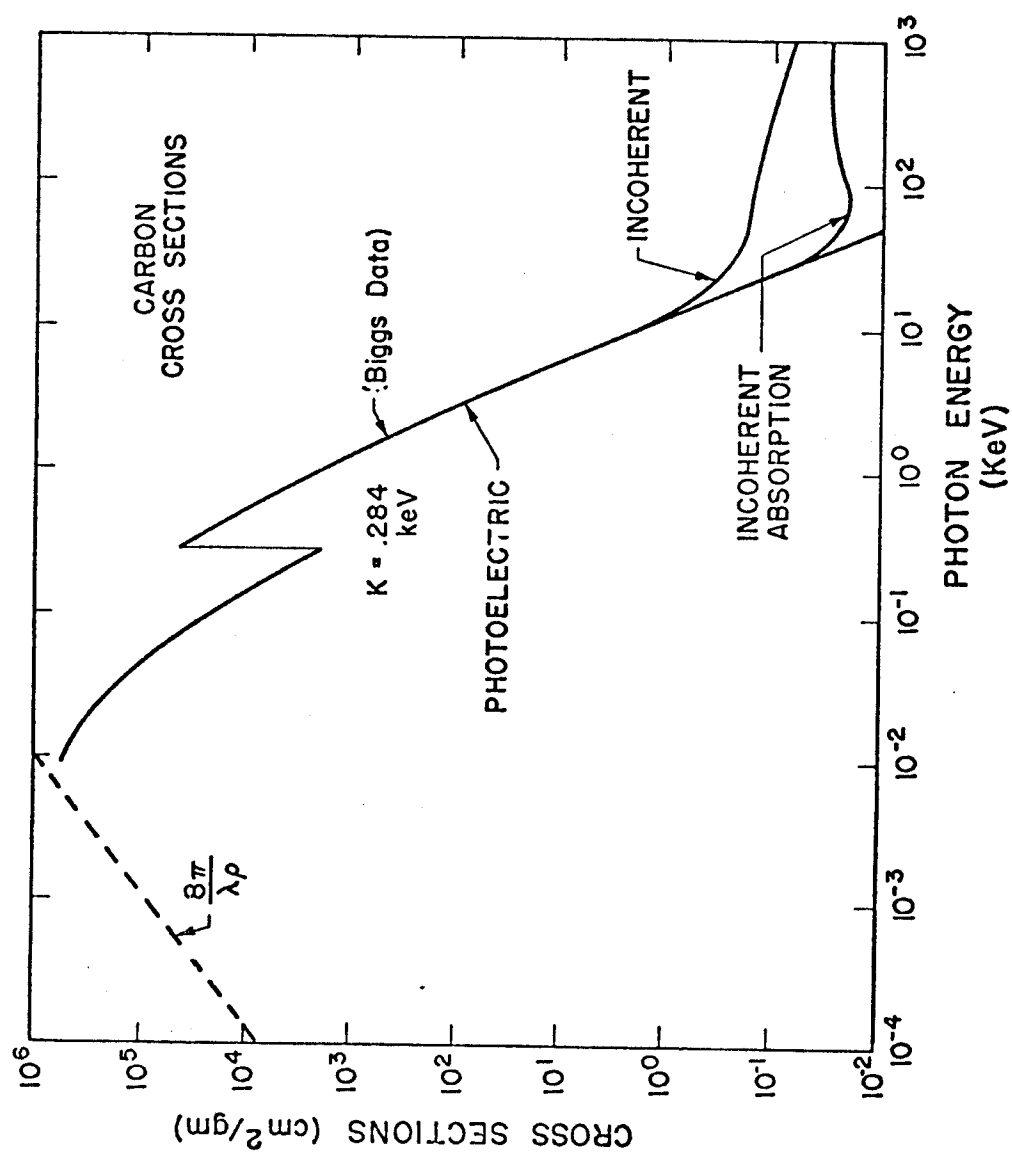
Fig. IV. 3. Carbon Photon Cross Sections

IV. A. 6. Comparison of Cross Sections

A comprehensive tabulation of parameters to be used in the previous equations have been made by Biggs.[46] These values have been examined for accuracy by comparing with other cross section files such as ENDF/B and by Simmons and Hubbell.[56,57] An example of the cross section from reference 46 for carbon and x-ray energies from 10 eV through 1 MeV was shown in Figure IV. 3.

An increase of a factor of 10 in the photoelectric cross section is noted at the K shell resonance (284 eV for carbon). This effect will result in a marked spectral sensitivity for first wall response and will be important for all materials. Figure IV. 4, from data taken from reference 58, shows how the absorption edges vary with atomic number.

Determination of the energy deposited from a given spectrum must account also for transport of any scattered photons. If, however, the primary interaction is photoelectric effect, the scattering can be ignored and an exponential deposition profile can be assumed. A reasonable criterion for determining if a spectrum is in the photoelectric region can be found from examination of Figure IV. 5 which displays the ratio of the photoelectric cross section to the total cross section. As shown, the photoelectric effect comprises 90% of the interactions for photon energies up to 10 keV, 30 keV, 70 keV for carbon, iron, and molybdenum respectively.

A summary of the qualitative material and spectral dependence of the basic attenuation mechanisms is given in Table IV. 1.
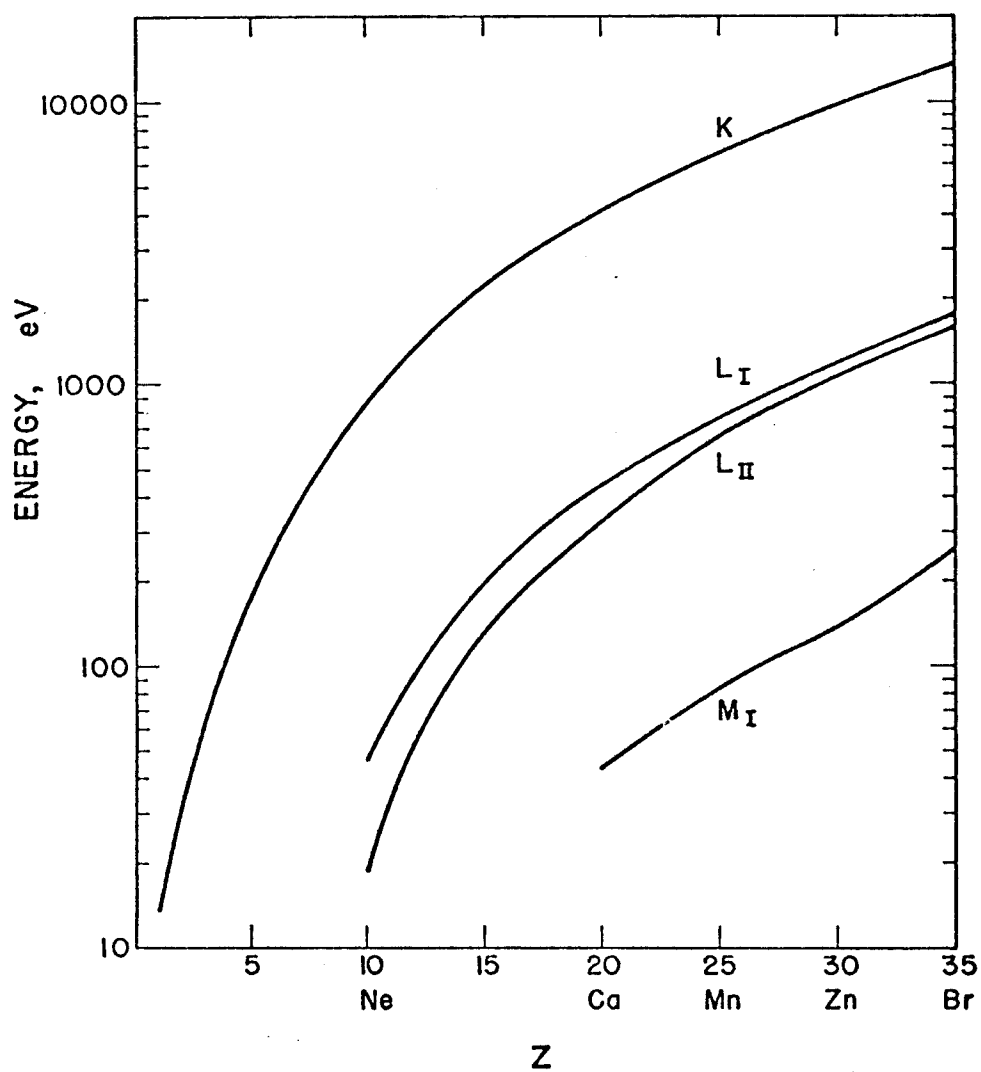
Fig. IV. 4.   X-Ray Atomic Energy Levels
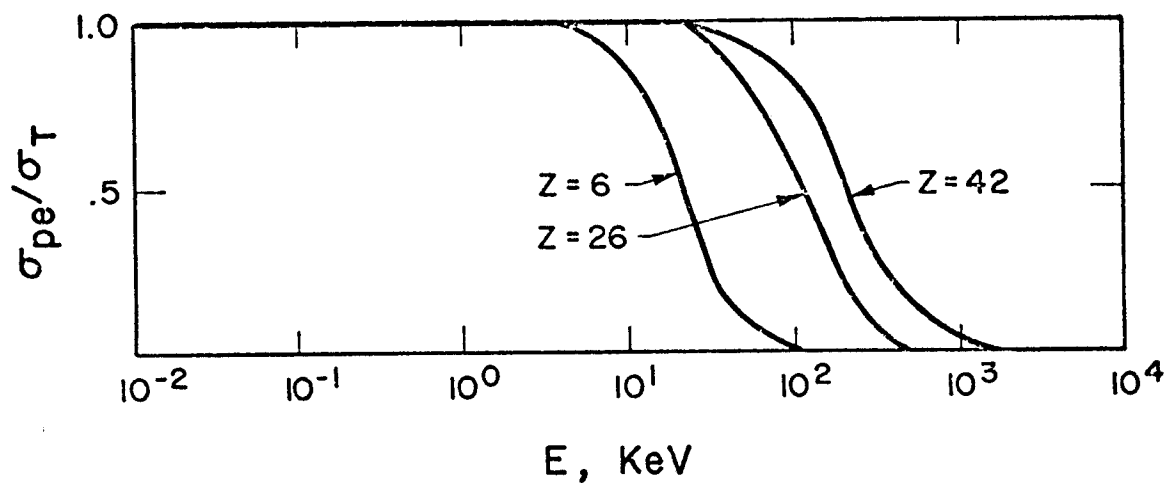
Fig. IV. 5.   Ratio of Photoelectric to Total Cross Section

Table IV. 1

MATERIALS AND SPECTRAL DEPENDENCE OF PHOTON CROSS SECTIONS

	Photo Electric	Coherent	Incoherent	Pair Pro- duction
Atomic Number	$Z^{3 \text{ to } 4}$	Z	Z	Z^2
Energy	$(1/E)^{3 \text{ to } 4}$	$(1/E)^{1 \text{ to } 2*}$	NSR	E

*E > 10 keV   NSR = no simple relationship

IV. B.   Ion Interaction

The slowing down of ions in materials is primarily due to two processes: the interaction of the electric fields of the ion with the electrons in the material (inelastic) and the collision of the ion with nuclei (elastic). The relative importance of these two phenomena is dependent upon the instantaneous energy of the ion and the energy loss associated with each can be determined if appropriate interaction potentials can be specified. For particles other than electrons, any radiation losses such as bremsstrahlung or Cerenkov can be neglected if the energies do not exceed 10 MeV.

IV. B. 1.   Electronic Energy Loss

The interaction of a charged particle with the electrons in a material is usually divided into three energy regimes: (i) a high energy regime in which the velocity of the particle greatly exceeds the velocities of the orbital electrons, (ii) an intermediate energy regime in which these velocities are on the same order, and (iii) a low energy regime in which the velocity of the particle is much smaller than the orbital velocities of the electrons.

The first region was investigated years ago by Bohr,[51] Bethe,[59] Bloch[59] and Fermi.[54] The most commonly accepted formula is that by Bethe-Bloch which is a quantum mechanical derivation of the original classical result by Bohr. The Bethe-Bloch formula for non-relativistic velocities is given as:

$$19) \quad \left.\frac{dE}{dx}\right)_e = \frac{4\pi Z_1^2 e^4 \; NZ_o}{m_o v^2} \; \ln \; \frac{2m_o v^2}{I}$$

where Z_1 = particle charge

   e = electron charge

   N = atom density

   Z_o = material atomic number

   m_o = electron mass

   v = particle velocity

   I = mean ionization potential

The parameter I is a representation of the lower limit over which energy can be transferred in a coulomb collision and is given approximately by[51]

$$20) \quad I = 12Z \; (ev)$$

In practice, I becomes an empirically adjusted factor for each target material. Numerous modifications have been proposed to equation 19 but in general its energy dependence is reasonable accurate.

The most general treatment of fast particles in matter is given by the Fermi formula[54] which accounts for the modification of the electric field of the particle by the dielectric characteristics of the material. This formula will not be repeated here since it is most applicable at very high energies $(E > 5mc^2)$, where m is the particle mass. Implicit in all the above models is total stripping of

all electrons from the incident ion.

At low energies the particles tend to retain all their electrons and can be modeled by treatments developed by Lindhard[60] (LSS) or Firsov.[61] In these models the energy loss is attributed to the electron flux between colliding atoms and is consequently proportional to the particle velocity. The Lindhard model for electronic losses is normally presented in non-dimensional form as:

21)
$$\frac{d\epsilon}{d\rho} = k \; \epsilon^{\frac{1}{2}}$$

where $\epsilon = E/E_L$

$\rho = R/R_L$

$$k = \frac{0.0793 \; z_1^{2/3} \; z_2^{1/2} \; (1+A)^{3/2}}{(z_1^{2/3} + z_2^{2/3})^{3/4} \; M_2^{1/2}}$$

where Z_1e = particle charge

Z_2e = target charge

A = ratio of target mass to particle mass

M_2 = target mass (amu)

and
$$E_L = \left[\frac{1+A}{A}\right] \; \frac{Z_1 Z_2 e^2}{a} \quad \text{(ergs)}$$

$$R_L = \frac{(1+A)^2}{4A_\pi N a^2} \quad \text{(cm)}$$

$$a = 0.4683 \; (z_1^{2/3} + z_2^{2/3})^{-1/2} \; \times \; 10^{-8} \quad \text{(cm)}$$

N = target atom density (a/cm^3)

In a more practical form

22)
$$\frac{dE}{dx} = C\ E^{\frac{1}{2}} \qquad (keV/\ \mu m)$$

where $C = \dfrac{k\ (E_L/1.602 \times 10^{-9})^{\frac{1}{2}}}{R_L \times 10^4}$

Equations 21 or 22 are normally considered applicable for particle velocities below the orbital velocity of the target electrons. Assuming a Thomas-Fermi atomic model, this maximum energy becomes:

23)
$$E_{max} = 25\ M_1\ Z_1^{4/3} \qquad (kev)$$
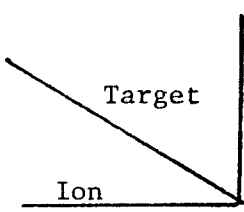
where M_1 = particle mass (amu)

A tabulation of LSS parameters for various ions target combinations is given in Table IV. 2.

The intermediate energy regime between the upper limit of LSS theory and the Bethe-Bloch has no basic theoretical treatment at present. This region is characterized by a partially ionized particle. As a result, modifications to the effective charge and the interaction with outer shell electrons are sometimes incorporated into the Bethe-Bloch model which in its standard form (Eqn. 19) predicts a greater stopping power than observed experimentally.

Table IV. 2

LINDHARD PARAMETERS

$$\{\frac{k}{E_L(keV)}\}$$

Ion \ Target	C	Al	Ni	Mo	Ta	U
C	.127 / 5.7	.208 / 10.3	.388 / 22.0	.601 / 34.2	1.10 / 65.4	1.44 / 86.8
Al	.105 / 23.2	.142 / 34.6	.228 / 62.8	.328 / 90.3	.567 / 161.	.730 / 208.
Ni	.103 / 108.	.119 / 136.	.161 / 207.	.209 / 269.	.326 / 430.	.407 / 537.
Mo	.104 / 273.	.112 / 320.	.137 / 440.	.165 / 533.	.236 / 784.	.285 / 950.
Ta	.111 / 987.	.113 / 1080.	.124 / 1330.	.137 / 1480.	.173 / 1940.	.199 / 2240.
U	.115 / 1720.	.115 / 1840.	.122 / 2180.	.131 / 2360.	.157 / 2940.	.176 / 3320.

A comprehensive semiphenomenological model has been proposed by Brice[42] which can predict the electronic stopping for all three energy regimes. This model is based on a modification of the Firsov method by giving a quantum mechanical treatment of the electron flux between adjacent interacting particles in terms of bound state wave functions. When this formalism is used with a hydrogenic 1s wave function, a general relationship is determined which depends on only three adjustable parameters which can be determined from experiments. One parameter is necessary for the low energy regime and the other two are used for extension to higher energies.

The result of this model is given[45] by the following formulae:

24) $\quad S(E) = N\ (Z_1 + Z_2)\ S_e\ (u)\ f(u)$

where $\quad S(E)$ = electronic stopping power (eV/cm)

$\qquad\qquad E$ = particle energy (keV)

$\qquad\qquad Z_1$ = particle atomic number

$\qquad\qquad Z_2$ = target atomic number

$\qquad\qquad N$ = target atomic density (a/cm^3)

and

25) $\quad S_e(u) = A\ \left(u^{\frac{1}{2}}\ [\dfrac{30u^2 + 53u + 21}{3(1 + u)^2}] + (10u + 1)\ \arctan(u^{\frac{1}{2}}) \right)$

$\quad A = 0.60961 \times 10^{-15}\ \text{eV-cm}^2/\text{atom}$

$\quad u = E/(\ \zeta^2 M_1 E_1)$

where M_1 = particle mass (amu)

E_1 = 100 keV

* ζ = adjustable parameter

and

26) $\quad f(u) = [1 + (4 \zeta^2 a'^2 u)^{n/2}]^{-1}$

*a' = adjustable parameter

*n = adjustable parameter

The three adjustable parameters can be determined from sources of reliable experimental data or semi-empirical values determined from data in each of the three energy regimes. A tabulation of a significant number of calculations for various ions and targets has been compiled in reference 45. In this reference parameters were determined from Ziegler and Chu[62] for the ions and the tabulated stopping powers of Northcliffe and Schilling.[63] The former represents a tabulation of at least squares fitting to a large number of published experimental results and an interpolation to other materials by correlating with theoretical models for the Z dependence of stopping power. The latter is based on determining relative stopping cross sections for other materials and comparing with a set of particular known set of cross sections (aluminum in this case).

A comprehensive tabulation of stopping powers and range data have recently been completed by Ziegler and Anderson.[64] Extensive data, both experimental and analytical fits, are given for Hydrogen, Helium, and heavier ions. An extensive bibliography is also included.

An example of electronic energy loss from the previously discussed models is shown in Figure IV. 6. The LSS model is seen to predict large stopping powers (about 45% high) in the low energy region. The Bethe-Bloch model (BB) is normalized to the experimental points by adjusting I to 20 eV and shows a gross divergence at low energies. The Brice model, however, gives a reasonable fit over the entire spectrum.

IV. B. 2. Nuclear Energy Loss

Elastic collisions of a moving particle with the nuclei will be a competing process for reducing the kinetic energy of the particle. The rate of interaction will be determined by the nuclear cross section. Theoretical values for nuclear cross sections are determined by the interatomic potential chosen between the nuclei and the particle.

The most widely accepted model is the nuclear elastic cross section derived by Lindhard[60] in which a relatively simple analytic expression is derived using a shielded Coulomb interaction with a Thomas-Fermi atomic model. The differential cross section is given by:[45]
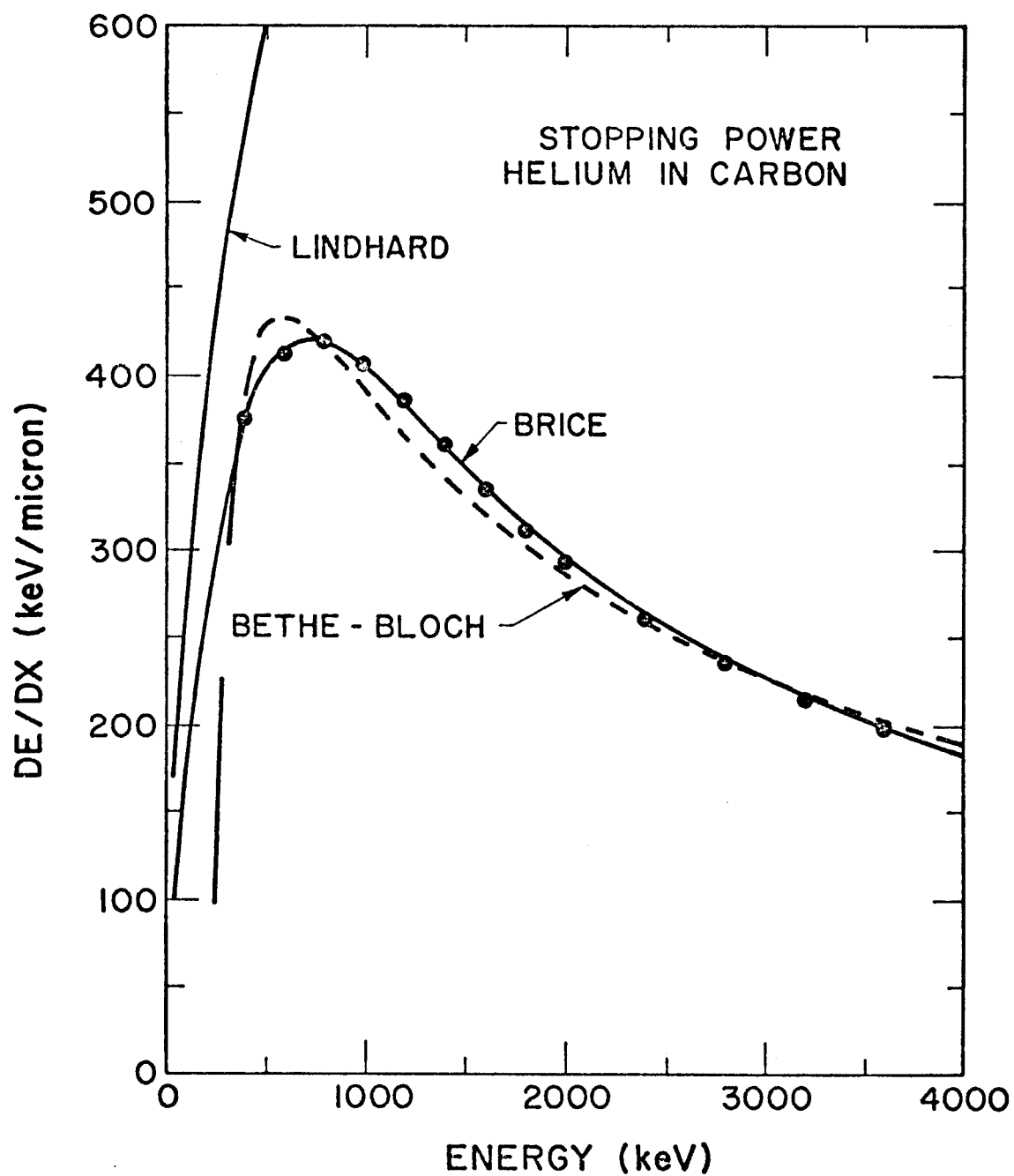
Fig. IV. 6. Comparison of Electronic Stopping Power in Carbon

27) $$d\sigma \ (E,T) = \pi a^2 \ f(t) \ dt/t^2$$

where   E = particle energy

         T = kinetic energy of the struck atom after the collision

         a = screening parameter given by:

$$.8853 \ a_o/(z_1^{2/3} + z_2^{2/3})^{1/2}$$

      a_o = Bohr radius

    f(t) = is a tabulated scattering function (ref. 45)

      $t = E/E_o \sqrt{T/T_m}$

and $E_o = Z_1 Z_2 e^2 \quad (m_1 + m_2)/am_2$

$$T_m = \text{maximum energy transferable} = \frac{4m_1 m_2 E}{(m_1 + m_2)^2}$$

The total elastic cross section is obtained by integrating Equation 27 over all possible energy transfers. The average energy lost per collision can also be obtained and an expression derived for the energy loss per unit path length. An approximation put in the same non-dimensional form as the electron loss is given by Oen and Robinson[65] as:

28) $$\left(\frac{d\varepsilon}{d\rho}\right)_n = \frac{9}{8\varepsilon} \ \{\ln[u + (1 + u^2)^{1/2}] - u \ (1 + u^2)^{-1/2}\}$$

where $\epsilon = E/E_L$, $\rho = R/R_L$ as before

$$u = (2\lambda)^{1/3} \epsilon^{4/9}$$

$$\lambda = 1.309$$

A qualitative measure of the relative roles of electronic loss versus elastic or nuclear loss can be seen in Figure IV. 7 which is taken from data in reference 45 for Helium into a carbon target. Obviously the nuclear energy loss is very low over the range of energies listed and, as a general rule, the electronic loss will dominate down to "A" keV where A is the particle mass in amu. Thus for high energy particles the nuclear energy deposition is negligible since a 400 keV alpha particle would dissipate 80% of its energy before the nuclear contribution was .1% of the electronic.

The relationship between nuclear and electronic energy loss can be in the non-dimensional form of LSS theory given by Figure IV. 8.[60] These data indicate that considering the range of the parameter "$\underline{k}$" a more practical criterion for the lower limit of the energy region where electronic process dominate would be a reduced energy value of approximately 5.

Additional data will be given for ion interactions both electronic and nuclear in Chapter V where the concept of general deposition functions is introduced and displacement cross sections are developed from nuclear interaction data.
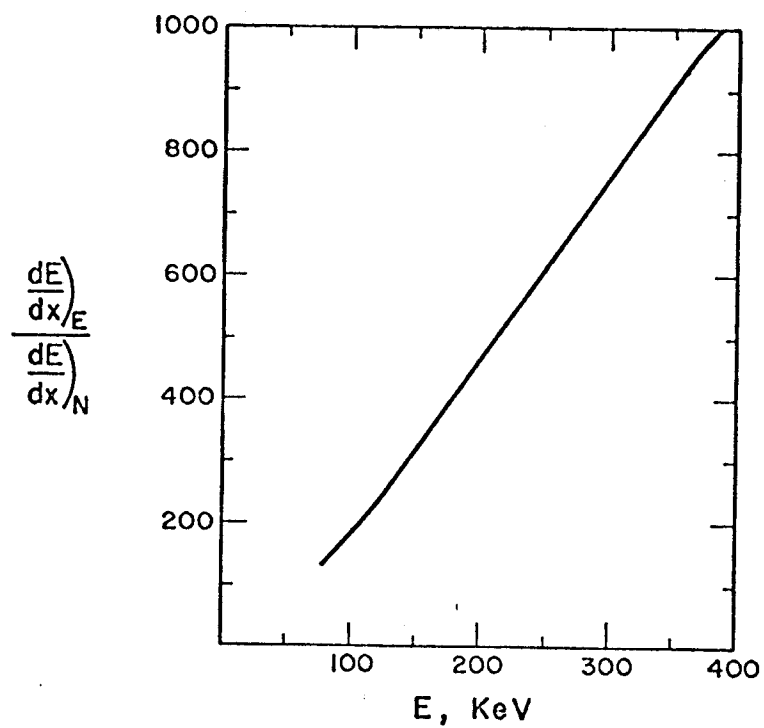
Fig. IV. 7. Ratio of Electric and Nuclear Energy Loss for Helium in Carbon
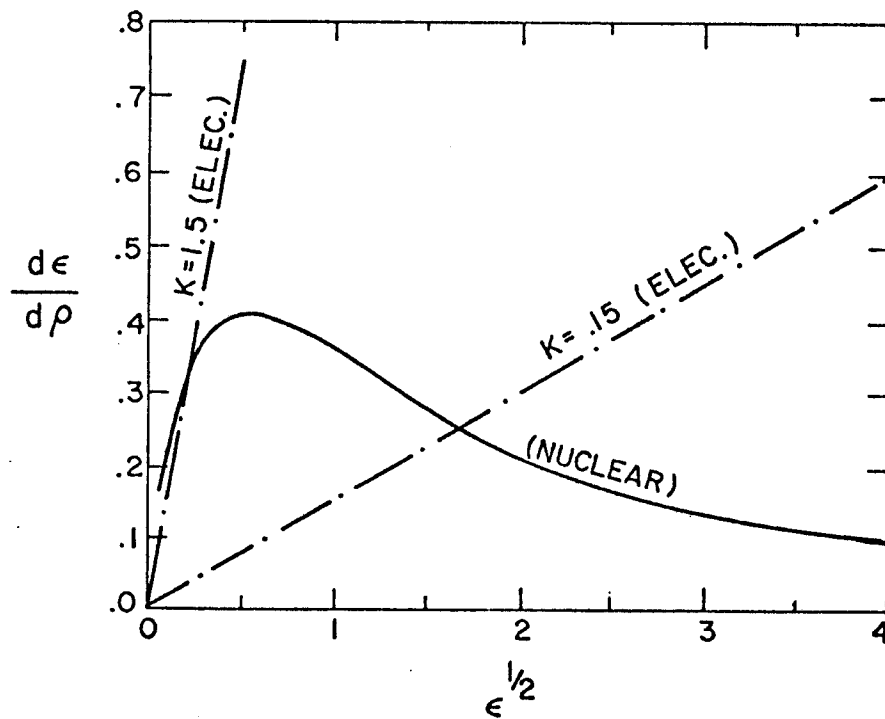
Fig. IV. 8. LSS Stopping Functions (Ref. 60)

IV. C. Neutron Interactions

The primary interaction rates in first walls to the current
of neutrons from a pulsed fusion source will be determined by the
corresponding neutron cross sections of the material. Each possible
reaction will deposit some local energy and produce products such
as neutrons, charged particles, or photons. A discussion of the
theory of all possible cross sections would be inappropriate here,
but a brief discussion of the amplitudes of the reaction rates will
be informative.

The local heating due to neutrons can be determined from the
neutron flux and knowledge of an energy dependent KERMA* factor.
Recent work by Abdou, et al.,[66] have determined such KERMA factors
for most potential fusion materials. These have been used to es-
tablish heating rates in magnetic confinement fusion reactors.[67]
An example of this work for low Z elements is shown in Figure IV. 9.
Carbon is typical of a nuclide in which the elastic scattering is the
primary interaction up through the MeV region making the KERMA
factor almost proportional to the energy. A rough estimate of the
volumetric heating rate from source neutrons can be made by simply
multiplying the 14 MeV KERMA factor by the integrated neutron wall
current for a laser fusion pulse (Table I. 2), yielding a volumetric
energy deposition of approximately 1 J/cm^3.

---

* KERMA = Kinetic Energy Released in Materials.
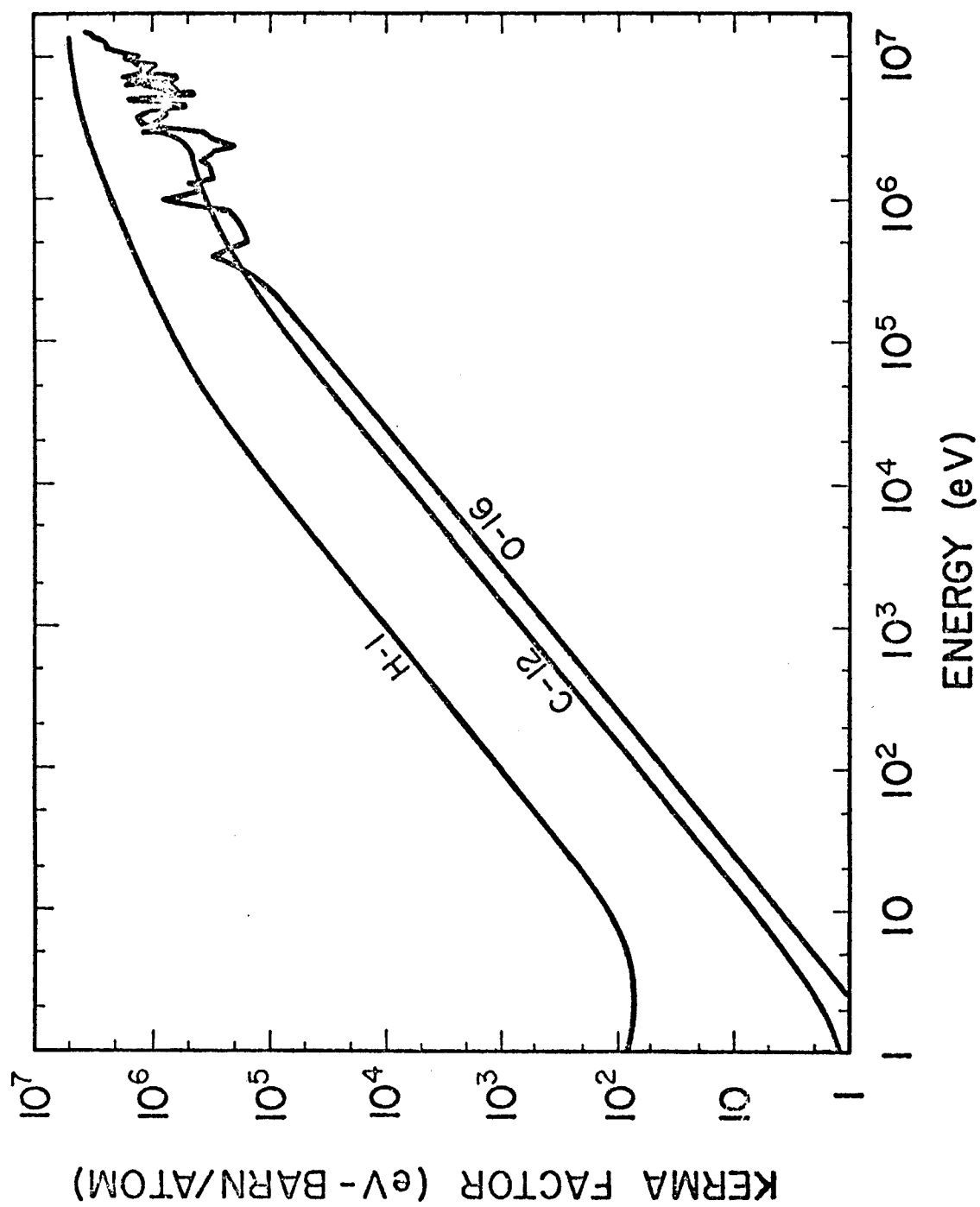
Fig. IV. 9. Neutron KERMA Factors (Ref. 67)

This small deposition of energy represents a temperature increase of about 0.2°C/pulse and thus represents an insignificant perturbation to the pulse heating. This energy will however contribute to the net operating temperature of a first wall.

A proper analysis of the neutron heating can only be done by performing a neutron transport calculation for the entire reactor blanket. Determination of the neutron and gamma flux in the first wall multiplied by the previously discussed KERMA factor will yield the total heating. Calculations of this kind have been performed with the ANISN code[68] for simple spherical blankets and the total heating was found to be about a factor of 2 higher than the simple example above.

The total number of atomic displacements occurring during each pulse can also be estimated in a similar fashion. The displacement cross section for stainless steel is approximately 2220 barns[69] assuming an effective displacement energy of 40 eV. The number of displacements from a source current of 1.7×10^{13} n/cm^2 would be 3.8×10^{-8} dpa. A comparison with time dependent ANISN[68] again shows this is about 50% of the total displacements per pulse.

Similar estimates can also be made for gas production and other transmutation reactions. Interaction rates reactions which have threshold energies of a few MeV can be accurately estimated by the above simple procedure since the source current is the primary contribution to the high energy portion of the neutron spectrum.

Chapter V

RESPONSE OF MATERIALS TO PULSED IRRADIATION

This chapter presents the models developed in this research which can be used to determine the energy deposition, temperature, stress, and displacement production response of materials to an arbitrary set of radiation spectra.

As an introduction, discussion is presented on the use of representative spectra to parameterize the various radiation components. In addition, examples of the time history of first wall loadings and fluxes for selected photon and ion spectra are given to establish the general time domain of the response functions. Specific examples of complete spectra and responses will be given later in Chapter VII.

V. A. Spectra and Wall Loading

Specific spectra for certain pellets were discussed in the previous section. These spectra are dependent on the details of the energy source - pellet-fusion interaction and can only be described in detail by sophisticated computer codes such as LASNEX,[70] which will not be discussed here. However, the response of a first wall can be determined if the photon, ions, and neutrons are characterized by common spectral forms. The wall loading of various particles for a given spectrum can then be found by determining the

spectral dependence of the energy deposition and an assumption

about propagation of energy from the source to the wall.

V. A. 1. Photon Spectra

An often used spectrum for low energy photons is the "Black

Body" or Plankian spectrum[71] which is used when radiation emission

is characterized by the temperature of the emitter. A 1 keV black-

body spectrum with a total fluence of 1 Joule/cm^2 is depicted in

Figure V. 1 and is given in practical units by the relation:

1) $$S(E) = \frac{B}{kT} \left(\frac{U^3}{e^U - 1} \right) \quad (J/keV-cm^2)$$

where $U = E/kT$

   kT = characteristic energy, (keV)

   $B = 15 \ F/ \ \pi^4$

   F = total fluence (J/cm^2)

Although the limits on the spectra are 0 and ∞ , integration

from .1 kT to 10 kT yields 99% of the total fluence.

In a medium with a frequency-independent dielectric constant

the propogation of all energies will be at the same velocity. As a

result the wall loading from source photons will occur at the time

$\frac{R}{c}$ after creation. The temporal shape of the source will be the
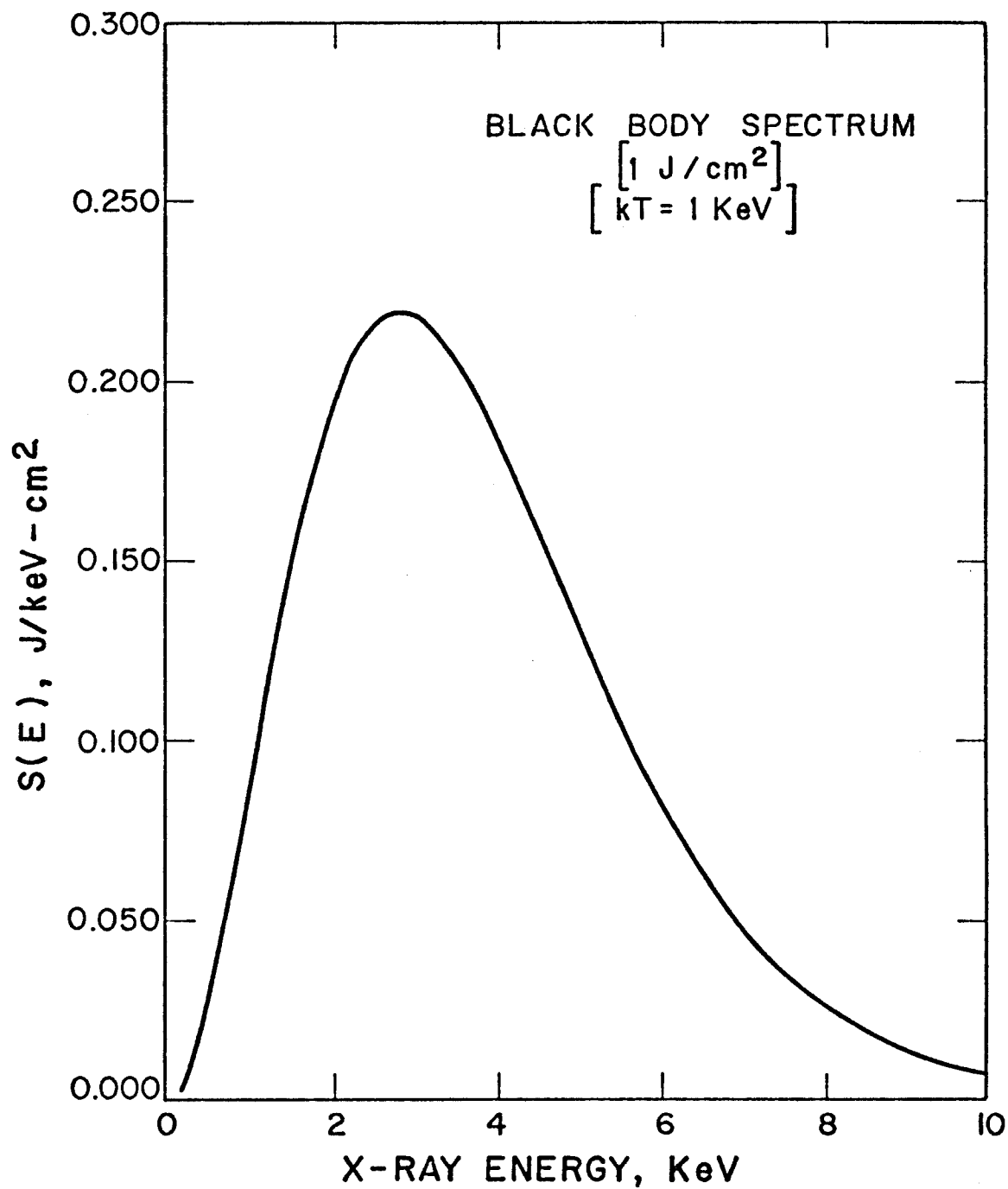
Fig. V. 1. Blackbody Photon Spectrum

temporal shape of the loading pulse. Thus the photon wall loading rate is independent of the spectrum. The x-ray production time quoted for D-T pellets has been quoted as approximately 10 psec.[72]

V. A. 2. Ion Spectra

The true ion spectra from a fusion source can again only be determined by a complicated calculation from LASNEX[70] or other codes as stated previously. However, pellet debris calculations[25] indicate that reasonable characterization can be made with either a Maxwellian or Gaussian distribution. A Maxwellian is characterized by a mean energy E_m and can be represented in the practical form:

2) $$S(E) = \frac{2N}{\pi^{\frac{1}{2}} E_m} \left(\frac{E}{E_m}\right)^{\frac{1}{2}} e^{-E/E_m} \qquad (1/keV)$$

where E_m = characteristic energy

E = ion energy (keV)

N = total number of ions or ions/cm^2
if F is to be a fluence

The Gaussian distribution is useful when a spectrum of a specific width is required. Two parameters are necessary to describe the distribution as:

3) $$S(E) = \frac{N}{\sqrt{2\pi}\,\sigma} e^{-\frac{1}{2}\left(\frac{E-E_m}{\sigma}\right)^2} \qquad (1/keV)$$

where E_m = mean energy (keV)

σ = standard deviation (keV)

Both spectra range from 0 to ∞ but practical limits of $E_m/8$ to 4 E_m yield 91% of the total fluence in Maxwellian distribution; similarly, a range of $\pm 2\ \sigma$ yields 95% of the total for a Gaussian distribution.

If the ion production time is short compared to the transit time to the first wall, the entire ion distribution may be assumed to be created as an impulse function in time at a single point in space. The time duration of the loading of the first wall will be determined by the time for each species to arrive. This assumption is only valid for collisionless plasma which does not have significant self encounters or encounters with gas species which reside in the chamber. If significant collisions with chamber gas atoms, a spherical blast wave can be generated[22] and hence a loading pulse applied to the first wall. A general method for estimating the effect of chamber gas on ion spectra is presented in section V. F.

In the collisionless case, the loading function for the first wall may be derived for a given wall radius if the spectrum at $t = 0$ and $r = 0$ is specified. This can be done by transforming the distribution from energy to time as:

4) $S\ (E)\ \ dE = -F(t)\ dt$

5) $t = B/E^{\frac{1}{2}}\ \ (sec)$

where B = 2284 x 10^{-9} r A

r = wall radius (meters)

A = ion mass (amu)

thus

6) $\qquad F(t) = S(E)\dfrac{2E^{3/2}}{B} \qquad (sec^{-1} cm^{-2})$

The incident energy arrival rate is given by

7) $\qquad W(t) = F(t) \ 1.6 \ x \ 10^{-16} \ E \ (J/sec \ -cm^2)$

where E = keV

and the pressure due to the momentum of the particles is

8) $\quad P(t) = 7.29 \ x \ 10^{-17} \ A^{\frac{1}{2}} \ E^{\frac{1}{2}} \ F(t) \quad (dynes/cm^2) \ or (10^{-6} \ bars)$

Equation 6 also represents the temporal distribution of the energy disposition at any point in the material. This is valid because the slowing down time for an ion is on the order of 10^{-12} seconds[73] while the time duration of the ion pulse is on the order of 10^{-6} seconds. (A 100 keV Alpha particle has a velocity of 2 x 10^8 cm/sec and slows down in approximately 10^{-4} cm hence: $\Delta t = 10^{-4}/10^8$ seconds.) Equation 7 represents the energy which crosses

the inner boundary of the first wall and the spatial distribution

of the deposition must be specified to obtain a true loading rate.

Finally Equation 8 has meaning only if the particles are stopped

within the first wall.

V. A. 3. Neutron Spectra

It is erroneous to assume that neutron production from the

fusion pellet can be characterized as a monoenergetic 14.1 MeV

neutron source. Reference to Figure II. 2 indicates that the spec-

trum has finite width for the thermonuclear neutrons.

This broadening of the neutron spectrum is a natural conse-

quence of the motion of the fusing nuclei. These nuclei have both

a directed and thermal velocity. Each velocity component will

alter the energy partitioning between the fusion products. The

energy of the emitted neutron is a function of the relative veloci-

ties of the two colliding nuclei and of the angle of emission of

the neutron, which is usually assumed isotropic in D + T plasmas.

Combination of these effects will give a considerable spread to

the neutron spectrum of a fusing source.

This effect has been calculated by Lessor[74] for stationary

plasmas which might be typical of Tokamaks or Mirrors and an example

of a spectrum for a 100 keV plasma is shown in Figure V. 2.

A similar calculation has been performed for a fusing pellet by

Shuy,[75] accounting for both thermal and directed motion. Both these

calculations show broadening of about $\pm$ 1 MeV which is in reasonable

agreement with Figure II. 2. In addition, these spectra can be approximated by a Gaussian pulse (Eqn. 23) as previously described.

For higher ρr pellets (as discussed in Chapter II), the neutrons can undergo significant interactions resulting in a modification of the neutron spectrum and the total energy contained in neutrons from a pellet. Neutron spectra for high ρr pellets have recently been calculated using transport theory methods by Berenek.[7] An example of calculated down scattered spectra for a ρr of 3 is given in Figure V. 3.

An important aspect of this spectral broadening is that the temporal loading of the first wall is not determined by the source duration. Instead the pulse duration is determined by the transit time broadening as calculated by Eqn. 6 which accounts for the variation in arrival times for different energies. This effect will determine the interaction rates for neutrons in the first wall.

V. A. 4. Summary of Wall Loadings

The photon, neutron, and ions can be approximated as all created instantaneously with spectra given by the previous generalizations. The wall fluxes from these sources can then be calculated from the relations developed above. An example of the wall loadings for three general sources (Table V. 1) at a radius of 5 meters is given in Figure V. 4.
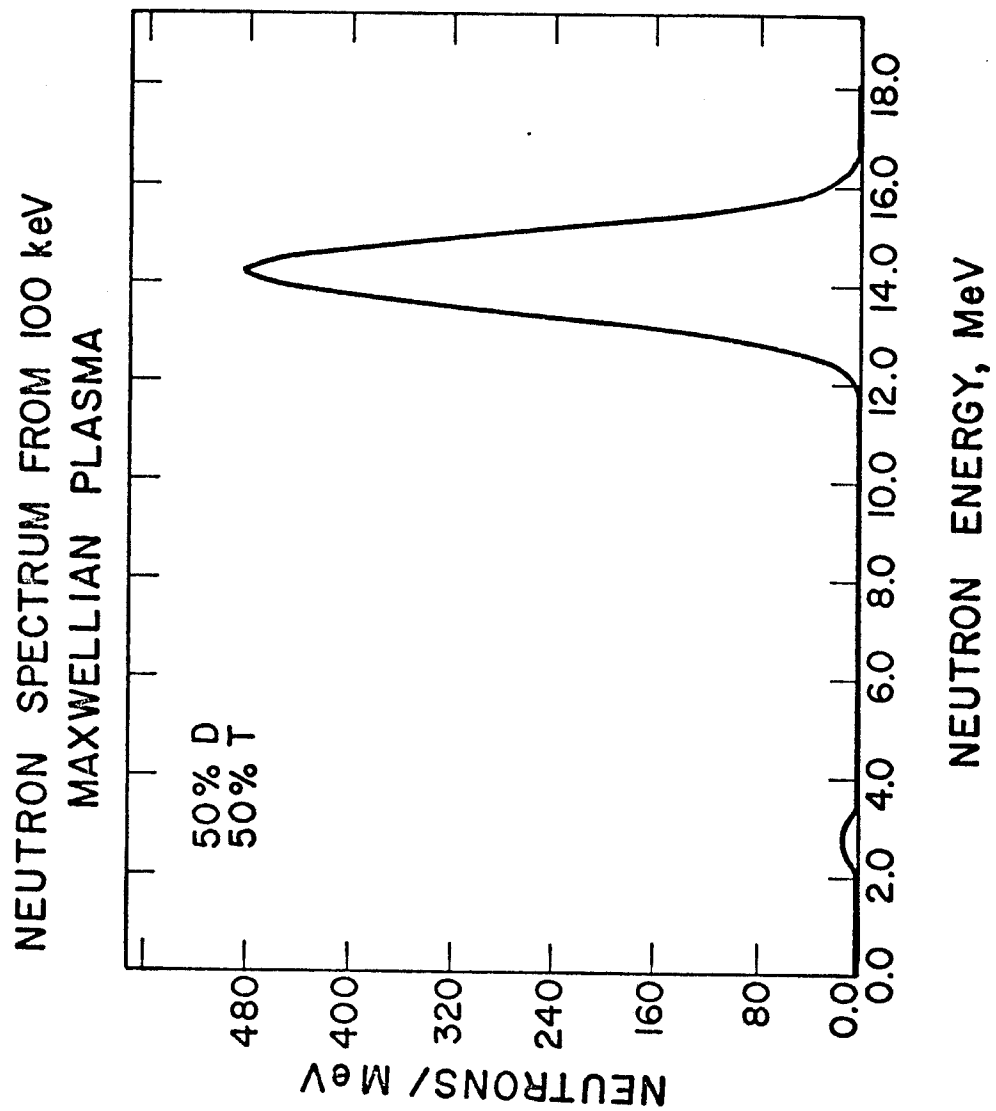
Fig. V. 2. Neutron Spectrum from Magnetic Confinement Plasma

EFFECT OF FUEL COMPRESSION ON NEUTRON SPECTRA
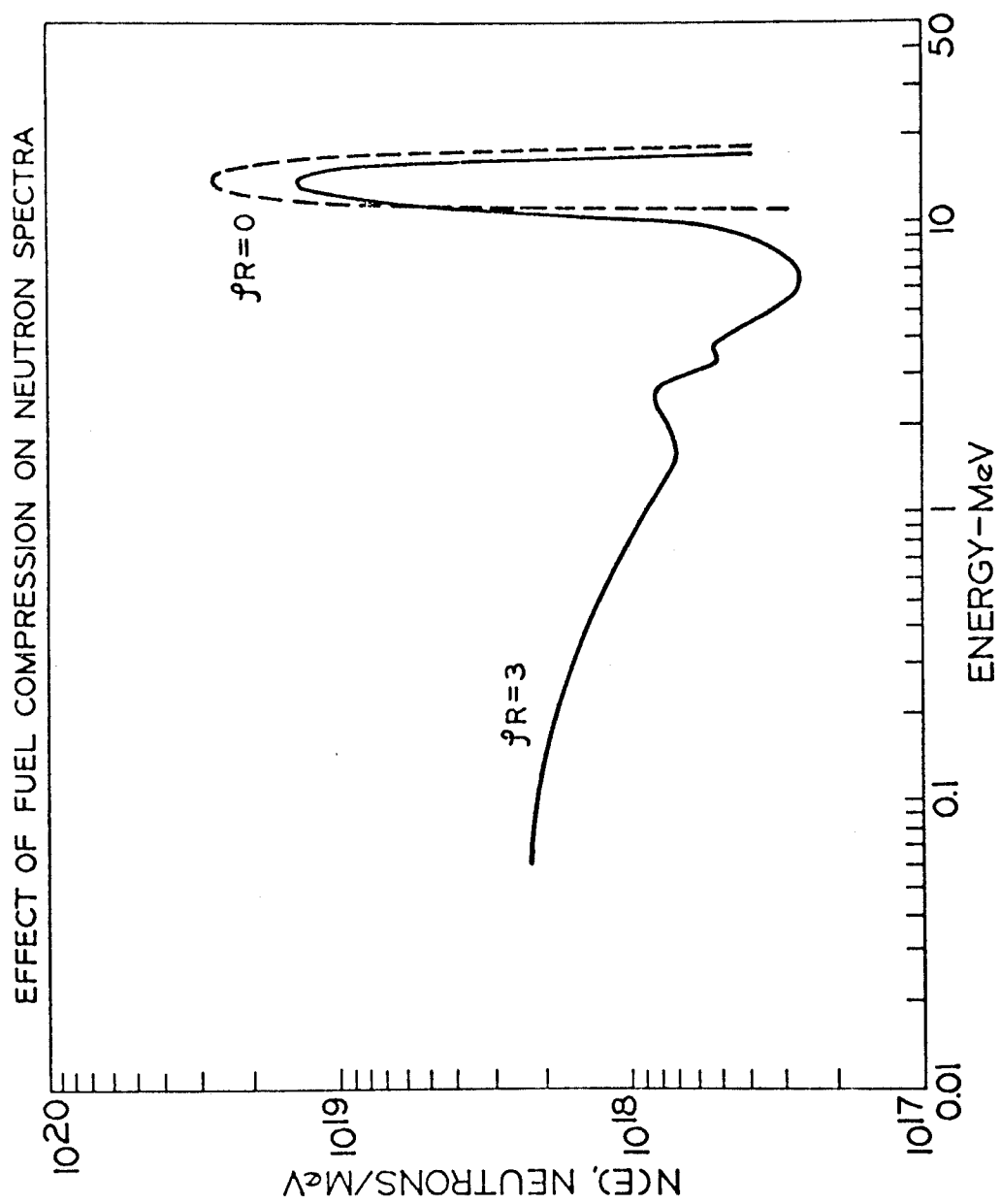
Fig. V. 3.. Neutron Spectra from Inertial Confinement Fusion

(Ref. 7)

Table V. 1

Characteristic Thermonuclear Radiation Components

	Spectrum	Fluence/Pulse	
		Particles	Energy
Photons --	500 eV		
	Black Body	$1 \times 10^{15}/cm^2$	$0.30 \ J/cm^2$
Neutrons --	14 MeV $\pm$ 1 MeV		
	(Gaussian)	$10^{13} \ n/cm^2$	$22.4 \ J/cm^2$
Alphas --	200 keV		
	(Maxwellian)	$10^{13} \ a/cm^2$	$0.48 \ J/cm^2$

These spectra are representative of three individual radiation types which are used to demonstrate the response of materials. They do not represent a complete set of radiation types or spectra from an inertially confined fusion microexplosion. Analysis of the response to a complete set of spectra from typical pellets will be discussed in Chapter VII.

V. B.   Energy Deposition

The energy deposited in a material can be calculated from the appropriate relation for energy loss for each radiation type. Photons are exponentially attenuated with absorption coefficients given in Section IV, source neutrons with appropriate KERMA factors and ions by general methods given in subsequent equations. The temporal distribution is given by Equation 6 upon specification of a spectrum.
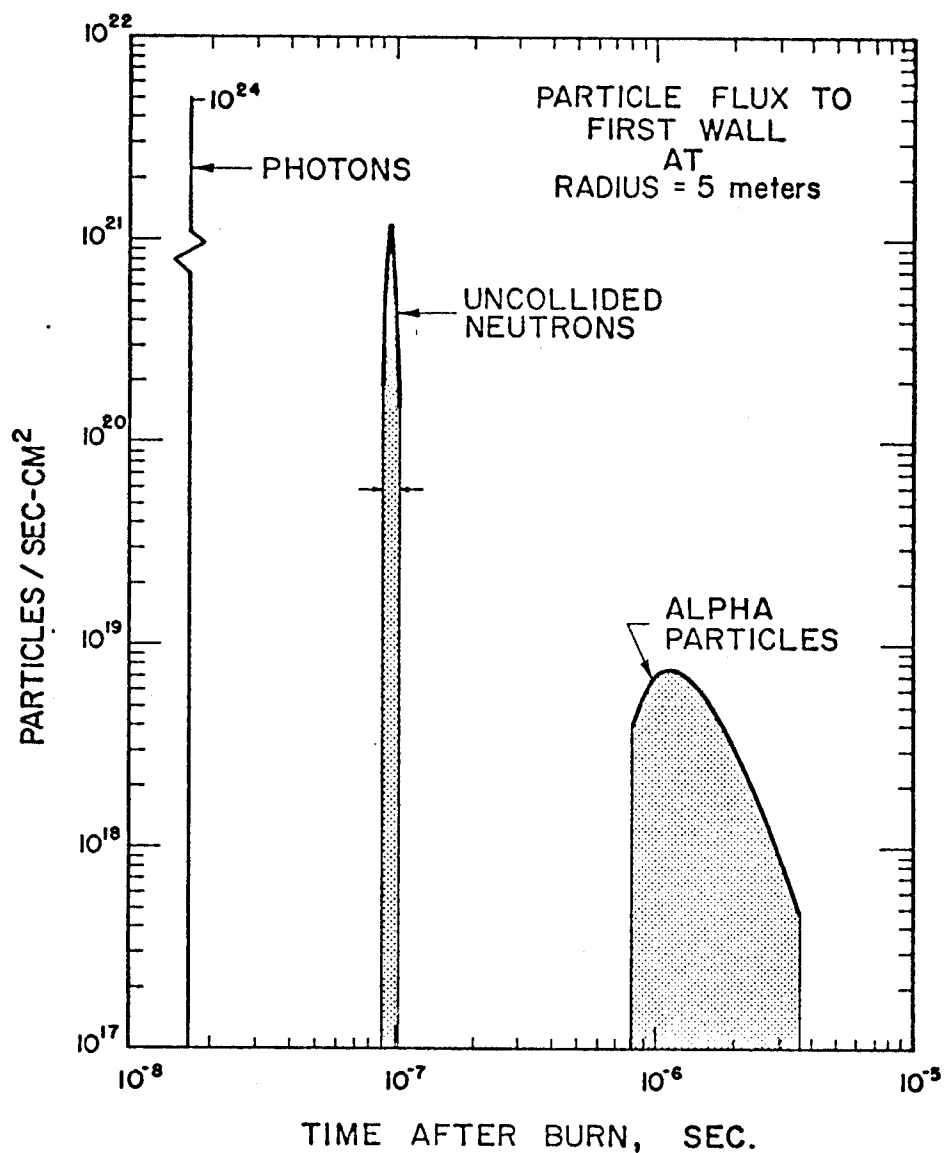
Fig. V. 4. Characteristic Particle Fluxes from Inertial Confine-
ment Fusion

The heating rate from the three reference radiation distributions in graphite can be determined from the appropriate energy deposition rate and is displayed in Figure V. 5. The greatest rate is given by the photons which are assumed to be deposited over a period of 1 ns. The correct deposition time would be a combination of the source time and the electron slowing down time, but the latter was not considered here.

The data in Figure V. 5 can be deceptive, since it represents the power into the material. A more meaningful comparison would be the total deposited energy or the time integral of the power curves. These data are shown in Figure V. 6. In this case the maximum energy deposited is due to the alpha particles.

The response of the material to these radiations is a function of the amplitude and the rate of the deposition, because it is necessary to account for energy which is transferred away from the deposition region. Since the deposition, temperature, and displacement response of a material are functions of the flux, energy, and type of the irradiating species, it is convenient for determining each phenomena to segregate the species into four categories.

a) photons

b) ions ($Z \leq 2$)

c) ions ($Z \geq 2$)

d) neutrons

The models for associated response for each category is presented in the following sections.
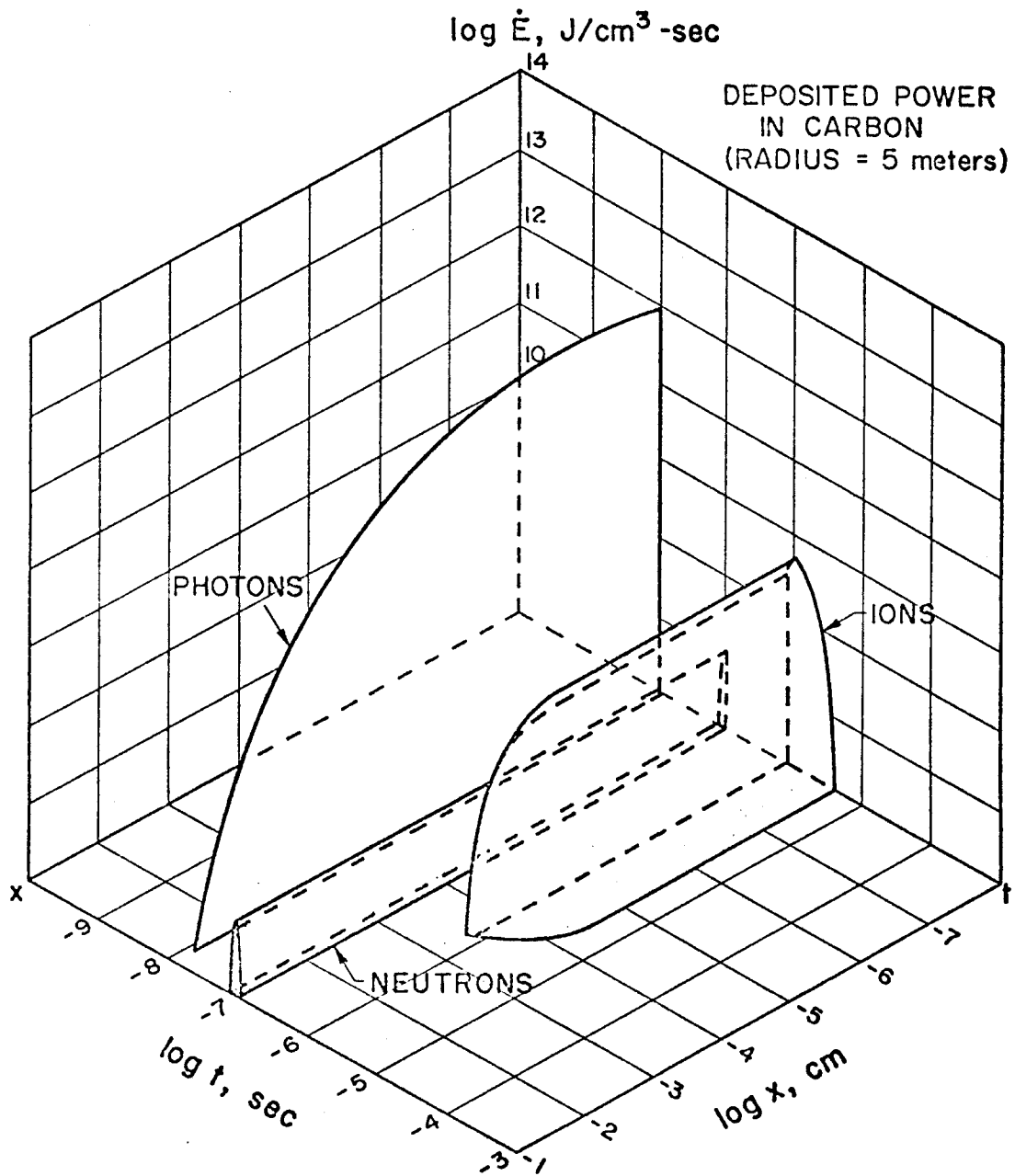
Fig. V. 5.   Energy Deposition Rates from Inertial Confinement Fusion
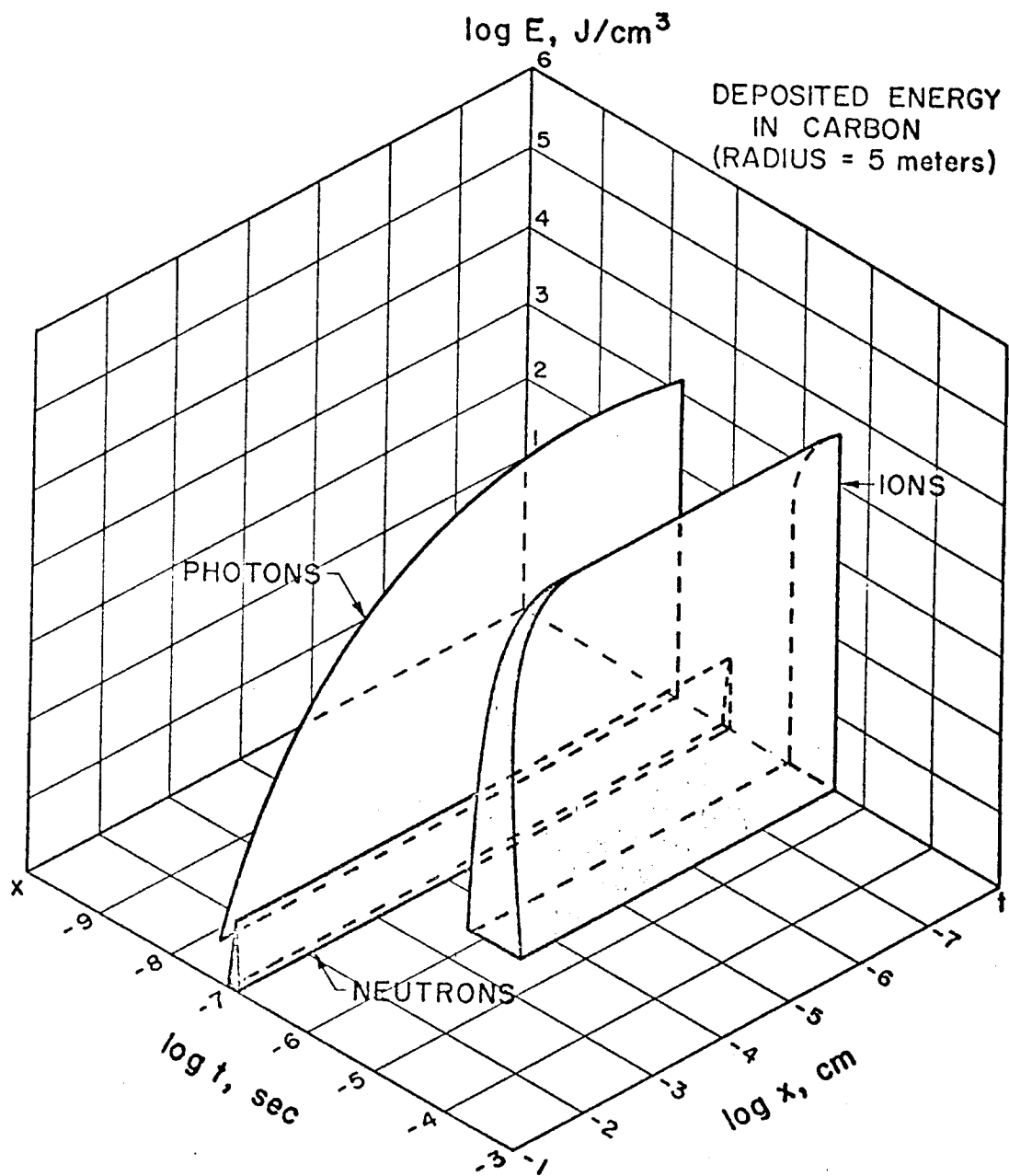
Fig. V. 6.   Energy Deposition from Inertial Confinement Fusion

V. B. 1. Photons

The X-ray data are based on the work of Biggs[46] and have been incorporated into this study by developing a general library of photoelectric cross sections for all elements ($1 < Z \leq 100$), which can be accessed by specification of the atomic number of a material and photon energy considered. Incoherent cross sections are derived from the representation of the Klein-Nishina formula developed by Biggs. (Egn. IV. 4) The cross sections determine the absorption profiles which are considered pure exponentials in space. For high energy photons (>30 keV for carbon), the photoelectric cross sections are negligible compared to those associated with incoherent scattering. For these spectra the total incoherent cross sections are used in this study. This assumption will always overestimate the primary energy near the surface since scattering and transport are not assumed. The fact that the energy deposition may be overestimated near the exposed surface of a material means it may be underestimated further into the material. However, this approximation is considered reasonable for most applications, since the average scattered photon energy is significantly lower than the incident photon energy and, as a result, is shifted toward the region where it will be more readily absorbed by the photoelectric process. Examples of the sum of the photoelectric and incoherent total cross section for C, Cu, Mo, and Ta are shown in Figure V. 7.
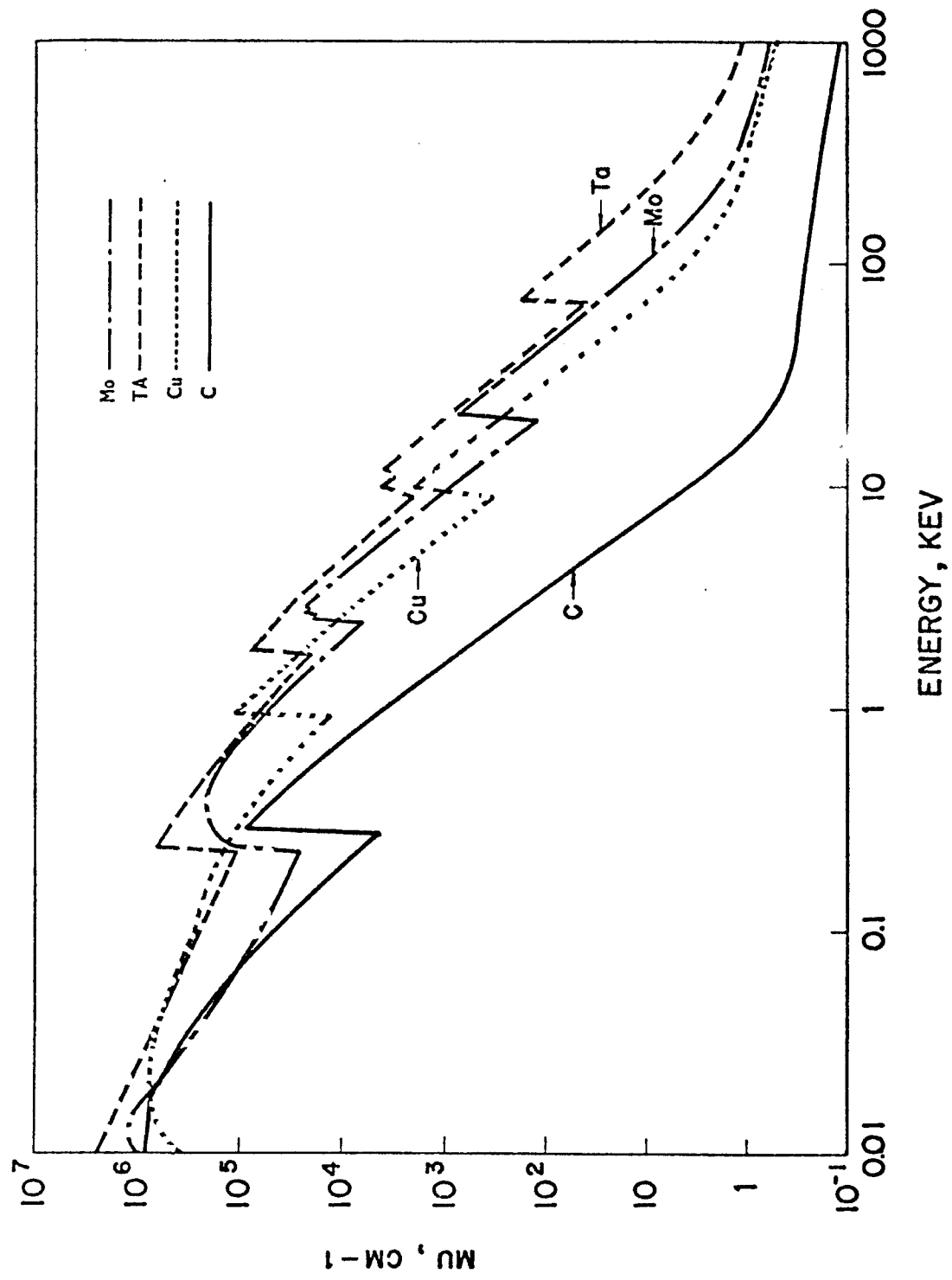
Fig. V. 7. Total Photon Cross Sections

V. B. 2.   Ions (Z ≤ 2)

Energetic light ions which are present in inertial con-
finement fusion systems, e.g., He, D, T, lose kinetic energy in ma-
terials primarily by electronic interaction when their energy is
above a few keV. Consequently, the transport equation which governs
their spatial distribution is dominated by the ionization or "fric-
tional" term. This feature was illustrated in Chapter IV, where
a comparison of the nuclear and electronic loss terms for He in
carbon was made. This domination by electronic processes allows
the spatial distribution to be determined upon knowledge of the
stopping power for the ion in a material.

The spectra from thermonuclear microexplosions consist of ions
whose energies fall in the three regions of energy loss discussed
in Chapter IV:

Region I   the low energy region where the incoming ion has

            lost its original charge state and where energy

            loss increases with energy.

Region II   the intermediate region where the charge state can

            vary from zero to a finite value less than the

            total ionization state and energy loss reaches a

            maximum.

Region III   the high energy region where total ionization is

            achieved and energy loss decreases with increasing

            energy.*

* for non-relativistic particles

Neither the Bethe-Bloch[59] or Lindhard[60] (LSS) models are entirely adequate in all of the regions. The Brice[42] formulation, however, since it is semi-empirical, can reproduce the experimental data with reasonable accuracy. This study has, therefore, relied on the Brice formulation for the generation of electron energy loss data. The defining equations for this model are Equations 24, 25, and 26 in Chapter IV. Any set of experimentally derived data will be compatible with the models developed here if, for example, Brice coefficients are not available.

These equations will reproduce the stopping power data as function of energy. The desired result for response studies is energy deposited as a function of distance. Hence, a transformation must be made to determine the mean location of an ion. The Brice formulae cannot be easily transformed to yield a closed form expression for the mean spatial distribution and, hence, difference codes are normally used which integrate the transport equations numerically.

This study required analytic forms for the spatial distribution which could be readily evaluated and which yielded accuracy comparable to the data available. As a result the deposition and local mean ion energy were determined in terms of a standard set of functions of space.

The stopping power data were divided into three regions roughly corresponding to those mentioned above as shown in Figure V. 8. In each region, a function was found which would reproduce the data and
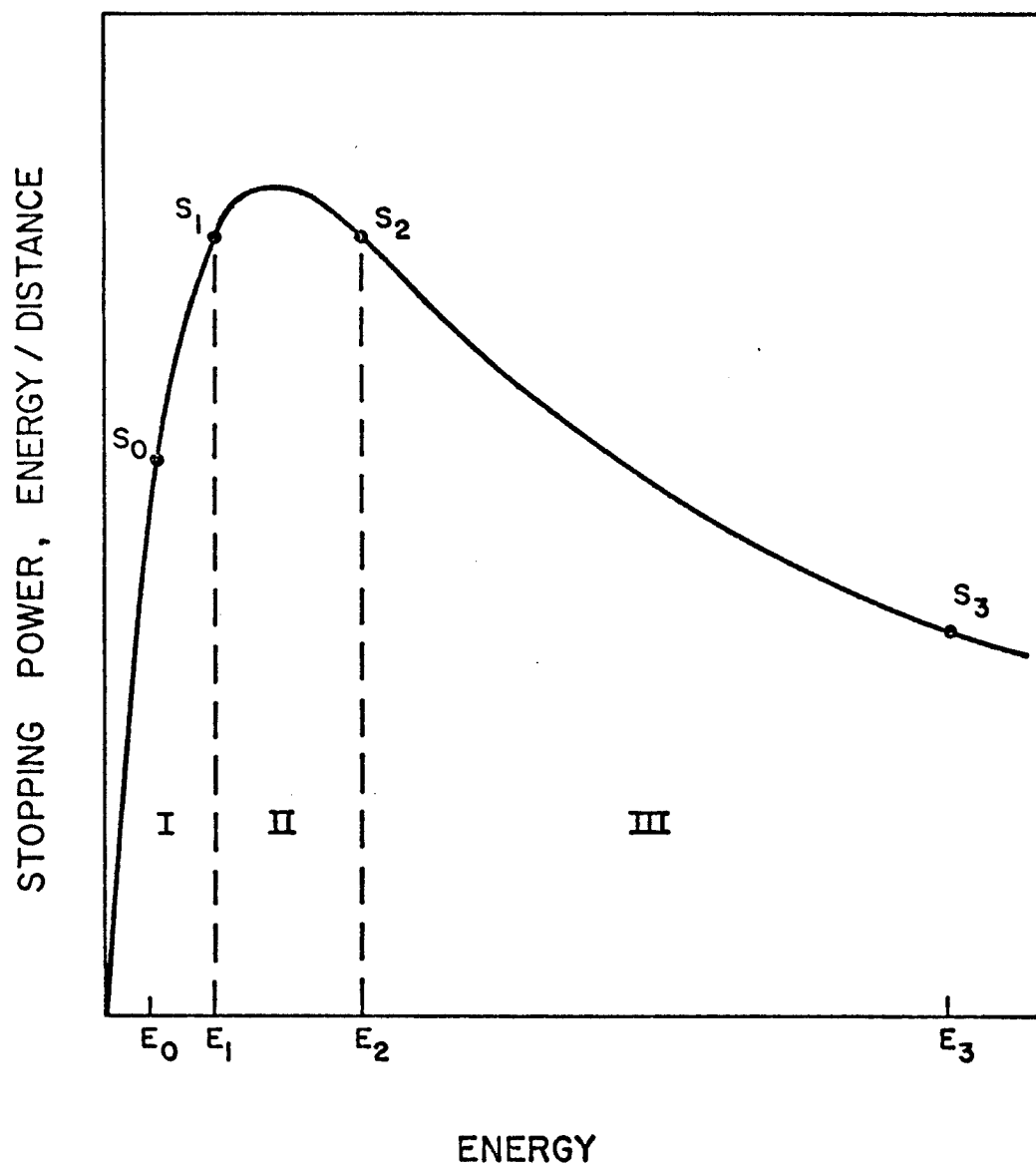
Fig. V. 8. General Electronic Energy Loss Function

which could be transformed into spatial functions which are in a closed form.

The following functions were found:

9) $\dfrac{dE}{dx}(E) = -S_o (E/E_o)^{1/2}$ Region 1

10) $\dfrac{dE}{dx}(E) = -A_1 (1 - e^{-B_1 E})$

Region 2

11) $\dfrac{dE}{dx}(E) = -[D^2 - P^2 (E - B_2)^2]$

12) $\dfrac{dE}{dx}(E) = -A_3 e^{-E/B_3}$ Region 3

where S_o, E_o, A_1, B_1, D, P, B_2, A_3, B_3 are all constants.

These equations were chosen because they can be readily transformed by the process:

13) $X(E) = \int_{E*}^{E} \dfrac{1}{dE/dx(E)} \, dE$

where $E*$ is the incident ion energy.

Equation 13 can then be solved for E, such as,

14) $E = F(x, E*)$

and

15) $\dfrac{dE}{dx}(x) = \dfrac{dE}{dx}(F(x, E*))$ or $= \dfrac{d}{dx} F(x, E*)$.

The results of performing these transformations for each of the equations yields the spatial distributions and local energy fractions given in Table V. 2.

The constants for each region can be determined by selecting reference points, as illustrated in Figure V. 8, from the stopping power curve and using the relation shown in Table V. 3.

Upon determination of the constants in Equations 9-12, the depositions are completely determined as functions of space. The deposition functions will be continuous in space, but the curvature of each function will be discontinuous where the regions I, II, and III are joined.

Equations 9-12, although useful in specifying the depositions, are not necessarily in a form which can be utilized by a response model; consequently, a standard form was chosen for expressing the general deposition function. The form chosen was a general polynomial represented by

16) $\quad D(x) = A_1 + A_2 x + A_3 x^2 + A_4 x^3 + A_5 x^4, \quad x_a < x < x_b.$

This form can be derived from the relations 1-4 if the spatial domain is divided into three regions (Figure V. 9) which correspond to the energy regions shown in Figure V. 8. The values are chosen so that the following correspondence is maintained:

Table V. 2

Results of Electronic Stopping Power Relations

Equation Number	Spatial Distribution	Local Energy
Region I 9	$\dfrac{dE}{dx}(x) = S_o \left(\dfrac{E^*}{E_o}\right)^{1/2} - \dfrac{S_o^2 x}{2E_o}$	$E(x) = E^* - S_o x \left(\dfrac{E^*}{E_o}\right)^{1/2} + \dfrac{S_o^2 x^2}{4E_o}$
Region II 10	$\dfrac{dE}{dx}(x) = \dfrac{A_1}{e^{B_1(A_1 x - Q_1)} + 1}$ $Q_1 = E^* + \dfrac{\ell n\,(1 - e^{-B_1 E^*})}{B_1}$	$E(x) = \dfrac{1}{B_1}\,\ell n\,(1 + e^{+B_1(Q_1 - A_1 x)})$
11	$\dfrac{dE}{dx}(x) = D^2\,\dfrac{4z}{(1+z)^2}$ $z = e^{(Q_2 - x)2D\sqrt{p}}$	$E(x) = \dfrac{D}{p}\,\dfrac{(z-1)}{(z+1)} + B_2$ $Q_2 = \dfrac{1}{2Dp}\,\ell n\,\dfrac{D/p + E^* - B_2}{D/p - E^* + B_2}$
Region III 12	$\dfrac{dE}{dx}(x) = \dfrac{A_3 e^{-E^*/B_3}}{1 - \dfrac{A_3 x}{B_3}\,e^{-E^*/B_3}}$	$E(x) = B_3\,\ell n[e^{E^*/B_3 - A_3 x/B_3}]$

In all cases x is measured from the point where E = E*

Table V. 3.

Evaluation of Constants

Equation	
1	S_o, E_o read directly from curve
2	$A_1 = \dfrac{S_o^2}{2S_o - S_1}$ $B_1 = - \ln(1 - S_o/A_1)$ where E_o, S_o; E_1, S_1 are given and $E_1 = 2\,E_o$
3	$D^2 = S_{max}$ $B_2 = (E_1 + E_2)/2$ $P = (S_{max} - S_2)/(E_2 - B_2)^2$
4	$B_3 = (E_3 - E_2)/ \ln(S_2/S_3)$ $A_3 = S_2\, e^{E_2/B_3}$
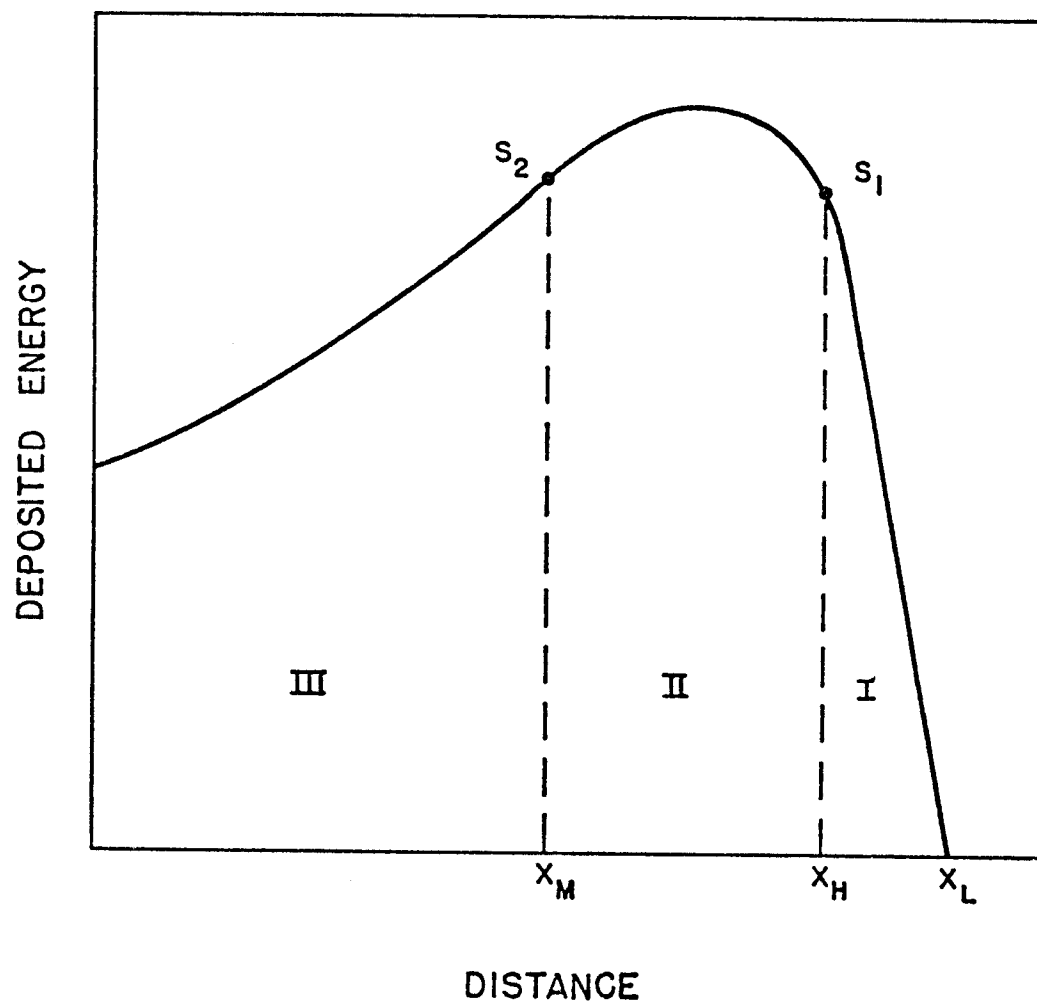
Fig. V. 9. General Energy Deposition Profile

Location	Energy
x_L	0
x_H	E_1
x_M	E_2
0	E^*

where E^* is the incident energy of the ion. If E^* is less than E_2 but greater than E_1, the value for x_m simply vanishes and the point $x = 0$ is simply within region II.

A similar modification is made for ions with energies less than E_1 where x_H and x_M vanish and the entire distribution is within region I.

Within each region a relation similar to Equation 14 can be derived and the coefficients determined. The result is a general expression

$$D(x) = 0 \qquad x_L < x$$

17)
$$D(x) = \sum_{N=1}^{5} A_{1N} x^{N-1}, \quad x_H < x < x_L$$

$$D(x) = \sum_{N=1}^{5} A_{2N} x^{N-1}, \quad x_m < x < x_H$$

$$D(x) = \sum_{N=1}^{5} A_{3N} x^{N-1}, \quad 0 < x < x_m.$$

A set of relations (eq. 17) can be derived for each incident ion energy and is than available for subsequent use for any response which needs an analytic expression for the deposition.

The deposition function for region III (Equation 12) can easily be transformed into the form given in Equation 9 since it is of the form

18) $\quad y = \dfrac{c}{1 - Bx}$

which for small values of x can be expanded as

$$y = c \ (1 + BX + (Bx)^2 + (Bx)^3 + \ldots);$$

hence the relations become

$$A_{31} = A_3 e^{-E^*/B_3} \qquad A_{32} = A_{31}^2/B_3 \qquad A_{33} = A_{31}^3/B_3^2$$

19) $\qquad A_{34} = A_{31}^4/B_3^3 \qquad\qquad A_{35} = A_{31}^5/B_3^4$

For Equations 10 and 11 no simple expansion is available. In this case the coefficients can be found by evaluating a few points (e.g., n points) directly from the equations and fitting these points with an interpolatory polynomial (of order n-1).

It should be noted that Equation 9 is already in the form of Equation 17 so that:

20) $\quad A_{11} = S_o \left(\dfrac{E^*}{E_o}\right)^{1/2} \qquad A_{12} = -S_o^2/2E_o \qquad A_{13} = A_{14} = A_{15} = 0.$

Examples of the accuracy of this technique are given in Figures V. 10, V. 11, and V. 12, in which deposition functions are depicted for helium ions into nickel for energy ranges from 200 keV to 4 MeV. Figure V. 10 gives the stopping power for the Brice electronic energy loss formulation (solid line) with a comparison of the function of equations (9-12) (dotted line). Figure V. 11 shows the spatial deposition functions as generated from this work corresponding to various incident energies. Also in Figure V. 11 are deposition values determined by the more formal ion implantation computer codes by Brice.[37] The agreement by the simple calculation developed in this study is notable. Figure V. 12 gives the mean local ion energy (calculated from equation in Table V. 2) as a function of space for the various incident energies.

V. B. 3. Ion Deposition (Z >2)

For heavy ions, the energy deposition is more complex since it is no longer possible to exclude the nuclear energy loss from consideration. Consequently, the general transport equation must be solved taking into account the energy dependent nuclear interaction cross sections which are also anisotropic. The various approximate solutions available for such calculations are discussed in Chapter III. Three of the most widely used methods are those of Brice,[37] Winterbon,[38] and Manning and Mueller.[36]
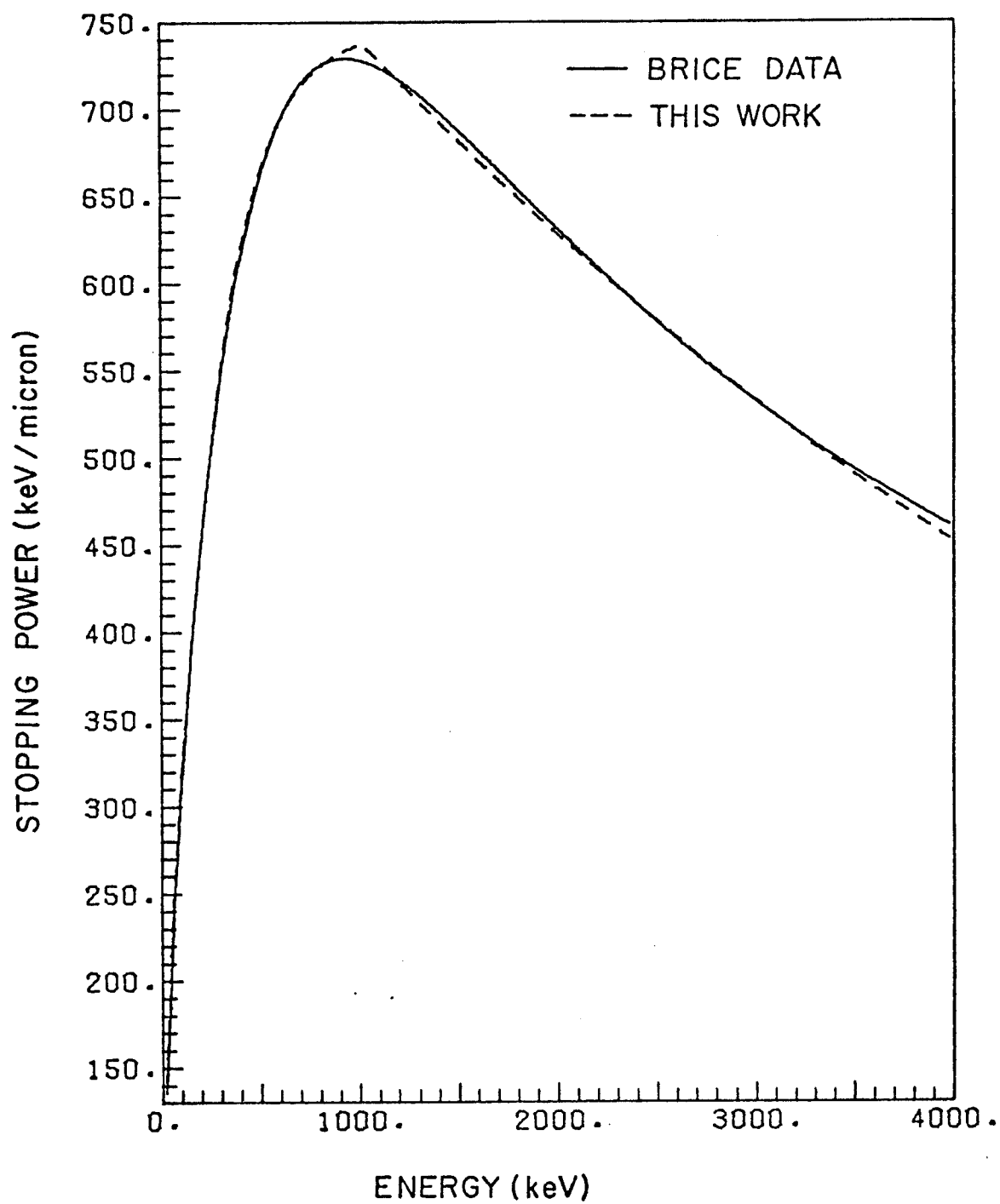
Fig. V. 10.   Comparison of Electronic Stopping Power for He in Nickel
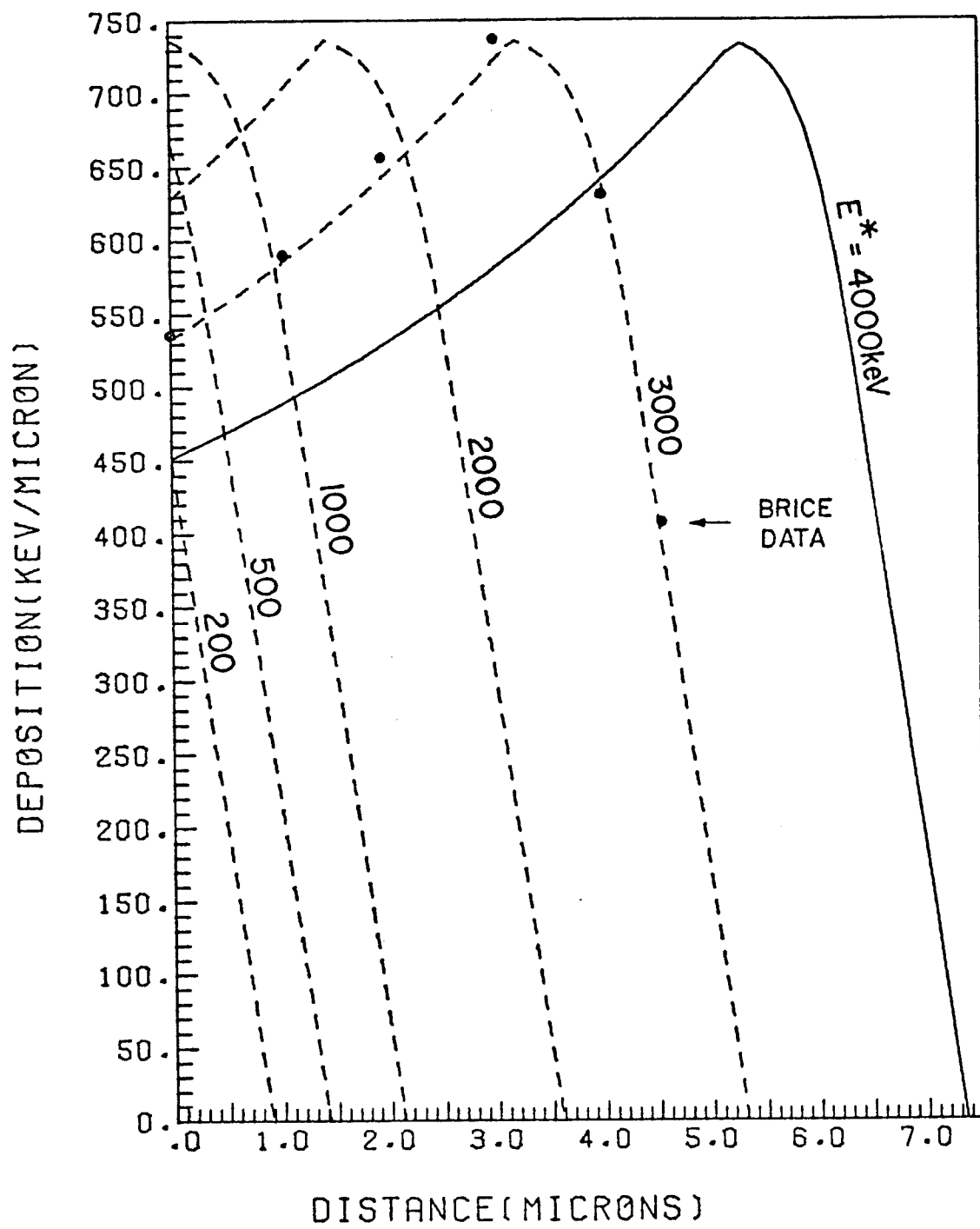
Fig. V. 11. Electronic Energy Spatial Deposition He in Nickel
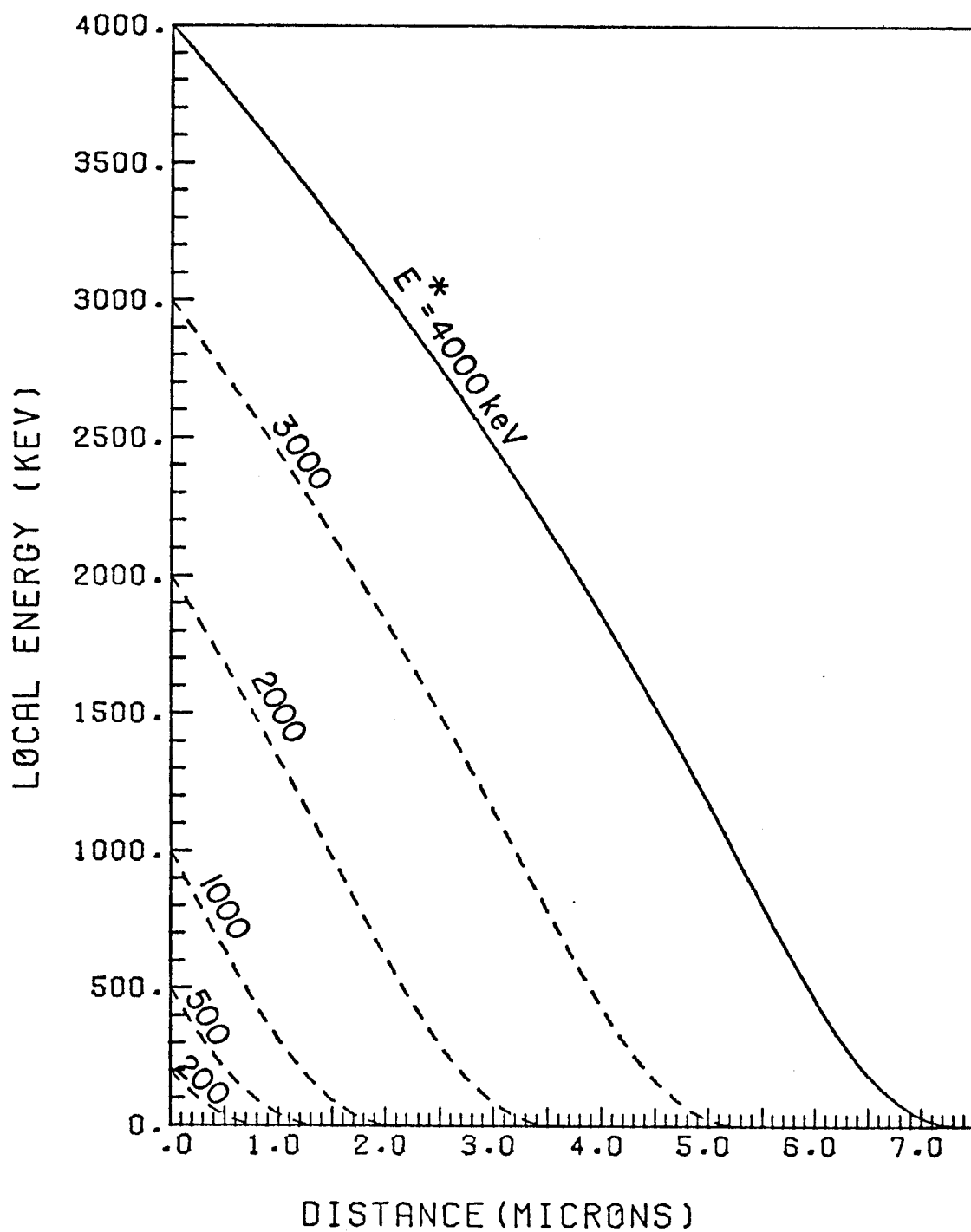
Fig. V. 12. Local Mean Energy He in Nickel

V. B. 3. a. Concept of Deposition Functions

In this study, an examination of the results of the RASE4

and DAMG2 computer codes developed by Brice[37] was made to develop

a general method of reproducing the results for use in a response

calculation. The goal was to develop a method which could produce

the deposition distribution for a wide range of incident ion energies

and would be efficient for numerical evaluation. The methodology

closely follows that used in neutronics in which neutron cross

sections are processed into a form in which the spatial transfer

characteristics are in terms of Legendre polynomial coefficients

which are in turn dependent on the incident neutron energy.

The method chosen was to establish for each ion target combina-

tion a set of "Deposition Functions" which consisted of polynomials

which could reproduce the spatial profile of the deposition distri-

butions. Separate functions were chosen for electronic energy

distributions and nuclear energy distributions. The coefficients of

these polynomials are then considered functions of incident ion

energy. Therefore, the procedure was to establish the coefficients

for a few selected incident energies, using the implantation computer

codes or published data on deposition distributions. These coef-

ficients become then a reference set for the ion target combination

and are placed in a form for rapid computer access.

Complete distribution for any arbitrary incident ion energy

can then be developed by interpolating between these reference

coefficients. The numerical procedure used for this process is

extensive and is outlined in Chapter VI as an integral part of the T-DAMEN computer code.

An example of the use of these deposition functions for the deposition of aluminum ions into nickel is given in Figures V. 13, V. 14, and V. 15. The nuclear damage is shown in Figure V. 13 for 5 incident ion energies. It can be seen that the peak damage values occur when the interaction cross section reaches a maximum and there is a depression of damage near the surface which is due to the anisotropic redistribution of damage energy by the primary knock-on atoms (PKA). The electronic energy loss is shown in Figure V. 14 and shows a maximum value at the surface with a decreasing function thereafter. This result is consistent with ion target combinations in which the stopping power is primarily contained in region I discussed previously and encompasses virtually all heavy ions of interest in fusion systems.* The sum of the nuclear and electronic contributions is shown in Figure V. 15 and indicates that even for this combination the dominant factor is the electronic loss. This relationship is expected to occur in any model which is based on the LSS theory.

The use of polynomial functions as characteristic of ion spatial deposition profiles is expedient since nuclear and electronic coefficients can be summed to generate a total deposition function of the same form.

---

*This must be modified in the case of an extremely heavy projectile and a low Z target.
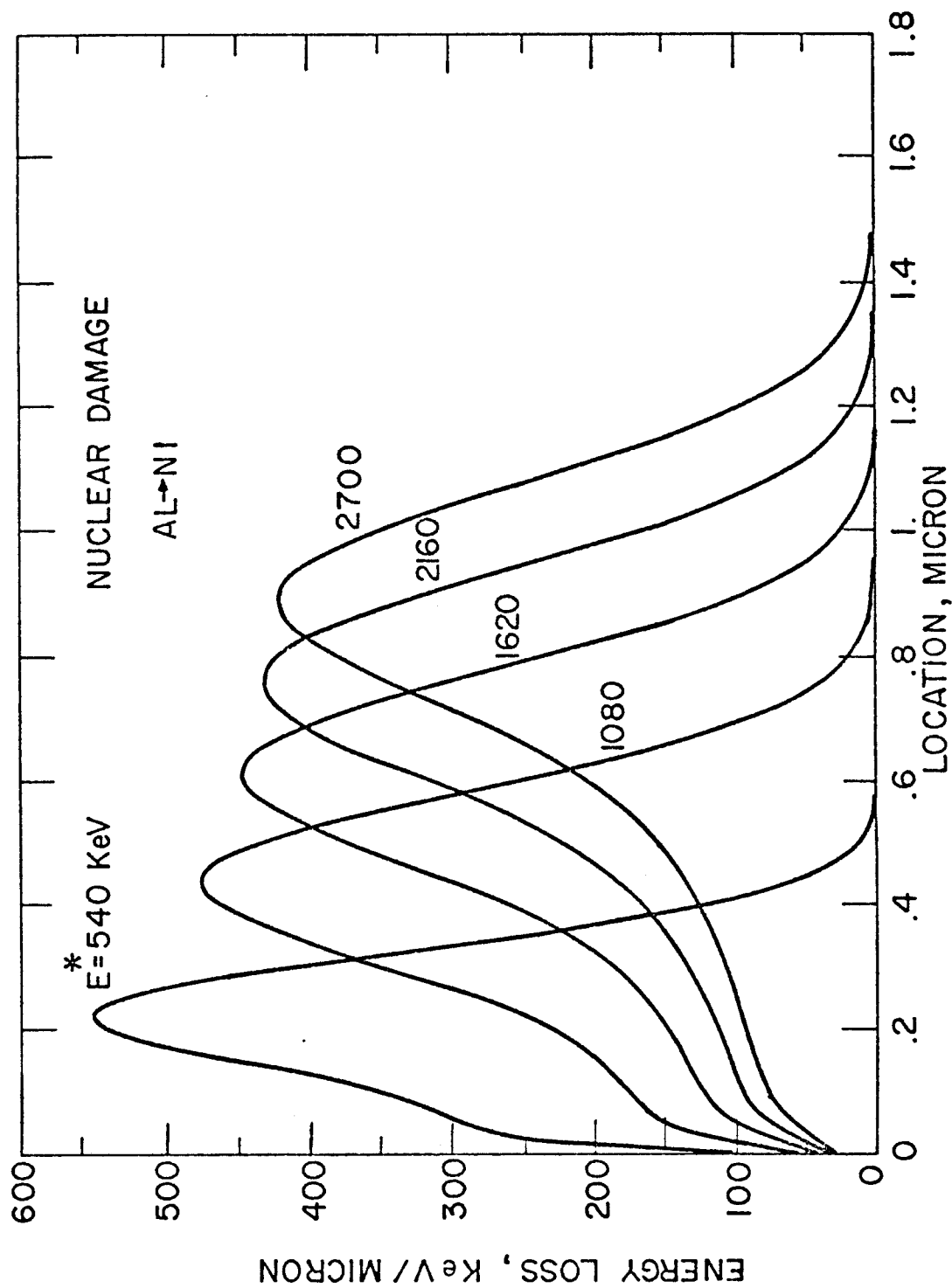
Fig. V. 13.   Nuclear Energy Deposition from Deposition Function
He in Nickel
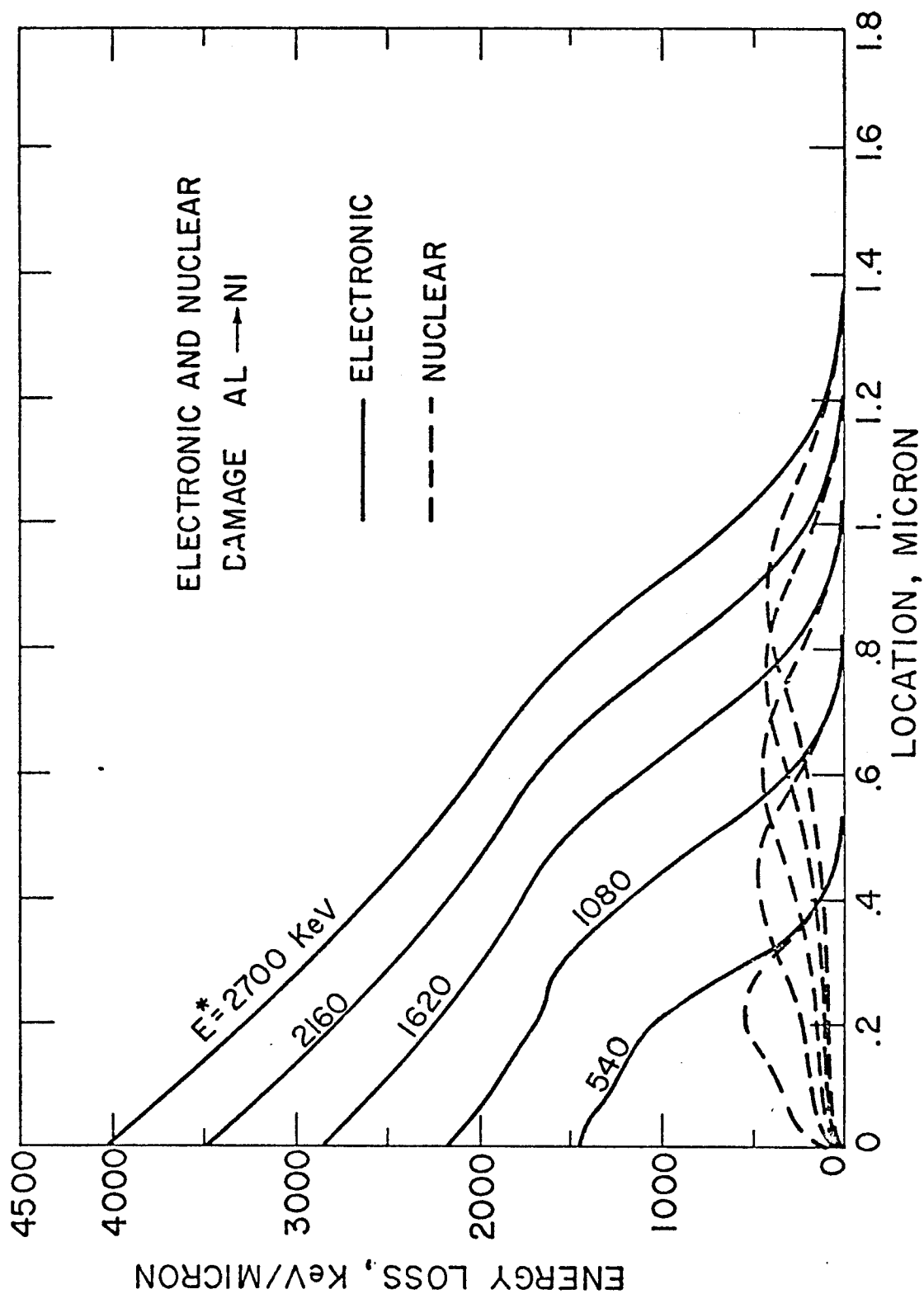
Fig. V. 14. Electronic Energy Deposition from Deposition Function He in Nickel

Fig. V. 15. Total Energy Deposition from Deposition Function
He in Nickel
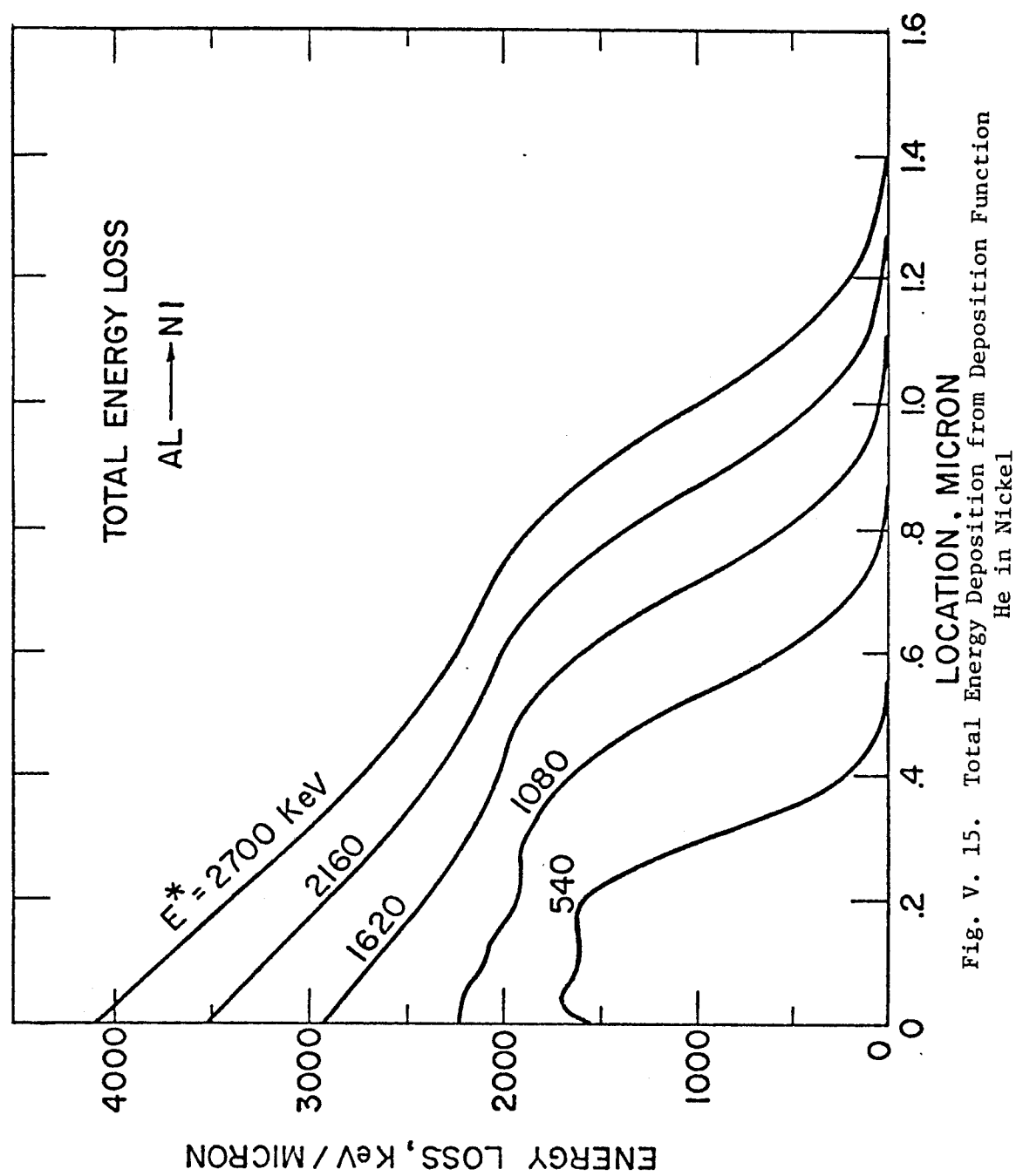
V. C. Temperature Response

The temperature history associated with the deposition of energy from the various radiation sources discussed in the previous sections can be determined by various calculational methods. The emphasis in this study was a parametric analysis and thus closed-form solutions were developed for thermal response of single phase materials with constant material properties. More refined calculations are readily done via numerical methods which can account for melting, vaporization, and non-linear material properties.

The temperature excursion from neutron radiation has been shown to be insignificant in pulsed fusion environments, hence we only need to develop models for photon and ion deposition.

V. C. 1. Response to Photon Irradiation

If the energy deposition from photons can be described by exponential attenuation (as in the case of photoelectric absorption), it is sufficient to develop a response model for monoenergetic radiation which can then be applied to arbitrary spectra by super-position.

The prompt temperature excursion following a pulse of electro-magnetic radiation can be determined easily if the pulse time is shorter than the thermal response time of the irradiated material. If this condition is met, the initial temperature transient can be calculated from an adiabatic model. It is therefore instructive to examine the photon durations which will satisfy these conditions.

V. C. 1. a. Adiabatic Response

An estimate of the thermal response time can be made from examination of the case of monoenergetic photon absorption in which the energy deposition is given by

$$21) \qquad q = \mu F_o \ e^{-\mu x}$$

where q = energy/unit volume

F_o = incident intensity, energy/unit area

If the energy were deposited instantaneously, the material would respond adiabatically and the resulting temperature change profile would be of the form

$$22) \qquad T(x) = T_o \ e^{-\mu x}$$

where $\quad T_o = \dfrac{\mu F_o}{\rho c}$

A conservative estimate of the thermal response time can be made by examining the heat conduction equation[76]

$$23) \qquad k \nabla^2 T + \dot{q} = \rho c \ \frac{\partial T}{\partial t}$$

Since the first term of Equation 23 represents the power lost (or gained) by a volume element, the <u>maximum</u> rate of energy transfer by conduction can be estimated from the temperature gradient derived from Equation 22:

24) $\qquad \dfrac{\partial T}{\partial X}(x=0) = -\mu T_o\, e^{-\mu(0)} = -\mu T_o$

25) $\qquad \dfrac{\partial^2 T}{\partial X^2}(x=0) = \mu^2 T_o = \dfrac{\mu^3 F_o}{\rho c}$

A comparison of the first and second terms in Equation 23 can then be made for depositions over finite time Δt, in which

26) $\qquad \dot{q} = \dfrac{\mu F_o}{\Delta t}\, e^{-\mu x}$

hence the rates of terms 1 and 2 in Equation 23 become equal, at $x = 0$, when

27) $\qquad \dfrac{k\nabla^2 T}{\dot{q}} = \dfrac{k\mu^2 \Delta t}{\rho c} \quad \underset{\sim}{} \quad 1$

or the deposition time in which the maximum conduction loss rate is equivalent to the energy deposition rate is

28) $\qquad \Delta t = \dfrac{\rho c}{k\mu^2} = \dfrac{1}{\alpha \mu^2}$

where $\quad \alpha$ = thermal diffusivity, cm^2/sec

$\qquad\quad \mu$ = absorption coefficient, cm^{-1}

Typical data for graphite and copper are given in Table V. 4.

Table V. 4

Thermal Response Characteristic Parameters

	Δt(sec)	ρ(gm/cm^3)	$c(\frac{cal}{gm^\circ K})$	$k(\frac{cal}{cm^\circ K\ sec})$	μ(cm^{-1}@1keV)
C	4×10^{-7}	2.3	.4	.1	5000
Cu	1.07×10^{-10}	8.9	.092	.85	95000

Conservative choices would be to choose values of a factor of 10 lower than those shown in Table V. 4. Thus, for pulse time of 10 psec, the response of graphite to 1 keV photons is very nearly adiabatic; whereas, for more strongly absorbing materials like Cu, the adiabatic assumption may slightly overestimate the temperature.

Using this adiabatic assumption, the temperature excursions from each photon pulse in an inertially confined fusion environment can be found using Equation 22 upon specification of the source spectrum and the photon cross section. An example of these peak temperatures is shown in Figure V. 16. The maximum front temperature and the maximum temperature at a penetration distance of $x = 1$ μm are given as a function of blackbody temperature. A spatial profile of temperature at various positions within the material is shown in Figure V. 17 for blackbody temperatures of .4, .5, and .6 keV.

V. C. 1. b.   General Response to Photons

The adiabatic response to a given photon spectrum only
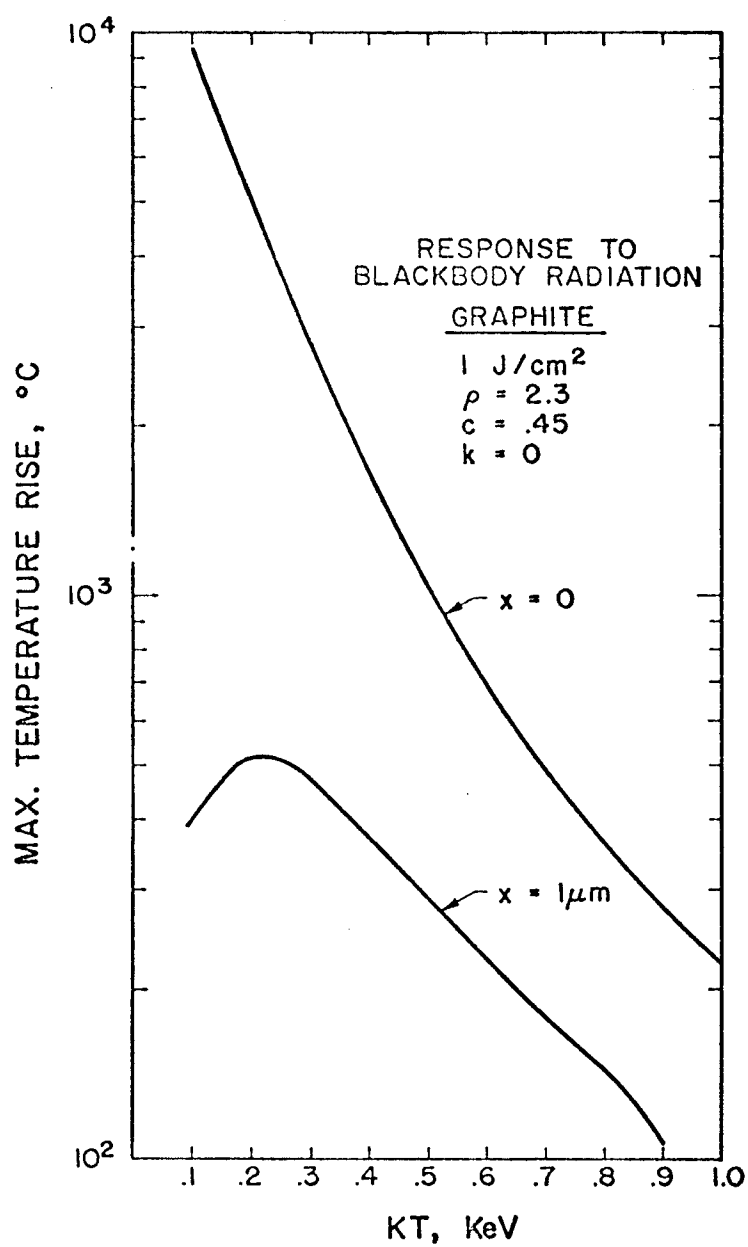
Fig. V. 16. Adiabatic Response of Graphite to Blackbody Radiation
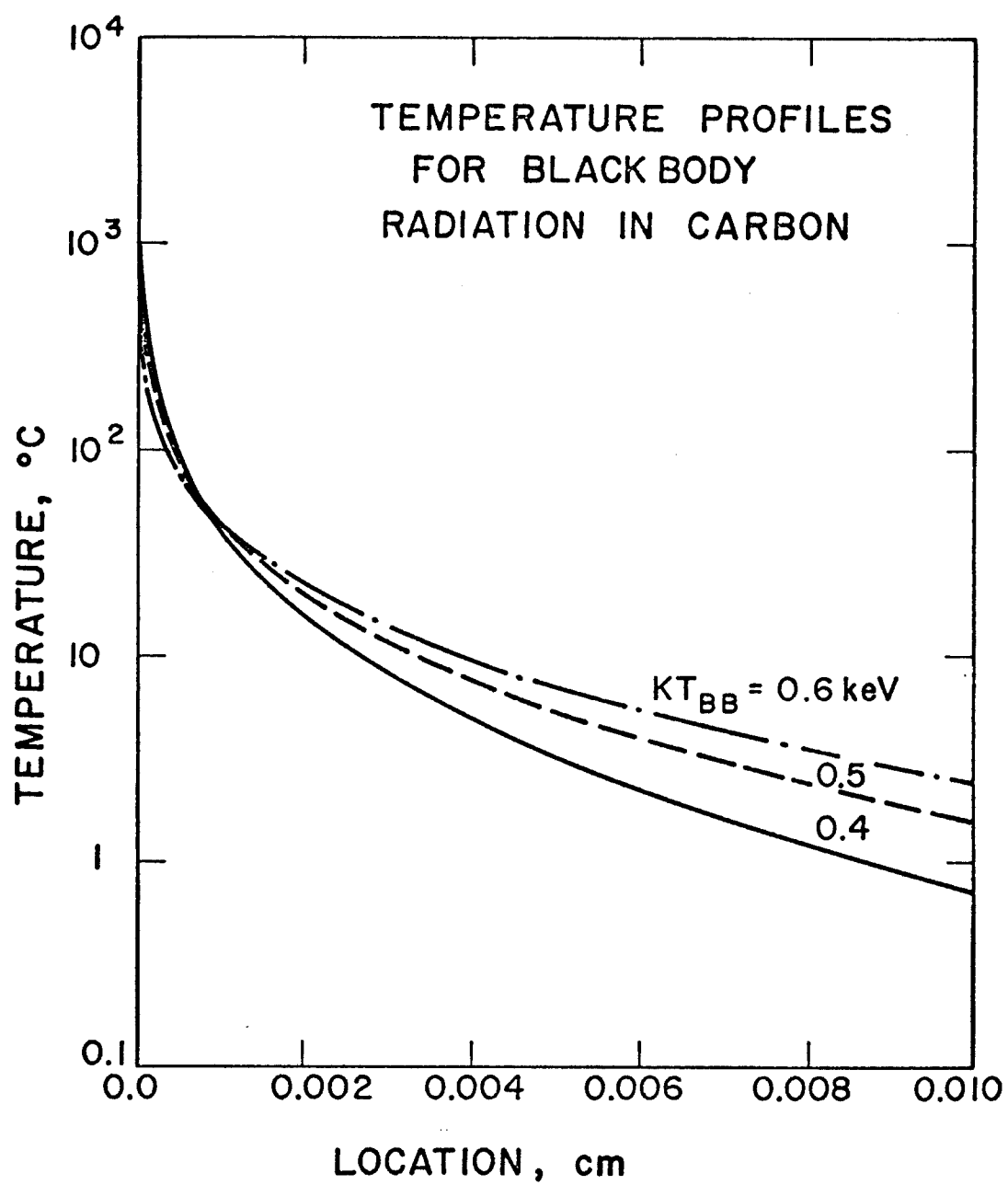
Figure V. 17. Temperature Profiles for Blackbody Radiation in Carbon

yields the maximum temperature excursion which can take place. In this section,models are given which can be used to evaluate the time dependence of the response at any position.

Solutions will be given for semi-infinite media which are used to develop prompt transients from a single pulse. An alternate solution for finite width slabs will also be given which can be used to assess the long term response to many consecutive pulses. The general technique is based on developing impulse solutions (Green's functions)[77] which can then be used to evaluate any photon spectrum with an arbitrary deposition history.

V. C. 1. b. i.   Exponential Impulse Into a Semi-Finite Medium

The defining equations are:

$$k\frac{\partial^2 T}{\partial x^2} = \rho c \frac{\partial T}{\partial t} - \dot{q}(x,t)$$

where

29) $\frac{\partial T}{\partial x}(0) = 0$ (insulated exposed surface)

$T(\infty,t) = 0$

$\dot{q}(x,t) = \delta(t) \; T_o \, e^{-\mu x}$

$T_o = \frac{\Delta E \mu}{\rho c}$ where ΔE is the energy in any portion of a spectrum.

This problem has the same solution as

30) $\quad k\dfrac{\partial T^2}{\partial x^2} = \rho c\dfrac{T}{\partial t}$

where,

$$\dfrac{\partial T}{\partial x}(0) = 0$$

$$T(\infty, t) = 0$$

$$T(x, o) = T_o e^{-\mu x}$$

The solution can be found by performing the integral[78]

31) $\quad T(x,t) = \dfrac{1}{2\sqrt{\pi\alpha t}} \int_0^\infty T_o e^{-\mu x'} \left\{ e^{-(x-x')^2/4\alpha t} + e^{-(x+x')^2/4\alpha t} dx' \right\}$

which yields the following result

32) $\quad T(x,t) = \dfrac{T_o}{2} e^{\mu^2 \alpha t} \left\{ e^{-\mu x} \left[1 + \text{erf} \left(\dfrac{x}{2\sqrt{\alpha t}} - \mu\sqrt{\alpha t} \right) \right] \right.$

$$\left. + e^{\mu x} \left[1 - \text{erf} \left(\mu\sqrt{\alpha t} + \dfrac{x}{2\sqrt{\alpha t}} \right) \right] \right\}$$

Although this expression is exact, it cannot be evaluated numerically for the very large values of μ which could be associated with low energy photon irradiation.

Therefore we make use of the explicit evaluation of the error function which is used for computer application.[79] That is,

33) $\quad \text{erf }(x) = 1 - f(Z) e^{-x^2}$

34) $f(Z) = a_1 t + a_2 t^2 + a_3 t^3 + a_4 t^4 + a_5 t^5$

$t = \dfrac{1}{1 + pZ}$

$p = a_1 - a_5$ are constants given in reference 79

Four cases can now be considered and as a convenience we let

$B = \mu \sqrt{\alpha t}$ $C = \dfrac{x}{2\sqrt{\alpha t}}$

1. $x = 0$

When equation 33 is substituted into equation 32 the following expression is obtained:

35a) $T(x,t) = T_o f(B)$

2. when $C > B$

35b) $T(x,t) = T_o \exp (B^2 - \mu x) + \dfrac{T_o}{2} [f(C+B) - f(C-B)] e^{-C^2}$

3. when $B > C$

35c) $T(x,t) = [f(B-C) + f(C+B)] e^{-C^2}$

4. when $B = C$

35d) $\quad T(x,t) = \dfrac{T_o}{2} e^{-B^2} [1 + f\ (C+B)]$

Equation 35 is used in a form where all the exponential terms are negative and can be evaluated accurately for computer analysis. These equations represent a Green's function in time and can be used to determine the response for any arbitrary temporal pulse shape. The application of these equations to a pulse of finite width and constant amplitude can be found by performing the integral

36) $\quad T(x,t) = \int_0^\tau d\ \dfrac{1}{t_d}\ \text{(equation 32)}\ dt'$

The result can be obtained by first getting the results for a continuous pulse which is turned on at $t = 0$.

In reference 78 this has been found to be:

37) $\quad T(x,t) = \dfrac{2A_o}{k\mu}(\alpha t)^{1/2}\ \text{ierfc}\ \dfrac{x}{2\sqrt{\alpha\ t}} - \dfrac{A_o}{\mu^2 k}\ e^{-\mu x}$

$\quad + \dfrac{A_o}{2k\mu^2}\ \left\{ e^{\mu^2\alpha t - \mu x}\ \text{erfc}\ \left(\mu\sqrt{\alpha\ t} - \dfrac{x}{2\sqrt{\alpha t}}\right)\right.$

$\quad + e^{\mu^2\alpha t - \mu x}\ \left.\text{erfc}\ \left(\mu\sqrt{\alpha t} + \dfrac{x}{2\sqrt{\alpha t}}\right)\right\}$

where $A_o = \dfrac{\rho C\ T_o}{t_d} = \dfrac{\Delta E_\mu}{t_d}$ and ierfc = first integral of the complimentary error function.

To evaluate this function it is possible to redefine equation 32 as

$$T(x,t) = H(x,t) = \text{equation } 32$$

Equation 37 contains equation 32 as follows:

$$38) \quad T(x,t) = \frac{A_o}{k\mu} \left\{ 2(\alpha t)^{1/2} \text{ ierfc } \frac{x}{2\sqrt{\alpha t}} - \frac{e^{-\mu x}}{\mu} \right\} + \frac{H(x,t)}{\alpha \mu^2 t_d}$$

Substituting for A_o and $\alpha = k/\rho c$, Equation 38 can be rewritten as:

$$39) \quad T(x,t) = \frac{1}{\alpha \mu^2 t_d} \left\{ T_o \mu \; 2(\alpha t)^{1/2} \text{ ierfc } \frac{x}{2\sqrt{\alpha t}} - T_o e^{-\mu x} + H(x,t) \right\}$$

$$= Q(x,t)$$

The solution for a pulse of finite width is simply the superposition of a pulse which starts at $t = 0$ and continues indefinitely and a pulse of equal and opposite intensity which starts at $t = t_d$ as

$$40) \quad T(x,t) = Q(x,t) - Q(x,t-t_d)$$

Equations 39 and 40 can then be used with superposition techniques and a cross section library to obtain the response to any general spectrum.

V. C. 1. b. ii. Multiple Pulse Solution for Finite Slabs

In addition to the temperature response from a single pulse, it may be necessary to determine a complete temperature history of the irradiated material for a number of sequential pulses. In the following development, a general model will be given for pulse train of photon irradiations. The impulse response will first be determined for a single pulse and then generalized to many pulses and finally related to photon pulses of finite duration.

The energy deposition can be assumed to be given by

$$41) \qquad q(t,x) = \delta(t) \, q(x) = \delta(t) \, q_o e^{-\mu x}$$

From consideration of the adiabatic response, the temperature in a finite slab of width L can again be formulated as

$$42) \qquad \nabla^2 T = \frac{1}{\alpha} \frac{\partial T}{\partial t}$$

subject to

$$T(x,0) = f(x) = \frac{q_o}{\rho C} e^{-\mu x} \quad \text{(initial condition due to adiabatic response)}$$

$$\frac{\partial T}{\partial x}(0,t) = 0 \quad \text{(insulated face)}$$

$$T(L,t) = 0 \qquad \text{(constant rear surface temperature)}$$

α = thermal diffusivity

By separation of variables or transform methods, the solution to the above problem can be shown to be[78]

43) $\quad T(x,t) = \sum_{N=0}^{\infty} \cos B_n \frac{x}{L} e^{-B_n^2 \Theta} \frac{2}{L} \int_0^L f(x) \cos B_n x/L \, dx$

where $B_n = (\frac{2n-1}{2}) \pi$

$\Theta = \frac{\alpha t}{L^2}$

Upon substituting for $f(x)$ and integrating the result is:

44) $\quad \frac{T(x,t)}{q_o/\rho c} = 2 \sum_{N=1}^{\infty} \cos B_n z \, e^{-B_n^2 \Theta} \left[\frac{b}{b + B_n} \right]$

$\left[1 - e^{-b} (\cos B_n - \frac{B_n}{b} \sin B_n) \right]$

where $b = L \qquad Z = x/L$

This is the response to a single photon pulse, a series of pulses as shown in Figure V. 18 can be accomodated by applying Laplace transform techniques to Equation 42.

The temporal behavior of the loading function is thus given by

45) $\quad q(t) = \sum_{n=0}^{M-1} \delta(t-n_\omega) = \delta(t) + \delta(t-\omega) + - - -$

where M = number of pulses which have occurred

ω = time between pulses
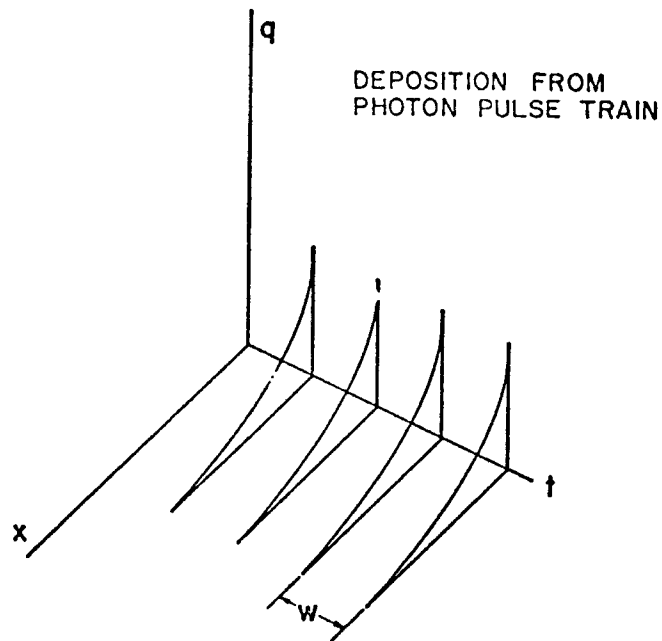
Fig. V. 18. Deposition from Photon Pulse Train

which has a transform of

46) $V(s) = 1 + e^{-\omega s} + e^{-2\omega s} + \_ \_ \_$

The transfer function for the system is the transform of Equation 44, which is

47).

$$H(s) = 2 \sum_{N=1}^{\infty} \cos B_n z \; \frac{1}{s + \dfrac{B_n^2}{L}} \left[\frac{b}{b^2 + B_n^2} \right] \left[1 - e^{-b} \left(\cos B_n - \frac{B_n}{b} \sin B_n \right) \right]$$

The response to a series of M pulses is then found by multiplying Equations 51 and 52 and finding the inverse transform as

$$48) \quad \frac{T(x,t)}{T_o} = 2 \sum_{n=1}^{\infty} \cos B_n z \, e^{-B_n^2 \Theta} \left[\frac{1-e^{-B_n^2 \gamma M}}{1-e^{-B_n^2 \gamma}} \right] \left[\frac{b}{b^2 + B_n^2} \right]$$

$$\left[1-e^{-b} \left(\cos B_n - \frac{B_n}{b} \sin B_n \right) \right]$$

where
$$B_n = \frac{(2n-1)\pi}{2} \qquad\qquad \gamma = \frac{\alpha \, \omega}{L^2}$$

$$b = \mu L \qquad\qquad\qquad \Theta = \frac{\alpha \delta}{L^2}$$

$$T_o = \frac{q_o}{\rho C} \qquad\qquad\qquad \delta = \text{fraction of pulse interval}$$

$$\alpha = \text{thermal diffusivity}$$

This solution can be generalized to pulses of finite duration by convolution or reapplying transforms, and this analysis will give a result identical to a variation of parameters analysis by Abdel-Khalik.[80] For short photon mean free paths, an analysis based on infinite half space solution is more appropriate for determining transients since it can be evaluated without the difficulty of evaluating an infinite series.

A most useful piece of information from the application of Equation 48 is the shape of the temperature profile, in a material just before a photon pulse, resulting from a large number of precedent pulses. Figure V. 19 shows such a pre-pulse profile for a .5 keV
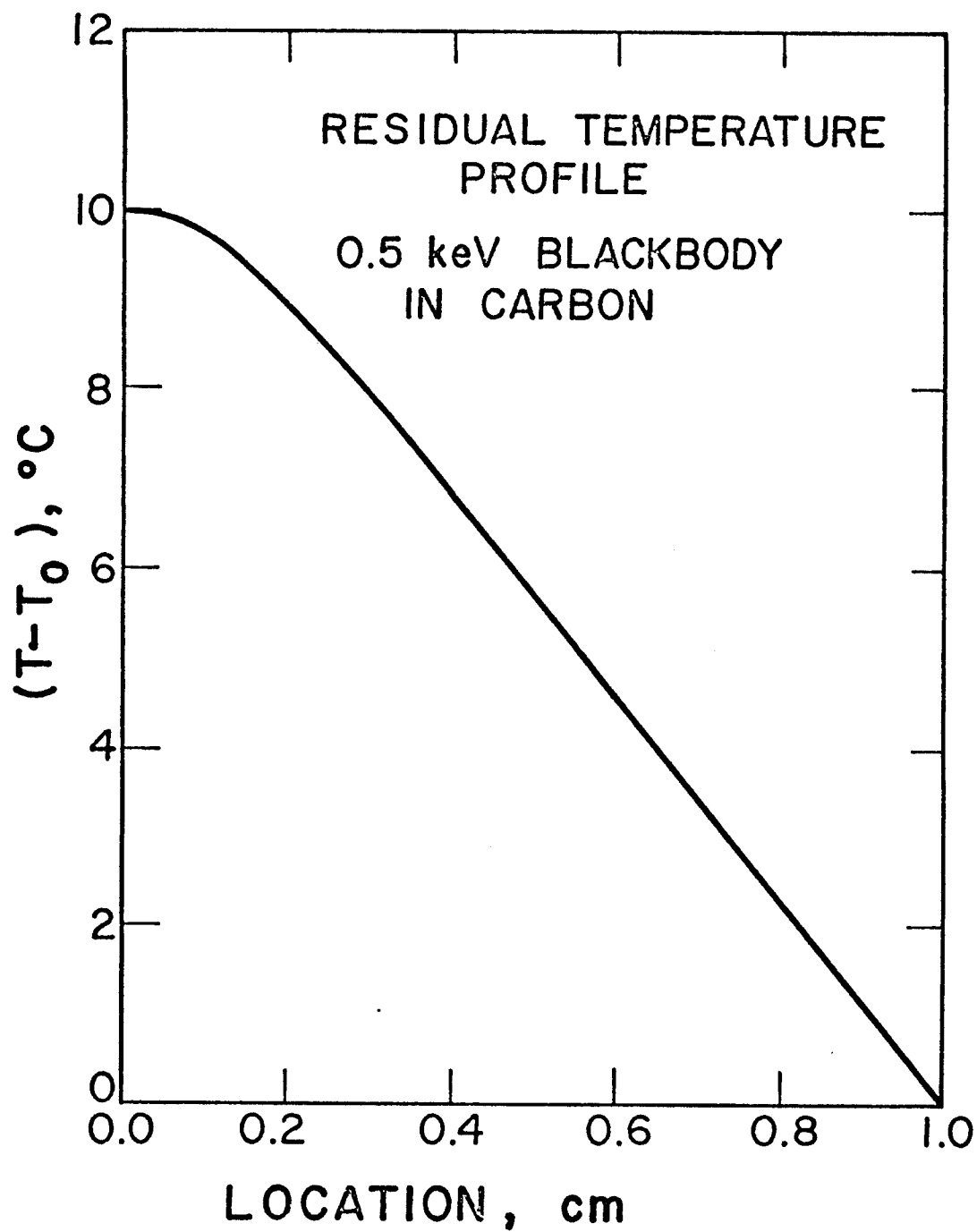
Fig. V. 19.   Residual Temperature Profile in Carbon

Blackbody of 1 J/cm^2 on a graphite slab 1 cm thick. The spacing between pulses was 1/15 seconds. The small variation in front to back surface temperatures ($10°C$) is to be contrasted to the prompt temperature excursion of $1000°C$ under the same irradiation conditions.

A treatment similar to the derivation of Equation 53 can be applied to a slab cooled by convection which results in a similar expansion with different eigenvalues as:

$$49) \quad \frac{T}{T_o}(x,t) = 2 \sum_{n=1}^{\infty} \frac{B_n}{B_n + \sin B_n \cos B_n} \cos B_n z \, e^{-B_n^2 \Theta}$$

$$\left[\frac{1 - e^{-B_n^2 \gamma M}}{1 - e^{-B_n^2 \gamma}} \right] \left[\frac{b}{b^2 + B_n^2} \right] \left[1 - e^{-b}(\cos B_n \frac{B_n}{b} \sin B_n) \right]$$

where B_n are the roots of $\cot B_n = \dfrac{b_n}{hL/k}$

V. C. 2. Thermal Response to Ion Sources

As previously discussed, energetic charged particles have different energy loss mechanisms than photons. Consequently different models are necessary to predict the thermal response. In this section models will be shown which utilize general forms of the deposition developed in section V. B.

Approximations for the thermal response to the deposition of charged particle energy have been made by various investigators.

Behrisch[81] used a model based on energy flux continuity at the irradiated surface. This model is also used for electromagnetic radiation by Ready[82] and for laser mirrors by Howard and Hunter.[83] Frank, et al.[84] used a model based on uniform spatial and temporal deposition taken from calculations by Axford.[85] Hovingh[35] used the same deposition assumption, but evaluated the temperature numerically with the Chart-D code. The solution given here is in a form which will accomodate any spatial profile which can be approximated by polynomials. The solutions are integrated analytically over all space leaving the form of a general Green's function in time which can be used for any commensurate ion flux and set of arrival times.

In the deposition section V. B., methods were shown by which any deposition can be transformed into the general form of a polynomial with coefficients determined by the energy of the ion. A general response model is developed for such depositions in this section. A solution is first obtained for the response in a semi-infinite medium which is used for transients and finally a result for a slab of finite width using lower order polynomial deposition is obtained for an arbitrary number of pulses.

V. C. 2. a. General Deposition in a Semi-Infinite Medium

The general solution for any deposition function can be obtained from the theory of Green's functions as:

$$50) \quad T(x,t) = \int_{t'} \int_{x'} \frac{f(t')}{\rho c} \, g(x') \, G(x,t,x',t') \, dx' \, dt'$$

where $\quad f(t') \, g(x') = \overset{\cdot}{q}(x',t') =$ volumetric energy

deposition rate

$\rho =$ density

$c =$ specific heat

and as before

$G(x,t,x',t') =$ the Green's function which for a semi-infinite slab[78] is:

$$51) \quad G = \frac{1}{2\sqrt{\alpha(t-t')} \ \sqrt{\pi}} \left\{ e^{-(x'-x)^2/4\alpha(t-t')} + e^{-(x'+x)^2/4\alpha(t-t')} \right\}$$

where $\quad \alpha =$ thermal diffusivity.

The Green's function can be written

$$52) \quad G = \frac{1}{A\sqrt{\pi}} \left\{ e^{-(x'-x)^2/A^2} + e^{-(x'-x)^2/A^2} \right\}$$

$$A = 2 \sqrt{\alpha(t-t')}$$

since the variables are separable equation 50 can be written

53) $T(x,t) = \int_{t'} \frac{f(t')}{\rho c} \int_{x'} g(x')G(x,t,x',t') \, dx' \, dt'$

Before addressing any particular problem such as deposition of energetic ions, a general solution will be developed for spatial distributions of the form

54) $g(x) = C_0 + C_1 x + C_2 x^2 + C_3 x^3 + C_4 x^4$

where C_i are in general functions of time (or ion energy).

The spatial integral becomes the evaluation of the following sequence

55) $S_N = \frac{C_N}{\sqrt{\pi}} \int (\frac{x'^N}{A} e^{-(x'-x)^2 /A^2} + \frac{x'^N}{A} e^{-(x'+x)^2 /A^2}) \, dx$

We make use of the following integral.

56) $\int x^N e^{-a^2 x^2 + bx} \, dx =$

$a^{-N-1} e^{b^2/4a^2} \sum_{k=0}^{N} \frac{N!}{k!(N-k)!} (\frac{b}{2a})^{N-k} \int u^k e^{-u^2} \, du = (III)$

where $ax - b/2a = u$

If the square is completed

$\int x^N e^{-a^2 x^2 + bx - b^2/4a^2} \, dx = e^{-b^2 /4a^2}$ (II)

then

58) $$\int x^N \; e^{-(ax-b/2a)^2} \; dx = a^{-N-1} \sum_{k=0}^{N} \frac{N!}{k!(N-k)!} \; (\frac{b}{2a})^{N-k} \int u^k e^{-u^2} du$$

The higher order integrals can now be expressed in terms of the first two (we will now ignore the constant terms $C_i/\sqrt{\pi}$). The integrals can now be represented as:

58) $$S_N = \int \frac{x'^N}{A} \; e^{-(\frac{x'}{A} - \frac{x}{A})^2} \; dx' + \int \frac{x'^N}{A} \; e^{-(\frac{x'}{A} + \frac{x}{A})^2} \; dx'$$

If the following convention is adopted

$$S_N = S_N^{(-)} + S_N^{(+)}$$

we have the form of equation (57) with

for $S_N^{(-)}$ $a = \frac{1}{A}$ $\frac{b}{2a} = \frac{x}{A}$

for $S_N^{(+)}$ $a = \frac{1}{A}$ $b/2a = - \frac{x}{A}$

Evaluating the S_N's

$$S_o^{(\mp)} = \int e^{-u^2} \; du = \int \frac{1}{A} \; e^{-(\frac{x'}{A} \mp \frac{x}{A})^2} \; dx' = I_o^{(\mp)}$$

if $u = \frac{x'}{A} \mp \frac{x}{A}$

and:

$$S_1 \; (\overline{+}) = \frac{1}{A} \; A^2 \; \left\{ \pm \frac{x}{A} \int e^{-u^2} \; du + \left(\pm \frac{x}{A} \right)^0 \int u' \; e^{-u^2} \; du \right\}$$

which can be expressed as

$$S_1 \; (\overline{+}) = \pm x \, I_o + A \, I_1$$

likewise

$$S_2 \; (\overline{+}) = (\pm x)^2 \, I_o + 2(\pm x) \, A \, I_1 + A^2 \, I_2$$

$$S_3 \; (\overline{+}) = (\pm x)^3 \, I_o + 3(\pm x)^2 A \, I_1 + 3 \, (\pm x) \, A^2 I_2 + A^3 I_3$$

$$S_4 \; (\overline{+}) = (\pm x)^4 \, I_o + 4(\pm x)^3 A \, I_1 + 6 \, (\pm x)^2 A^2 I_2 +$$

$$4(\pm x) \, A^3 I_3 + A^4 I_4$$

Summarizing

$$S_N \; (\overline{+}) = \int \frac{x'^N}{A} \; e^{-\left(\frac{x'}{A} + \frac{x}{A} \right)^2} dx'$$

which can be expressed in matrix form as

N	I_0	I_1	I_2	I_3	I_4
0	1				
1	$\pm x$	A			
2	$(\pm x)^2$	$2(\pm x)A$	A^2		
3	$(\pm x)^3$	$3(\pm x)^2 A$	$3(\pm x)A^2$	A^3	
4	$(\pm x)^4$	$4(\pm x)^3 A$	$6(\pm x)^2 A^2$	$+ \; 4(\pm x)A^3$	A^4

59)

in order to evaluate the I_N's the following convention is adopted

$$I_N^- = \int \left(\frac{x'}{A} - \frac{x}{A}\right)^N e^{-\left(\frac{x'}{A} - \frac{x}{A}\right)^2} dx'$$

$$I_N^+ = \int \left(\frac{x'}{A} + \frac{x}{A}\right)^N e^{-\left(\frac{x'}{A} + \frac{x}{A}\right)^2} dx'$$

The solution can be rewritten by adding $S^{(+)}$ and $S^{(-)}$

$$S_0 = [I_0^- + I_0^+]$$

$$S_1 = x [I_0^- - I_0^+] + A [I_1^- + I_1^+]$$

60) $$S_2 = x^2 [I_0^- + I_0^+] + 2xA [I_1^- - I_1^+] + A^2 [I_2^- + I_2^+]$$

$$S_3 = x^3 [I_0^- - I_0^+] + 3x^2 A [I_1^- + I_1^+] + 3xA^2 [I_2^- - I_2^+]$$
$$+ A^3 [I_3^- + I_3^+]$$

$$S_4 = x^4 [I_0^- + I_0^+] + 4x^3 A [I_1^- - I_1^+] + 6x^2 A^2 [I_2^- + I_2^+]$$
$$+ 4xA^3 [I_3^- - I_3^+] + A^4 [I_4^- + I_4^+]$$

The complete solution to equation 53 is then

61) $\quad T(x,t) = \int_{t'} dt' \frac{f(t')}{\rho c} \frac{1}{\sqrt{\pi}} \left[C_0 S_0 + C_1 S_1 + C_2 S_2 + C_3 S_3 + C_4 S_4 \right]$

evaluated at
limits of x'

I_N's can be evaluated in the following manner:

$$I_0 = \int e^{-u^2} du = \frac{\sqrt{\pi}}{2} \quad erf \ (u)$$

$$I_1 = \int u \ e^{-u^2} \ du = \frac{-1}{2} \ e^{-u^2}$$

and knowing $\quad \int u^N \ e^{-u^2} \ du = - \frac{1}{2} u^{N-1} \ e^{-u^2} +$

$$\frac{N-1}{2} \int u^{N-2} \ e^{-u^2} \ du$$

$$I_2 = - \frac{1}{2} u \ e^{-u^2} + \frac{1}{2} I_0 = - \frac{1}{2} F_1 + \frac{1}{2} I_0$$

$$I_3 = - \frac{1}{2} u^2 e^{-u^2} + I_1 = - \frac{1}{2} F_2 + I_1$$

$$I_4 = - \frac{1}{2} u^3 \ e^{-u^2} + \frac{3}{2} \int u^2 \ e^{-u^2} \ du = - \frac{1}{2} F_3 - \frac{3}{4} F_1 + \frac{3}{4} I_0$$

in terms of I_0, I_1 and F_N this may be summarized

I_N	I_0	I_1	F_1	F_2	F_3
I_0	1				
I_1		1			
I_2	1/2		-1/2		
I_3		1		-1/2	
I_4	3/4		-3/4		-1/2

where $F_N = u^N e^{-u^2}$

Equation 61 and 59 may be combined to give a general result

$$62) \quad T(x,t) = \int dt' \ \frac{f(t')}{\rho c} \ \frac{1}{\sqrt{\pi}} \sum c_N S_N \qquad \text{evaluated at}$$

$$\text{limits of } x'$$

where

S_N are the diagonal terms ($S_N \to NN$th term) of the matrix product

$$|Q| \qquad\qquad |M|$$

where $|Q|$ is

$$63) \quad \begin{vmatrix} 1 & & & & \\ x & A & & & \\ x^2 + A^2/2 & 2xA & \dfrac{-A^2}{2} & & \\ \dfrac{3A^2 x + x^3}{2} & 3x\,A + A^3 & \dfrac{-3xA^2}{2} & \dfrac{-A^3}{2} & \\ \dfrac{3A^4}{4}+\dfrac{6A^2}{2}\,x^2 + x^4 & 4xA^3 + 4x^3 A & \dfrac{-6A}{2}\,x^2 - \dfrac{3A^4}{4} & \dfrac{-4xA^3}{2} & -\dfrac{A^4}{2} \end{vmatrix}$$

and $|M|$ is

$$64) \quad \begin{vmatrix} I_0(+) & I_0(-) & I_0(+) & I_0(-) & I_0(+) \\ & I_1(+) & I_1(-) & I_1(+) & I_1(-) \\ & & F_1(+) & F_1(-) & F_1(+) \\ & & & F_2(+) & F_2(-) \\ & & & & F_3(+) \end{vmatrix}$$

where $I_N(+) = (I_N^- + I_N^+)$

$I_N(-) = (I_N^- + I_N^+)$

Equation 62 represents a general solution for any deposition interval when the functions are contained are evaluated at the limits of the region in which the polynomial applies. Substitution of the limits can simplify the result when the symmetry of the functions I_N and F_N are accounted for. The following relations are noted:

$$65) \quad \begin{aligned} I_0 &= \sqrt{\pi}/2 \ \text{erf } (u) = \text{odd} \\ I_1 &= -\frac{1}{2} \ e^{-u^2} = \text{even} \\ F_1 &= u \ e^{-u^2} = \text{odd} \\ F_2 &= u^2 \ e^{-u^2} = \text{even} \\ F_3 &= u^3 \ e^{-u^2} = \text{odd} \end{aligned}$$

when the limits $0 \rightarrow x_m$ are inserted into equation 60 the $|M|$ matrix is transformed as:

$$|M|_{LIMITS} = |M_L| =$$

66)

$$\begin{vmatrix} I_0(+) & I_0(-) + 2\,I_0(0) & I_0(+) & I_0(-) + 2\,I_0(0) & I_0(+) \\ & I_1(+) - 2\,I_1(0) & I_1(-) & I_1(+) - 2\,I_1(0) & I_1(-) \\ & & F_1(+) & F_1(-) + 2F_1(0) & F_1(+) \\ & & & F_2(+) - 2\,F_1(0) & F_2(-) \\ & & & & F_3(+) \end{vmatrix}$$

where $I_N(+) - 2\,I_N(0)$ is to be interpreted as

$$I_N(\frac{x_m - x}{A}) + I_N(\frac{x_m + x}{A}) - 2\,I_N(0 + \frac{x}{A})$$

Finally, a general solution is obtained when equation 62 is evaluated. The spatial contribution is contained in the evaluation of the function $\Sigma\ C_N S_N$ at the limits of the deposition region while the temporal contribution is done numerically to accomodate arbitrary spectrum.

If the deposition does not require all five coefficients, the formulation is of course much simpler. The solution derived by the author in reference 86 is actually the same as equation 62 if the coefficients C_2, C_3, C_4, $C_5 = 0$, which corresponds to an ion in region I with equation 1 chosen for the deposition. The equation is simplified as the matrices $|Q|$ and $|M|$ become:

$$|Q| = \begin{vmatrix} 1 & \\ x & A \end{vmatrix}$$

67) $$|M| = \begin{vmatrix} I_0(+) & I_0(-) \\ & I_1(+) \end{vmatrix} \quad \begin{array}{l} \text{evaluated} \\ \text{at limits} \\ \text{of region} \end{array}$$

The uniform deposition model, which was appropriate for some high mass-low energy ions, would result in an even more simplified result where

68) $$|Q| = |1|$$
$$|M| = |I_0(+)|$$

In summary, the complete solution for an ion which requires deposition functions in all regions (I, II, III) can then be expressed.

69) $$T(x,t) = \int_{t'} \frac{f(t')}{\rho c} \frac{dt'}{\sqrt{\pi}} \left\{ \sum_{N=0}^{4} C_{1N} S_N \Bigg| \begin{array}{l} \text{limits of} \\ \text{region III} \end{array} \right.$$

$$+ \sum_{N=0}^{4} C_{2N} S_N \Bigg| \begin{array}{l} \text{limits of} \\ \text{region II} \end{array} + \sum_{N=0}^{4} C_{3N} S_N \Bigg| \begin{array}{l} \text{limits of} \\ \text{region I} \end{array} \Bigg\}$$

where S_N are the NN elements of $|Q|$ (eqn. 63) and $|M|$ (eqn. 64).

$|Q|$ and $|M|$ consist of the functions

$$I_0 = \frac{\sqrt{\pi}}{2} \text{ erf } (u)$$

$$I_1 = -1/2 \ e^{-u^2}$$

$$F_1 = u \ e^{-u^2}$$

$$F_2 = u^2 \ e^{-u^2}$$

$$F_3 = u^3 \ e^{-u^2}$$

and the elements of eqn. 64 are interpreted as

$$I_N(+) = I_N(\frac{x'-x}{A}) + I_N(\frac{x'+x}{A})$$

$$I_N(-) = I_N(\frac{x'-x}{A}) - I_N(\frac{x'+x}{A})$$

where $A = 2\sqrt{\alpha(t-t')}$

V. C. 2.b. Ion Deposition in Finite Slabs

The formulation for the temperature response for a series of ion pulses is best developed for a finite width material since the sustained value of the temperature will be more directly influenced by a boundary condition at the rear surface. The same semi-infinite solution presented above would still, however, be used to evaluate the transients which are not influenced by the rear boundary.

For the case in which a radiation pulse train is incident on a slab of material, a solution can be developed for two simple deposition models: a uniform deposition and a linearly decreasing model. The procedure is easily extended to more general deposition models. At any given time the spatial deposition will be given by either of

the two functions shown in figure V. 20.   These functions will

vary for arbitrary spectra but their general shape will be the same.

The problem for a single group of ions which contains $f(t')$

dt' ions can be stated as

$$k\frac{\partial^2 T}{\partial x^2} = \rho c \, \frac{\partial T}{\partial t}$$

70)

$$\frac{\partial T}{\partial x} \, (0,t) = 0$$

$$T(x,0) = g(x)/\rho c = f(x)$$

$$T(L,t) = \text{(constant temperature rear surface)}$$

This has the solution[78].

71) $$T(x,t) = \sum_{N=1}^{\infty} \cos B_N \frac{x}{L} \, e^{-B_N^2 \, \Theta} \, \frac{2}{L} \int_0^L f(x) \cos \frac{B_N \, x}{L} \, dx$$

where $B_N = (2N-1) \, \pi/2 \qquad \Theta = \alpha t/L^2$

α = thermal diffusivity

L = slab width

Equation 71 has the form

72) $$T(x,t) = \sum_{N=1}^{\infty} A(Z) \, e^{-B_N^2 \, \Theta} \quad B(Z)$$

where $Z = x/L$
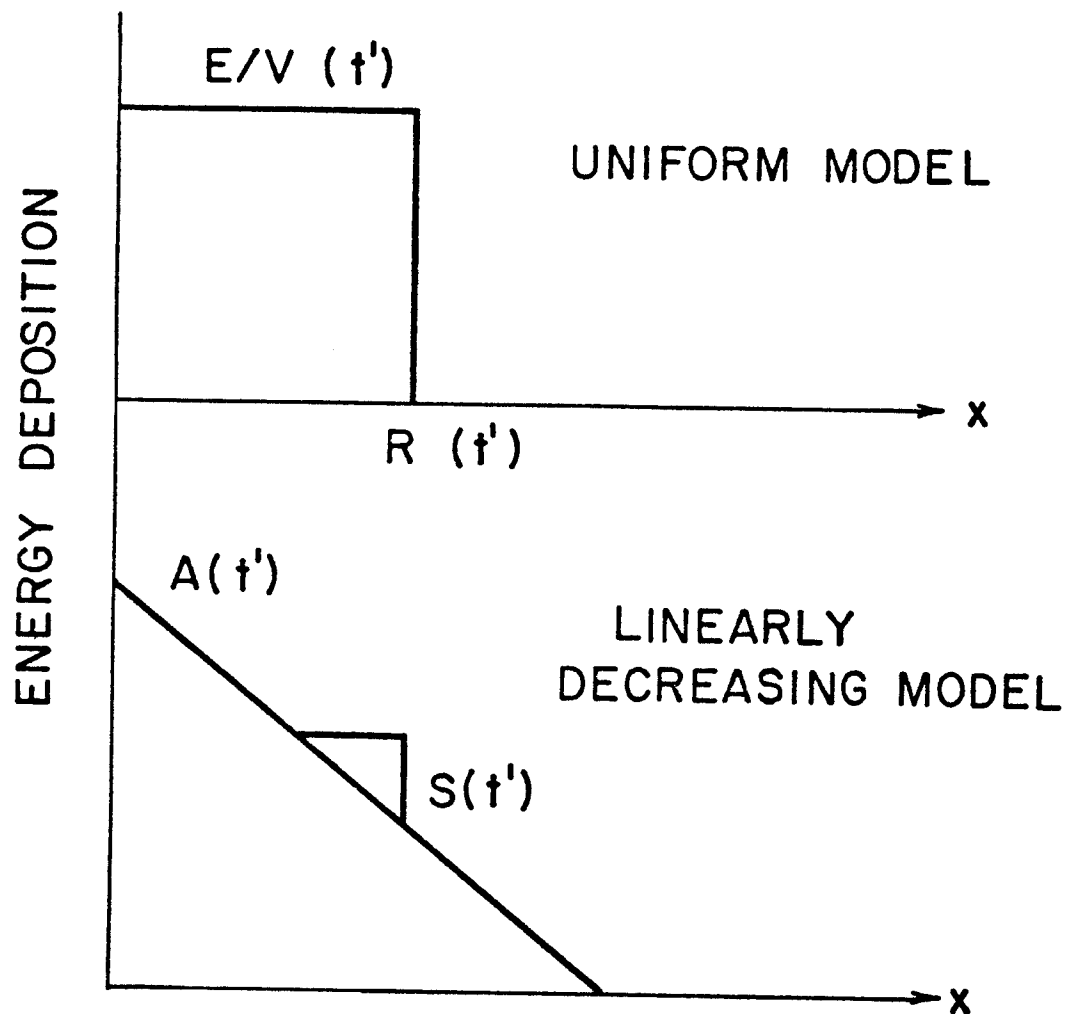
Fig. V. 20. Models for Spatial Energy Deposition

The solution to this same group for a series of pulses as shown in figure V. 21 can be obtained by Laplace transforms, similar to the method employed in section V. C. 1. b. ii for multiple photon irradiations.

In this case the transfer function is the transform of equation 70

$$73) \quad H(s) = \sum_{N=1}^{\infty} A(Z) \, B(Z) \, \frac{1}{s + \dfrac{B_N^2 \, \alpha}{L}}$$

The transform of the solution for a series of M pulses can be obtained by convolution since the transform of a series of impulses is

$$74) \quad V(s) = 1 + e^{-\omega s} + e^{-2\omega s} + - - -$$

then

$$75) \quad T(x,t) = \mathscr{L}^{-1} \, H(s) \, V(s)$$

which as shown in part section V. C. 1. b. ii is

$$76) \quad T(x,t) = \sum_{N=1}^{\infty} A(Z) \, B(Z) \, e^{-B_N^2 \, \Theta} \left[\frac{1 - e^{-B_N^2 \gamma \, M}}{1 - e^{-B_N^2 \, \gamma}} \right]$$

where $\Theta = \dfrac{\alpha \delta}{L^2}$ $\qquad \gamma = \dfrac{\alpha \omega}{L^2}$

$M = \#$ of pulses

$\delta =$ time from last impulse
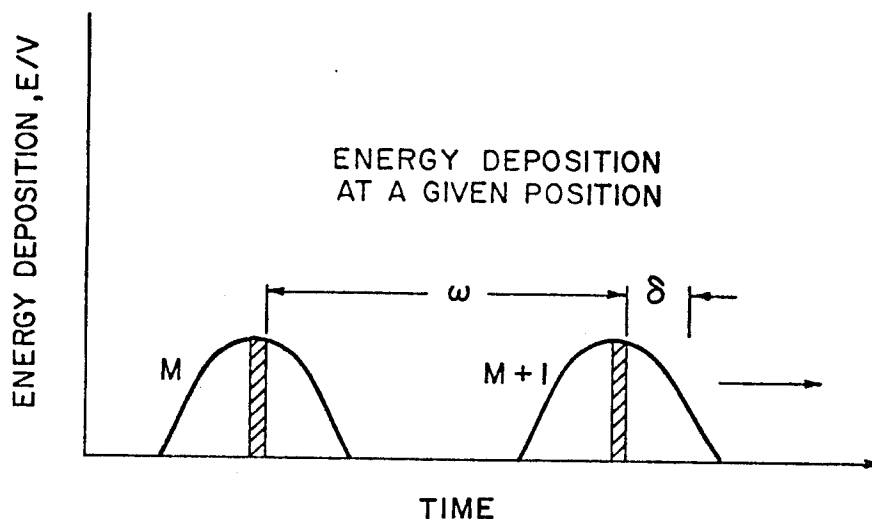
Fig. V. 21. Energy Deposition Rate at a Given Position

In a linear system equation 76 becomes a composite (meaning the response to all previous impulses) Green's function for M impulses.

The response at time t measured from the start of the M'th pulse (figure V.21) can be determined from the theory of Green's functions as

77) $\quad T(x,t) = \int_0^{t^*} G(x,t,t') \, dt'$

where $t^* = t \qquad t < t_{max}$

$t^* = t_{max}$

$t > t_{max} \qquad (t_{max}$ is taken at the end of a

single pulse)

and consideration of equation 76, the Green's function is actually just

$$78) \quad G(x,t,t') = \sum_{N=1}^{\infty} A(Z) \ B(t',Z) \ e^{-B_N^2 \Theta} \left[\frac{1 - e^{-B_N^2 \ \gamma M}}{1 - e^{-B_N^2 \ \gamma}} \right]$$

B is a function of t' since in general the limits of the integration over space will be a function of ion arrival time as

$$\Theta = \frac{\alpha(t-t')}{L^2}$$

At this point it is necessary to determine the function B for the spatial profile considered. B was defined in equation 72 as

$$79) \quad B(t',x) = \frac{2}{L}\int_0^L f(x) \ \cos B_N \ \frac{x}{L} \ dx$$

If the uniform deposition profile of figure V. 20 is used for f (x) this becomes

$$80) \quad B(t', x) = \frac{2}{L} \int_0^{R(t')} \frac{F(t')}{R(t') \ \rho c} \ \cos B_N \ x/L \ dx$$

where $R(t')$ is the end of the deposition region. This yields the result

$$81) \quad B(t',x) = 2 \ \frac{F(t')}{R(t') \ \rho c B_N} \ \sin \frac{B_N R}{L}$$

where $F(t')$ is the energy unit area in the interval dt'.

Equation 81 can then be put in equations 78 and 77 to obtain the solution for an entire spectrum of particles.

If the linearly decreasing deposition profile (figure V. 20) is chosen equation 79 becomes

$$82) \quad B(t',x) = \frac{2}{L} \int_0^{A(t')/S(t')} \frac{A(t') - S(t')x}{\rho c} \cos \frac{B_N x}{L} dx$$

where $A(t') - S(t')x$ represents the energy per unit volume in the interval dt' the result of this integration is

$$83) \quad B(t',x) = \frac{2 L S(t')}{B_N^2} [1 - \cos \frac{B_N A(t')}{S(t')L}]$$

Equation 83 can likewise be put into equation 78 and 77 to obtain a solution for a spectrum of particles.

V. D. Stress Response

Stresses will be produced in irradiated first walls by the momentum of the bombarding particles, the ablation of the exposed surface, and the thermoelastic response to the deposited energy.

The first of these effects is normally a negligible factor. An estimate of the magnitude of these stresses can be made by applying Equation 8 with the peak particle fluxes given in Figure V. 4. The pressures corresponding to these data are

neutrons $\sim$ 8×10^6 dynes/cm^2 = 8 atmospheres (max)

ions $\sim$ 1.5×10^4 = 0.15 atmospheres

The value for the neutrons is deceptive since only about 10% of the 14 MeV neutrons will have collisions in the first cm and each collision would represent only a few percent reduction in the

momentum of the neutron, hence the real value is several orders of magnitude less than the above. High energy alpha particles will however contribute higher stress values. For example, $10^{13}/cm^2$ of 3 MeV alphas deposited over 10 ns will yield about 8 atmospheres of normal stress on the first wall.

The stress developed due to ablation can be readily calculated with general material response numerical codes and will not be discussed here.

The third stress source, the thermoelastic response, can be estimated with methods of linear elasticity and thus is analytically tractable. The ability to develop solutions for a wide variety of energy depositions makes these methods interesting for parametric analyses.

The generation of thermoelastic stress waves is due to a thermodynamic requirement for a local expansion which occurs in a time which is short compared with the time for the material to relax.

The defining relations of thermally developed stress waves can be developed as follows:

In an isotropic material, the stress tensor is given as:[87]

84) $\quad \alpha_{ij} = \lambda e_{\mu\mu} \delta_{ij} + 2 G e_{ij} - \beta \delta_{ij} \Theta$

where $\quad \beta = \dfrac{\alpha E}{1 - 2\nu} = (3\lambda + 2G)\alpha$

λ, G = Lame's constants

E = Young's modulus

v = Poisson's Ratio

α = thermal coefficient of linear expansion

e_{ij} = strain tensor, $e_{\mu\mu} = e_{11} + e_{22} + e_{33}$

$\Theta = T - T_0$ where T_0 = reference temperature in stressed state

In the case of uniaxial strain, this relation yields the **axial** stress in terms of the axial strain and temperature as:

$$\sigma = \lambda e + 2Ge - \beta \Theta$$

or

85) $\sigma = (K + 4/3G)e - 3\alpha K \Theta$ where K = Bulk modulus

$$K = \frac{E}{3(1-2v)}$$

$$e = strain = \frac{\partial u}{\partial x}$$

The equation of motion in one direction is

86) $$\frac{\partial \sigma}{\partial x} = \rho \frac{\partial u^2}{\partial t^2}$$

Equations 67 and 68 can be combined to give the stress **wave** equation

87) $$\frac{\partial^2 \sigma}{\partial x^2} - \frac{1}{c^2} \frac{\partial^2 \sigma}{\partial t^2} = \frac{3\alpha K}{c^2} \frac{\partial^2 \Theta}{\partial t^2}$$

where c = dilational wave speed

$$c^2 = (K + 4/3G)/\rho$$

The temperature is given by a combination of the heat conduction equation and the energy equation as:

88) $\quad k \dfrac{\partial^2 \Theta}{\partial x^2} = \rho c \dfrac{\partial \Theta}{\partial t} + T\beta \dfrac{\partial e}{\partial t}$

Equations 87 and 88 are coupled equations which express the relation between temperature and stress in a uniaxial strain system. These equations have been treated by many investigators. Most applications treat them in an "uncoupled" manner in which the last term in Equation 88 is ignored. This term represents the work done per unit volume by dilational forces and is usually small in comparison with energy transfer by conduction.

A solution for step and ramp function temperature boundary counditions on an infinite half space was developed by Sternberg and Charkravorty[88] while a complete coupled solution for exponentially increasing surface temperature was presented by Daimaruya and Naito.[89] White[90] treated a variety of surface temperature conditions. A general assessment of transient coupled boundary value problem for a half space was performed by Baley and Tolins.[91]

For energy deposition into the material, Morland[92] developed a solution for electromagnetic radiation in a semi infinite solid. This model was later extended to viscoelastic materials with Hegemier.[95] A specific application for laser irradiation was treated by Penner and Sharma.[94]

A set of solutions for the half space and a finite slab were developed by Zaker.[95] Similar expressions were derived by Hedjazi and Lovell[17] for the analysis of materials to electromagnetic radiation. One application to the response of polycrystaline metals to relativistic electron beams was reported by Perry.[96] The later application was performed for delta function sources and uniform pulses of finite duration. Data were compared with experiments using E-beam irradiation of aluminum, copper, and tantalum.

In the papers by Morland,[92] Hegimier,[93] and Penner,[94] the solutions were developed on the assumption that the propagation of stress waves occurs in times which are much shorter than the times for temperature relaxation. The creation of thermoelastic stress can only occur if the energy is deposited in times which are short compared with the time for a stress wave to transmit the deposition region. Since wave velocities are on the order of 10^5 cm/sec, this corresponds to pulse durations which are less than

$$t_d < \ell/c$$

or

$$t_c < 10^{-8} \text{ sec}$$

for deposition over 10 μm intervals. An analysis will be presented here which will further quantify these characteristic time scales.

The amplitude of the stress generated by an instantaneous deposition can be determined from Equation 84 with the condition that $e_{ij} = 0$. In this case, for uniaxial strain

$$\sigma = \beta\Theta \quad , \quad \beta = \frac{\alpha E}{1 - 2\nu}$$

for graphite[97]

$$\alpha = 8 \times 10^{-6} \ {}^{\circ}C^{-1}, \quad E \approx 2 \times 10^{6} \ \text{psi} = 1.38 \times 10^{10} \ \text{N/m}^2$$

$$\nu = 0.12$$

therefore

$$\sigma/\Theta = 21 \ \text{psi}/{}^{\circ}C, \ 0.15 \ \text{MN/m}^2/{}^{\circ}C$$

For the photon radiation deposited into graphite as shown in Figure V. 17 an intensity of 1 J/cm^2 of 0.5 keV Blackbody radiation will yield a stress of 150 MN/m^2 (21000 psi).

This value represents the initial compression stress before the stress wave motion occurs. The amplitude of the rarefaction wave which develops as the wave propagates into the material is about 1/2 of this value.

These stress waves will be attenuated as they propagate into the material, but they may be of sufficient magnitude to cause surface spallation or failure by production of fatigue crack growth.[98]

This section will now address the solution of these equations and consider the temporal or spatial criteria necessary for establishment of a stress wave of significant amplitude from the transient deposition of energy.

The procedure will be to pick a deposition model, derive a set of equations for the temperature and stress responses and then examine the relation between the deposition depths and times which produce stress waves.

The emphasis will be on deriving the time scales over which energy must be deposited for wave generation. The result will be to establish that middle ground between the "instantaneous" deposition of energy which occurs faster than the material can expand thus producing stress waves and the slow heating of a specimen which produces an equilibrium expansion and does not generate stress waves in a one dimensional strain configuration.

An example of a particular deposition pulse is chosen which can be characterized in both time and space and which is similar to that encountered in ion irradiations.

Problem Statement

Consider a pulse of energy which arrives at the surface of a semi-infinite media (Figure V. 22).

The energy will penetrate into the material with some characteristic depth, δ, and will have a time history given by some function $f(t)$ which will have some characteristic width, θ. If θ is sufficiently small a stress wave will be generated which will propagate into
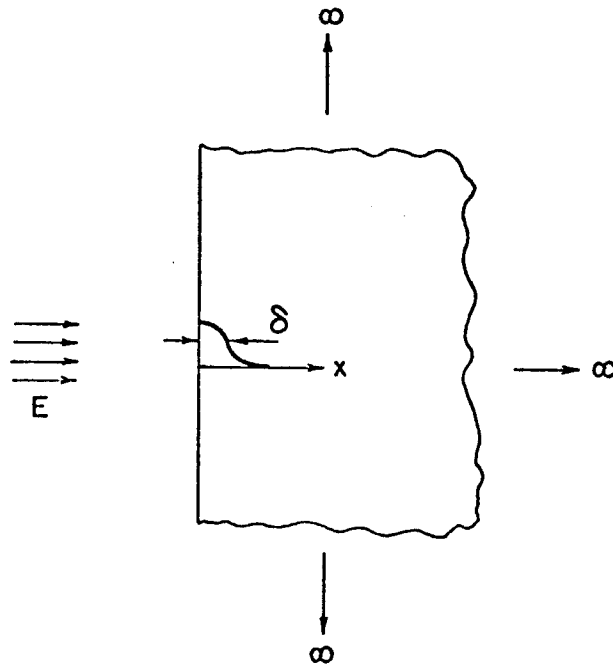
Fig. V. 22. Transient Energy Deposition Problem Statement

the material. The wave will have a wave length of the order of δ

and will propagate with some velocity, c, in the media.

Let us consider an energy pulse with the following character-

istics, a volumetric heating rate given by:

89) $\dot{q}(x,t) = f(t) \ g(x)$

90) where $g(x) = \dfrac{E}{\sqrt{2\pi} \ \delta} \ e^{-1/2(\frac{x}{\delta})^2}$

91) and $f(t) = \omega \ \sin \omega t$

so in space the function is gaussian with characteristic width, δ, as
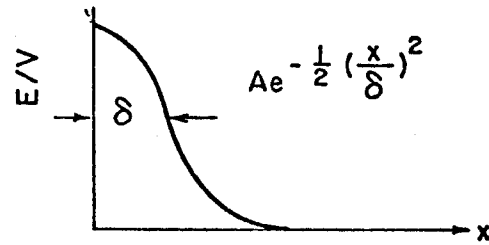
(Fig. V. 23):

Fig. V. 23.   Spatial Deposition Profile

and in time (Fig. V. 24)
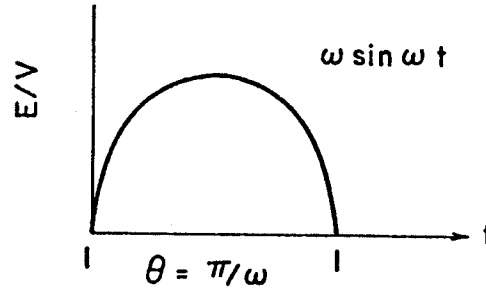
Fig. V. 24.   Deposition Time History

the integral over all space and time is seen to be

$$\int_0^{\pi/\omega} \int_0^\infty f(t)\ g(x) = \int_0^{\pi/\omega} \frac{1}{2}\ E\omega \sin\ \omega t = E \left\{\begin{array}{l} \text{the energy} \\ \text{in the} \\ \text{pulse} \end{array}\right\}$$

The defining equation for the stress response as given in equation 87 is

$$92) \quad \frac{\partial^2 \sigma}{\partial x^2} - \frac{1}{c^2} \frac{\partial \sigma}{\partial t^2} = A \frac{\partial^2 T}{\partial t^2}$$

$$c = \frac{E/\rho \ (1 - \nu)}{(1 + \nu) \ (1 - 2\nu)} \qquad \text{longitudinal wave velocity}$$

$$A = \rho\alpha \frac{(1 + \nu)}{(1 - \nu)}$$

α = coefficient of thermal expansion (linear)

The temperature response is given as in the previous section as

$$93) \quad k \frac{\partial^2 T}{\partial x^2} = c \frac{\partial T}{\partial t} - \dot{q} \ (x,t)$$

METHOD OF SOLUTION

The equations to be solved are 92 and 93. These equations are coupled since the wave equation is driven by the temperature equation, but the temperature equation is independent so in a true sense this represents an _uncoupled_ solution.

The procedure used here will be to assume that temperature diffusion is a "slower" process than wave propagation and hence the times of interest for the wave equation are short compared to the thermal response.

We will first solve the temperature equation completely and determine the deposition times in which the response is adiabatic, that is, when the temperature is given by:

94)
$$\frac{\partial T}{\partial t} = \frac{\dot{q}(x,t)}{\rho c}$$

in this case the temperature field is completely known, for short times, and its time dependence is given by the chosen energy deposition function, $f(t)$ - eqn. 91.

We will then solve the stress equation and examine the amplitude of the stress wave as a function of the characteristic deposition times. If the amplitude of the stress wave approaches zero while the deposition times are still short enough for the adiabatic assumption to be valid then the original assumption was valid and the solution is accurate.

TEMPERATURE SOLUTION

The equation to be solved* is

95)
$$k \frac{\partial^2 T}{\partial x^2} + \frac{E\omega}{\sqrt{2\pi}\delta} \sin \omega t \, e^{-x^2/\delta^2} = \rho c \frac{\partial T}{\partial t}$$

subject to

$$\frac{\partial T}{\partial x} = 0 \quad \text{at } x = 0 \qquad\qquad T \to 0 \quad \text{as} \quad x \to \infty$$

---

*This temperature solution is specific for a gaussian energy deposition and was chosen to illustrate the coupling of temperature and stress response. The general temperature is given in section V.C.

The solution can be obtained by a Green's function technique similar to that employed in the previous section with the following result:

$$96) \quad T(x,t) = \int_0^{\pi/\omega} T_o \frac{1}{\sqrt{1+y}} e^{-z^2/(1+y)} \sin \omega t' \, dt'$$

where

$$y = \frac{4\alpha(t-t')}{\delta^2}, \quad z = x/\delta$$

α = thermal diffusivity $\quad T_o = \dfrac{E\omega}{\sqrt{2\pi} \; \delta \; \rho c}$

If $\theta = \pi/\omega$ is very small, the problem will be adiabatic, and the solution for temperature will be the solution to equation 94 which by simple integration is:

$$97) \quad T^*(x,t) = \int_0^{MIN(t, \; \pi/\omega)} T_0 \sin \omega t \; e^{-z^2}$$

$$T^*(x,t) = (1 - \cos \omega t) \frac{T_o}{\omega} e^{-z^2}$$

The next step is to evaluate and compare the solution to Eqs. (96) and (97) so that we may determine which times (θ's = π/ω) are actually short enough to be considered adiabatic. These equations were incorporated into a computer program and were evaluated for various values of θ and τ, where θ is the deposition time and τ is the time at which the response is evaluated, as shown in figure V. 25.
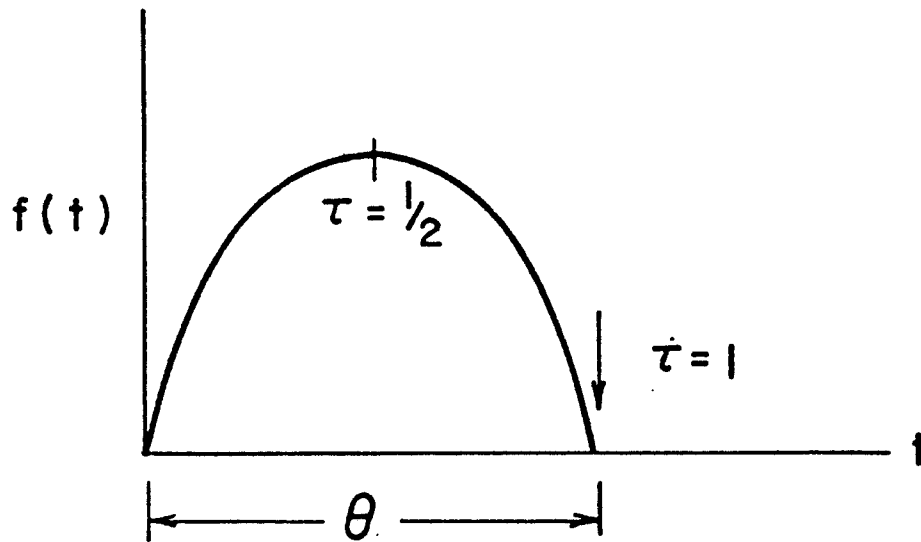
Fig. V. 25. Time Constants

The solution for θ's between 10^{-11} and 10^{-5} are given in Figure V. 26 for three values of x for α = .1, δ = 10^{-4}. Data are shown in terms of T/T^* for τ = 1/2 and 1.

It is seen in Figure V. 26 that for this case the response is essentially adiabatic (within 10%) for pulse durations (θ's) up to about 10^{-8} seconds at least out to x values of δ .

An examination of the dimensionless time parameter from equation 96 yields:

$$y = \frac{4\alpha t}{\delta^2} = \frac{4(.1)(10^{-8})}{(10^{-4})^2} = 0.4$$

or

$$y = \text{order } (1)$$
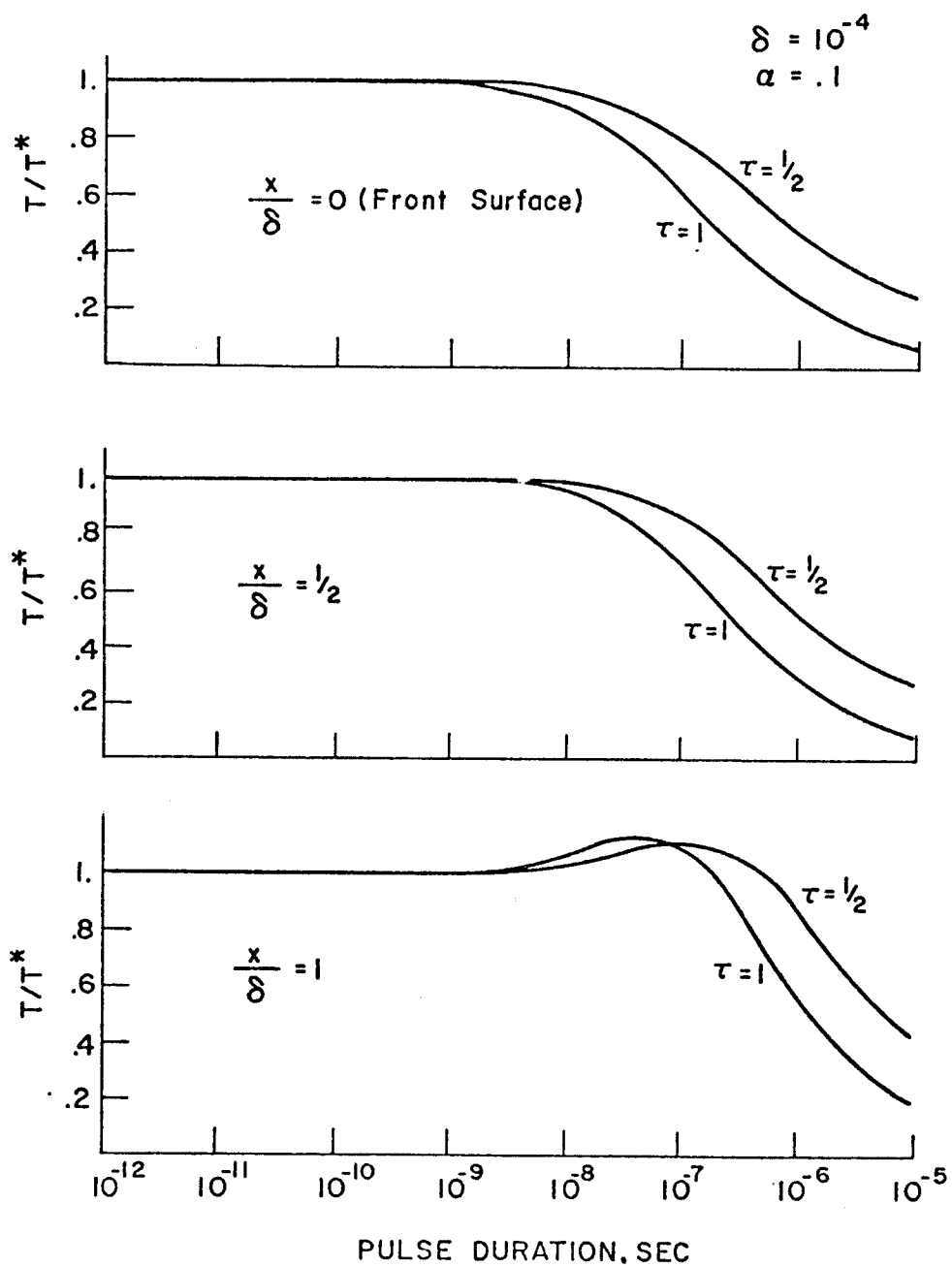
Fig. V. 26. Transient Temperature Response

During pulses with duration $\theta < 10^{-8}$ sec, the temperature solution is given by eqn. 97, and if we find that the durations for stress wave generation are smaller than these, then Eq. 97 will always be a good approximation for $T(x,t)$.

As a reference for numerical values, for the sample problem above, the defining parameters were:

Thermal diffusivity = 0.1 cm /sec

$$\delta = 1 \times 10^{-4} \text{ cm}$$

$$E = 0.1 \text{ J/cm}^2$$

$$\rho c = 1 \text{ J/}^{\circ}\text{C cm}^3$$

The adiabatic temperature at $x = 0$ for very short times is:

$$T_{MAX} = 796^{\circ}C$$

STRESS SOLUTION

Equation (92)

$$\frac{\partial^2 \sigma}{\partial x^2} - \frac{1}{c^2} \frac{\partial^2 \sigma}{\partial t^2} = \frac{\partial^2 T}{\partial t^2} \rho \alpha \frac{(1 + \nu)}{(1 - \nu)}$$

can be coupled with the constitutive relation for uniaxial strain

98)
$$\sigma = \frac{eE(1 - \nu)}{(1 + \nu)(1 - 2\nu)} - \frac{E\alpha}{(1 - 2\nu)}T$$

where e = strain

to set up a solution for the stress. Consider the case of an impulse of energy deposition which has spatial form g(x).   This deposition will result in an adiabatic temperature change as discussed above. It will also result in a stress increase, since it will happen in a time too short for the material to expand. The resulting stress profile will be

99) $\sigma(x) = (\dfrac{E\alpha}{1 - 2\nu})T(x) = \gamma T(x)$

The response of Eq. 92 in this case must be the same as the solution to the homogeneous wave equation with the initial condition of Eq. 99. The solution of the wave equation of the form

100) $\dfrac{\partial^2\phi}{\partial x^2} - \dfrac{1}{c^2}\dfrac{\partial^2\phi}{\partial t^2} = 0$

with boundary condition

$$\phi(0,t) = 0$$

and initial conditions

$$\phi(x,0) = \phi_0(x)$$

$$\dfrac{\partial\phi}{\partial t}\bigg]_{t=0} = V_0(x)$$

is the D'Alemberts solution which is[99]

101) $\phi(x,t) = \dfrac{1}{2} P(x - ct) + \dfrac{1}{2} P(x + ct) + \dfrac{1}{2c} \displaystyle\int_{x-ct}^{x+ct} Q(\zeta)\, d\zeta$

where

$$P(x) = \begin{cases} \phi_0(x) & x \geq 0 \\ -\phi_0(-x) & x < 0 \end{cases}$$

$$Q(x) = \begin{cases} V_0(x) & x \geq 0 \\ -V_0(-x) & x < 0 \end{cases}$$

In our case,

$$V_0(x) \equiv 0$$

$$\phi_0 = \gamma T(x)$$

hence the impulse solution is:

102)

$$\sigma_I(x,t) = \dfrac{1}{2}\left[T(x-ct)H(x-ct) - \gamma\, T(ct-x)H(ct-x) + \gamma T(x+ct) \right]$$

where $H(y)$ is the step function.

Equation 102 represents the solution for a single impulse of energy. The general time-dependent deposition problem may be treated by recognizing that any pulse is a summation of many impulses as in figure V. 27.
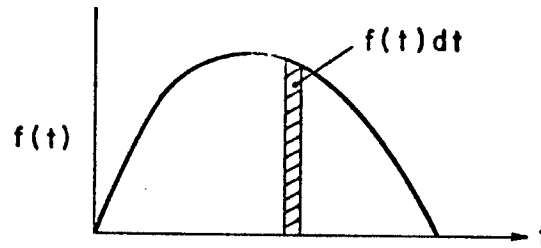
Fig. V. 27. Discretization of Deposition Pulse

Hence, a general solution is found by recognizing that the system is linear and summing over all the impulses in the time-dependent deposition, which the time variable is replaced by the _physical time_ minus the time the impulse occurred as:

103) $\sigma(x,t) = \Sigma \, f_i(t)dt_i \, \sigma_I(x, t - t_i)$

or

104) $\sigma(x,t) = \int_{t'} \sigma_I(x, t - t') \, f(t')dt'$

where σ_I is given by Eq. (102) and

$$T(x) = T_0 \, e^{-z^2}$$

Equations (102),(103) and (104) were derived on a semi-intuitive basis and may seem somewhat unsatisfying. As a result, a rigorous solution of the inhomogeneous wave equation for this case was obtained and presented in Appendix A of Reference 100. The resulting solutions are identical to those developed here.

Equation 104 is similar in concept to that of Zaker[95] and Hedjazi and Lovell[17] but was developed here in the form of a general Green's function which could be applied to the energy depositions anticipated in transient ion irradiations of arbitrary spectra. This form of solution will now be used to determine the radiation conditions which must be met for, stress waves to develop.

If the deposition time were very short, the temperature response would be adiabatic and the stress response would at the end of the pulse be given by:

$$105) \quad \sigma* \ (x,\theta) = \gamma T* \ (x,\theta) = \gamma 2 \ \frac{T_o}{\omega} \ e^{-z^2}$$

which would look like that of Figure V. 28.
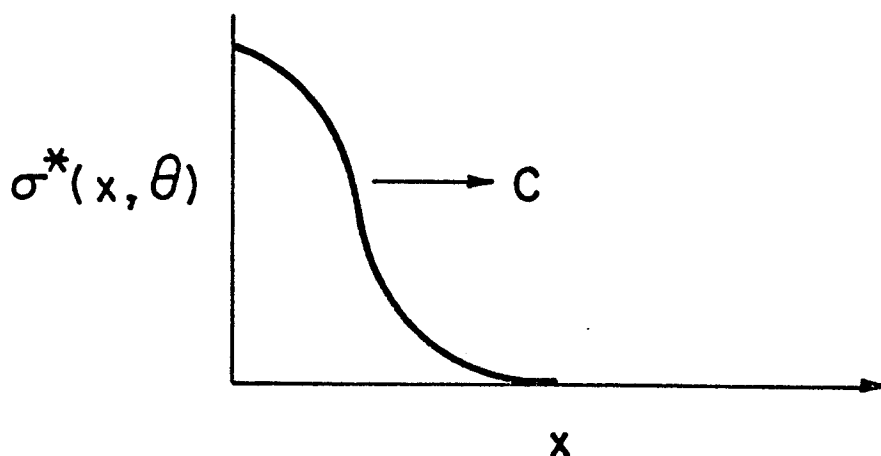
Fig. V. 28. Initial Stress Wave from Impulse Deposition

This stress profile will then propagate into the material and be modified by a rarefaction wave which proceeds from the free surface so that at large distances into the material the profile will look like that in Figure V. 29.
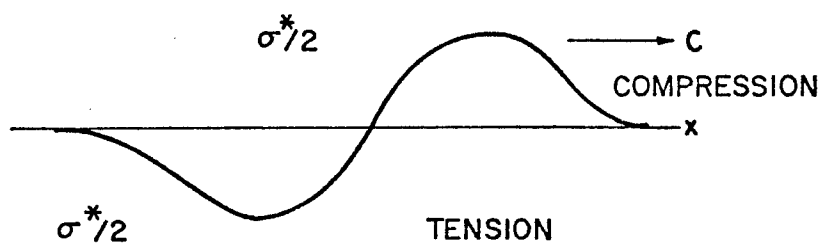
Fig. V. 29. Stress Wave After Propagation into Material

Equation 104 has been evaluated by numerical integration to provide a general solution for arbitrary deposition as long as the temperature is given by the adiabatic assumption. In order to see

the results of this calculation, the condition was solved for various values of deposition time, θ , and the stress was examined deep into the material as the stress wave passed.

The amplitude of the stress wave was determined as a function of time by picking a time just before any disturbance within 2δ of the surface could arrive at a position Y

$$t_0 = \frac{Y - 2\delta}{c}$$

and a time which a wave of duration θ would be fully developed

$$t_1 = \frac{Y}{c} + \theta + \frac{2\delta}{c}$$

and observing the pulse during this interval. Results for stress as a function of time are shown in Figure V. 30.

It is seen in Figure V. 30 that for pulse durations of 10^{-10} seconds, the maximum wave amplitude is 3938 psi with a γ of 10 psi/ °C. This corresponds to

$$\sigma_{MAX} = \frac{\gamma \, T_{MAX}}{2}$$

one-half of the maximum possible initial compressive wave amplitude predicted by Eq. 99. At longer pulse durations, this amplitude diminishes, as for the case of $\theta = 3 \times 10^{-9}$ sec, in Figure V. 30.

STRESS vs. TIME

$x = .1$ cm

$C = 10^5$ cm/sec

$\delta = 10^{-4}$ cm

$\gamma = 10 = \dfrac{\sigma}{T}$ PSI/°C

$\theta = 10^{-10}$

$\theta = 3 \times 10^{-9}$

STRESS, ksi

TIME FROM START OF DEPOSITION, NS
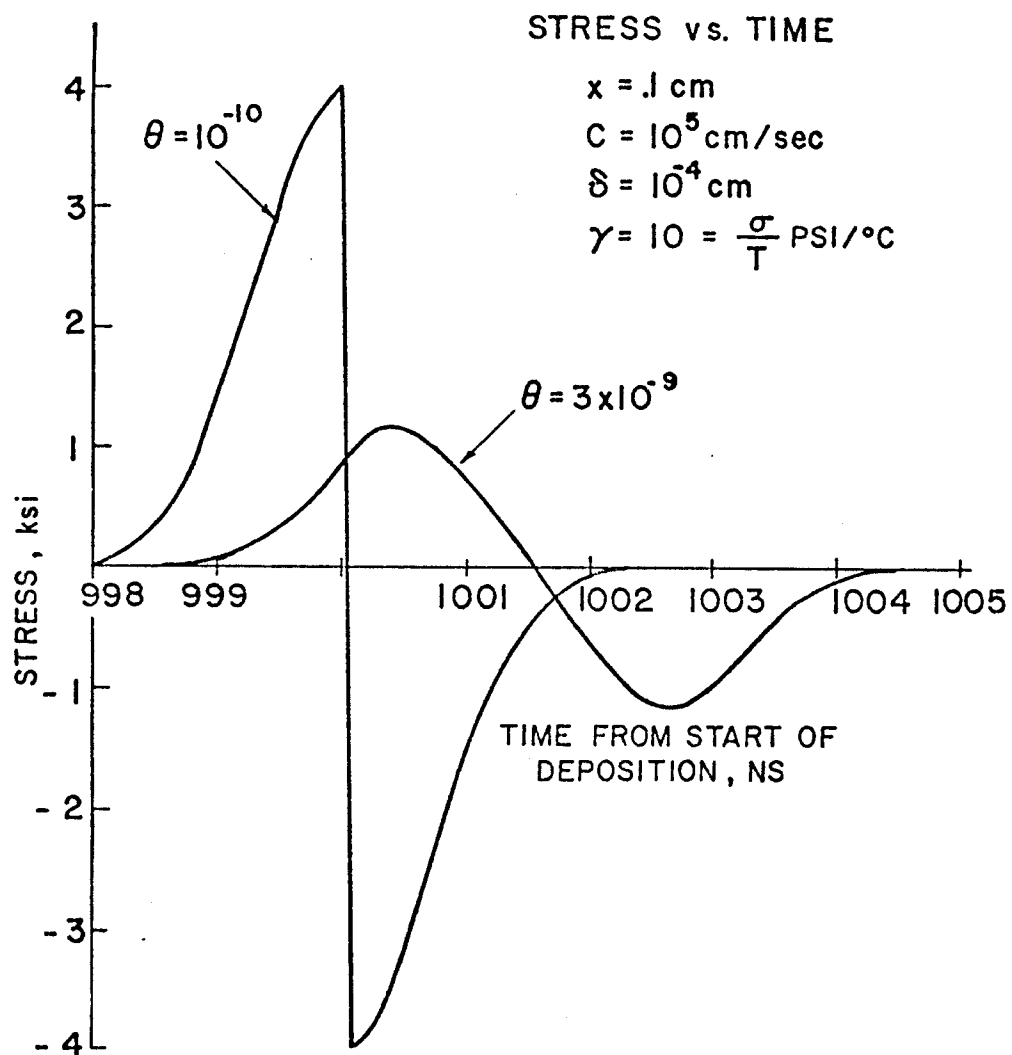
Fig. V. 30.   Stress Histories for Various Pulse Duration

The ratio of the stress wave amplitude divided by maximum initial compressive wave is given for various values of pulse duration in Figure V. 31. The stress wave amplitude approaches zero as the pulse gets longer than $\sim 3 \times 10^{-8}$ sec. Notice that a useful criterion for this case is that an approximate measure of the response time is given by

$$t_r \sim \frac{\text{deposition range}}{\text{velocity}} \sim \frac{2(1 \times 10^{-4})}{10^5} = 2 \times 10^{-9} \text{sec}$$

At any time longer than this, the amplitude is reduced as the stress is propagating away faster than it is created. Also shown in Figure V. 31 is the front surface temperature response from Figure V. 26 which indicates that for all times of interest for stress wave generation, there is negligible heat conduction. If spatial profiles were chosen with sharper gradients, the relative response times between stress and temperature might be closer.

This analysis indicates that for deposition profiles characteristic of ion irradiations, the characteristic times for temperature response are longer than the characteristic times for formation of stress waves. In addition, only those ion spectra which have very narrow energy limits are likely to cause significant creation of stress waves. Most ion spectra will deposit their energy in times which are much longer than the characteristic times.

STRESS WAVE AMPLITUDE
vs.
PULSE DURATION

$x = .1$ cm

$C = 10^5$ cm/sec

$\delta = 10^{-4}$ cm

$\gamma = \dfrac{\sigma}{T} = 10$

$\dfrac{\sigma}{\sigma^*/2}$

$\dfrac{T}{T^*}$
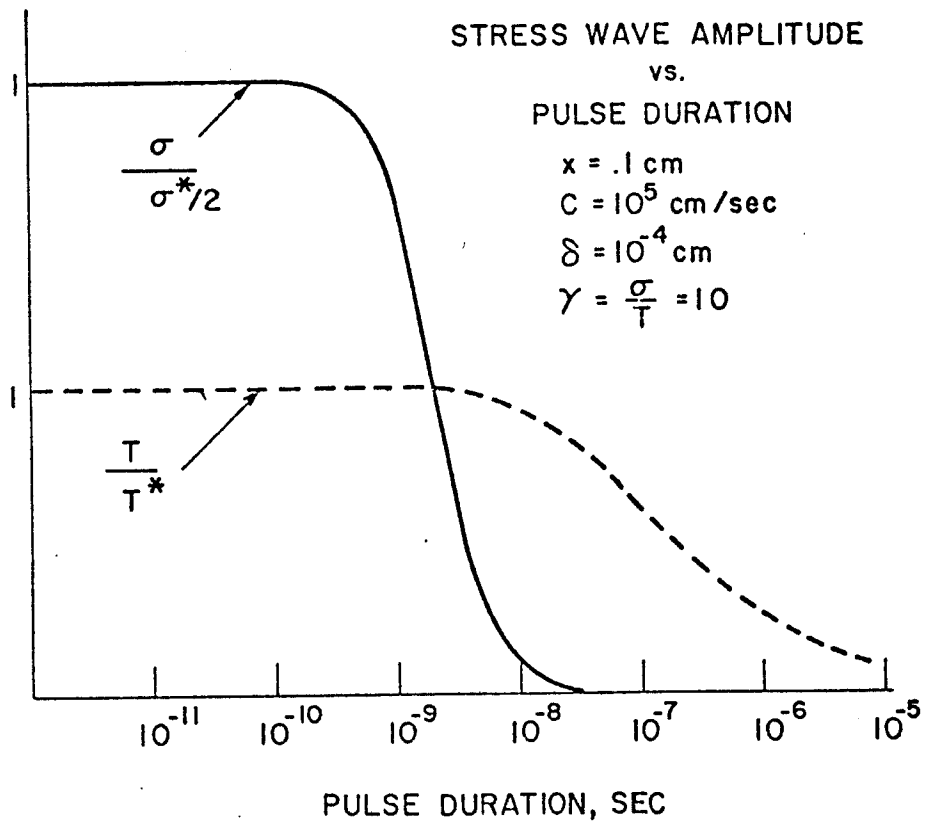
PULSE DURATION, SEC

Fig. V. 31. Stress Wave Amplitudes versus Pulse Duration

Photons, however, may be deposited in sufficiently short times to generate such stress waves and may require coupled solution. The methods given here can be used to analyze both the temperature and the stress associated with photon deposition. The impulse solutions for photons which yield the maximum stress wave amplitude have been investigated by Hejazi and Lovell with similar methods, and with results given in reference 17.

V.E. Displacement Response

The radiation damage in a pulsed fusion first wall will be due to neutron and ion bombardment. The displacement rate from neutrons will be determined by the duration of the primary and back scattered neutron fluxes and the appropriate displacement cross section. The neutron damage, like the energy deposition, will also be uniformly distributed through the first wall, at least on a macroscopic scale. As discussed earlier, approximately 50-70% of the displacements will be due to the source neutrons.

The damage production by the ions will be limited to the first few microns near the exposed surface. The spatial extent of the damage will be determined by the amount of energy lost by the ion which is attributable to nuclear collisions at any location. The temporal behavior of the damage production will be determined by particle flux at the surface, since the slowing down time will normally be insignificant (10^{-12} seconds).

The amount of displacent damage by ions can be determined at any location in the material at which the energy of the ion is known by[101]

106)
$$\dot{D}(x) = \sum_i F(x) \int_{E_d}^{\Lambda E_i} \sigma(E_i, E) \ \nu(E) \ dE$$

where F_i = local ion flux at position x

E_d = effective displacement energy

ΛE_i = maximum PKA energy

σ = cross section for transfer of energy
E to PKA from ion of energy E_i

$$\nu(E) = \text{number of displaced atoms from PKA of energy } E$$

The local displacement rate can be estimated by assuming suitable cross sections in Equation 106 and integrating. The spatial distribution of damage, however, requires knowledge of the energy at a given location. Consequently, for rigorous solutions, the transport equations for the ions must be solved with proper partitioning of nuclear and electronic energy losses and with consideration of the statistical variation in the particles' energy and, hence, penetration. This calculation of range and energy partitioning for monoenergetic ions is done by the numerical techniques discussed in Chapter III.

The deposition of bombarding species is also determined by these methods, since the expected value of the range parallel and normal to the ion's original path and the spatial moments are calculated.

In this study, a wide variation of incident ion energies must be evaluated if arbitrary pellet spectra are to be addressed. In addition, efficient calculations of both damage and ion implantation must be performed so that a comparison with thermal and stress response can be made without incurring excessive calculational costs. Consequently, approximations are made to the solutions mentioned above in a manner similar to the energy deposition calculations discussed earlier. These approximates will then be used to determine the response for the ion spectra to be considered.

The displacement production from an arbitrary spectrum of charged particles or neutrons can also be determined upon specification of the spatial and temporal distributions of the fluxes and an appropriate

dpa cross section. This is conceptually easy for neurons if the flux, as determined by time dependent neutronics, is multiplied by the cross section for the material in question. For ions, the definition of dpa cross section is more complex. In this study, this concept was extended to include two aspects: a) for light ions, the spatial transport and the nuclear damage were separated since, at high energies, the transport is dominated by electronic processes--hence a standard cross section could be defined for the local ion energy; and b) for heavy ions, a new concept is introduced which incorporates both the ion damage production and the spatial transport.

V. E. 1. Ions $Z \leq 2$

A model for displacement production by light ions with energies greater than a few tens of keV can be developed from the spatial energy distribution which were presented in Section V.B. This formulation allows the ion energy to be specified at any position and is accurate at all points except very near the end of range. Although the nuclear damage is ignored in determining the transport characteristics, it can still be evaluated as a function of ion energy. This damage then becomes the local displacement rate at the position where the energy is specified.

The methodology in this paper is commensurate with that of Doran, et al,[102] in a working group report on displacements and procedures for damage calculations. The approach in this study was to extend these procedures to determine energy and spatial dependence.

Upon determination of the mean ion energy as a function of position, it is necessary to develop an appropriate displacement cross section. Two alternative procedures are available:

1) a Binary Rutherford interaction model which accounts for the effective charge of the ion; and

2) the Lindhard (LSS)[52] model based on a Thomas-Fermi potential.

The former is consistent with reference 102 and consists of expressing the Rutherford differential scattering cross section as

$$107) \qquad d\sigma(E) = \frac{B\gamma^2}{E} \frac{dT}{T^2}$$

where

$$107a) \qquad B = \frac{4\pi a_0^2 m_1 z_1^2 z_2^2 E_r^2}{m_2}$$

a_0 = Bohr radius = 0.53 $\overset{\circ}{A}$

m_1 = ion mass

z_1 = ion atomic number

z_2 = target atomic number

E_r = Rydberg energy = 13.6 ev

m_2 = target mass

T = PKA energy

γ = effective charge given by Bichsel[103] as

$$107b) \qquad \gamma = 1 \exp(-1.316y + 0.1112y^2 - 0.0650y^3)$$

$$y = 100B/Z^{2/3}$$

$$B = v/c$$

v = ion velocity

c = velocity of light

Z = ion atomic number

A displacement cross section can be determined from the differential cross section if the number of displacements produced by a PKA of energy T can be established. This is usually accomplished by the selection of an energy partition model and a secondary displacement model.

The energy partition model accounts for the relative distribution of the PKA energy loss between the electrons and nuclei. The latter process is the only one used in determining displacements. A convenient form which approximates the function discussed in LSS theory is given by Robinson[104] as

108)
$$T_{damage} = \frac{T}{g(\epsilon)}$$

where

109)
$$g(\epsilon) = 1 + k\epsilon + 0.40244k\epsilon^{3/4} + 3.4008k\epsilon^{1/6}$$

k = LSS stopping parameter which for PKA's is

$$k = 0.1337 \ z^{2/3}/A^{1/2}$$

ϵ = Lindhard reduced energy = T/E_L

$$E_L = 0.08693 \ z^{7/3}$$

The secondary displacement model accounts for the displacements produced in a cascade of a PKA with a specified damage energy. The recommended value in Reference 102 is

$$N_d = 0 \qquad T < E_d$$

110) $\qquad N_d = 1 \qquad E_d \leq T < 2E_d$

$$N_d = \frac{0.8}{2E_d} T_{dam} \qquad 2E_d \leq T$$

where E_d is the effective displacement energy. Combining Eqs. (107), (108) and (110) yields the displacement cross section as

111) $\qquad \sigma_d(E) = \frac{B\gamma^2}{E} \left\{ \int_{E_d}^{2E_d} \frac{dT}{T^2} + \int_{2E_d}^{T_{MAX}} \frac{0.8}{2E_d} T \frac{dT}{g(T)} \right\}$

where

$$T_{MAX} = \Lambda E = \frac{4m_1 m_2}{(m_1 + m_2)^2} E$$

Equation (111) can only be easily evaluated by numerical integration, which tends to limit its utility. The difficulty in obtaining a closed form integral is the function $g(T)$. The Rutherford cross section, however, is very small angle (or low energy transfer) biased and the function $g(T)$ is a slowly varying function of T at low energies, hence it is reasonable to assume $g(T)$ is approximately a constant whose value is equal to the function evaluated at the average PKA energy where

$$T_{AVE} = 2E_d Log(T_{MAX}/2E_d)/(1 - 2E_d/T_{MAX})$$

The range of the function $g(T)$ for protons on nickel is shown in the following data:

E (keV)	$T_{MIN}(2E_d)$ (keV)	T_{AVE} (keV)	T_{MAX} (keV)
50	.080	.1786	3.294
$g(T) =$	1.148	1.169	1.280
100	.080	.2054	6.588
$g(T) =$	1.148	1.173	1.318

The data indicate that for a low energy transfer cross section g(T) can be assumed constant with only a few percent error. If this assumption is made, Eq. (111) can be integrated as:

$$112) \qquad \sigma_d(E) = \frac{B\gamma^2}{E\,E_d} \left\{ 0.5 + \frac{0.4}{g(\overline{T})}\ \ell n\ \frac{T_{MAX}}{2E_d} \right\}$$

units $= \overset{\circ}{A}{}^2$, energy $=$ eV

$B =$ Equation (76a)

$\gamma =$ Equation (76b)

$E =$ ion energy

$E_d =$ displacement energy

$T_{MAX} =$ maximum PKA energy

Results from Eq. (112) were found to yield the same values (within a few percent) as numerically integrated values in Reference 102 for protons on nickel for ion energies of 100 keV - 2MeV.

An alternative method for determining the displacement damage in terms of dpa cross section is to use the nuclear stopping power derived in LSS theory. This is the basis of the model used in the methods of Brice, Winterbon, and Manning and Mueller. The essential difference between their approach and the modified Rutherford method

discussed above is the treatment of electron screening. In the LSS model, the screening is treated explicitly by assuming an interaction potential based on the Thomas-Fermi model. The modified Rutherford model accounts implicitly for screening by allowing the charge of the moving ion be a function of energy. These approaches, although different in concept, tend to accomplish the same thing.

The differential cross section based on the LSS model was given in Chapter IV (Eq. 27), in terms of the Lindhard tabulated screening function. Winterbon, et al.,[105] also give the analytic approximation:

$$113) \qquad d\sigma(E) = \frac{\pi a^2}{2} \lambda \, t^{-4/3}[1 + (2\lambda t^{2/3})^{2/3}]^{-3/2} dt$$

where

$$\lambda = 1.309$$

$$t = \epsilon^2 \, T/T_{MAX} = \epsilon^2 \, \sin^2\theta/2$$

$$a = 0.468(z_1^{2/3} + z_2^{2/3})^{-1/2} \overset{\circ}{A}$$

$$\epsilon = E/E_L$$

$$E_L = \frac{1 + A}{A} \, \frac{z_1 z_2 e^2}{a}$$

$$A = m_2/m_1$$

$$T = \text{PKA Energy}$$

$$E = \text{ion energy}$$

The nuclear energy loss can be derived from Eq. (113) by performing the integral

$$114) \qquad \left.\frac{d\epsilon}{d\rho}\right|_N = \frac{NR_L}{E_L} \int_{\gamma^2}^{\epsilon^2} \frac{T_m t}{\epsilon^2} \frac{d\sigma}{dt} \, dt$$

where

$$\rho = r/R_L = \text{reduced length}$$

$$R_L = \frac{(m_1 + m_2)^2}{N\, a^2 4 m_1 m_2}$$

$$N = \text{atomic number density}$$

$$\gamma = \varepsilon (T_L/T_M)^{1/2}$$

$$T_L = \text{lower limit of PKA spectra}$$

Oen, et al., [106] give the value for this integral as

115) $$\left.\frac{d\varepsilon}{d\rho}\right|_N = \frac{9}{8\varepsilon}\; \ln\left[\frac{(2\lambda)^{1/3}\varepsilon^{4/9} + (1 + (2\lambda)^{2/3}\varepsilon^{8/9})^{1/2}}{(2\lambda)^{1/3}\gamma^{4/9} + (1 + (2\lambda)^{2/3}\gamma^{8/9})^{1/2}}\right.$$

$$\left. + \frac{(2\lambda)^{1/3}\gamma^{4/9}}{(1 + (2\lambda)^{2/3}\gamma^{8/9})^{1/2}} - \frac{(2\lambda)^{1/3}\varepsilon^{4/9}}{(1 + (2\lambda)^{2/3}\varepsilon^{8/9})^{1/2}}\right]$$

In order to evaluate a dpa cross section, the following integral must be performed:

116) $$\sigma(E) = \int_{E_d}^{2E_d} \frac{d\sigma}{dT}\; dT + \int_{2E_d}^{T_M} \frac{d\sigma}{dT}\left(\frac{0.8T}{2E_d}\frac{dT}{g(T)}\right)$$

Again, if $g(T)$ is approximately constant, this can be transformed into

117) $$\sigma(E) = \int_{E_d}^{2E_d} \frac{d\sigma}{dT}\; dT + \frac{E_L}{NR_L}\;\frac{0.4}{E_d\;\bar{g}(T)}\;\left.\frac{d\varepsilon}{d\rho}\right|_N$$

where the term $\left.\dfrac{d\varepsilon}{d\rho}\right|_N$ is [Eq. (115)] evaluated for ε and $\gamma = (2E_d/T_m)^{1/2}$. The first integral in Eq. (116) can be estimated by

$$\frac{d\sigma}{dt}(t_0)\Delta t$$

where

$$\Delta t = \varepsilon^2 E_d/T_m$$

$$t_0 = \varepsilon^2 3E_d/2T_m$$

$$\frac{d\sigma}{dt} = \text{Equation (113)}$$

An estimate of the dpa cross section for light ions can, at this point, be derived from Eq. (112) (modified Rutherford) or Eq. (117) (LSS, Thomas-Fermi). A comparison of these two values for protons on copper is shown in figure V.32. In this case, the energy partition function was assumed to be unity for both cases. It is noted that small differences are noted at higher energies (100 keV and up) but differences of a factor of 5 or more are evident in the few keV regions. In this study, the LSS value was used so that results could be compared with the ion implantation codes which use the same formulation. A more rigorous approach to resolve the discrepancies evident at low energies would be to use alternate potential functions in such codes. The methods in this study are approximate and are most accurate at higher energies where the disagreement is negligible.

The procedure for evaluating the local displacement rate for light ions would be as follows:

$$118) \qquad \dot{D}(x,t) = f(t)\sigma_{dpa}[E(x,E^*)]$$

where $f(t)$ is the instantaneous flux of ions of energy E^* at the exposed surface. $E(x,E^*)$ is the energy of an ion of incident energy E^*
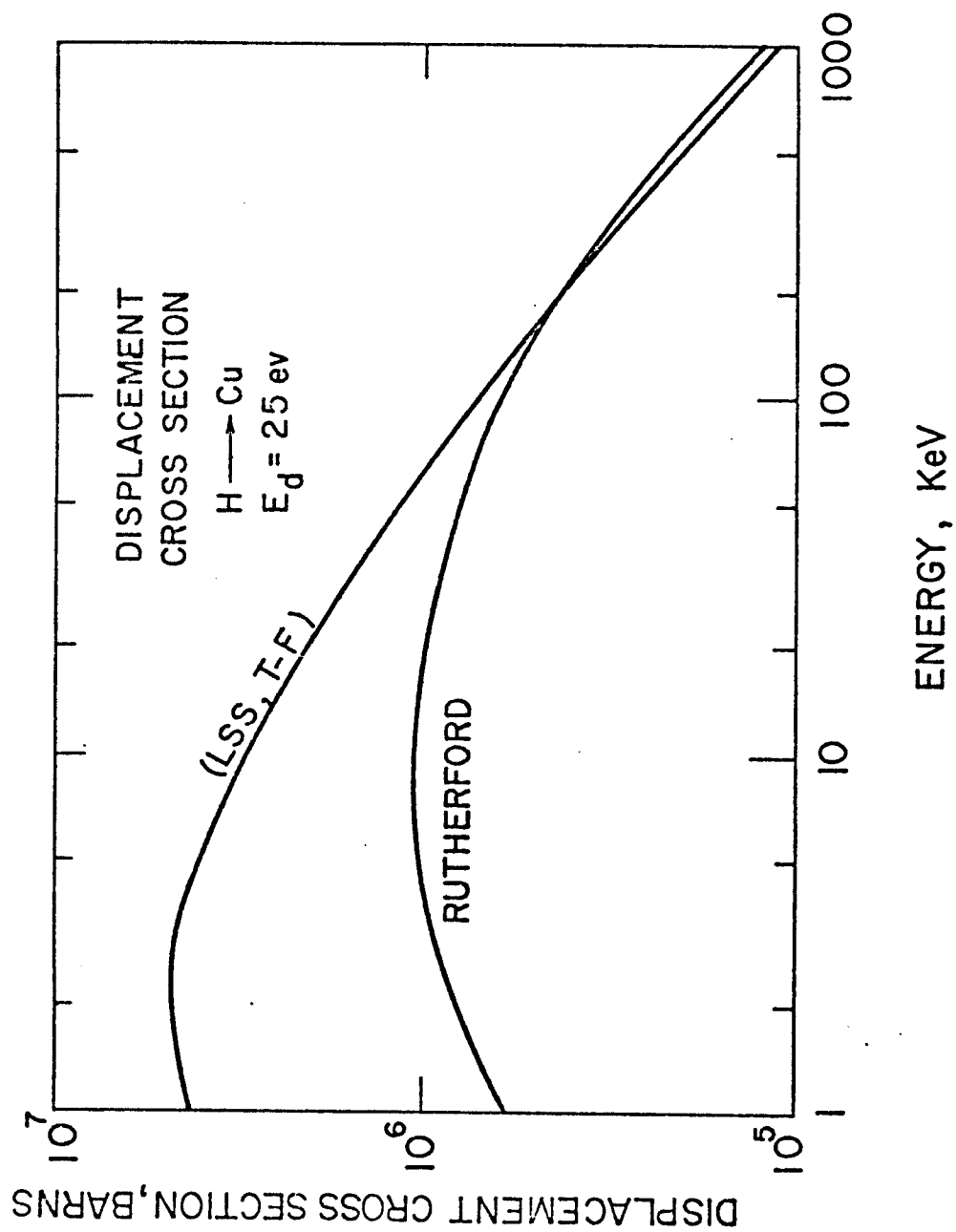
Figure V. 32.   Comparison of Displacement Cross Sections

at position x (Table V.2) $\sigma_{dpa}(E)$ is the dpa cross section for an ion of energy E in the target [Eq. (112) or (117)].

V. E. 2. Displacement for Ions of Z > 2

For heavier ions, the determination of local displacement production is more complex, because the mean energy of an ion is not so easily determined, and the effects of scattering and straggling are more pronounced. One must, therefore, rely initially on one of the ion implantation codes. If various spectra of ions are to be studied, however, it is necessary to develop a technique to determine the spatial displacement profiles in a more efficient form.

This requirement is in part due to the considerable expense associated with multiple runs of the ion codes.

The technique developed in this study involves the definition of a new form of the dpa cross section (or damage factor) as:

$$119) \qquad \sigma_{dpa}^{*} = \sigma_{dpa}^{*}(E^{*},x)$$

In this case, the cross section contains information on both the amplitude and spatial extent of the displacement of an ion of incident energy E*. These damage factors can be used to calculate the damage at any position as simply:

$$120) \qquad \dot{D}(x,t) = f(t)\sigma_{dpa}^{*}(E^{*},x)$$

These damage factors are determined from the nuclear energy deposition functions which are obtained by performing a single set of ion implantation calculations (as with the Brice codes[37] RASE 4 and

DAMG 2 in this study) at selected ion energies covering all potential

spectra of interest. These functions were discussed in section V.B.,

and consist of further processing the results of these calculations,

and then parameterizing them by determining a numerical fitting func-

tion or a set of functions whose defining coefficients can be expressed

as functions of energy. These deposition functions must only then be

combined with an appropriate defect production model (such as Eq. 110)

to develop a dpa cross section. The phenomena of PKA redistribution

and energy partitioning are already considered in the creation of the

deposition function. An example of the damage distribution from which

the damage factors can be determined is shown in figure V.33. These

data are for aluminum ions onto nickel, although similar data were

employed for other ion-target combinations.
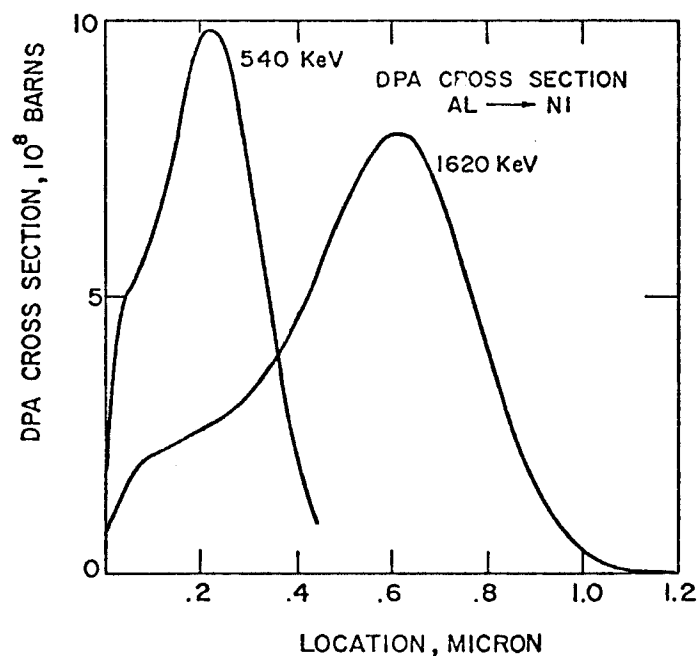
Fig. V. 33. DPA Cross Section from Deposition Function

V.F. Modification of Response by Gaseous Layers

This section will investigate one of the methods discussed in Chapter II for protection of pulsed fusion reactor first walls. Models will be developed which modify the flux and spectra of the radiation as it proceeds from the point of ignition across the reactor cavity. Techniques are outlined and examples are given for ions, both heavy and light, and photons.

Inherent in all the subsequent discussions is that as a first approximation the ion spectra from a pellet microexplosion can be considered as fully developed into directed kinetic energy at radial distances large compared to the pellet but small compared to the wall radius or position of an exposed component. In addition, the slowing down characteristics of ions in rarefied gases is assumed to be the same as in any homogeneous isotropic material except for the proportionality to atom density.

The emphasis of this study was on developing approximate solutions to the ion transport process which could be efficiently utilized for a wide range of ion spectra.

In this section a general method will be developed which can be used to estimate the modification of the energy spectra of the ions as they proceed through a material. This method will first be developed for a monoenergetic spectrum and then generalized for an arbitrary spectrum. Separate treatments are used for heavy ions (or low energy light ions) and light ions of higher energy. The former is based on a diffusion approximation to the transport of ions where the

distributions for monoenergetic ions must consider more than one moment. The light ion method will be based on the stopping power functions given in section V.B.

V. F. 1. Diffusion Approximation to Ion Transport in Materials

The penetration and distribution of ions in materials can be rigorously solved by obtaining a solution of the transport equation accounting for the interaction of the ions with the electrons and nuclei in the material. In this development a simple treatment will be given which will allow an approximate determination of the spatial distribution of ions at various times between impact and stopping. This information can then be used to determine the flux and spectrum of the ions at any position within the materials.[107]

Various treatments are available to evaluate the moments of the final ion distribution, i.e., when the ion comes to rest. The methods, discussed in Chapter III, of Gibbons and Johnson, Winterbon and Brice are examples. Brice also presents a direct method for determining the first and second central moments of the distribution at intermediate energies. These data have been used by Tsurushima and Tmoue[108] to determine the ion spectra at a specified position in the material.

Unfortunately, Brice's method requires an appreciable amount of computation using the RASE 4 code even if only a few incident energies are examined. If a large number of incident energies (e.g., typical of the debris spectra from a TN pellet burn) are examined, the computation can become quite expensive. Consequently, this, and the

method of Tsurushima and Tanoue are not considered appropriate when as
many as 5 to 8 different ions, each with broad energy spectra, are
considered for one pellet design.

All the above treatments incorporate the nuclear cross sections
and ion-electron interactions and solve for the moments of the ion
distributions with an expansion solution to the transport equation.
The approach taken in this study was to assume that the first and
second moments of the final ion distribution are available. Data for
ranges of selected ions in thermonuclear spectra are shown in figure
V.34. Similar data may be obtained for any ion-target combination by
any of the above formulations.

V. E. 1. a. Monoenergetic Solutions

When an ion of incident energy E_* passes through a finite density
of target atoms and comes to rest, the probability of finding it any-
where around the projected range will have a gaussian shape with mean
R and standard deviation σ. As stated above, for any ion it is assumed
that this represents the distribution when the energy is zero and that
R (range) and σ (ΔR) are well known. In addition, it is assumed that
this distribution is reached when the time after impact has some
finite value, t_o.

The gaussian distribution of implanted particles can be assumed
to be the result of two processes:

1) A general slowing down which determines the position of the
mean of the distribution, and

2) A diffusive process which determines the spread or second
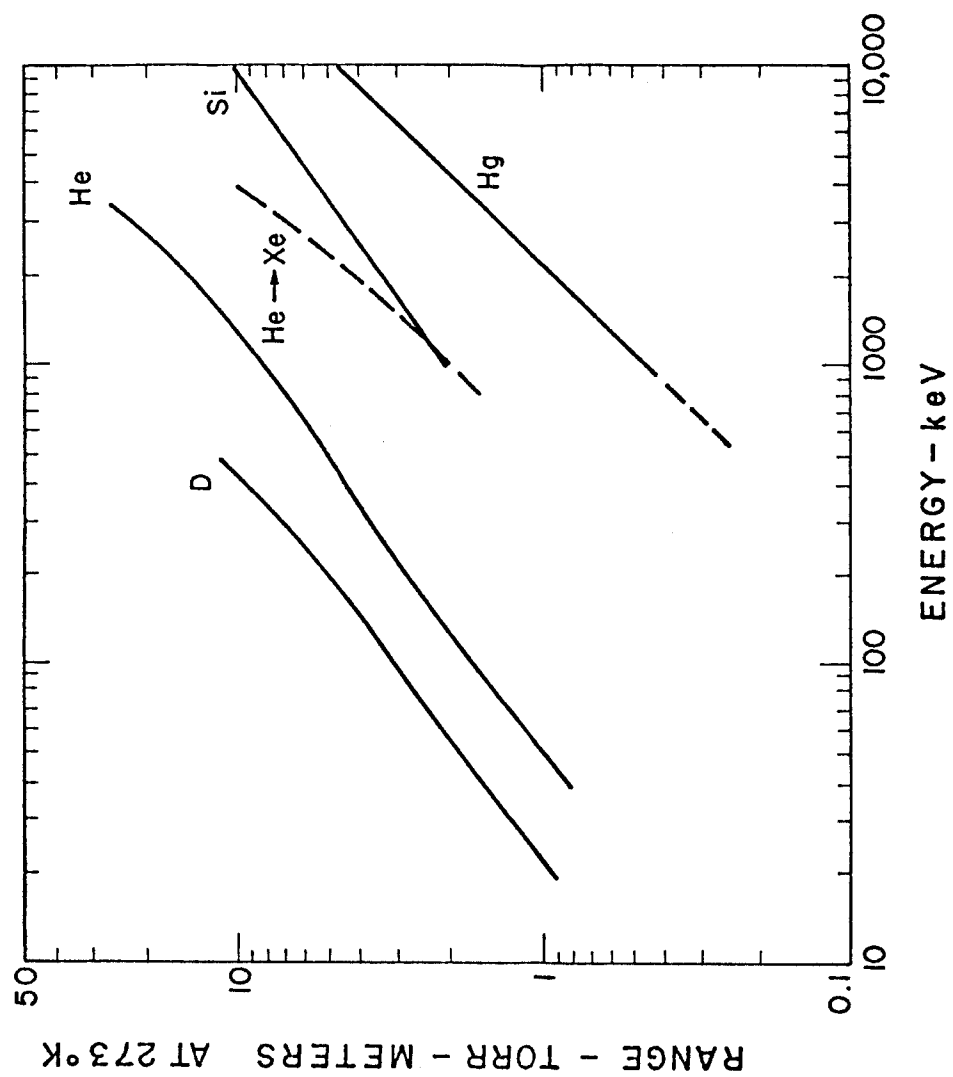
Fig. V. 34. Range of Ions in Neon

central moment.

The latter assumption is analogous to the diffusion of neutrons produced by their scattering interactions with the host atoms.

The initial conditions are established by the assertion that at impact the distribution is centered at the origin ($x = 0$) and has no spatial or spectral variance. A solution will now be developed which satisfies the initial and final values as boundary conditions, and which can then be used to approximate the distribution anywhere in between. The ion distribution is assumed to be "diffusing" about the center-of-mass or the mean of the distribution. It is also assumed that the motion of the center-of-mass can be determined from the range-energy relationship for the ion-target combination considered.

V. F.1.a. i.   Diffusion in Center-of-Mass

Consider a solution for the concentration of ions in the "center-of-mass" (COM) reference frame. At time = 0 (impact), the distribution was a delta function in space centered at $r = 0$ if x is the spatial variable in the COM frame.

The diffusion equation is then

121) $$\frac{\partial^2 c}{\partial x^2} - \frac{1}{\gamma^2} \frac{\partial c}{\partial t} = C_o \, \delta(x) \, \delta(t)$$

where c is the concentration of ions per unit volume at time t and position x, γ is a diffusion coefficient as yet undetermined, and

$$\int_t C_o \, \delta(t) \, dt = F$$

where F is the incident fluence, ions/cm^2. The solution to 121) is

well-known as[99]

122)
$$c(x,t) = \frac{C_o}{(4\pi\gamma^2 t)^{1/2}} \exp\left(- \frac{x^2}{4\gamma^2 t}\right)$$

The effect of the nuclear interaction contribution to the scattering is contained in the term γ. This term would be difficult to obtain from first principles; however, we can determine an estimate of its value from the knowledge of its effect on the final distribution. This is given by the gaussian approximation as:

123)
$$c(x,t_o) = \frac{C_o}{(2\pi)^{1/2}\sigma} \exp. \left(-x^2/2\sigma^2\right)$$

Thus an estimate for γ is

$$\gamma = \sigma/ \sqrt{2t_o}$$

where t_o is the time when $E = 0$.

V.F.1.a.ii. Motion of Center-of-Mass

In addition to the diffusion in the center-of-mass it is necessary to determine motion of the center-of-mass. If it is assumed that motion of the COM is independent of the dispersion of the distribution, the equation of motion can be solved directly.

In general it will be assumed that the range energy relationship can be expressed in the following functional form:

124)
$$R = C V_*^{\frac{1}{1-k}}$$

where R = range (position when $V = E = 0$)

V_* = incident velocity

and C,k are constants determined from range-energy data. In addition, it is assumed that

126)
$$\frac{dr}{dV} = \frac{dR}{dV_*}$$

where r is the position of the COM (in the lab system) at any time, V is the velocity of the COM at any time. The position is then given by

126)
$$r = C \{V_*^{\frac{1}{1-k}} - V^{\frac{1}{1-k}}\}$$

The form of equation (124) was chosen because it closely resembles the stopping of heavy ions in materials. The case of k = 1/2 (R = CV^2) corresponds to a uniform spatial energy deposition over the range of the ion which is characteristic of low velocity ions when nuclear and electronic stopping powers are equivalent.

The case of k = 0 (R = CV) corresponds to a deposition relationship of

$$\frac{dE}{dx} \propto E^{1/2}$$

which is the anticipated form for an interaction, which is electronic dominated with the form of the stopping taken from LSS theory.[60]

Values of k and C may be easily determined if two data points are known for the ion-target combination. Hence, given V_{*1}, R_1 and V_{*2}, R_2, the following simple conditions yield the constants.

$$k = 1 - \frac{\ln V_{*1}/V_{*2}}{\ln R_1/R_2}$$

$$C = \frac{R_1}{(V_{*1})^{1/(1-k)}}$$

The standard deviation at the end-of-range can be expressed as

127) $\tilde{\sigma}(V_*) = F(V_*)R(V_*)$

where $F(V_*)$ has been assumed for this study to be:

$$F(V_*) = A \exp(-V_*/B)$$

and from two data points

$$B = \frac{(V_2 - V_1)}{\ln\left(\frac{\tilde{\sigma}_1 R_2}{\tilde{\sigma}_2 R_1}\right)}$$

$$A = (\tilde{\sigma}_1/R_1)\exp(V_1/B)$$

Equations (124) and (127) allow the determination of the normal range and standard deviation in normal range when the ion has come to rest for any incident energy ion.

The time for an ion of incident energy E_* (or velocity V_*) to reach a position r between o and R is

128) $$t = \int_o^r \frac{dr}{V} = \int_o^r \frac{dr}{(V_*^{1-k} - r/C)^{\frac{1}{1-k}}} \quad \text{for } r < R$$

which has the result

129) $$t = \frac{C}{k}\{V_*^{k/1-k} - (V_*^{\frac{1}{1-k}} - r/C)^k\}$$

in terms of velocity equation 129 can be written

130) $$t = \frac{C}{k}\{V_*^{k/1-k} - V^{k/1-k}\}.$$

Equation 129 can also be rewritten for more accurate numerical evaluation as

131)
$$t = \frac{C}{k} V_*^{\frac{1}{1-k}} \{1 - (1 - \frac{r}{C} V_*^{\frac{1}{k-1}})^k\}$$

The inverse functions to equations 129 to 130 can be used to evaluate the position of the mean at a given time and the velocity at a given time as:

132)
$$r = C V_*^{\frac{1}{1-k}} \{1-(1 - \frac{tk}{C} V^{\frac{k}{k-1}})^{1/k}\}$$

and

133)
$$V = \{V_*^{\frac{k}{1-k}} - \frac{tk}{C}\}^{\frac{1-k}{k}}$$

V.F.1.a.iii. General Solution

The results can now be superimposed combining the center-of-mass motion and the "diffusion" of the distribution. The distribution at any time would be given as

134)
$$c(x,t) = \frac{C_o}{(4\pi\gamma^2 t)^{1/2}} \exp - \frac{(r(t)-x)^2}{4\gamma^2 t}$$

where $r(t)$ is given by equation 132) at time t, x is any position within the material where the distribution is desired. The distribution at any intermediate velocity is

135)
$$c(x,V) = \frac{C_o}{(4\pi\gamma^2 t(V))^{1/2}} \exp -\left(\frac{(r(V)-x)^2}{4\gamma^2 \, t(V)}\right)$$

where $t(V)$ = equation (130) and $r(V)$ = equation (126).

The previous relations allow an estimate of the position of the

mean and of the standard deviation of the ion distribution at any time or intermediate energy between impact and stopping. These results, therefore, represent a simple method for determining the same results as the Brice analysis in the RASE4 code.[37] The relations here clearly do not maintain the accuracy or the elegance of Brice's solution but they can allow approximate determination of the distributions with a relatively small amount of numerical calculation. These results will now be used to evaluate the normal flux and spectra passing through any intermediate position.

V.F.1.a.iv. Flux and Spectra at Arbitrary Position

The instantaneous flux of particles passing through any position can be determined as the product of the concentration and the normal velocity as

136) $F(t,x) = c(t,x) \, V(t,x)$

Since the velocity is the same for each ion in any given gaussian distribution, the flux can be evaluated as:

137) $$F(t,x) = \frac{C_o}{(4\pi\gamma^2 t)^{1/2}} \exp - \frac{(r(t)-x)^2}{4\gamma^2 t} \{ V_*^{\frac{k}{1-k}} - \frac{tk}{C} \}^{\frac{1-k}{k}}$$

= eqn 134 x eqn. 133.

The velocity spectrum can be determined as

138) $G(V,x) = - F(t,x)\frac{dt}{dV}$

which by differentiating equation 130

139) $G(V,x) = F(t,x) \frac{C}{1-k} V^{\frac{2k-1}{1-k}}$

The energy spectrum is given by

140)
$$S(E,x) = G(V,x) \frac{dV}{dE}$$

Since $V = [4.39 \times 10^7] (E/m)^{1/2}$ (141)

where $E = keV$, $m = amu$, and $V = cm/sec$, then

142)
$$S(E,x) = [2.20 \times 10^7] G(V,x)/(mE)^{1/2}$$

Equations (137), (139) and (142) are the functions which can be used for evaluation of the flux and spectra at any intermediate position or time.

To this point, the discussion has pertained only to monoenergetic incident ions and must now be generalized to the case where the incident spectrum is considered. Before addressing the case of an arbitrary spectrum we make a comparison of the results of the above analysis with the same analysis using the RASE4 code for Ni ions passing through nickel (figure V.35). The agreement, although not precise, is sufficiently close considering the inherent accuracy of any ion implantation theoretical analysis. The principal advantage of the technique derived in this paper is that it can be applied in a rather inexpensive calculation of a large number of incident ions.

V.F.1.b. Application to an Incident Spectrum

If the incident spectrum is not monoenergetic, it is necessary to determine the spectra and temporal characteristics of all the ions as they pass through the material.

The incident spectrum is described at time = 0 in figure V.36.
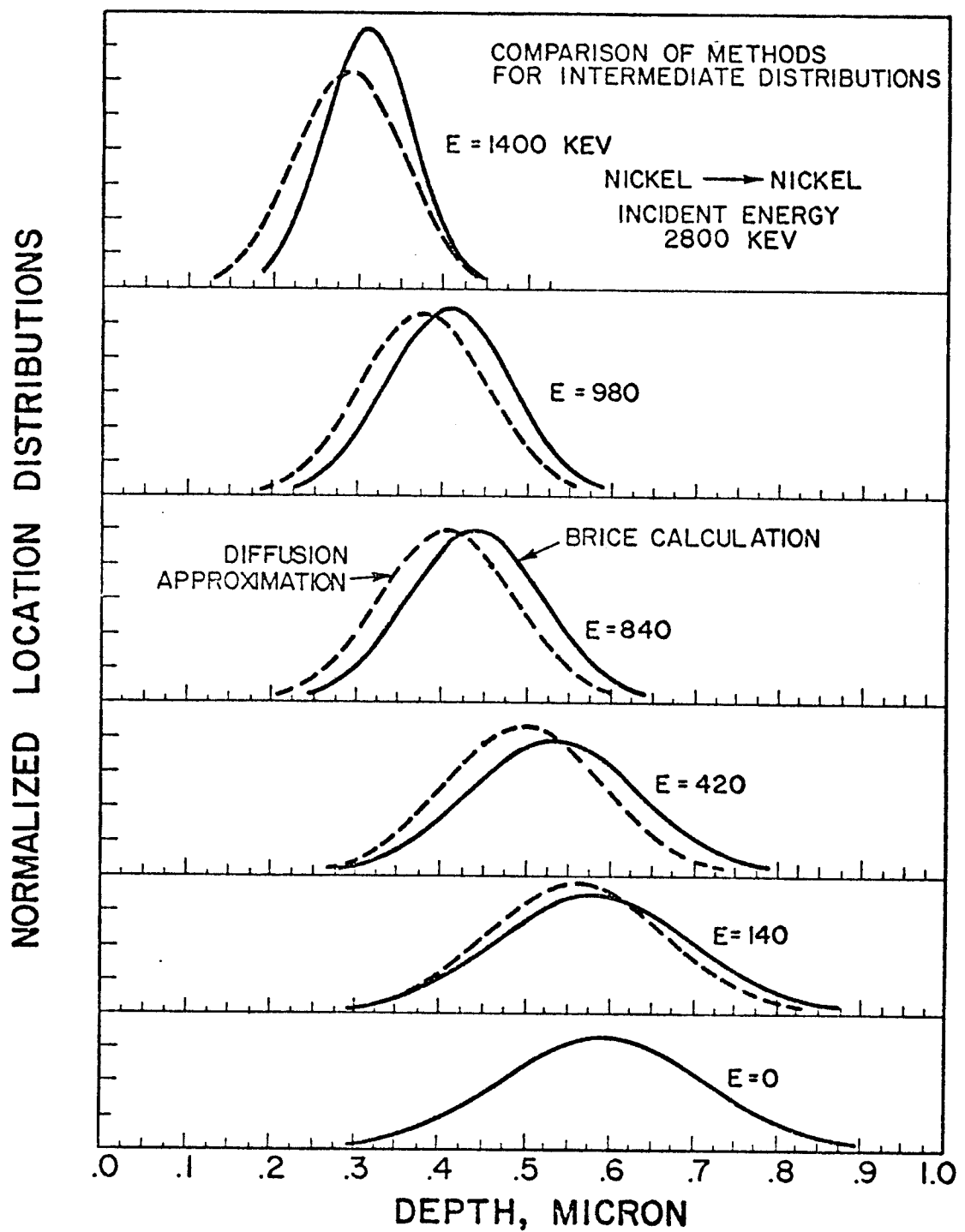
Fig. V. 35. Comparison of Methods for Intermediate Ion Distributions
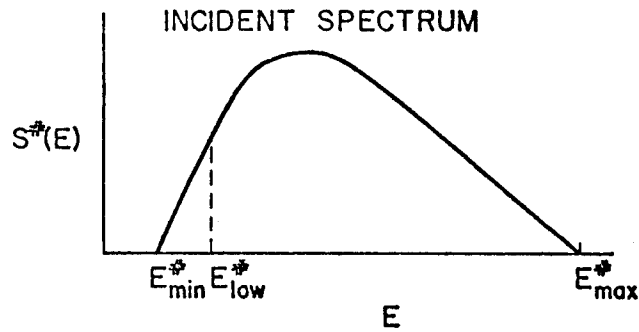
Fig. V. 36.   Incident for Spectrum

where S*(E) is an arbitrary function.

If this spectrum is to pass through a buffer material in which its form will be modified, it is necessary to evaluate the modified flux and spectra at some position, Z, with the material.

At position Z the ion flux will take the form $F(t,Z)$ as figure V.37:
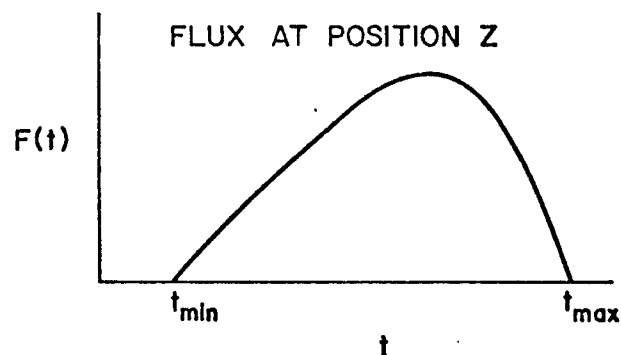
Fig. V. 37.   Flux at Position Z

To evaluate this distribution for finite spectra, it is first necessary to determine the time limits. This procedure is essential for numerical analysis considering that some of the ions $(E^* < E^*_{low})$ will never make any contribution to the flux at position Z.

An estimate for t_{min} is that time at which the most energetic ion in the spectrum has reached position within 2σ of Z as shown in figure V.38.
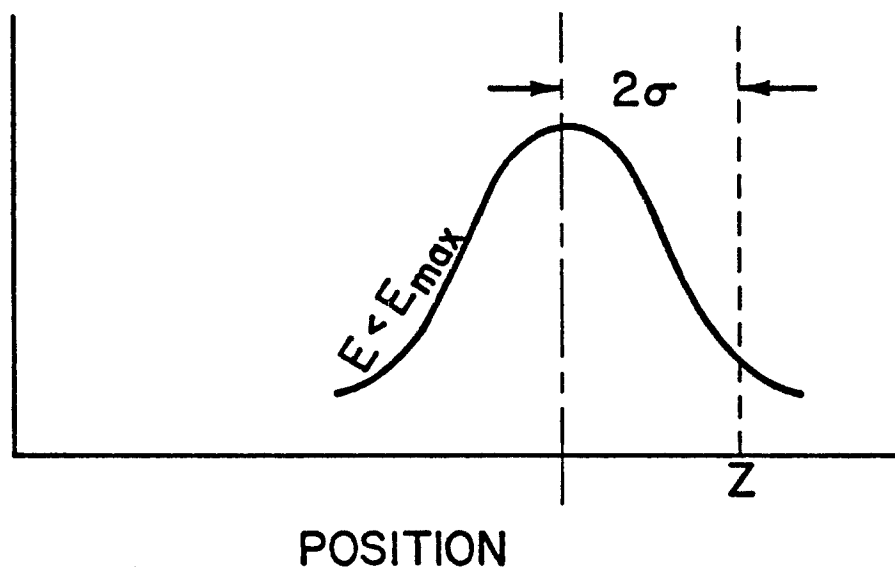
Fig. V. 38. Distribution at t_{min} for maximum Ion Energy

Thus t_{min} is the time when the mean location is

$$143) \qquad r_{min} = Z - 2\sigma \ (r_{min}, E^*_{max})$$

Equation (143) requires an iterative evaluation but will converge within a few trials if an initial estimate of r is

$$144) \qquad r_{min} = Z - 2\sigma \ (R, E^*_{max})$$

where R is the range when E^*_{max} has been reduced to 0.

The time, t_{min}, when an appreciable flux of particles will appear at position Z, is then given by equation 131 evaluated at the value of r determined in equation 143. Thus,

$$t_{min} = t\ (r, E^*)$$

at $$r = r_{min}$$

$$E^* = E_{max}$$

The maximum time of interest, t_{max}, is given by the time when the lowest energy (E^*_{low}) particle can reach within 2σ of Z is approaching E = 0.

Hence, E^*_{low} is determined by the lowest energy (greater than E^*_{min}) which has range + 2σ which is greater than Z or:

145) $$R(E^*_{low}) + 2\sigma\ (R, E^*_{low}) \geq Z$$

At position Z, therefore, the limits on the flux are from t_{min} to t_{max} and the limits on the spectrum at E^*_{low} and E^*_{max}. It is possible at large values of Z that E^*_{low} will exceed E^*_{max} and no flux will occur. At small values of Z, E^*_{low} may be less than E^*_{min} and all ions in the incident spectrum will give a contribution.

The flux at position Z can be evaluated by summing the contributions of each ion in the incident spectrum at a specific time, t, or:

146) $$F(t,Z) = \int_{max(E^*_{min}, E^*_{low})}^{E^*_{max}} Q(t, E^*)dE^*$$

where $Q(t, E^*)$ is the flux at time t from that portion of the incident

spectrum $S*(E)dE*$. $Q(t,E*)$ may be evaluated by solving equation (137) at time t and V_* corresponding to $E*$ with the value of $C_0 = S*(E)dE*$.

It is sometimes necessary to obtain a single energy to correlate with the flux at time t. This can be accomplished by determining the average energy as:

$$147) \qquad \overline{E}(t) = \frac{\int Q(t,E*) \; E(E*,Z)dE*}{\int Q(t,E*)dE*}$$

where $Q(t,E*)$ is the same as in Equation (146), and $E(E*,Z)$ is the energy at position Z for an ion of incident energy $E*$ taken from equation (126).

The spectrum at position Z will be defined between the limits of E_{min} and E_{max}, which are determined from the velocity calculated using equation (133) at times, t_{max} and t_{min}, and incident energies $E*_{min}$ and $E*_{max}$, respectively.

The amplitude of the spectrum at the transmitted energy, E, is the summation of the contribution of all ions in the incident spectrum which have energy E at position Z. Hence

$$148) \qquad S(E,Z) = \int_{E*} S*(E*)dE* \; H(Z,E*,E)$$

where $S(E,Z)$ is the value of the spectrum at position Z, $S*(E*)dE*$ is the incident spectrum, $H(Z,E*,E)$ is the portion of ions around $E*$ which have incident energy E at position Z, given by equation 140 with the value of C_0 given by $S*(E)dE*$.

The relations developed above allow a complete, yet approximate, estimation of the flux and spectrum of an ion distribution as it

passes through a material. It is readily applied to heavy ions or light ions of low energy as they pass through gases. It is however, applicable to solids and liquids as well.

These models have been incorporated into the T-DAMEN code so that any arbitrary incident spectrum can be modified by a protective gaseous layer of arbitrary pressure and temperature. The calculated form of the flux and spectra are identical in format to that in the case of no gases; consequently all subsequent response calculations (temperature displacement, etc.) can be easily performed with the models discussed in section V.B. - V.E.

An example of this model is given in figure V.39. Energy spectra are shown for a mercury spectrum (Gaussian, 3 MeV $\pm$ 1 MeV) which is incident on a surface at a 6 meters location. Curves are shown for the case of no gas and 0.1, 0.2, 0.3 torr of neon, respectively.

At this point it should be noted that spectra, such as those in figure V.35 calculated by these methods are approximations to the complex phenomena associated with ion transport in finite media. The previously presented comparison with a more complex solution for mono-energetic ions indicate that estimates of range and straggling of intermediate energy ion distribution differ by no more than 20%. This difference is, however, small in comparison to the large variation in range and straggling values associated with a broad spectrum of incident ions.

An additional caution should be noted when using data such as that in figure V.35. The flux and associated spectra arriving at a
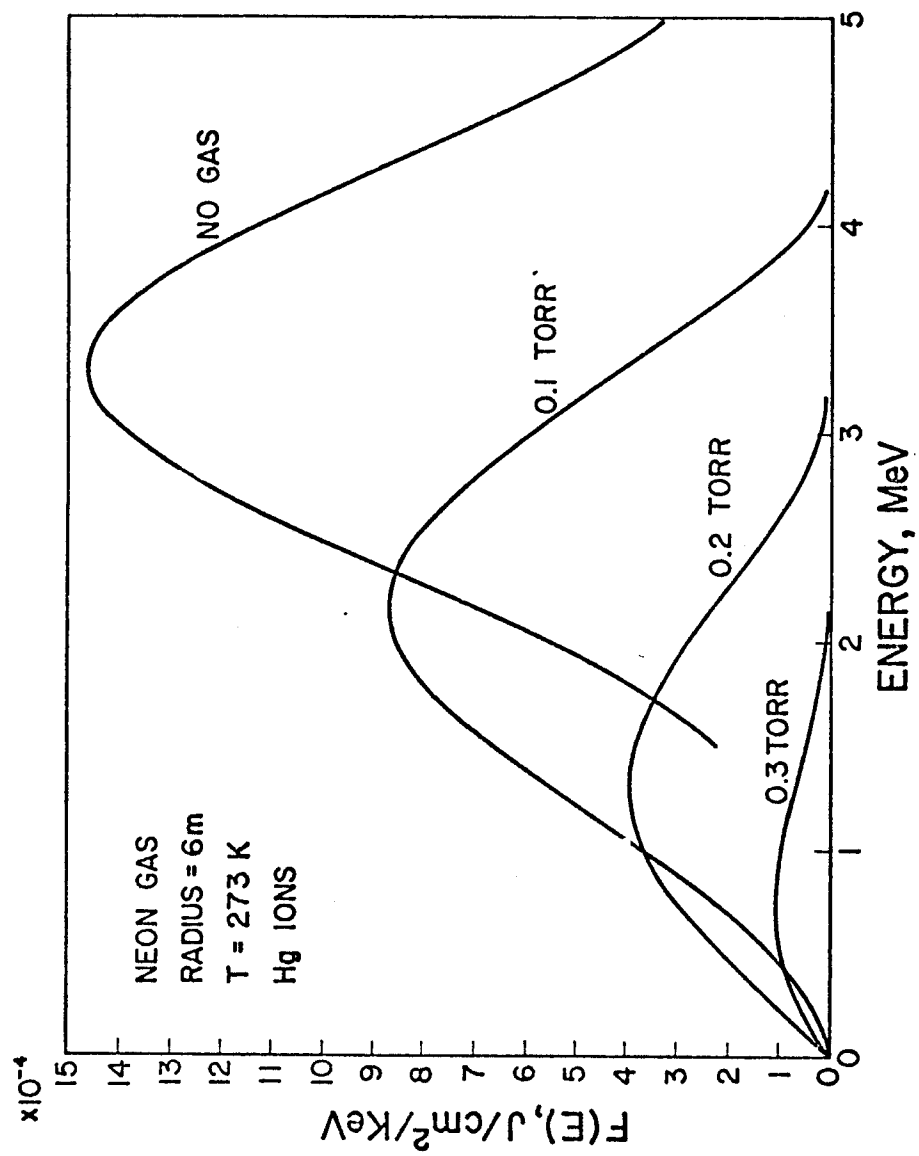
Fig. V. 39. Effect of Gas on Incident Heavy Ion Spectrum

point from a pulsed fusion source are functions of both the gas density

and the path length. Hence, in contrast to modification of photon

fluxes, results cannot be generalized to a normalized basis such as

torr-meters of buffer gas.

V.F.2. Spectral Modification of Light Ions (Z ≤ 2)

If the energy of light ions is sufficiently high (> 10 keV/amu) a

simple method can be developed to modify an incident spectrum by a

gaseous layer. This procedure is based on the stopping power formula-

tions and energy-location relations developed in section V.B. This

formulation is considered accurate when the incident ion energy is

high or when the range of the particle exceeds the thickness of the

gas by a factor of 2 or more. In both cases the difference in path

length and range is small and the standard deviation of the distribu-

tion of each ion is small compared to the distribution for a spectrum

as a whole.

Section V.B. gave relations which allowed the determination of

the mean local energy of an ion of incident energy E*, as:

$$E = E(E^*, Z)$$

Here it is assumed that a relation can be developed which allows

the determination of the mean time to reach position Z as:

$$t = t(E^*, Z)$$

Formulae for estimating these times are dependent on the stopping

power regimes of the incident ion and will be developed later in

this section.

If relations for energy and time as a function of position are known, the modified spectrum can be determined easily from:

149) $S(E,Z) = S(E^*)dE^*/dE$

where E is determined from the relation $E(E^*,Z)$, dE is estimated from $E_N(E_N^*,Z) - E_{N-1}(E_{N-1}^*,Z)$, and dE^* is a specified discretization of the incident spectrum. N is an arbitrary energy group in the spectrum.

The limits of the transmitted spectrum will be the energy of the maximum energy incident ion at position Z and the larger of a) the energy of the minimum energy incident ion at position Z, or b) the incident ion energy whose mean range is Z.

The flux can likewise be determined from the transformation

150) $F(t) = S(E^*)dE^*/dt$

where F is the flux at time t, and dt is estimated from $t(E_{N-1}^*,Z) - t(E_N^*,Z)$.

An outline of the processes described above is shown schematically in figure V.40.

V.F.2.a. Time Functions

The mean time of an ion of incident energy E* to position Z can be estimated for light ions from stopping power relations discussed in section V.B. These relations were based upon a three region stopping power formulation. We will now develop formulae for the time associated with each energy interval. The summation of time for each interval then represents the total time to reach an energy E at position Z. For the low velocity region, the relation is
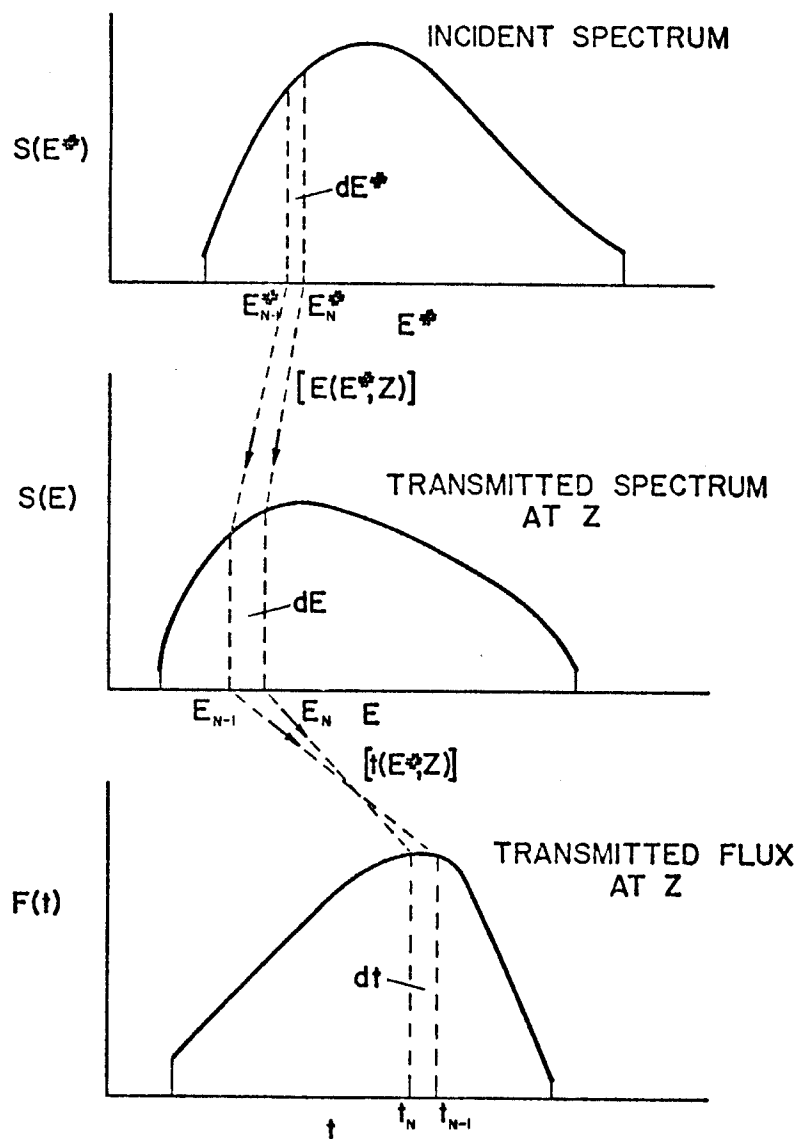
Fig. V. 40. Analysis Procedure for Light Ions

151) $$\frac{dE}{dx} = S_0 (E/E_o)^{1/2}$$

Hence the mean time is

152) $$<t>_1 = \int_{E}^{E^*} \frac{dE}{V\frac{dE}{dx}}$$

which, when equation (151) is substituted and the integration is performed, gives:

153) $$<t>_1 = \frac{\sqrt{mE_o}}{DS_o} \, \ell n \, E^*/E$$

where

$$S_o = keV/cm$$

$$m = amu$$

$$E_o = keV$$

$$D = 4.38 \times 10^7 \frac{cm \, amu^{1/2}}{sec \, kev^{1/2}}$$

Equation (153) is valid until the local energy reaches about "2A"* keV in which case deceleration from nuclear processes must be considered. In this analysis it was assumed that the stopping power below 2A keV was a constant value equal to the value of equation (151) at "2A" keV. Hence,

154) $$\frac{dE}{dx} = S_o (\frac{2A}{E_o})^{1/2}$$

and defining the position at which that energy is reached as

155) $$Z_{2A} = \frac{2E_o^{1/2}}{S_o} (E_*^{1/2} - 2A^{1/2})$$

the local ion energy between Z_{2A} and 0 is determined by

---

*A here is the atomic weight.

156) $E(x) = 2A - S_o (2A/E_o)^{1/2} x$

and the approximate time from Z_{2A} to position Z $(Z > Z_{2A})$ is

157) $t' = \dfrac{Z - Z_{2A}}{[V(2A) + V(E(Z))]/2}$

where V is the velocity corresponding to the energy at that point and $E(Z)$ is taken from equation (156).

For the intermediate and high velocity regimes regions 2 and 3, the relations for energy at any position were given in section V.B. The most direct method for determining the time to an intermediate energy is to assume a piecewise linear velocity profile and to define 3 reference points.

X_1, V_1 - the velocity and position of the incident ion into
either regions 2 or 3.

X_{mid}, V_{mid} - the velocity and position halfway between
incidence and leaving regions 2 or 3.

X_2, V_2 - the velocity and position leaving regions
2 or 3.

A piecewise linear approximation between each point gives the total transit time in any region as:

158) $t_{X_1 - X_2} = B \ln V_{mid}/V_1 + B' \ln V_2/V_{mid}$

where

$$B = \dfrac{X_{mid} - X_1}{V_{mid} - V_1} \quad \text{and} \quad B' = \dfrac{X_2 - X_{mid}}{V_2 - V_{mid}}$$

where the velocities are determined from the incident energy, $E(X_{mid})$,

and $E(X_2)$ where X_2 is the position leaving the region or Z if X_2 is greater than Z.

The relations have all been incorporated into the T-DAMEN for modification of light ion spectra and, as in the case for heavy ions, have output formats which are compatible with the subsequent response calculations. An example of the modification of a tritium spectrum is shown in figure V.41. In this case a 320 keV Maxwellian spectrum is shown at a position of 7 meters for a neon buffer gas at pressures of 0.1, 0.5, 1, and 2 torr, respectively.

V.F.3. Energy Deposition in the Gas

If gaseous protection makes a significant modification of the ion spectra, a substantial amount of energy will be released in the gas. In the case of a pellet microexplosion, the spherical divergence of the flux makes the initial volumetric energy disposition very high, even for modest gas pressures. This energy deposition is sufficient to heat and ionize the gas thereby setting up the condition for development of a shock wave and reradiation of the energy.

The methods discussed in the previous sections can be used to estimate the time dependent energy deposition at any point in the gaseous layer. For heavy ions the spectral dependence of the energy deposition can be developed starting from equation (124).

$$R = C \, V_*^{\frac{1}{1-k}}$$

then:159) $\quad \dfrac{dr}{dV} = \dfrac{C}{1-k} \, V^{\frac{k}{1-k}}$

NEON GAS
RADIUS = 7 m
T = 273 K
TRITIUM IONS

NO GAS

0.1 TORR

0.5 TORR

1 TORR

2 TORR

$F(E)$, J/cm^2/KeV

x10^{-4}

ENERGY, KeV
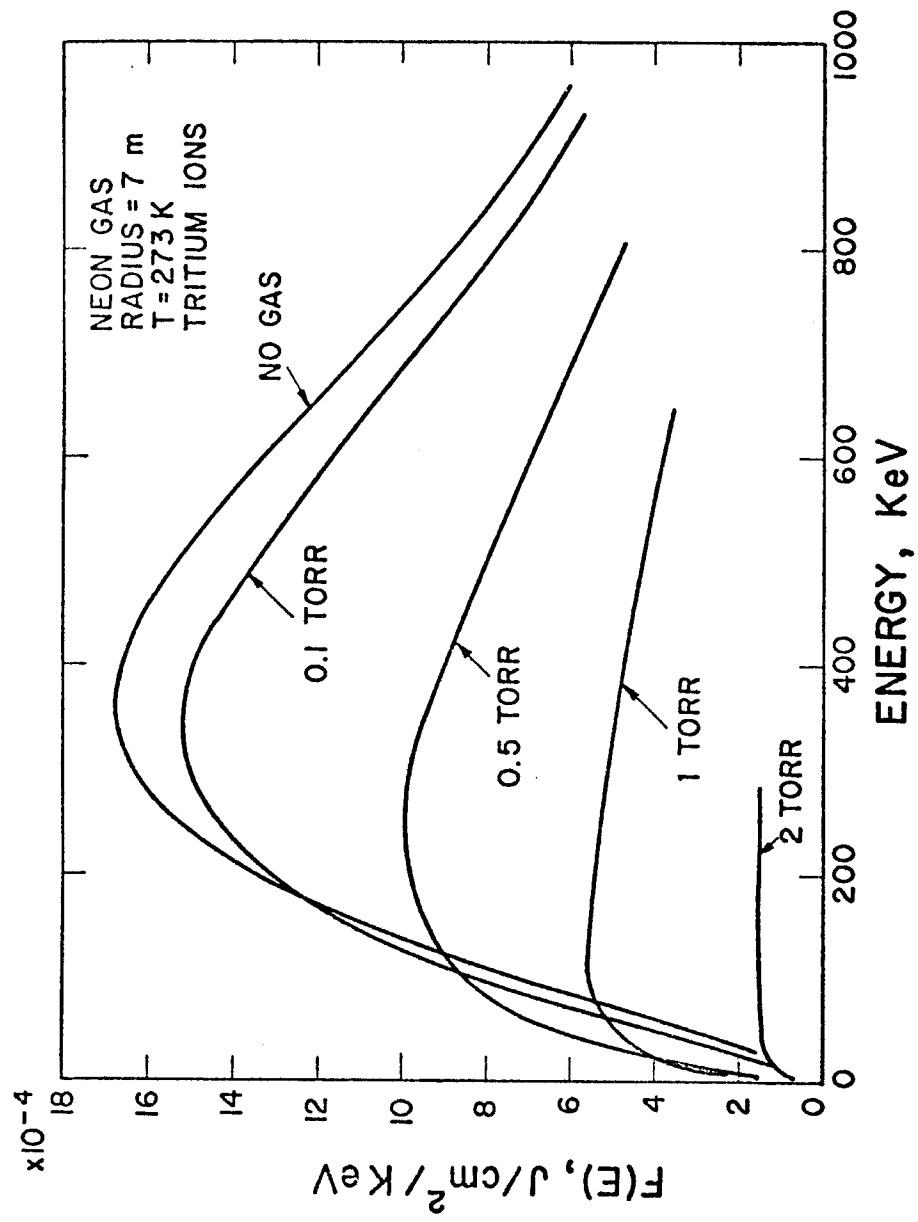
Fig. V. 41. Effect of Gas on Incident Light Ion Spectrum

and using $\quad \dfrac{dE}{dR} = \dfrac{dE}{dV}\dfrac{dV}{dR}$

with
$$\dfrac{dE}{dV} = \dfrac{2mV}{(4.39\times10^7)^2}$$

yields the energy deposition rate as a function of ion velocity as:

160) $\qquad \dfrac{dE}{dr} = \dfrac{1-k}{C}\dfrac{m}{9.64\times10^{14}} V^{\frac{2k-1}{k-1}}$

where $\qquad$ V = instantaneous ion velocity, cm/sec

$\qquad$ m = ion mass, amu

$\qquad$ k,C $\quad$ are defined in equation (124)

$\qquad \dfrac{dE}{dr}$ = energy deposition, keV/cm

These relations can be coupled with the relations for instantaneous flux and spectra (developed in section V.F.1) and with the appropriate divergence in spherical geometry to determine the deposition rate from an arbitrary ion spectra. The relations for the time, local energy, and energy deposition for light ions are readily applied to the appropriate flux and spectra in a spherical coordinate system to yield a similar result.

These above relations are incorporated into the T-DAMEN code so that energy depositions can be obtained at arbitrary position in a buffer gas. This data can be used as the driving force for initiation of the general response of the gas including subsequent hydrodynamics and radiation.[109] Results of the energy deposition calculations for Si ions and fast helium ions in 0.5 torr neon are shown in figure V.42 and V.43, respectively. Spatial energy deposition profiles may be
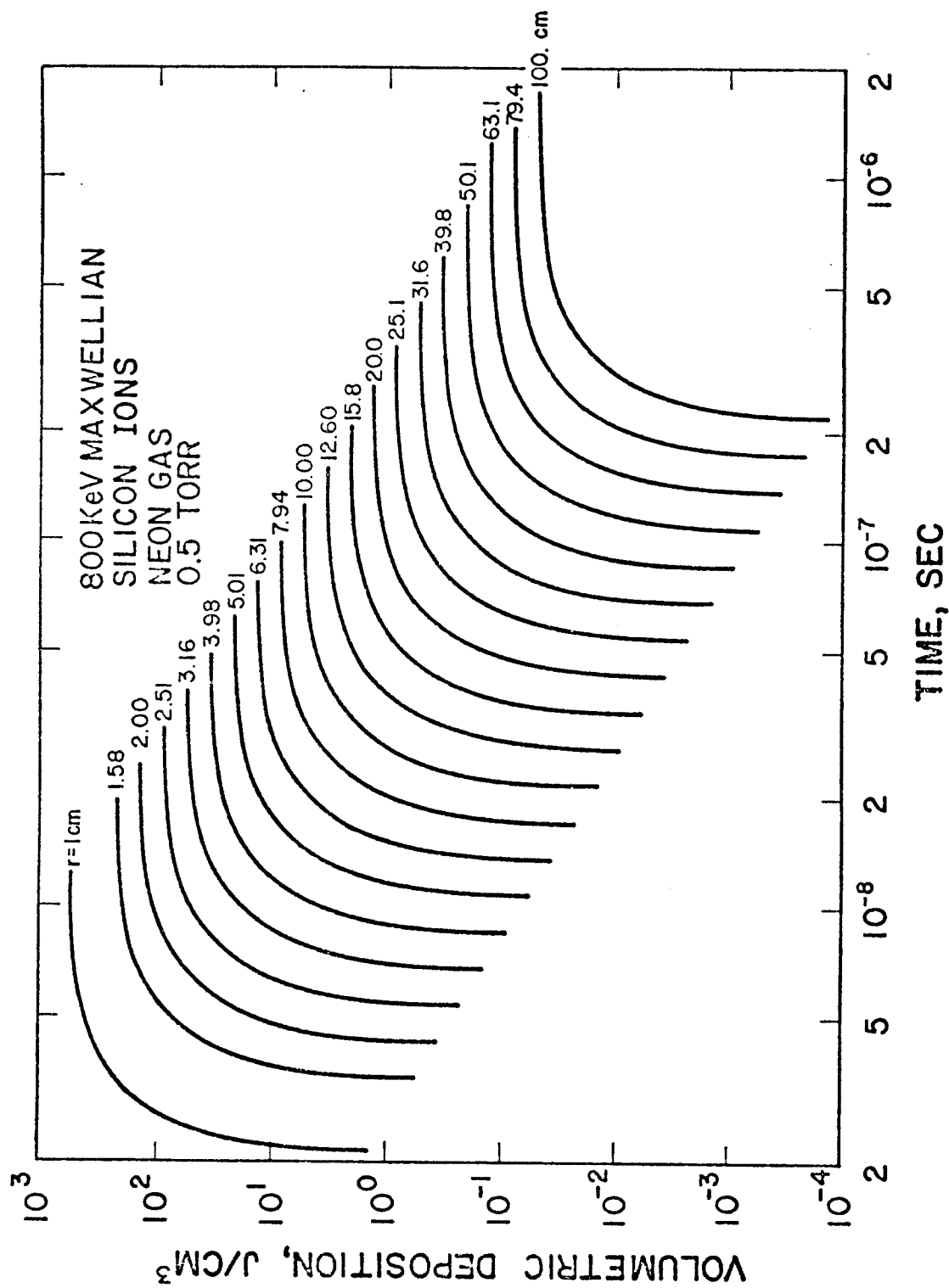
Fig. V. 42. Energy Deposition from Silicon Ions in Neon
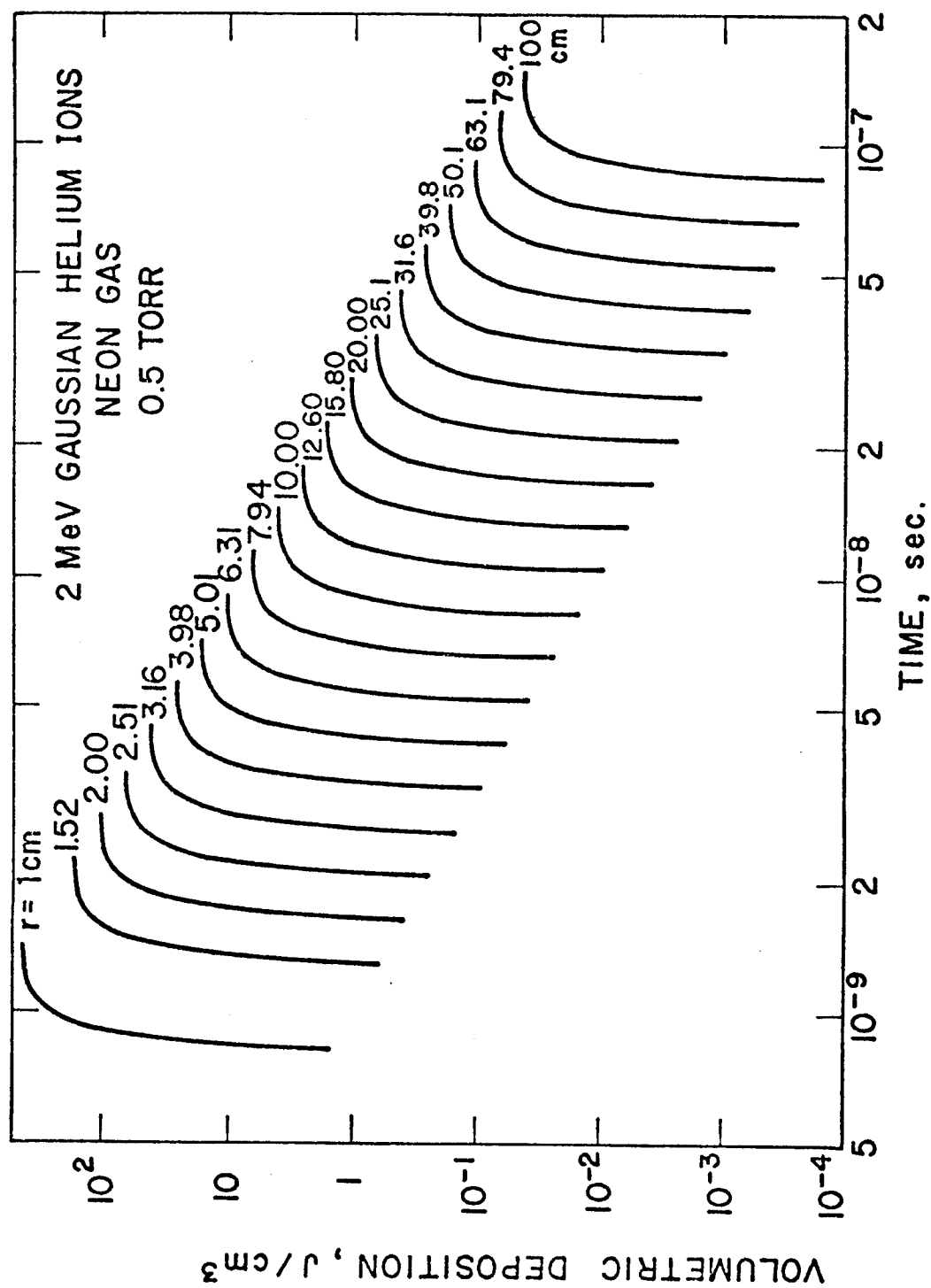
Fig. V. 43. Energy Deposition from Helium Ions in Neon

developed from these data by selecting a time along the abcissa and reading the cumulative deposition value at various positions. This self-consistent incorporation of the deposition in the gas into the T-DAMEN code allows assessment of the deposition in the gas and commensurate response of an exposed material for variations in gas type and density and ion spectra.

The data in figure ^{V}. 42 indicate that volumetric deposition of several hundred joules/cm^3 are released in less than 20 ns in the first few centimeters surrounding the thermonuclear source. These high depositions will cause ionization of the gas which in turn will allow energy to be radiated away upon recombination. In addition, the subsequent ion stopping will also be influenced by this ionization, but the spectrum reaching the first wall will not be substantially different than predicted here since the first few centimeters make a small contribution to the spectra at radii of several meters.

It should also be noted that it is likely that the gas will reradiate the energy deposited by both ions and X-rays before it is exhausted from the chamber. This radiation must also be absorbed by the walls of the chamber. It is not the intent of this study to analyze this aspect of wall response although such analysis may be easily performed with a transient surface heat flux calculation which is a method also contained in the T-DAMEN code. The time scale for such energy release becomes the critical parameter in these calculations and estimates for the various radiation properties of gases are being assessed in reference 109.

V.F.4. Modification of X-ray Spectra

Gaseous protection reduces the severity of the response of a material to a pulsed thermonuclear source not only because it stops or slows down energetic ions, but because it can significantly modify the X-ray spectrum as well. This modification is, however, extremely sensitive to the initial X-ray spectrum and the gas chosen. An example of this relationship is shown in figure V.44 where the total cross section of He, Ne, and Xe are shown as a function of photon energy. These data are taken from the T-DAMEN code which are based on the data of Biggs.[49]

The T-DAMEN code contains the ability to examine the X-ray deposition in as many as four successive layers. If the first layer is a gas, the spectra onto the second layer and the subsequent temperature response of the second layer give a measure of the protection provided by the gas against the initial radiation burst. An example of the modification of an initial 1 keV black body spectrum by 7 meters of 0.5 torr neon gas is shown in Figure V.45. It should be noted from these data that any single gas can appear transparent to radiation near an absorption edge and consequently mixtures of gases may be necessary. A more general study of the response of several materials to a variety of X-ray spectra and gases will be presented in the form of a parameter study in Chapter VII.
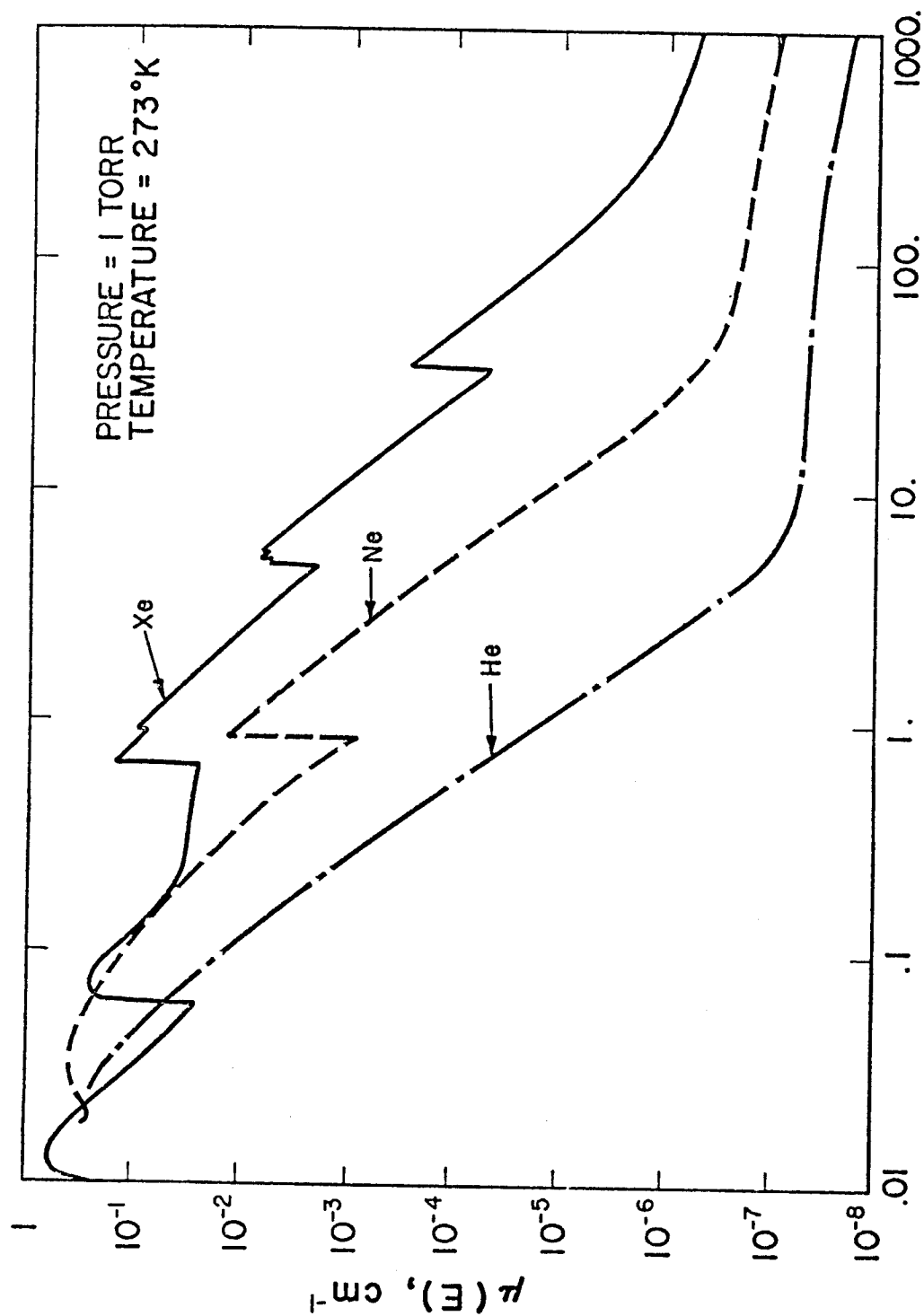
Fig. V. 44. Total X-Ray Interaction Cross Sections
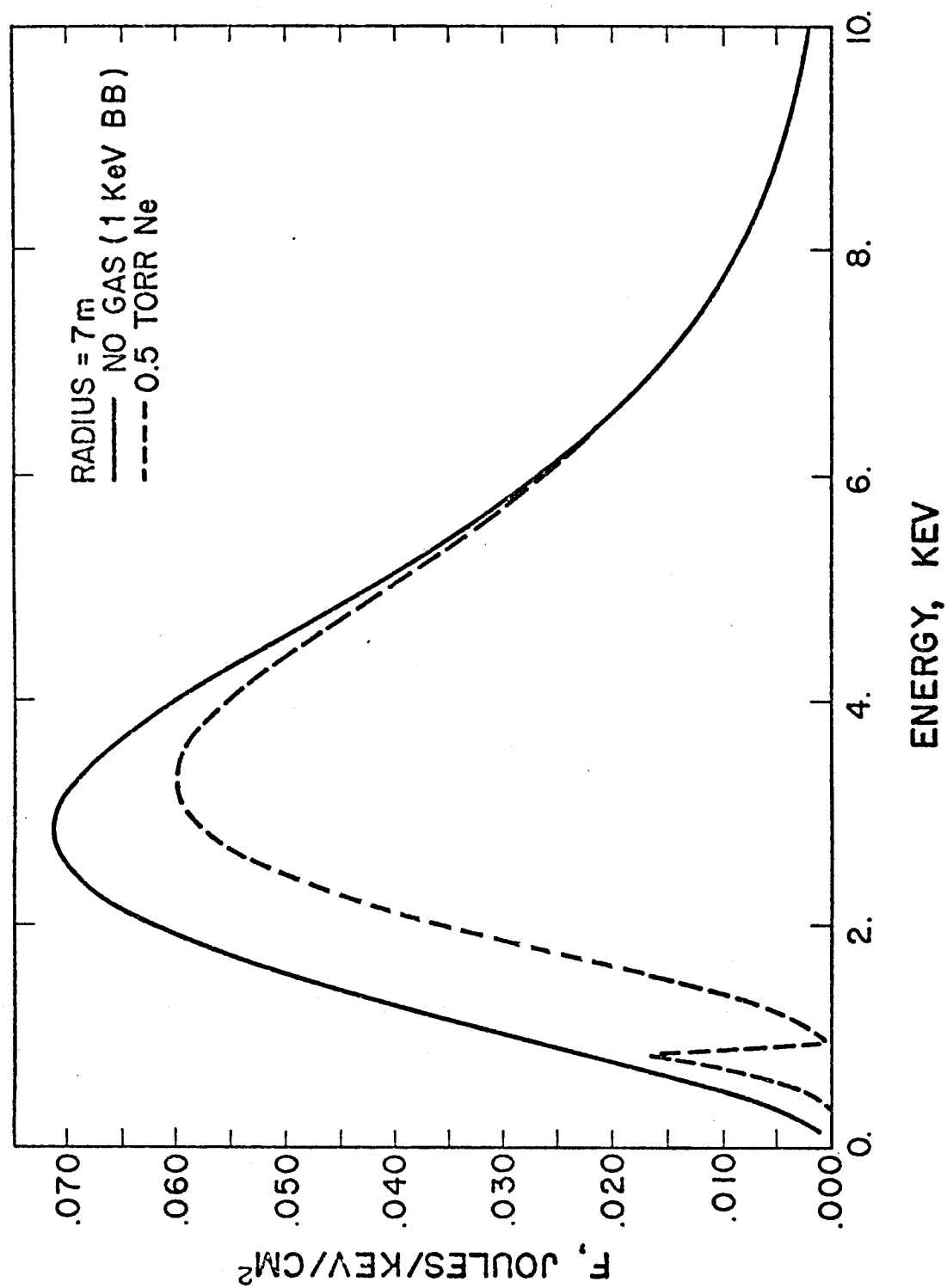
Fig. V. 45.   Modification of X-Ray Spectrum by Neon Gas

CHAPTER VI

THE T-DAMEN COMPUTER CODE

VI.A. INTRODUCTION

The T-DAMEN computer code[47] is a general program for analysis of the transient radiation damage produced in materials from pulsed thermonuclear radiation. The various models incorporated are discussed in Chapter V. The code was developed to provide a first order analysis of the energy deposition, temperature response, displacement production, and other subsequent effects produced in materials by transient pulses of photons or ions. The models used are approximate solutions to problems of ion and photon transport, radiation deposition, heat conduction, and primary defect production. These solutions are sufficiently efficient to allow simultaneous analysis of a wide range of ion and photon spectra which may be arbitrarily specified.

T-DAMEN is not meant to be used as a tool for precise analysis of any one specific phenomena, e.g., ion implantation distributions; but rather as a tool for assessment of combined effects and parametric analyses. It is for these reasons that the code has been used for applications such as the response of first walls in inertial confinement fusion reactors.

The code contains a complete data handling package including generation of spectra, intermediate data storage, and plotting. In addition, various independent routines for developing input data are included in the code. T-DAMEN is written in Fortran

for the UNIVAC-1110 at the University of Wisconsin, Madison.[110] All
routines with the exception of the file handling and plotting should
be readily adaptable to any computer system.

Specific instructions for using the code, listings of the various
routines, and example problems were too extensive to be included here
but can be obtained in reference.[47]

The code was written to be compatible with the UNIVAC file system
for mass storage devices. The entire program is contained in one
file which is divided into many elements. Elements on the UNIVAC-1110
are of the following three types:

> Symbolic - Fortran and run stream statements (similar to card
>   images).
>
> Relocatable - Compiled versions of FORTRAN symbolic elements.
>
> Absolute - Executable machine language combinations of various
>   relocatables.

Subsequent discussion will describe each major section of the
code and the structure of the symbolic elements associated with each
absolute element.

VI.B. Description

The T-DAMEN code is divided into two major categories: Ion
response and photon response. Each of these is in turn supported by
routines which can develop input data, superimpose results, file
output, and plot results.

The major sections and respective absolute elements of the code

are shown in figure VI.1 and are outlined in subsequent sections.

Each section contains a block diagram and outline of the respective FORTRAN symbolic elements (card images) for each of the program segments.

The block diagrams display the functional relationship between each routine within a given segment. The element outline gives a brief description of each subroutine in that segment, and in addition, identifies a) the absolute element (executable) for a segment, b) the name of an element containing the pertinent read statements, c) an element which is used to collect all the subroutines into an absolute element, and d) an element which can be used to obtain a listing of all of the elements for a given segment.

V. B. 1. Photon Response

[P-1] Spectral Deposition and Temperature - This routine calculates the volumetric energy deposition for X-ray spectra and monoenergetic photons. Spectra may be specified as black bodies or histogram form. Deposition is based on a general library of photoelectric and incoherent cross sections. This library includes all elements and is accessed by specifying the element atomic number and the photon energy. Temperature calculations are done for the adiabatic case, an impulse solution, and a finite duration deposition. Gas protection is incorporated by allowing a total of 4 material layers through which the spectrum is modified. The absolute element (executable) is M/E.
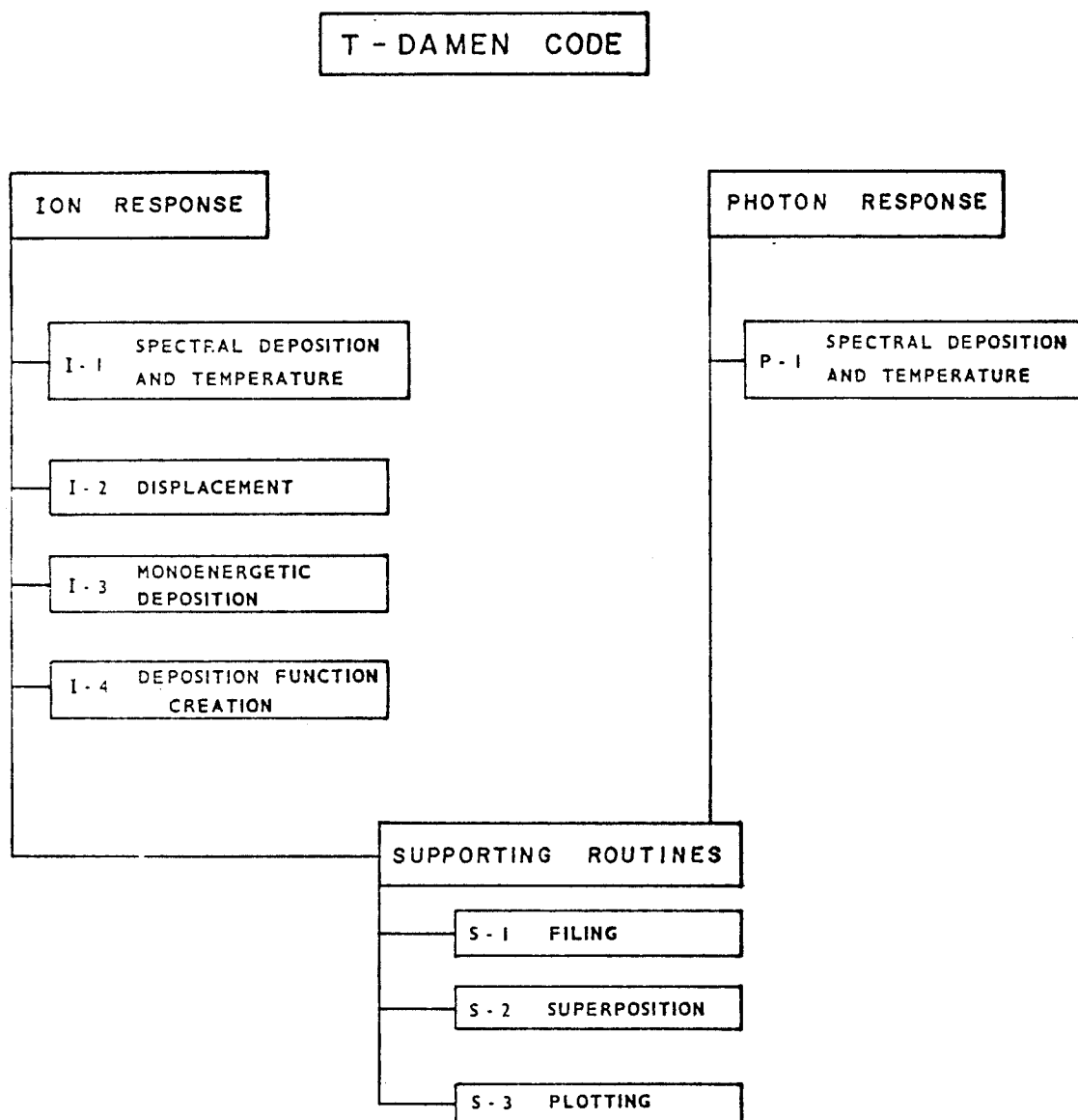
Fig. VI. 1.   General Outline of the T-DAMEN Code

The output of these calculations include the energy deposition and transmitted spectra for each of the layers. Temperature is given as a function of position and time whose values are user specified as input.

The output can be sent to a data file for future use such as plotting or superposition with response from other components.

The block diagram for the photon code is given in figure VI.2 followed by the element description in Table VI.1.

VI.B.2. Ion Response

VI.B.2.a. [I-1] Spectral Deposition and Temperature - (IONCODE)

This is the largest routine in T-DAMEN and contains numerous sub-routines for the general responses of ions in materials. This program can generate ion spectra in the form of Maxwellians, Gaussians, or histograms. These spectra can define either light ions ($Z \leq 2$) at high energy or other ions at any energy. The original spectra can be modified by a gaseous layer of specified pressure, temperature and type and the time dependent energy deposition can be obtained.

The flux which strikes the material is transformed into the time and energy dependent deposition profiles which are in the form of polynomials. These polynomials are then used to reconstruct the volumetric energy deposition as a functions of time.

The coefficients of the deposition polynomials can then be supplied to the temperature routine to determine the temperature histories at various positions. Temperature may be determined on a
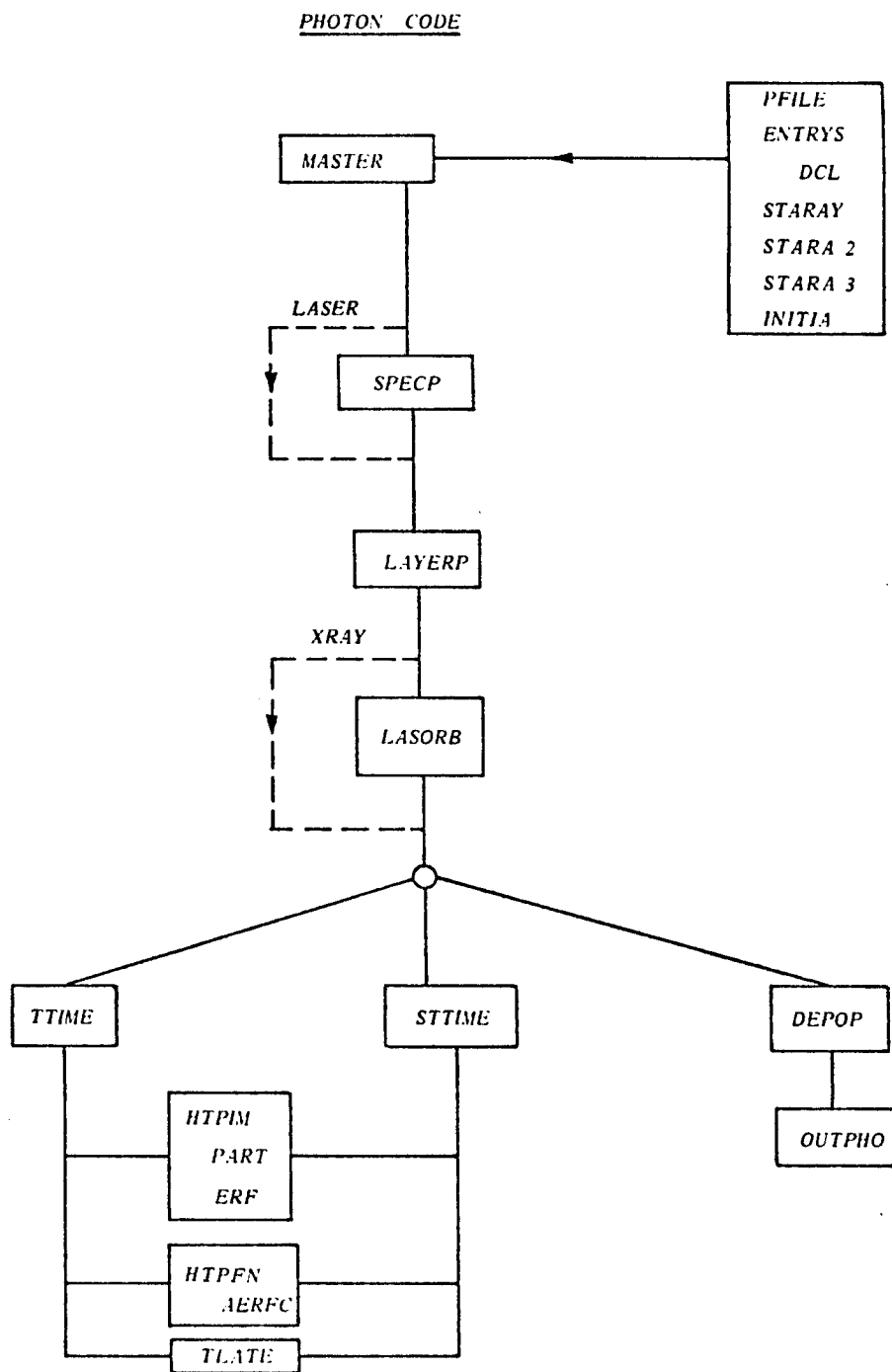
PHOTON CODE

Fig. VI. 2. Block Diagram for General Photon Code

Table VI. 1. Photon Response Section of T-DAMEN Code

ABSOLUTE
     M/E

READER
     READ/PHOTON

MAPPER
     MAP/PHOTON

LISTER
     LIST/PHOTON

SYMBOLICS
     MASTER --MASTER ROUTINE FOR CALLING EACH SECTION
     SPECP   --CALCULATES A BLACK BODY SPECTRUM FOR A GIVEN
               TEMPERATURE AND TOTAL FLUX
     LAYERP --SETS UP MATERIAL GRID UP TO 4 LAYERS WITH ANY
               NUMBER OR MATERIAL'S PER LAYER, DETERMINES
               COMPOSITE ABSORPTION COEF.,DENSITY,GAS PROP. ETC
     INITIA --CALLS CROS TO GET CROSS SECTION DATA FROM
               ELT/ATOM
     CROS   --SELECTS FROM THE CROSS SECTION LIBRARY THE PHOTON
               ELECTRIC AND INCOHERENT VALVES FOR A GIVEN Z,
               READS IN ENTIRE LIBRARY
     ELT/ATOM-ALL PHOTON CROSSECTIONS Z FROM 1-100, PLUS CALL TO
               INITIA WHICH READS THEM
     GEN/XMU--CALCULATE PHOTON CROSSECTION FOR A GIVEN ENERGY
               FROM COEFFICIENTS IN CROS
     DEPOP   --CALCULATES PHOTON DEPOSITION, J/CUBIC CM,
               TRANSMITTED SPECTRA, ADIABATIC TEMPERATURE
     TTIME   --EVALUATES TEMPERATURE AT ANY TIME OR POSITION
               FOR ANY OF 3 MODELS
     STTIME --SAME AS TTIME EXCEPT X AND T ARE STANDARD ARRAYS
     HTPIM   --EXPONENTIAL IN SPACE, IMPULSE IN TIME TEMPERATURE
               SOLUTION (MODEL 1)
     HTPFN   --EXPONENTIAL IN SPACE, FINITE DURATION IN TIME
               TEMPERATURE SOLUTION (MODEL 2)
     PART   --A SUBROUTINE NECESSARY IN HTPIM DERIVED FROM
               EXPRESSION FOR ERROR FUNCTION
     AERFC   --INTEGRAL COMPLEMENTARY ERROR FUNCTION
     ERF   --ERROR FUNCTION, SINGLE PRECISION
     TLATE   --A SOLUTION TO THE FINITE SLAB FOR EXPONENTIAL
               IN SPACE AND IMPULSE IN TIME (MODEL 3)

Table VI. 1., Cont'd

```
OUTPHO --A ROUTINE FOR OUTPUTTING THE RESULTS OF THE PHOTON
          CODE
LASORB --GENERATES A SINGLE MONO ENERGETIC ATTENUATION
          COEFFICIENT SIMILIAR TO LASER ATTENUATION
STARAY --GENERATES THE STANDARD X AND TIME ARRAYS
PFILE/IODR--FILES THE COMMON BLOCK DATA FROM THE PHOTON
          CODE INTO A PHOTON IODR FILE
ENTRYS/IODR--BASIC SUBROUTINE FOR IODR DATA BLOCKS
DCL/IODR-STRUCTURE OF DATA BLOCKS FOR IODR FILE SYSTEM
```

time base which is determined by the ion arrival times or on a pre-
determined standard time base which allows comparison of response
from various components.

The related thermal response solution for a heat flux on a semi-
infinite slab is also contained as an independent routine. In addi-
tion, the eigenvalue solution for finite width materials after many
pulses is also contained as a subroutine. Routines for assessment of
temperature dependent sputtering, evaporation, and ion implantation
profiles are also included.

Output consists of listings of the flux and energy spectra due
to the original spectra or after modification by gases. The energy
deposition as a function of time and position is also listed as are
the temperatures.

As in the photon code, data may be sent to a data file for
future use. The block diagram and element description are given in
figure VI.3 and Table VI.2

VI.B.2.b.   [I-2] Displacement

This routine provides the displacement production from arbitrary
ion spectra. Spectra are generated and modified by gaseous layers as
described above for spectral depositions and temperatures. Response
is again performed for either light or heavy ions.

Light ion displacement calculations are performed by determining
the mean local ion energy and an appropriate displacement cross
section. Heavy ion calculations are based on the nuclear energy
deposition functions described in section VI. B. 2. d.
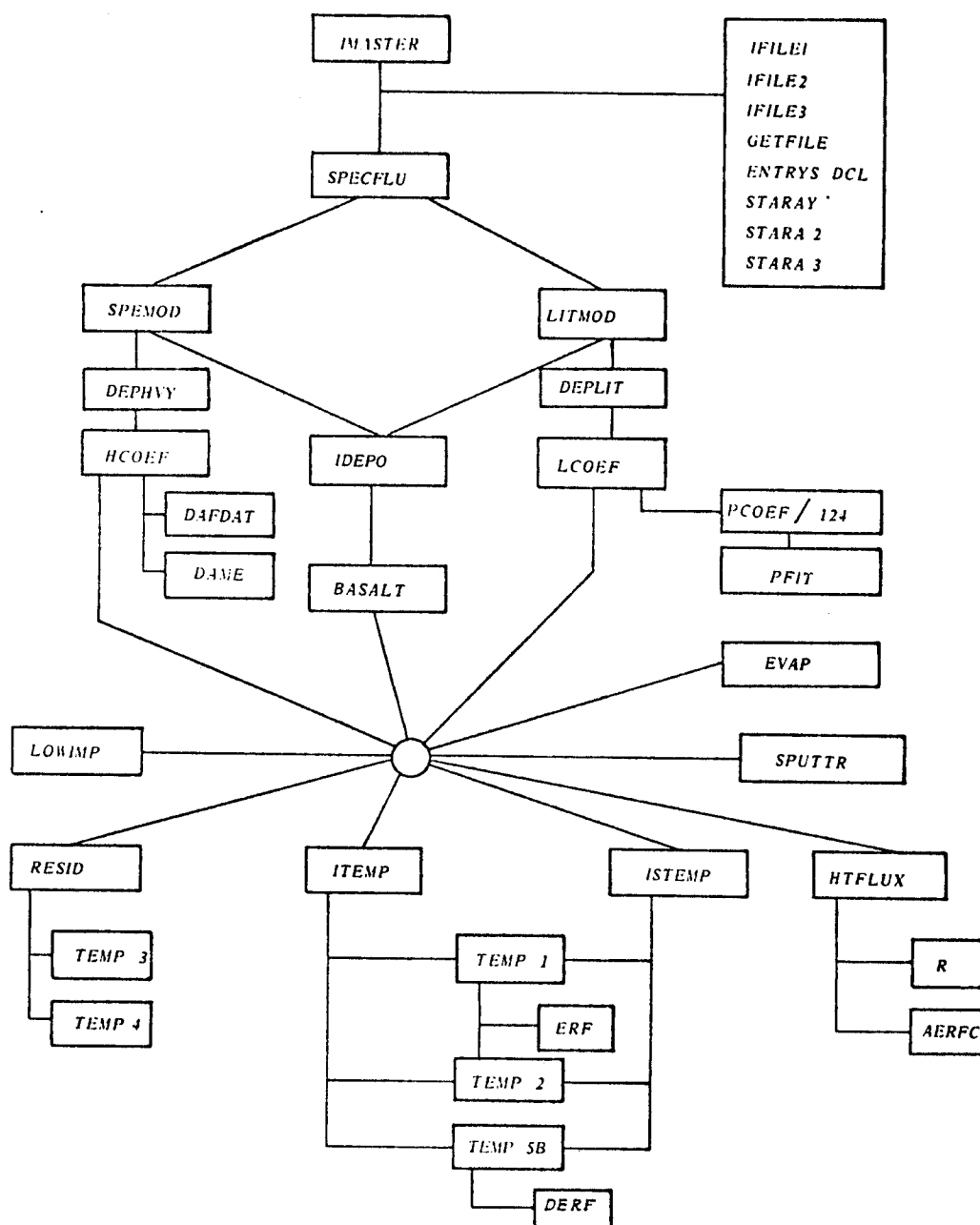
Fig. VI. 3. Block Diagram for General Ion Code

Table VI. 2.   Ion Response Section of T-DAMEN Code

ABSOLUTE
    IONCODE

READER
    READ/ION

MAPPER
    MAP/ION

LISTER
    ION/LIST

SYMBOLICS
    IMASTER--MASTER ROUTINE FOR CALLING EACH SECTION
    SPECFLU--CREATES THE PARTICLE FLUXES FROM THE SPECTRA
    SPECTR --GENERATES MAXWELLIAN OR GAUSSIAN SPECTRUM
    SPEMOD --MODIFIES A HEAVY ION SPECTRUM VIA DIFFUSION
            APPROXIMATION
    LITMOD --MODIFIES A LIGHT ION SPECTRUM USING SLOWING
            DOWN APPROXIMATION
    HCOEF --GENERATES COEFFICIENTS MATRIX FOR HEAVY ION
            DEPOSITION
    DEPLIT --CALCULATES DEPOSITION RATE IN BUFFER GAS FOR
            LIGHT IONS
    DEPHVY --CALCULATES DEPOSITION RATE IN BUFFER GAS FOR
            HEAVY IONS
    LCOEF --GENERATES COEFFICIENTS MATRIX FOR LIGHT ION
            DEPOSITION
    PCOEF/124--GENERATES POLYNOMIAL COEFFICIENTS FOR SET
              OF INCIDENT ENERGIES
    DAME   --CALCULATES COEFFICIENTS OF DAMAGE FUNCTIONS
            A GIVEN VALUE OF ENERGY
    DAFDAT --READS DAMAGE FUNCTIONS FROM FILE 11 BY A
            NUMBER WHICH INDICATES A CERTAIN ION-TARGET
            COMBINATEION
    PFIT   --A GENERAL 1-4TH ORDER POLYNOMIAL INTERPOLATION
            ROUTINE
    IDEPO --DOES ENERGY DEPOSITION FOR THE IONS
    STARAY --GENERATES 15 VALUES OF X (10-7--10-2) AND 115
            VALUES OF TIMES (10-10--10-2)
    STARA2 --STANDARD ARRAY FOR 15 VALUES OF X (10-7--10-2)
            AND 115 VALUES OF TIMES (10-7--10-4)

Table. VI. 2., Cont'd

```
STARA3  --STANDARD ARRAY FOR 50 VALUES OF X (LIMIT IS
             READ IN) AND 115 VALUES OF TIMES
STARAY/PRINT--SYMBOLIC AND ABSOLUTE ELEMENT FOR
                PRINTING STANDARD TIMES AND LOCATIONS
                FROM STARAY
STARA2/PRINT--SYMBOLIC AND ABSOLUTE ELEMENT FOR
                PRINTING STANDARD TIMES AND LOCATIONS
                FROM STARA2
BASALT  --TRANSFORMS ARBITRARY TIME BASE TO STANDARD TIME BASE
ITEMP   --EVALUATES TEMPERATURE (X,T) FOR ARBITRARY VALUES
ISTEMP  --EVALUATES TEMPERATURE (X,T) FOR THE STANDARD TIMES
             AND LOCATIONS (FROM STARAY)
TEMP1   --TEMPERATURE RESPONSE AT ONE TIME FOR LINEARLY
             DECREASING DEPOSITION
TEMP2   --TEMPERATURE RESPONSE AT ONE TIME FOR UNIFORM
             RESPONSE
TEMP3   --TEMPERATURE FOR FINITE SLAB WITH LINEARLY
             DECREASING DEPOSITION
TEMP4   --TEMPERATURE FOR FINITE SLAB WITH UNIFORM DEPOSITION
TEMP5B  --GENERAL TEMPERATURE RESPONSE MODEL FOR DEPOSITION
             IN FORM OF POLYNOMIAL COEFFICIENTS
DERF    --ERROR FUNCTION, DOUBLE PRECISION
ERF     --ERROR FUNCTION, SINGLE PRECISION
IFILE/IODR--FILING OF COMMON BLOCK  IN IODR FILE
ENTRYS/IODR--ROUTINES FOR FILING MECHANICS
DCL/IODR-BASIC FILE STRUCTURE FOR IODR DATA BLOCKS.
LOwIMP  --DETERMINES IMPLANTATION DISTRIBUTION FOR LIGHT IONS
HTFLUX  --CALCULATES T(X,T) FOR A FLUX OF FINITE
             DURATION USING HEAT FLUX BOUNDARY CONDITION
R       --SUPPORTING FUNCTION FOR HTFLUX
AERFC   --INTERGRAL COMPLEMENTARY ERROR FUNCTION
RESID   --CALCULATES RESIDUAL TEMPERATURE FROM N PREVIOUS
             PULSES
SPUTTR  --CALCULATES SPUTTERING YIELD FOR HEAVY IONS
             INCLUDING TEMPERATURE DEPENDENCE
EVAP    --CALCULATES EVAPORATION RATE FROM SURFACE
             TEMPERATURE AND VAPOR PRESSURE DATA
```

Either method can develop the temporal and spatial dependent displacement production on a time base imposed by the ion arrivals or on a standard time base compatible with all the ion components.

Output data can be placed into a data file using the same filing system as the ion code. Displacement rate and total displacement histories are handled in exactly the same manner as the energy depositions of the ion code; consequently, subsequent operation such as plotting follow the same format.

The block diagram and following element description is shown in figure VI.4 and Table VI.3.

VI.B.2.c. [I-3] Single Ion Deposition

This routine allows determination of the deposition of a mono-energetic ion into a material. Either light or heavy ions can be considered. Light ion calculations are based on the stopping power theory of Brice and the relations developed in Chapter V. Heavy ion calculations are based on the deposition functions of section V.B.

The light ion version contains an internal plotting package and is primarily used to evaluate input parameters for data supplied to the spectral deposition and temperature routine. The heavy ion version does require an external data file (see d below) from which deposition coefficients are obtained. These routines are primarly used to develop and checkout input data for the ion code; hence, there is no provision for the output to be included in the general filing and plotting system.

Output includes a listing of electron stopping power for several
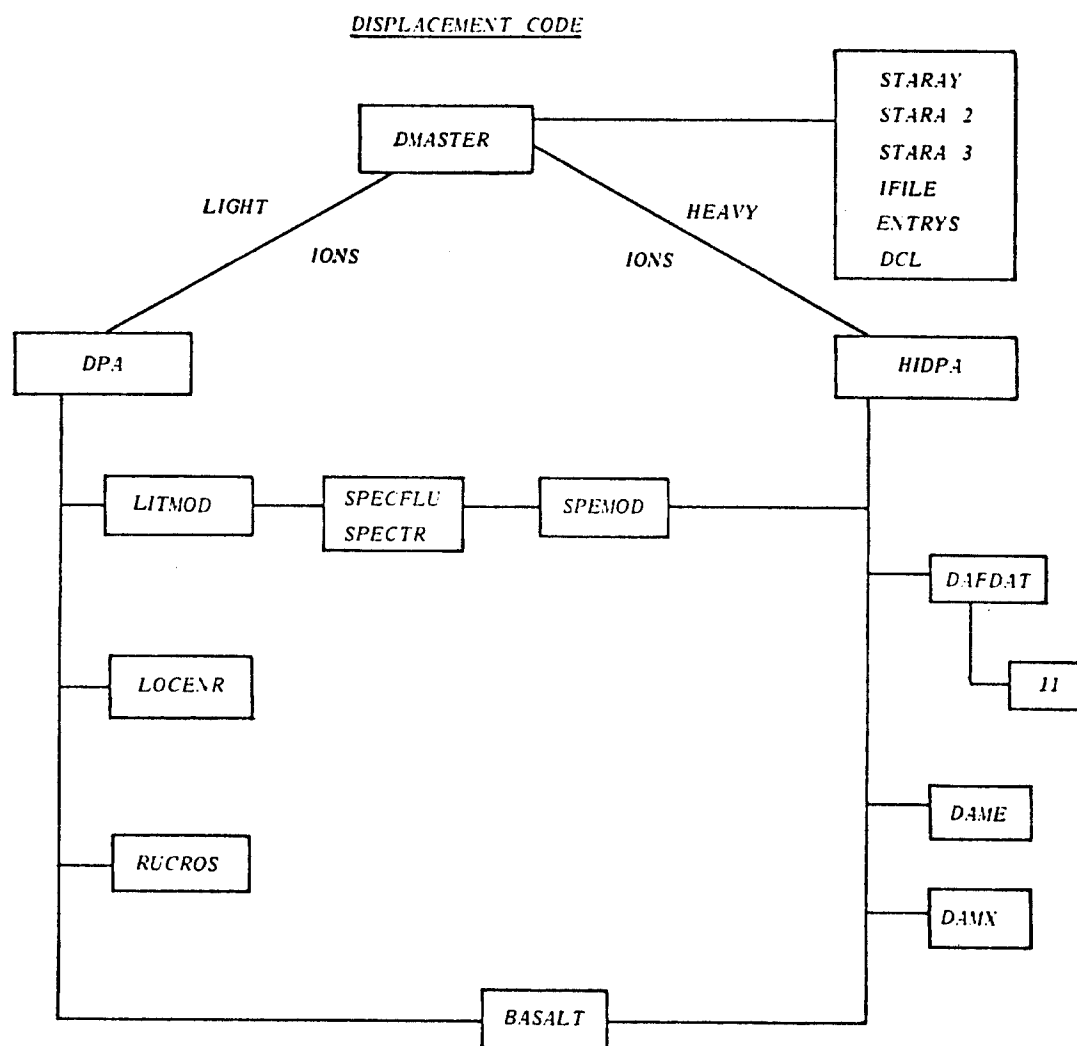
DISPLACEMENT CODE

Fig. VI. 4.   Block Diagram for Displacement Code

Table VI. 3.   Displacement Section of T-DAMEN Code

ABSOLUTE
    DISPLACEMENT

READER
    READ/DPA

MAPPER
    MAP/DISPLACEMENT

LISTER
    LIST/DISPLACEMENT

SYMBOLICS
    DMASTER--A MASTER ROUTINE FOR CALLING EACH SUBROUTINE
    DPA   --CALCULATES LOW Z ION DPA RATES FOR STANDARD ARRAY
    RUCROS --EVALUATES THE RUTHERFORD CROSSECTION OR LINDHARD
              NUCLEAR DERIVED CROSS SECTION FOR IONS OF
              ENERGY E
    SPECFLU--CREATES THE PARTICLE FLUXES FROM THE SPECTRA
    SPECTR --GENERATES MAXWELLIAN OR GAUSSIAN SPECTRUM
    SPEMOD --MODIFIES A HEAVY ION SPECTRUM VIA DIFFUSION
              APPROXIMATION
    LITMOD --MODIFIES A LIGHT ION SPECTRUM USING SLOWING
              DOWN APPROXIMATION
    LOCENR --GENERATES THE ENERGY AS A FUNCTION OF X FOR
              AN ION OF INCIDENT ENERGY E*
    STARAY --GENERATES THE STANDARD X AND T ARRAYS
    STARA2 --STANDARD ARRAY FOR 15 VALUES OF X(LIMIT IS READ IN)
              AND 115 VALUES OF TIME (10-7--10-4)
    STARA3 --STANDARD ARRAY FOR 50 VALUES OF X(LIMIT IS READ IN)
              AND 115 VALUES OF TIME (10-7--10-4)
    HIDPA   --CALCULATES DPA-RATES FOR HIGH Z IONS OR LOW ENERGY
              LOW Z IONS
    BASALT --TRANSFORMS ARBITRARY TIME BASE TO STANDARD TIME BASE
    DAFDAT --READS DAMAGE FUNCTIONS FROM FILE 11 BY
              A NUMBER WHICH INDICATES A CERTAIN ION-TARGET
              COMBINATION
    DAME   --CALCULATES COEFFICIENTS OF DAMAGE FUNCTIONS
              FOR A GIVEN VALUE OF ENERGY
    DAMX   --CALCULATES THE DAMAGE FUNCTION AT A POSITION
              FOR THE COEFFICIENTS FOUND IN PREVIOUS CALL TO
              DAME
    IFILE/IODR--FILING OF COMMON BLOCK IN IODR FILE
    ENTRYS/IODR--ROUTINES FOR FILING MECHANICS

different models and spatial profiles of energy deposition based on those models.

The block diagram and element outline is given in figure VI.5 and Table VI.4.

DEPOSITION

```
┌──────────────┐                          ┌──────────────┐
│  LOW ZDEP    │                          │  HIGH ZDEP   │
└──────┬───────┘                          └──────┬───────┘
       │                                         │
       ├──┌──────────────┐                       ├──┌──────────────┐      ┌──────┐
       │  │ PCOEF/ 124   │                       │  │   DAFDAT     │------│  11  │
       │  └──────────────┘                       │  └──────────────┘      └──────┘
       ├──┌──────────────┐                       ├──┌──────────────┐
       │  │   PFIT       │                       │  │   DAME       │
       │  └──────────────┘                       │  └──────────────┘
       │  ┌──────────────┐                       └──┌──────────────┐
       └──│   MACC       │                          │   DAMX       │
          │  GRAPHICS    │                          └──────────────┘
          └──────────────┘
```
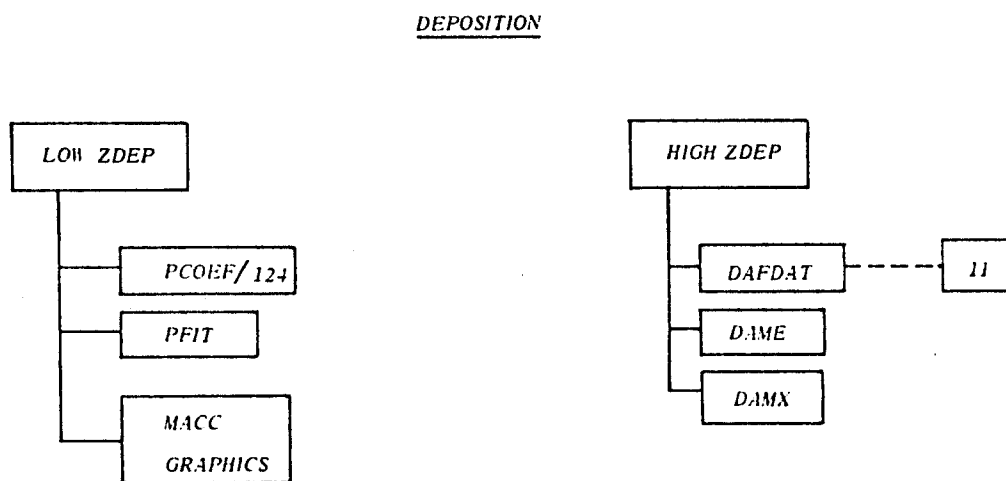
Fig. VI. 5. Block Diagram for Monergetic Ion Deposition Code

Table VI. 4.   Deposition Section of T-DAMEN Code

ABSOLUTE
    LOWZDEP--LOW Z IONS CODE, MODEL 1 (LINEAR), MODEL 2 (CUBIC),
            MODEL 4 (QUART), PLOTS CALCULATES ELECTRONIC
            STOPPING POWER, SPATIAL DEPOSITION AND LOCAL
            MEAN ENERGY FOR LIGHT IONS
    HIGHZDEP-HIGH Z IONS CORE, BASED ON DEPOSITION FUNCTIONS

READER
    READ/DEPOSITION

MAPPER
    MAP/LOWZDEP
    MAP/HIGHZDEP

LISTER
    LIST/DEPOSITION

SYMBOLICS
    PCOEF/124--GENERATES POLYNOMIAL COEFFICIENTS FOR SET
                OF INCIDENT ENERGIES
    LOWZDEP--MAIN ROUTINE CALCULATES NUCLEAR STOPPING POWER,
            AND DEPOSITION FROM SET OF COEFFICIENT
    PFIT   --A GENERAL 1-4TH ORDER POLYNOMIAL INTERPOLATION
            ROUTINE
    HIGHZDEP-MAIN ROUTINE FOR EVALUATING ENERGY DEPO-
            SITION FROM COEFFICIENTS IN FILE 11
    DAFDAT --READS DAMAGE FUNCTIONS FROM FILE 11 BY A
            NUMBER WHICH INDICATES A CERTAIN ION-TARGET
            COMBINATION
    DAME   --CALCULATES COEFFICIENTS OF DAMAGE FUNCTIONS
            A GIVEN VALUE OF ENERGY
    DAMX   --CALCULATES THE DAMAGE FUNCTION AT A POSITION
            X FOR THE COEFFICIENT FOUND IN PREVIOUS CALL
            TO DAME

RUNSTREAMS

VI.B.2.d. [I-4] Deposition Function Creation

This routine generates the deposition functions which are used to determine the volumetric deposition of energy from both nuclear and electronic processes. This routine is used in conjunction with either the Brice implantation codes or tabulated deposition profiles available in the literature.

In the former case the Brice codes are used to obtain deposition profiles of a few energies for a specific ion target combination. These data are than transformed to proper format and placed in a data file. The file is read by the DEPFUN routine and the spatial profiles fit with polynomials by a least squares technique.[111] The polynomials and their associated energies are stored in another data file for access by the routines above.

For tabulated data the procedure is identical except the data are just placed in a data element. After the deposition coefficients are created, deposition profiles may also be reproduced and plotted for comparison with the original values.

The polynomial coefficients are stored in a data file named 11 which must then be used by the deposition codes and the displacement code. This file is indexed for various ion-target combinations.

The block diagram for the position function creation routine is shown in figure VI.6. Also shown are the codes of Brice[37] which were obtained from Sandia Laboratories as part of this study. The element outline is given in table VI.5.

Fig. VI. 6. Block Diagram for Deposition Function Creation Code

Table VI. 5.   Deposition Function Creation Section of T-DAMEN Code

ABSOLUTE
    DEPFUN
    11-READER

READER
    READ/DEPFUN

MAPPER
    MAP/DEPFUN

LISTER
    LIST/DEPFUN

SYMBOLICS
    DEPFUN --MASTER ROUTINE FOR CALLING EITHER BRYOUT,
              GENOR,OR REGEN,AND PLOT
    BRYOUT --READS FILE 26 FOR DEPOSITION PROFILE FROM
              BRICE CODE,FILLS D AND Z ARRAYS IN
              KEV/MICRON,MICRON
    GENOR   --READS TABULATED DATA FROM FILES OF DEPOSITION
              DATA FILLS D AND Z ARRAYS IN KEV/MICRON,MICRON
    LSTFIT --FITS THE DATA FROM GENOR OR BRYOUT WITH A 4TH
              DEGREE POLYNOMIAL UP TO AND BEYOND PEAK FOR
              EACH ENERGY
    LSTFEL --FITS DATA FROM GENOR OR BRYOUT (ASSUMING PEAK
              AT X=0),WITH UP TO 4TH DEGREE POLYNOMIAL FOR
              EACH ENERGY
    GENCOF --GENERATES THE ENERGY COEFFICIENT MATRIX FROM
              LSTFIT DATA AND WRITES IN FILE 11
    REGEN   --PRODUCES A DEPOSITION PROFILE FROM DATA
              ON FILE 11 FOR SPECIFIED ENERGY VALUES
    DAFDAT --READS DAMAGE FUNCTIONS FROM FILE 11 BY
              A NUMBER WHICH INDICATES A CERTAIN ION-TARGET
              COMBINATION
    DAME   --CALCULATES COEFFICIENTS OF DAMAGE FUNCTIONS
              FOR A GIVEN VALUE OF ENERGY
    DAMX   --CALCULATES THE DAMAGE FUNCTION AT A POSITION
              FOR A PREVIOUS CALL TO DAME
    PLOT   --MAKES PLOTS OF EITHER:
                    BRYOUT DATA
                    GENOR DATA
                    REGEN DATA
    11-READER--READS COEFFICIENTS STORED IN FILE 11 DIRECTRY
    UNFORM/FORM--CHANGE BRICE DATA FROM UNFORMATTED TO
              FORMATTED

VI.B.3.   Supporting Routines

VI.B.3.a.   [S-1] Filing

This routine is a general data handling system based on the IODR random access file system on the Univac-1110. Data which are generated by the photon or ion code may be placed in a data file according to a prescribed format. In addition, a directory of file contents is simultaneously maintained so that the results from many executions may be identified. Any portion of the data may be subsequently addressed for superposition, printed output, or plotting.

VI.B.3.b.   [S-2] Superposition

Once data have been filed in a standard format it is possible with this routine to superimpose the results of several independent calculations; e.g., photons and ions. Selected "bins" within a data file are accessed, the results are combined, and the summation are refiled in another data bin with appropriate directory notation.

VI.B.3.c.   [S-3] Plotting

A plotting package for two-dimensional plots of selected variable from either ion or photon calculations is contained in this routine. Fifteen basic plots are available. Each may be obtained from any "bin" within the data file discussed above. The format is set up for interactive graphics terminals and allows instantaneous selection of logarithm or linear scales and choice of variable.

In the standard package the number of points for each plot is predetermined by the filing code and the data are all drawn from the

same data file. An alternate routine is available for used specified

number of points. Another routine is available for plotting of data

from several data files.

Block diagrams followed by element descriptions for each of these

sections are given in figures VI.7, .8, and .9, and tables VI.6, .7,

and .8, respectively.
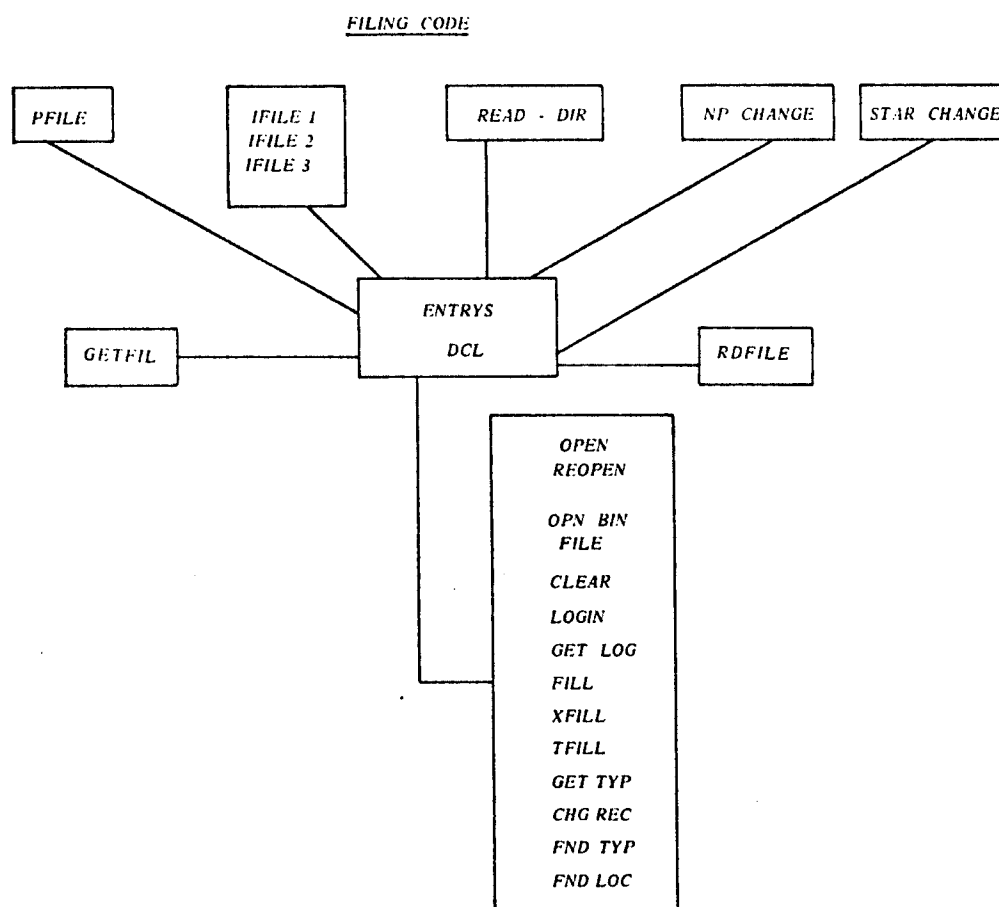
FILING CODE

Fig. VI. 7. Block Diagram for Filing Code

ADDITION CODE
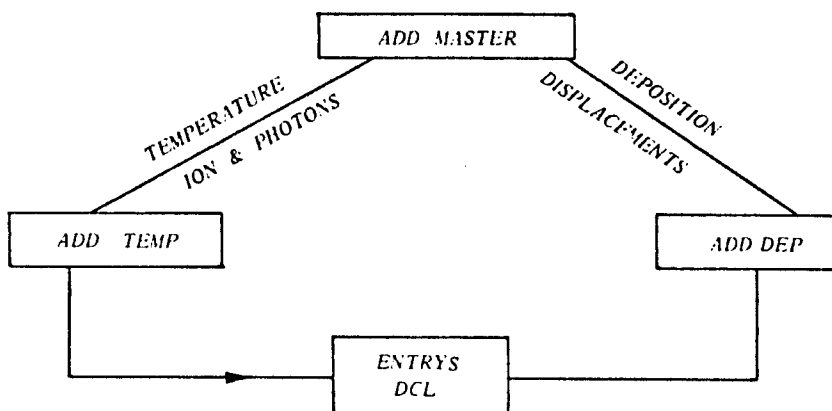
Fig. VI. 8. Block Diagram for Addition Code

PLOT CODE
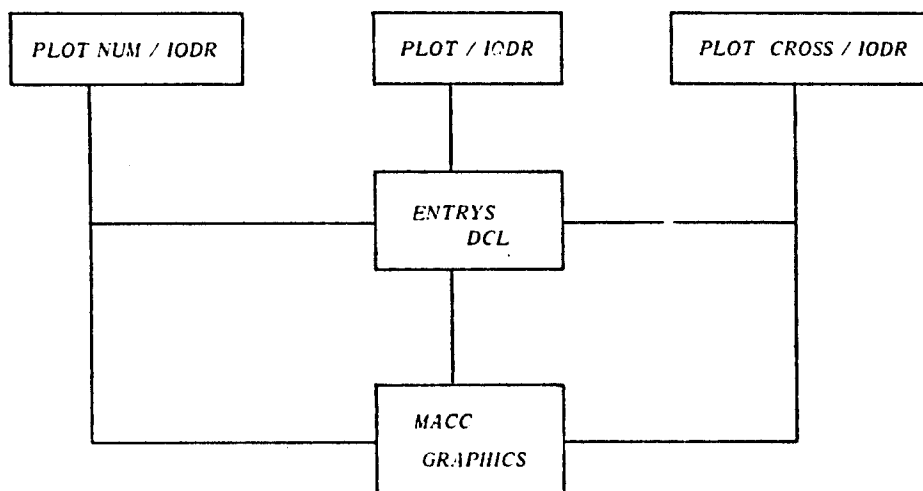
Fig. VI. 9. Block Diagram for Plotting Code

Table VI. 6.   Filing Section of T-DAMEN Code

ABSOLUTE
     READ-DIR/IODR
     RDFILE/IODR

READER
     READ/IODR

MAPPER
     MAP/RDFILE

LISTER
     LIST/IODR

SYMBOLICS
     IFILE/IODR--ROUTINE FOR FILING COMMON BLOCKS IN ION CODE
     PFILE/IODR--ROUTINE FOR FILING COMMON BLOCKS IN PHOTON
                     CODE
     ENTRYS/IODR--BASIC IODR HANDLING SUBROUTINES
     READ-DIR/IODR--WILL READ COMPLETE DIRECTORY OF ANY IODR
                     FILE
     ENTRYSNUM/IODR--SAME AS ENTRYS/IODR EXCEPT SUPPORTS
                     PLOTNUM
     DCL/IODR--STRUCTURE OF DATA BLOCKS IN IODR FILES
     NPCHANGE/IODR--WILL CHANGE # OF POINTS IN ANY FILE
     STARCHANGE/IODR--WILL CHANGE X,T ARRAYS IN A FILE
     RDFILE/IODR--READS ION DATA AND PRINTS OUT
     GETFIL/IODR--READS ION DATA INTO COMMON BLOCKS

RUNSTREAMS

Table VI. 7. Addition Section of T-DAMEN Code

ABSOLUTE
     ADDITION

READER
     READ/ADD

MAPPER
     MAP/ADDITION

LISTER
     LIST/ADDITION

SYMBOLICS
     ADDMASTER   --CALLS EITHER ADDTEMP OR ADDDEP
     ADDTEMP   --READS AN ION-3 FILE OR A PHOTON FILE AND
                    ADDS THE RESULTS TOGETHER AND FILLING
                    THE PHOTON ARRAY; FILES RESULT AS AN
                    ION-3 FILE
     ADDDEP   --READS AN ION-1 FILE OR ION-2 FILE AND ADDS
                    RESULTS TOGETHER, ALSO ADDS DISPLACEMENTS
                    FILES RESULT AS ION-2 FILE
     ENTRYS/IODR--BASIC SUBROUTINE FOR IODR HANDLING
     DCL/IODR   --BASIC FILE STRUCTURE FOR IODR DATA BLOCKS

RUNSTREAMS
     RUNADDITION

Table VI. 8. Plotting Section of T-DAMEN Code

```
ABSOLUTE
    PLOT/IODR    --PLOTTER FROM IODR FILES
    PLOTNUM/IODR--PLOTTER FROM IODR FILES SPECIFY #OF PTS
    PLOTCROSS/IODR--SELECTS DATA FROM DIFFERENT IODR FILES


READER
    READ/PLOT


MAPPER
    MAP/PLOT


LISTER
    LIST/PLOT


SYMBOLICS
    PLOT/IODR--BASIC PLOT PACKAGE FOR PLOTTING FROM ANY
               IODR FILE 1-15 POSSIBLE
    PLOTNUM/IODR--SAME AS PLOT/IODR EXCEPT # OF POINTS
                  IN EACH LINE MUST BE SPECIFIED
    PLOTCROSS/IODR--SAME AS PLOT/IODR EXCEPT DATA ARE FROM
                    DIFFERENT FILES
    ENTRYS/IODR--BASIC IODR HANDLING SUBROUTINES
    ENTRYSNUM/IODR--SAME AS ENTRYS/IODR EXCEPT SUPPORTS
                    PLOTNUM
    DCL/IODR--STRUCTURE OF DATA BLOCKS IN IODR FILES
    PLT-ID--A LISTING OF THE 15 PLOT COMBINATIONS


RUNSTREAMS
    TOTALPLOT
```

CHAPTER VII

APPLICATION TO PULSED FUSION SPECTRA

VII.A. Introductory Remarks

In this chapter the methods discussed in Chapter V, as contained
in the T-DAMEN code, discussed in Chapter VI, are applied to various
materials and representative thermonuclear spectra. The results are
presented in three forms:

a) a parametric analysis of response to X-rays and helium ions.

b) the response of unprotected carbon and molybdenum to two
specific pellet spectra and the response of copper to a general set
of spectra both unprotected and protected by a neon layer.

c) the effect of temperature transients induced by spectra in
b) on the subsequent effects of sputtering, evaporation, and
blistering.

These examples were selected because they demonstrated the general
utility of the methods developed in this research. These results also
show the response associated with irradiation of selected materials
with spectra from current conceptual designs for laser fusion reactor
and they indicate the effectiveness of gas protection in mitigating the
consequences of the energy depositions. Finally these data show the
synergism between related effects and indicate the extent of the
complexity of material response in pulsed fusion environments.

VII.B. Parametric Analysis

One of the principal current uncertainties in the design of

inertial confinement reactor cavities is in the pellet output spectra.
As was demonstrated in Chapter I and IV the response of a first wall
or other exposed material can be extremely sensitive to variations in
either photon or ion spectra. This section provides results of an
analysis using the T-DAMEN code which demonstrates the effect of
various cavity design parameters on the temperature response of
several exposed materials. The results are in a general form such that
the response to a specific spectrum can be inferred from the data
presented.

VII.B.1. X-ray Response

A general study was performed to examine the response of three
materials to variations in X-ray spectra, in type or amount of gas
protection, and in X-ray radiation source duration. The results are
presented in terms of general tables covering all the parametric
variations and in the form of selected curves demonstrating specific
effects. The parameters chosen are present in table VII.1.

All calculations were performed for temperature response at 2.82
meters from 1 MJ of X-ray output. This corresponds to a wall loading
(in the absence of gas) of 1 J/cm^2. The areal density of gas protec-
tion is thus normalized to 2.82 times the gas pressure in torr-meters.
The results are generalized in that the same response will be exhibited
at a given areal density (torr-meters) for an equivalent bare wall
loading. All results are to be interpreted as ΔT per J/cm^2 since the
entire problem is linear with respect to flux. (Caution the problem
is, of course, not linear with respect to areal density of protective

gas.)

Data are presented in tables VII.2 to VII.10. Each table represents the combination of one gas and material. Within each table are the variations of gas pressure, source time, and black body temperature.

TABLE VII.1

X-RAY ANALYSIS PARAMETERS

<u>Source</u>

Spectrum - (Black Body Temperature)

0.1   0.2   0.3   0.4   0.5   0.75   1   2   5   10

Duration (Seconds)

Impulse 10^{-11} 10^{-10} 10^{-9} 10^{-8} 10^{-7}

<u>Gas</u>

Type

He,   Ne,   Xe

Pressure (at 273°K)

0.   0.1   0.5   1   5   10

<u>Material</u>

C,   Cu,   Mo

Selected data from these tables are given in figures VII.1, .2, .3, and .4. The effect of gas type on the response of copper at 2.8 torr-meters is shown in figure VII.1 as a function of X-ray spectrum for a source duration of 1 nanosecond. The significant variation with the atomic number of the gas indicates that much greater pressure

Table VII. 2.   Normalized Thermal Response from X-Rays in Carbon with Helium Gas Protection

Surface Temperature Rise
[°C per J/cm²]
(Gas at 273 °K)

log Δt (sec)	BLACKBODY TEMPERATURE (KEV)									
	.1	.2	.3	.4	.5	.75	1.	2.	5.	10.
TORR=0.										
ADB	.838+4	.456+4	.230+4	.144+4	.890+3	.378+3	.198+3	.407+2	.312+1	.459+C
-11	.795+4	.440+4	.224+4	.140+4	.873+3	.372+3	.195+3	.400+2	.311+1	.459+0
-10	.723+4	.411+4	.213+4	.134+4	.840+3	.361+3	.19C+3	.388+2	.310+1	.459+0
-9	.574+4	.344+4	.187+4	.118+4	.759+3	.332+3	.177+3	.360+2	.306+1	.458+C
-8	.363+4	.239+4	.140+4	.915+3	.610+3	.278+3	.152+3	.314+2	.294+1	.455+0
-7	.178+4	.133+4	.872+3	.600+3	.423+3	.207+3	.117+3	.257+2	.266+1	.447+0
TORR=.1										
ADB	.757+4	.439+4	.225+4	.142+4	.881+3	.376+3	.197+3	.405+2	.312+1	.459+3
-11	.722+4	.425+4	.220+4	.138+4	.864+3	.370+3	.194+3	.399+2	.311+1	.459+C
-10	.661+4	.398+4	.209+4	.132+4	.832+3	.359+3	.189+3	.386+2	.310+1	.459+0
-9	.532+4	.336+4	.184+4	.117+4	.753+3	.331+3	.176+3	.350+2	.305+1	.458+0
-8	.340+4	.234+4	.139+4	.907+3	.606+3	.277+3	.151+3	.313+2	.294+1	.455+C
-7	.168+4	.131+4	.864+3	.597+3	.421+3	.206+3	.117+3	.257+2	.266+1	.447+0
TORR=.5										
ADB	.674+4	.417+4	.217+4	.137+4	.860+3	.369+3	.194+3	.399+2	.312+1	.459+3
-11	.643+4	.404+4	.212+4	.134+4	.844+3	.364+3	.192+3	.393+2	.311+1	.459+C
-10	.589+4	.379+4	.202+4	.128+4	.814+3	.353+3	.187+3	.381+2	.309+1	.459+0
-9	.474+4	.320+4	.178+4	.114+4	.737+3	.326+3	.174+3	.355+2	.305+1	.458+0
-8	.303+4	.225+4	.135+4	.887+3	.596+3	.274+3	.150+3	.311+2	.293+1	.455+0
-7	.150+4	.126+4	.845+3	.587+3	.415+3	.204+3	.116+3	.256+2	.266+1	.447+C
TORR=1.										
ADB	.624+4	.398+4	.211+4	.134+4	.840+3	.362+3	.191+3	.392+2	.311+1	.459+0
-11	.594+4	.386+4	.206+4	.131+4	.825+3	.357+3	.189+3	.386+2	.310+1	.459+0
-10	.544+4	.362+4	.196+4	.125+4	.796+3	.347+3	.184+3	.376+2	.309+1	.459+0
-9	.437+4	.307+4	.173+4	.111+4	.723+3	.321+3	.172+3	.351+2	.305+1	.458+C
-8	.279+4	.216+4	.132+4	.869+3	.586+3	.270+3	.148+3	.308+2	.293+1	.455+C
-7	.137+4	.121+4	.828+3	.578+3	.410+3	.203+3	.115+3	.255+2	.267+1	.447+C
TORR=5.										
ADB	.418+4	.302+4	.174+4	.112+4	.731+3	.325+3	.174+3	.351+2	.308+1	.459+C
-11	.397+4	.294+4	.171+4	.110+4	.720+3	.320+3	.172+3	.347+2	.307+1	.458+C
-10	.364+4	.278+4	.164+4	.106+4	.698+3	.313+3	.166+3	.341+2	.305+1	.458+0
-9	.294+4	.240+4	.147+4	.957+3	.642+3	.292+3	.159+3	.324+2	.301+1	.457+0
-8	.189+4	.175+4	.114+4	.770+3	.532+3	.251+3	.139+3	.292+2	.290+1	.454+0
-7	.924+3	.101+4	.739+3	.528+3	.382+3	.192+3	.111+3	.247+2	.265+1	.446+0
TORR=10.										
ADB	.285+4	.232+4	.145+4	.947+3	.639+3	.292+3	.159+3	.322+2	.303+1	.458+C
-11	.270+4	.227+4	.142+4	.932+3	.631+3	.289+3	.157+3	.319+2	.302+1	.458+C
-10	.248+4	.217+4	.137+4	.904+3	.614+3	.283+3	.154+3	.315+2	.301+1	.457+0
-9	.203+4	.191+4	.125+4	.832+3	.572+3	.267+3	.147+3	.303+2	.297+1	.457+0
-8	.134+4	.143+4	.998+3	.667+3	.484+3	.234+3	.131+3	.279+2	.289+1	.454+0
-7	.672+3	.864+3	.665+3	.485+3	.357+3	.183+3	.106+3	.240+2	.262+1	.446+0

Table VII. 3. Normalized Thermal Response from X-Rays in Carbon with Neon Gas Protection

Surface Temperature Rise
[°C per J/cm^2]
(Gas at 273 °K)

log Δt (sec)	BLACKBODY TEMPERATURE (KEV)									
	.1	.2	.3	.4	.5	.75	1.	2.	5.	10.
TORR=0.										
ADB	.838+4	.456+4	.230+4	.144+4	.890+3	.378+3	.198+3	.407+2	.312+1	.459+0
-11	.795+4	.440+4	.224+4	.140+4	.873+3	.372+3	.195+3	.400+2	.311+1	.459+0
-10	.723+4	.411+4	.213+4	.134+4	.840+3	.361+3	.190+3	.388+2	.310+1	.459+0
-9	.574+4	.344+4	.187+4	.118+4	.759+3	.332+3	.177+3	.360+2	.306+1	.458+0
-8	.363+4	.239+4	.140+4	.915+3	.610+3	.278+3	.152+3	.314+2	.294+1	.455+0
-7	.178+4	.133+4	.872+3	.600+3	.423+3	.207+3	.117+3	.257+2	.268+1	.447+0
TORR=.1										
ADB	.524+4	.349+4	.186+4	.118+4	.750+3	.326+3	.173+3	.350+2	.299+1	.447+0
-11	.501+4	.338+4	.182+4	.115+4	.737+3	.321+3	.170+3	.345+2	.298+1	.447+0
-10	.461+4	.318+4	.174+4	.111+4	.711+3	.312+3	.166+3	.336+2	.297+1	.447+0
-9	.373+4	.270+4	.154+4	.986+3	.647+3	.289+3	.156+3	.315+2	.292+1	.446+0
-8	.239+4	.191+4	.117+4	.773+3	.525+3	.244+3	.134+3	.270+2	.281+1	.443+0
-7	.117+4	.108+4	.733+3	.513+3	.367+3	.183+3	.105+3	.233+2	.257+1	.436+0
TORR=.5										
ADB	.211+4	.175+4	.104+4	.666+3	.451+3	.205+3	.113+3	.228+2	.256+1	.408+0
-11	.202+4	.171+4	.102+4	.655+3	.445+3	.203+3	.112+3	.226+2	.256+1	.408+0
-10	.187+4	.163+4	.980+3	.634+3	.432+3	.199+3	.110+3	.223+2	.255+1	.408+0
-9	.155+4	.144+4	.884+3	.579+3	.400+3	.187+3	.104+3	.214+2	.251+1	.407+0
-8	.104+4	.107+4	.694+3	.469+3	.333+3	.162+3	.923+2	.197+2	.242+1	.405+0
-7	.527+3	.629+3	.444+3	.319+3	.238+3	.124+3	.741+2	.172+2	.223+1	.400+0
TORR=1.										
ADB	.938+3	.954+3	.604+3	.400+3	.282+3	.135+3	.769+2	.165+2	.220+1	.373+0
-11	.890+3	.937+3	.595+3	.394+3	.279+3	.133+3	.764+2	.164+2	.220+1	.373+0
-10	.828+3	.904+3	.578+3	.384+3	.273+3	.131+3	.753+2	.162+2	.219+1	.373+0
-9	.707+3	.818+3	.531+3	.357+3	.256+3	.125+3	.722+2	.159+2	.216+1	.373+0
-8	.502+3	.638+3	.430+3	.297+3	.218+3	.110+3	.653+2	.149+2	.209+1	.371+0
-7	.271+3	.391+3	.281+3	.206+3	.159+3	.867+2	.537+2	.134+2	.194+1	.362+0
TORR=5.										
ADB	.102+3	.904+2	.656+2	.494+2	.410+2	.248+2	.176+2	.596+1	.119+1	.262+0
-11	.749+2	.896+2	.651+2	.490+2	.408+2	.247+2	.175+2	.595+1	.119+1	.262+0
-10	.553+2	.881+2	.640+2	.483+2	.403+2	.245+2	.174+2	.595+1	.119+1	.262+0
-9	.411+2	.836+2	.610+2	.463+2	.388+2	.239+2	.171+2	.592+1	.118+1	.262+0
-8	.307+2	.720+2	.530+2	.409+2	.350+2	.224+2	.163+2	.584+1	.117+1	.262+0
-7	.196+2	.499+2	.376+2	.304+2	.273+2	.192+2	.147+2	.569+1	.114+1	.261+0
TORR=10.										
ADB	.699+2	.153+2	.113+2	.958+1	.950+1	.781+1	.698+1	.367+1	.871+1	.242+0
-11	.432+2	.152+2	.112+2	.953+1	.946+1	.779+1	.697+1	.367+1	.871+0	.248+0
-10	.243+2	.150+2	.110+2	.941+1	.937+1	.775+1	.695+1	.367+1	.871+1	.247+0
-9	.120+2	.144+2	.106+2	.909+1	.912+1	.764+1	.690+1	.366+1	.870+0	.247+0
-8	.639+1	.127+2	.939+1	.821+1	.841+1	.734+1	.674+1	.365+1	.867+0	.247+0
-7	.355+1	.914+1	.687+1	.636+1	.689+1	.669+1	.641+1	.363+1	.861+0	.247+0

Table VII. 4. Normalized Thermal Response from X-Rays in Carbon with Xenon Gas Protection
Surface Temperature Rise
[°C per J/cm^2]
(Gas at 273 °K)

log Δt (sec)	BLACKBODY TEMPERATURE (KEV)									
	.1	.2	.3	.4	.5	.75	1.	2.	5.	10.
TORR=0.										
ADB	.838+4	.456+4	.230+4	.144+4	.890+3	.378+3	.198+3	.407+2	.312+1	.459+?
-11	.795+4	.440+4	.224+4	.140+4	.873+3	.372+3	.195+3	.400+2	.311+1	.459+0
-10	.723+4	.411+4	.213+4	.134+4	.840+3	.361+3	.190+3	.388+2	.310+1	.459+0
-9	.574+4	.344+4	.187+4	.118+4	.759+3	.332+3	.177+3	.360+2	.306+1	.458+0
-8	.363+4	.239+4	.140+4	.915+3	.610+3	.278+3	.152+3	.314+2	.294+1	.455+0
-7	.178+4	.133+4	.872+3	.600+3	.423+3	.207+3	.117+3	.257+2	.268+1	.447+0
TORR=.1										
ADB	.304+4	.171+4	.820+3	.502+3	.314+3	.137+3	.777+2	.178+2	.168+1	.364+0
-11	.291+4	.165+4	.797+3	.488+3	.307+3	.134+3	.767+2	.175+2	.168+1	.364+0
-10	.266+4	.153+4	.752+3	.461+3	.294+3	.130+3	.746+2	.173+2	.166+1	.363+0
-9	.213+4	.127+4	.645+3	.398+3	.261+3	.119+3	.693+2	.168+2	.167+1	.363+0
-8	.134+4	.843+3	.462+3	.293+3	.203+3	.982+2	.596+2	.143+2	.166+1	.362+0
-7	.650+3	.435+3	.266+3	.181+3	.137+3	.744+2	.476+2	.126+2	.162+1	.358+0
TORR=.5										
ADB	.112+3	.694+2	.355+2	.240+2	.189+2	.137+2	.111+2	.456+1	.859+0	.240+0
-11	.108+3	.671+2	.346+2	.235+2	.186+2	.136+2	.111+2	.455+1	.859+0	.240+0
-10	.994+2	.627+2	.328+2	.224+2	.180+2	.135+2	.110+2	.453+1	.859+0	.240+0
-9	.802+2	.524+2	.284+2	.198+2	.167+2	.130+2	.108+2	.449+1	.858+0	.240+0
-8	.510+2	.353+2	.206+2	.154+2	.141+2	.121+2	.103+2	.442+1	.857+0	.240+0
-7	.245+2	.180+2	.120+2	.106+2	.111+2	.110+2	.971+1	.433+1	.853+0	239+0
TORR=1.										
ADB	.205+1	.144+1	.106+1	.153+1	.232+1	.361+1	.378+1	.215+1	.551+0	.188+0
-11	.198+1	.140+1	.105+1	.152+1	.232+1	.360+1	.376+1	.215+1	.551+0	.188+0
-10	.184+1	.132+1	.101+1	.150+1	.231+1	.360+1	.377+1	.215+1	.551+0	.188+0
-9	.151+1	.113+1	.922+0	.144+1	.227+1	.358+1	.377+1	.215+1	.551+0	.188+0
-8	.990+0	.792+0	.754+0	.135+1	.221+1	.356+1	.375+1	.215+1	.550+0	.188+0
-7	.487+0	.420+0	.551+0	.122+1	.212+1	.350+1	.371+1	.213+1	.549+0	.188+0
TORR=5.										
ADB	.285-12	.946-11	.217-4	.242-2	.173-1	.539-1	.758-1	.108+0	.132+0	.986-1
-11	.281-12	.945-11	.217-4	.242-2	.173-1	.539-1	.758-1	.108+0	.132+0	.986-1
-10	.273-12	.943-11	.217-4	.242-2	.173-1	.539-1	.757-1	.108+0	.132+0	.986-1
-9	.251-12	.937-11	.216-4	.242-2	.173-1	.539-1	.757-1	.108+0	.132+0	.986-1
-8	.198-12	.920-11	.216-4	.242-2	.173-1	.538-1	.756-1	.108+0	.132+0	.986-1
-7	.118-12	.880-11	.213-4	.240-2	.172-1	.536-1	.754-1	.107+0	.132+0	.986-1
TORR=10.										
ADB	.274-27	.186-21	.114-8	.123-4	.452-3	.156-2	.246-2	.185-1	.712-1	.736-1
-11	.271-27	.186-21	.113-8	.123-4	.452-3	.156-2	.246-2	.165-1	.712-1	.736-1
-10	.264-27	.185-21	.113-8	.123-4	.452-3	.156-2	.246-2	.185-1	.712-1	.736-1
-9	.246-27	.185-21	.113-8	.123-4	.452-3	.155-2	.246-2	.185-1	.712-1	.736-1
-8	.201-27	.183-21	.113-8	.123-4	.451-3	.155-2	.246-2	.165-1	.712-1	.736-1
-7	.125-27	.177-21	.112-8	.122-4	.450-3	.155-2	.245-2	.185-1	.712-1	.736-1

Table VII. 5. Normalized Thermal Response from X-Rays in Copper with Helium Gas Protection

Surface Temperature Rise
[°C per J/cm^2]
(Gas at 273 °K)

log Δt (sec)	BLACKBODY TEMPERATURE (KEV)									
	.1	.2	.3	.4	.5	.75	1.	2.	5.	10.
TORR=0.										
ADB	.248+5	.139+5	.116+5	.905+4	.741+4	.426+4	.285+4	.800+3	.193+3	.553+2
-11	.183+5	.115+5	.997+4	.798+4	.660+4	.389+4	.261+4	.764+3	.190+3	.549+2
-10	.122+5	.868+4	.778+4	.644+4	.541+4	.332+4	.225+4	.705+3	.185+3	.541+2
-9	.616+4	.507+4	.474+4	.413+4	.357+4	.236+4	.165+4	.593+3	.173+3	.523+2
-8	.247+4	.226+4	.219+4	.202+4	.183+4	.135+4	.100+4	.443+3	.154+3	.488+2
-7	.859+3	.832+3	.821+3	.790+3	.749+3	.622+3	.507+3	.291+3	.125+3	.427+2
TORR=.1										
ADB	.216+5	.133+5	.114+5	.897+4	.736+4	.425+4	.285+4	.799+3	.193+3	.553+2
-11	.165+5	.112+5	.985+4	.793+4	.657+4	.368+4	.261+4	.764+3	.190+3	.549+2
-10	.112+5	.849+4	.772+4	.641+4	.540+4	.332+4	.225+4	.703+3	.185+3	.541+2
-9	.577+4	.499+4	.471+4	.411+4	.357+4	.236+4	.165+4	.593+3	.173+3	.523+2
-8	.233+4	.223+4	.218+4	.201+4	.182+4	.134+4	.100+4	.443+3	.154+3	.468+2
-7	.815+3	.823+3	.818+3	.789+3	.748+3	.621+3	.507+3	.291+3	.125+3	.467+2
TORR=.5										
ADB	.169+5	.123+5	.110+5	.880+4	.727+4	.422+4	.283+4	.798+3	.193+3	.553+2
-11	.134+5	.105+5	.959+4	.781+4	.650+4	.386+4	.260+4	.767+3	.190+3	.549+2
-10	.940+4	.807+4	.756+4	.653+4	.535+4	.330+4	.224+4	.705+3	.185+3	.541+2
-9	.500+4	.479+4	.463+4	.407+4	.355+4	.235+4	.165+4	.593+3	.173+3	.523+2
-8	.206+4	.216+4	.215+4	.200+4	.181+4	.134+4	.100+4	.443+3	.154+3	.468+2
-7	.724+3	.799+3	.808+3	.784+3	.745+3	.620+3	.506+3	.290+3	.125+3	.427+2
TORR=1.										
ADB	.141+5	.116+5	.107+5	.866+4	.719+4	.419+4	.282+4	.797+3	.193+3	.553+2
-11	.114+5	.996+4	.938+4	.770+4	.645+4	.384+4	.259+4	.762+3	.190+3	.549+2
-10	.816+4	.772+4	.742+4	.626+4	.531+4	.329+4	.223+4	.704+3	.185+3	.541+2
-9	.444+4	.463+4	.457+4	.404+4	.353+4	.235+4	.164+4	.592+3	.173+3	.523+2
-8	.185+4	.210+4	.212+4	.198+4	.181+4	.134+4	.100+4	.443+3	.154+3	.488+2
-7	.655+3	.777+3	.799+3	.779+3	.743+3	.619+3	.506+3	.290+3	.125+3	.427+2
TORR=5.										
ADB	.695+4	.925+4	.973+4	.814+4	.688+4	.408+4	.277+4	.790+3	.193+3	.553+2
-11	.588+4	.810+4	.856+4	.728+4	.619+4	.375+4	.254+4	.756+3	.190+3	.548+2
-10	.451+4	.641+4	.683+4	.595+4	.512+4	.322+4	.220+4	.699+3	.184+3	.541+2
-9	.266+4	.394+4	.425+4	.387+4	.342+4	.231+4	.162+4	.589+3	.173+3	.522+2
-8	.117+4	.182+4	.199+4	.191+4	.176+4	.132+4	.991+3	.442+3	.154+3	.488+2
-7	.425+3	.679+3	.751+3	.752+3	.726+3	.613+3	.503+3	.290+3	.125+3	.427+2
TORR=10.										
ADB	.440+4	.804+4	.912+4	.780+4	.667+4	.400+4	.272+4	.784+3	.193+3	.552+2
-11	.378+4	.707+4	.803+4	.698+4	.600+4	.368+4	.251+4	.751+3	.190+3	.548+2
-10	.299+4	.564+4	.642+4	.572+4	.498+4	.316+4	.217+4	.695+3	.184+3	.540+2
-9	.184+4	.349+4	.401+4	.373+4	.333+4	.227+4	.161+4	.587+3	.173+3	.522+2
-8	.839+3	.163+4	.188+4	.185+4	.172+4	.131+4	.983+3	.440+3	.154+3	.468+2
-7	.309+3	.610+3	.713+3	.730+3	.712+3	.607+3	.499+3	.289+3	.125+3	.427+2

Table VII. 6. Normalized Thermal Response from X-Rays in
Copper with Neon Gas Protection

Surface Temperature Rise
[°C per J/cm²]
(Gas at 273 °K)

log Δt (sec)	BLACKBODY TEMPERATURE (KEV)									
	.1	.2	.3	.4	.5	.75	1.	2.	5.	10.
TORR=0.										
ADB	.248+5	.139+5	.116+5	.905+4	.741+4	.426+4	.285+4	.800+3	.193+3	.553+2
-11	.183+5	.115+5	.997+4	.798+4	.660+4	.389+4	.261+4	.764+3	.190+3	.549+2
-10	.122+5	.868+4	.778+4	.644+4	.541+4	.332+4	.225+4	.705+3	.185+3	.541+2
-9	.616+4	.507+4	.474+4	.413+4	.357+4	.236+4	.165+4	.593+3	.173+3	.523+2
-8	.247+4	.226+4	.219+4	.202+4	.183+4	.135+4	.100+4	.443+3	.154+3	.488+2
-7	.859+3	.832+3	.821+3	.790+3	.749+3	.622+3	.507+3	.291+3	.125+3	.427+2
TORR=.1										
ADB	.113+5	.974+4	.911+4	.751+4	.631+4	.378+4	.255+4	.756+3	.190+3	.549+2
-11	.921+4	.843+4	.800+4	.671+4	.568+4	.348+4	.236+4	.725+3	.187+3	.545+2
-10	.671+4	.659+4	.638+4	.549+4	.472+4	.299+4	.205+4	.673+3	.182+3	.538+2
-9	.371+4	.401+4	.397+4	.358+4	.317+4	.217+4	.153+4	.571+3	.171+3	.520+2
-8	.157+4	.184+4	.187+4	.178+4	.165+4	.125+4	.947+3	.432+3	.153+3	.487+2
-7	.558+3	.682+3	.706+3	.703+3	.683+3	.586+3	.485+3	.286+3	.125+3	.426+2
TORR=.5										
ADB	.329+4	.453+4	.475+4	.435+4	.387+4	.259+4	.181+4	.633+3	.180+3	.537+2
-11	.258+4	.405+4	.428+4	.396+4	.356+4	.243+4	.171+4	.613+3	.176+3	.534+2
-10	.230+4	.333+4	.353+4	.334+4	.305+4	.215+4	.153+4	.579+3	.175+3	.529+2
-9	.143+4	.216+4	.232+4	.229+4	.215+4	.163+4	.120+4	.507+3	.166+3	.513+2
-8	.657+3	.104+4	.114+4	.119+4	.118+4	.990+3	.787+3	.397+3	.150+3	.483+2
-7	.243+3	.398+3	.443+3	.465+3	.508+3	.483+3	.421+3	.270+3	.123+3	.424+2
TORR=1.										
ADB	.144+4	.235+4	.259+4	.258+4	.244+4	.182+4	.134+4	.542+3	.172+3	.526+2
-11	.126+4	.215+4	.238+4	.239+4	.228+4	.173+4	.128+4	.529+3	.171+3	.523+2
-10	.107+4	.183+4	.202+4	.207+4	.200+4	.156+4	.117+4	.506+3	.165+3	.519+2
-9	.705+3	.125+4	.140+4	.149+4	.149+4	.123+4	.963+3	.454+3	.161+3	.506+2
-8	.343+3	.633+3	.722+3	.810+3	.856+3	.790+3	.661+3	.365+3	.147+3	.479+2
-7	.130+3	.247+3	.287+3	.341+3	.382+3	.401+3	.368+3	.257+3	.122+3	.422+2
TORR=5.										
ADB	.124+3	.199+3	.228+3	.310+3	.392+3	.468+3	.446+3	.325+3	.150+3	.492+2
-11	.890+2	.190+3	.218+3	.298+3	.380+3	.458+3	.441+3	.322+3	.149+3	.491+2
-10	.709+2	.173+3	.199+3	.277+3	.357+3	.438+3	.426+3	.317+3	.146+3	.468+2
-9	.506+2	.134+3	.157+3	.228+3	.303+3	.388+3	.387+3	.502+3	.144+3	.460+2
-8	.278+2	.770+2	.934+2	.147+3	.205+3	.293+3	.308+3	.266+3	.135+3	.460+2
-7	.114+2	.323+2	.407+2	.708+2	.109+3	.175+3	.199+3	.203+3	.115+3	.410+2
TORR=10.										
ADB	.610+2	.340+2	.394+2	.740+2	.121+3	.205+3	.236+3	.251+3	.139+3	.475+2
-11	.290+2	.326+2	.380+2	.721+2	.118+3	.202+3	.233+3	.249+3	.139+3	.474+2
-10	.168+2	.300+2	.353+2	.664+2	.114+3	.196+3	.228+3	.246+3	.138+3	.472+2
-9	.975+1	.239+2	.288+2	.590+2	.101+3	.181+3	.214+3	.238+3	.135+3	.465+2
-8	.502+1	.142+2	.181+2	.415+2	.759+2	.147+3	.182+3	.216+3	.128+3	.447+2
-7	.204+1	.611+1	.821+1	.219+2	.437+2	.962+2	.127+3	.171+3	.110+3	.401+2

Table VII. 7. Normalized Thermal Response from X-Rays in Copper with Xenon Gas Protection

Surface Temperature Rise
[°C per J/cm²]
(Gas at 273 °K)

log Δt (sec)	BLACKBODY TEMPERATURE (KEV)									
	.1	.2	.3	.4	.5	.75	1.	2.	5.	10.
TORR=0.										
ADB	.248+5	.139+5	.116+5	.905+4	.741+4	.426+4	.285+4	.800+3	.193+3	.553+2
-11	.183+5	.115+5	.997+4	.798+4	.660+4	.389+4	.261+4	.764+3	.190+3	.549+2
-10	.122+5	.868+4	.778+4	.644+4	.541+4	.332+4	.225+4	.705+3	.185+3	.541+2
-9	.616+4	.507+4	.474+4	.413+4	.357+4	.236+4	.165+4	.593+3	.175+3	.523+2
-8	.247+4	.226+4	.219+4	.202+4	.183+4	.135+4	.100+4	.443+3	.154+3	.468+2
-7	.859+3	.832+3	.821+3	.790+3	.749+3	.622+3	.507+3	.291+3	.125+3	.427+2
TORR=.1										
ADB	.737+4	.401+4	.331+4	.291+4	.261+4	.186+4	.135+4	.529+3	.167+3	.515+2
-11	.583+4	.340+4	.291+4	.262+4	.240+4	.174+4	.128+4	.515+3	.165+3	.513+2
-10	.410+4	.261+4	.234+4	.219+4	.206+4	.156+4	.116+4	.490+3	.163+3	.508+2
-9	.217+4	.154+4	.148+4	.149+4	.147+4	.120+4	.938+3	.437+3	.156+3	.496+2
-8	.883+3	.678+3	.708+3	.776+3	.820+3	.759+3	.635+3	.352+3	.142+3	.496+2
-7	.308+3	.246+3	.270+3	.319+3	.362+3	.383+3	.351+3	.244+3	.116+3	.414+2
TORR=.5										
ADB	.209+3	.125+3	.146+3	.224+3	.300+3	.378+3	.360+3	.250+3	.130+3	.446+2
-11	.174+3	.110+3	.135+3	.214+3	.290+3	.369+3	.354+3	.256+3	.129+3	.445+2
-10	.130+3	.885+2	.118+3	.196+3	.272+3	.353+3	.341+3	.252+3	.128+3	.443+2
-9	.738+2	.553+2	.867+2	.158+3	.229+3	.312+3	.309+3	.239+3	.125+3	.436+2
-8	.314+2	.255+2	.490+2	.102+3	.159+3	.236+3	.245+3	.210+3	.117+3	.418+2
-7	.111+2	.941+1	.210+2	.500+2	.844+2	.140+3	.156+3	.158+3	.100+3	.375+2
TORR=1.										
ADB	.339+1	.269+1	.125+2	.411+2	.773+2	.136+3	.152+3	.161+3	.107+3	.398+2
-11	.293+1	.243+1	.121+2	.401+2	.759+2	.135+3	.150+3	.159+3	.107+3	.397+2
-10	.228+1	.202+1	.112+2	.363+2	.732+2	.131+3	.146+3	.157+3	.106+3	.395+2
-9	.137+1	.133+1	.930+1	.336+2	.658+2	.121+3	.137+3	.152+3	.104+3	.390+2
-8	.605+0	.644+0	.609+1	.246+2	.506+2	.980+2	.115+3	.137+3	.988+2	.376+2
-7	.218+0	.243+0	.292+1	.135+2	.300+2	.631+2	.780+2	.107+3	.855+2	.341+2
TORR=5.										
ADB	.510-12	.292-09	.794-3	.963-1	.723+0	.227+1	.375+1	.265+2	.467+2	.232+2
-11	.478-12	.279-09	.780-3	.953-1	.716+0	.225+1	.372+1	.264+2	.466+2	.232+2
-10	.419-12	.255-09	.753-3	.935-1	.708+0	.222+1	.368+1	.262+2	.464+2	.232+2
-9	.299-12	.198-09	.676-3	.881-1	.679+0	.214+1	.355+1	.257+2	.459+2	.230+2
-8	.153-12	.114-09	.507-3	.742-1	.598+0	.190+1	.319+1	.241+2	.443+2	.225+2
-7	.593-13	.474-10	.277-3	.490-1	.434+0	.140+1	.240+1	.203+2	.402+2	.211+2
TORR=10.										
ADB	.513-27	.599-20	.419-7	.499-3	.194-1	.667-1	.163+0	.768+1	.252+2	.155+2
-11	.484-27	.574-20	.412-7	.495-3	.193-1	.663-1	.162+0	.706+1	.252+2	.155+2
-10	.430-27	.525-20	.399-7	.487-3	.190-1	.656-1	.161+0	.762+1	.251+2	.154+2
-9	.314-27	.410-20	.361-7	.462-3	.184-1	.634-1	.156+0	.750+1	.249+2	.154+2
-8	.166-27	.237-20	.275-7	.398-3	.166-1	.572-1	.141+0	.715+1	.243+2	.151+2
-7	.651-28	.993-21	.153-7	.272-3	.126-1	.434-1	.109+0	.624+1	.227+2	.145+2

Table VII. 8. Normalized Thermal Response from X-Rays in
Molybdenum with Helium Gas Protection
Surface Temperature Rise
[°C per J/cm^2]
(Gas at 273 °K)

log Δt (sec)	BLACKBODY TEMPERATURE (KEV)									
	.1	.2	.3	.4	.5	.75	1.	2.	5.	10.
TORR=0.										
ADB	.350+5	.262+5	.170+5	.118+5	.880+4	.537+4	.379+4	.137+4	.271+3	.842+2
-11	.290+5	.224+5	.149+5	.106+5	.802+4	.503+4	.361+4	.133+4	.266+3	.839+2
-10	.211+5	.171+5	.119+5	.873+4	.683+4	.450+4	.332+4	.127+4	.262+3	.834+2
-9	.113+5	.990+4	.754+4	.593+4	.492+4	.355+4	.275+4	.113+4	.248+3	.817+2
-8	.468+4	.438+4	.372+4	.321+4	.287+4	.233+4	.192+4	.881+3	.216+3	.779+2
-7	.165+4	.161+4	.149+4	.139+4	.132+4	.119+4	.105+4	.567+3	.173+3	.702+2
TORR=.1										
ADB	.338+5	.259+5	.169+5	.117+5	.877+4	.536+4	.379+4	.137+4	.271+3	.842+2
-11	.279+5	.221+5	.149+5	.105+5	.799+4	.503+4	.361+4	.133+4	.260+3	.839+2
-10	.203+5	.169+5	.119+5	.870+4	.651+4	.450+4	.332+4	.127+4	.262+3	.834+2
-9	.109+5	.979+4	.750+4	.591+4	.491+4	.355+4	.275+4	.113+4	.248+3	.817+2
-8	.446+4	.433+4	.370+4	.320+4	.286+4	.232+4	.192+4	.881+3	.216+3	.779+2
-7	.157+4	.159+4	.149+4	.139+4	.132+4	.11?+4	.105+4	.567+3	.173+3	.702+2
TORR=.5										
ADB	.316+5	.252+5	.166+5	.116+5	.869+4	.???+4	.377+4	.136+4	.271+3	.842+2
-11	.260+5	.215+5	.146+5	.104+5	.792+4	.???+4	.360+4	.137+4	.266+3	.839+2
-10	.188+5	.164+5	.117+5	.860+4	.676+4	.448+4	.331+4	.126+4	.262+3	.834+2
-9	.995+4	.952+4	.739+4	.585+4	.487+4	.354+4	.275+4	.113+4	.246+3	.817+2
-8	.403+4	.421+4	.365+4	.317+4	.285+4	.232+4	.192+4	.880+3	.216+3	.778+2
-7	.141+4	.155+4	.147+4	.138+4	.132+4	.118+4	.105+4	.567+3	.173+3	.702+2
TORR=1.										
ADB	.297+5	.245+5	.163+5	.114+5	.859+4	.529+4	.376+4	.136+4	.271+3	.842+2
-11	.244+5	.209+5	.143+5	.102+5	.784+4	.497+4	.358+4	.133+4	.266+3	.839+2
-10	.176+5	.160+5	.115+5	.849+4	.670+4	.445+4	.330+4	.126+4	.262+3	.834+2
-9	.923+4	.927+4	.728+4	.579+4	.484+4	.353+4	.274+4	.112+4	.247+3	.817+2
-8	.370+4	.410+4	.360+4	.315+4	.283+4	.231+4	.192+4	.880+3	.218+3	.777+2
-7	.129+4	.151+4	.145+4	.137+4	.131+4	.118+4	.105+4	.567+3	.173+3	.702+2
TORR=5.										
ADB	.206+5	.204+5	.144+5	.104+5	.798+4	.507+4	.365+4	.135+4	.271+3	.842+2
-11	.169+5	.175+5	.127+5	.938+4	.733+4	.478+4	.349+4	.131+4	.266+3	.839+2
-10	.121+5	.135+5	.103+5	.736+4	.633+4	.432+4	.323+4	.125+4	.262+3	.833+2
-9	.632+4	.797+4	.665+4	.545+4	.464+4	.345+4	.270+4	.112+4	.247+3	.817+2
-8	.249+4	.357+4	.334+4	.300+4	.274+4	.228+4	.190+4	.877+3	.216+3	.777+2
-7	.852+3	.132+4	.136+4	.132+4	.128+4	.117+4	.104+4	.566+3	.173+3	.701+2
TORR=10.										
ADB	.147+5	.171+5	.127+5	.948+4	.745+4	.487+4	.356+4	.133+4	.270+3	.842+2
-11	.122+5	.146+5	.114+5	.863+4	.688+4	.461+4	.341+4	.130+4	.267+3	.839+2
-10	.877+4	.116+5	.930+4	.731+4	.599+4	.419+4	.317+4	.124+4	.261+3	.833+2
-9	.461+4	.696+4	.612+4	.515+4	.445+4	.338+4	.267+4	.111+4	.247+3	.817+2
-8	.183+4	.317+4	.312+4	.258+4	.267+4	.225+4	.188+4	.875+3	.216+3	.777+2
-7	.626+3	.118+4	.128+4	.128+4	.125+4	.116+4	.103+4	.565+3	.173+3	.701+2

Table VII. 9. Normalized Thermal Response from X-Rays in
Molybdenum with Neon Gas Protection

Surface Temperature Rise
[°C per J/cm²]
(Gas at 273 °K)

log Δt (sec)	.1	.2	.3	.4	.5	.75	1.	2.	5.	10
TORR=0.										
ADB	.350+5	.262+5	.170+5	.118+5	.880+4	.537+4	.379+4	.137+4	.271+3	.842+2
-11	.290+5	.224+5	.149+5	.106+5	.802+4	.503+4	.361+4	.133+4	.268+3	.839+2
-10	.211+5	.171+5	.119+5	.873+4	.683+4	.450+4	.332+4	.127+4	.262+3	.834+2
-9	.113+5	.990+4	.754+4	.593+4	.492+4	.355+4	.275+4	.113+4	.246+3	.817+2
-8	.468+4	.438+4	.372+4	.321+4	.287+4	.233+4	.192+4	.881+3	.218+3	.778+2
-7	.165+4	.161+4	.149+4	.139+4	.132+4	.119+4	.105+4	.567+3	.173+3	.702+2
TORR=.1										
ADB	.255+5	.218+5	.145+5	.102+5	.778+4	.491+4	.355+4	.132+4	.268+3	.839+2
-11	.210+5	.186+5	.127+5	.915+4	.710+4	.462+4	.339+4	.128+4	.265+3	.836+2
-10	.151+5	.142+5	.101+5	.758+4	.607+4	.415+4	.313+4	.122+4	.260+3	.831+2
-9	.794+4	.322+4	.643+4	.517+4	.440+4	.330+4	.261+4	.109+4	.245+3	.815+2
-8	.317+4	.362+4	.317+4	.282+4	.259+4	.218+4	.184+4	.862+3	.210+3	.776+2
-7	.110+4	.133+4	.128+4	.124+4	.121+4	.112+4	.101+4	.558+3	.172+3	.700+2
TORR=.5										
ADB	.115+5	.126+5	.871+4	.646+4	.527+4	.374+4	.291+4	.118+4	.259+3	.829+2
-11	.950+4	.109+5	.769+4	.563+4	.485+4	.355+4	.279+4	.115+4	.256+3	.827+2
-10	.687+4	.835+4	.618+4	.458+4	.420+4	.323+4	.261+4	.111+4	.251+3	.822+2
-9	.362+4	.487+4	.393+4	.338+4	.311+4	.263+4	.222+4	.101+4	.236+3	.807+2
-8	.144+4	.214+4	.196+4	.168+4	.188+4	.179+4	.160+4	.805+3	.211+3	.769+2
-7	.493+3	.785+3	.801+3	.848+3	.90?+3	.946+3	.899+3	.530+3	.170+3	.697+2
TORR=1.										
ADB	.575+4	.769+4	.548+4	.427+4	.371+4	.295+4	.245+4	.108+4	.250+3	.819+2
-11	.480+4	.669+4	.486+4	.388+4	.344+4	.282+4	.237+4	.106+4	.247+3	.817+2
-10	.354+4	.521+4	.393+4	.327+4	.301+4	.260+4	.223+4	.102+4	.243+3	.812+2
-9	.192+4	.307+4	.251+4	.229+4	.227+4	.215+4	.192+4	.935+3	.231+3	.798+2
-8	.774+3	.135+4	.125+4	.130+4	.140+4	.150+4	.141+4	.757+3	.200+3	.763+2
-7	.267+3	.494+3	.518+3	.597+3	.688+3	.805+3	.805+3	.505+3	.167+3	.693+2
TORR=5.										
ADB	.438+3	.918+3	.726+3	.759+3	.923+3	.120+4	.124+4	.744+3	.209+3	.774+2
-11	.349+3	.824+3	.659+3	.708+3	.879+3	.117+4	.122+4	.735+3	.206+3	.772+2
-10	.265+3	.671+3	.549+3	.622+3	.802+3	.111+4	.117+4	.717+3	.205+3	.768+2
-9	.157+3	.417+3	.362+3	.405+3	.647+3	.965+3	.105+4	.670+3	.196+3	.758+2
-8	.677+2	.187+3	.183+3	.280+3	.430+3	.711+3	.809+3	.563+3	.182+3	.730+2
-7	.240+2	.679+2	.760+2	.134+3	.220+3	.402+3	.487+3	.395+3	.152+3	.671+2
TORR=10.										
ADB	.134+3	.165+3	.138+3	.212+3	.349+3	.632+3	.753+3	.556+3	.183+3	.739+2
-11	.801+2	.149+3	.127+3	.201+3	.337+3	.620+3	.741+3	.551+3	.182+3	.738+2
-10	.517+2	.124+3	.107+3	.182+3	.315+3	.596+3	.718+3	.540+3	.181+3	.735+2
-9	.284+2	.788+2	.731+2	.144+3	.266+3	.533+3	.656+3	.511+3	.176+3	.726+2
-8	.121+2	.359+2	.378+2	.924+3	.185+3	.408+3	.524+3	.441+3	.164+3	.704+2
-7	.430+2	.131+2	.159+2	.453+2	.979+2	.240+3	.330+3	.322+3	.141+3	.653+2

Table VII. 10. Normalized Thermal Response from X-Rays in Molybdenum with Xenon Gas Protection

Surface Temperature Rise
[°C per J/cm²]
(Gas at 273 °J)

| log Δt (sec)	BLACKBODY TEMPERATURE (KEV)									
	.1	.2	.3	.4	.5	.75	1.	2.	5.	10
TORR=0.										
ADB	.350+5	.262+5	.170+5	.118+5	.880+4	.537+4	.379+4	.137+4	.271+3	.842+2
-11	.290+5	.224+5	.149+5	.106+5	.802+4	.503+4	.361+4	.133+4	.268+3	.839+2
-10	.211+5	.171+5	.119+5	.873+4	.683+4	.450+4	.332+4	.127+4	.262+3	.834+2
-9	.113+5	.990+4	.754+4	.593+4	.492+4	.355+4	.275+4	.113+4	.248+3	.817+2
-8	.468+4	.438+4	.372+4	.321+4	.287+4	.233+4	.192+4	.881+3	.218+3	.778+2
-7	.165+4	.161+4	.149+4	.139+4	.132+4	.119+4	.105+4	.567+3	.173+3	.702+2
TORR=.1										
ADB	.140+5	.910+4	.554+4	.395+4	.339+4	.271+4	.229+4	.102+4	.235+3	.801+2
-11	.115+5	.761+4	.477+4	.351+4	.310+4	.258+4	.222+4	.100+4	.233+3	.798+2
-10	.823+4	.560+4	.370+4	.289+4	.268+4	.238+4	.209+4	.968+3	.230+3	.794+2
-9	.429+4	.307+4	.227+4	.201+4	.202+4	.199+4	.191+4	.884+3	.220+3	.760+2
-8	.172+4	.130+4	.113+4	.116+4	.126+4	.141+4	.134+4	.715+3	.197+3	.746+2
-7	.597+3	.471+3	.472+3	.547+3	.641+3	.764+3	.764+3	.475+3	.160+3	.679+2
TORR=.5										
ADB	.551+3	.387+3	.280+3	.380+3	.575+3	.904+3	.961+3	.562+3	.171+3	.699+2
-11	.452+3	.322+3	.245+3	.356+3	.554+3	.884+3	.943+3	.555+3	.170+3	.698+2
-10	.322+3	.234+3	.196+3	.321+3	.513+3	.847+3	.909+3	.541+3	.166+3	.695+2
-9	.165+3	.125+3	.130+3	.259+3	.443+3	.753+3	.820+3	.503+3	.163+3	.686+2
-8	.646+2	.511+2	.733+2	.176+3	.317+3	.564+3	.632+3	.418+3	.150+3	.663+2
-7	.221+2	.182+2	.350+2	.917+2	.100+3	.319+3	.375+3	.289+3	.127+3	.616+2
TORR=1.										
ADB	.108+2	.890+1	.204+2	.926+2	.203+3	.412+3	.474+3	.319+3	.129+3	.624+2
-11	.892+1	.747+1	.193+2	.902+2	.199+3	.404+3	.467+3	.315+3	.129+3	.623+2
-10	.639+1	.551+1	.175+2	.858+2	.191+3	.390+3	.452+3	.308+3	.128+3	.621+2
-9	.330+1	.300+1	.142+2	.747+2	.169+3	.351+3	.412+3	.289+3	.125+3	.615+2
-8	.129+1	.126+1	.966+1	.532+2	.124+3	.268+3	.323+3	.245+3	.117+3	.600+2
-7	.438+0	.462+0	.501+1	.278+2	.676+2	.154+3	.196+3	.175+3	.103+3	.565+2
TORR=5.										
ADB	.237-11	.165-09	.242-2	.334+0	.256+1	.804+1	.116+2	.198+2	.544+2	.430+2
-11	.204-11	.162-09	.236-2	.328+0	.252+1	.794+1	.115+2	.197+2	.543+2	.430+2
-10	.155-11	.157-09	.223-2	.318+0	.246+1	.776+1	.112+2	.196+2	.542+2	.430+2
-9	.867-12	.144-09	.190-2	.287+0	.228+1	.723+1	.105+2	.191+2	.539+2	.428+2
-8	.354-12	.114-09	.127-2	.218+0	.185+1	.593+1	.879+1	.178+2	.530+2	.423+2
-7	.122-12	.672-10	.609-3	.122+0	.115+1	.374+1	.581+1	.154+2	.506+2	.409+2
TORR=10.										
ADB	.244-26	.332-20	.136-6	.175-2	.690-1	.238+0	.390+0	.378+1	.374+2	.341+2
-11	.213-26	.327-20	.133-6	.172-2	.683-1	.236+0	.386+0	.377+1	.374+2	.341+2
-10	.165-26	.319-20	.126-6	.167-2	.670-1	.231+0	.380+0	.376+1	.373+2	.340+2
-9	.937-27	.294-20	.107-6	.153-2	.629-1	.217+0	.360+0	.374+1	.372+2	.339+2
-8	.388-27	.235-20	.720-7	.119-2	.527-1	.182+0	.309+0	.366+1	.367+2	.336+2
-7	.135-27	.140-20	.344-7	.689-3	.343-1	.119+0	.215+0	.347+1	.353+2	.326+2
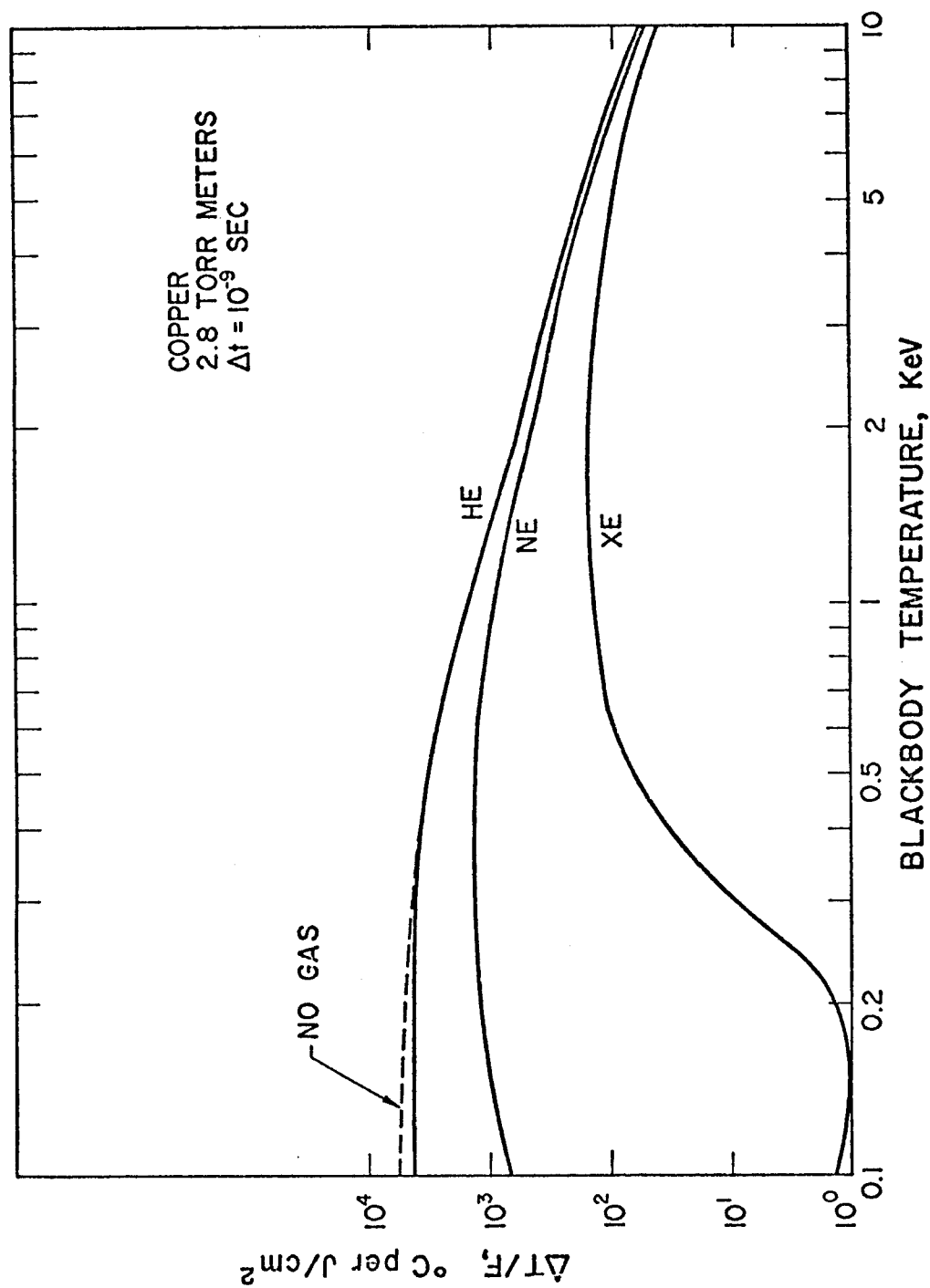
Fig. VII. 1. Effect of Gas Type on X-Ray Temperature Response
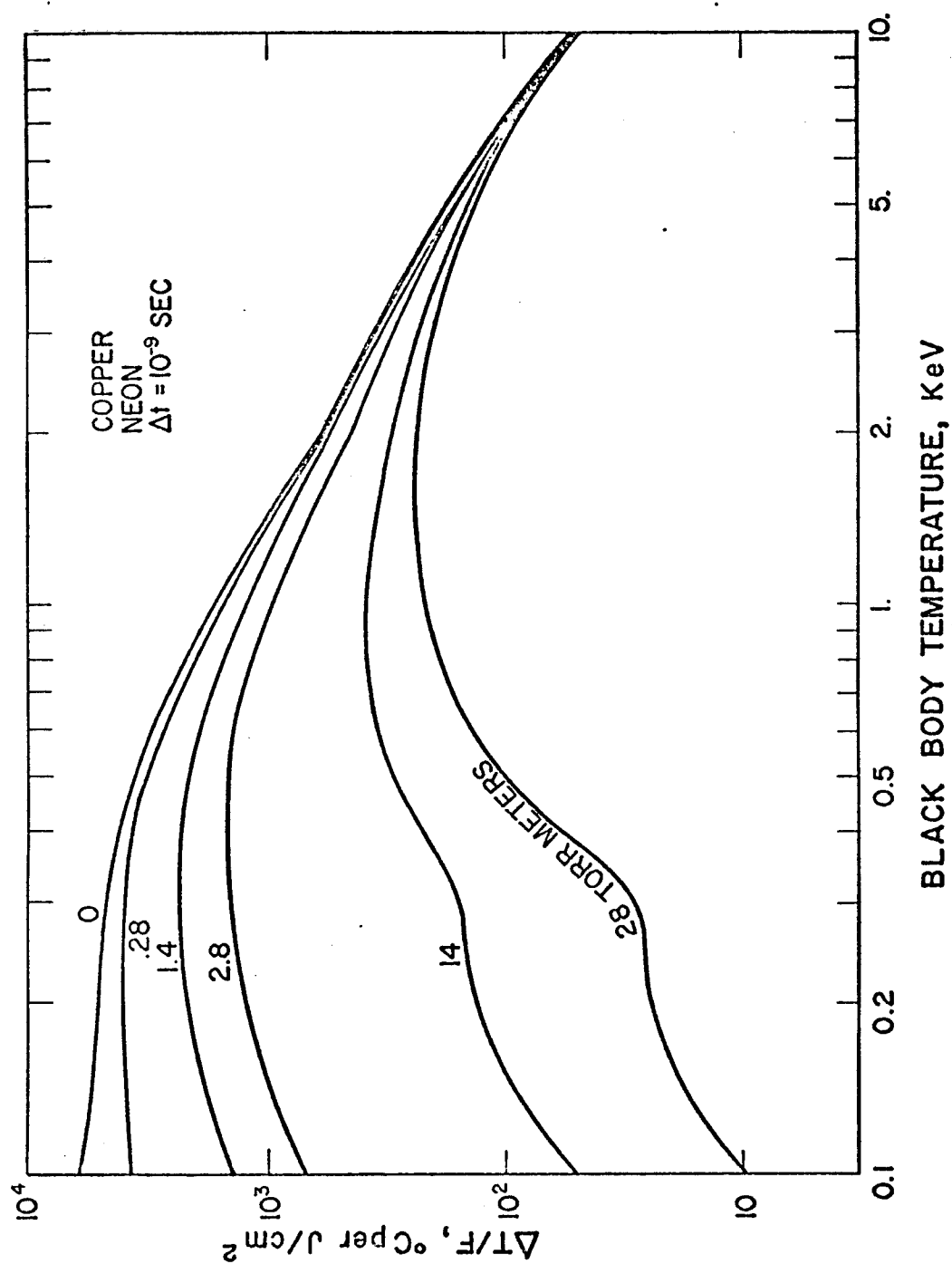
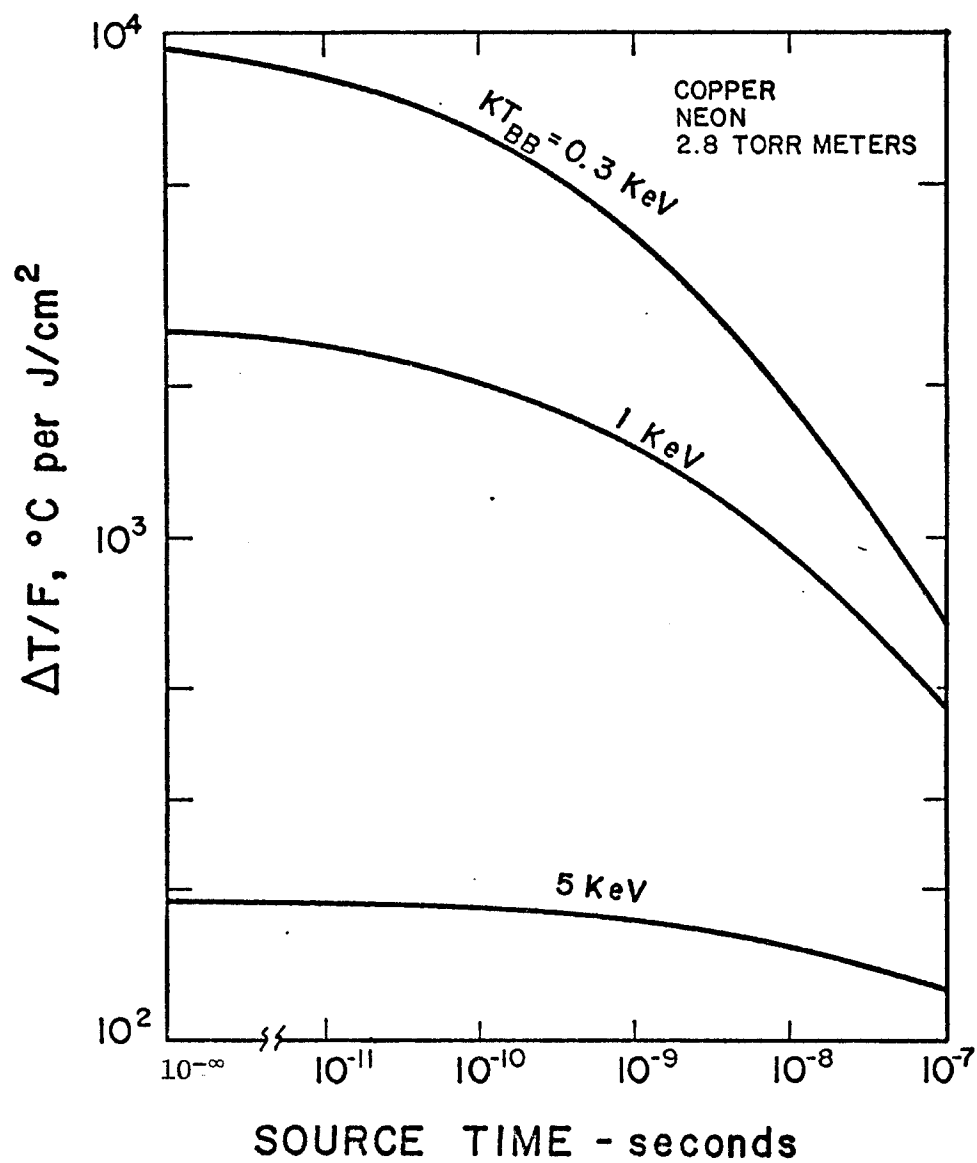Fig. VII. 2. Effect of Gas Pressure on X-Ray Temperature Response

Fig. VII. 3. Effect of Source Time on X-Ray Temperature Response

NEON
2.8 TORR METERS
$\Delta t = 10^{-9}$ SEC

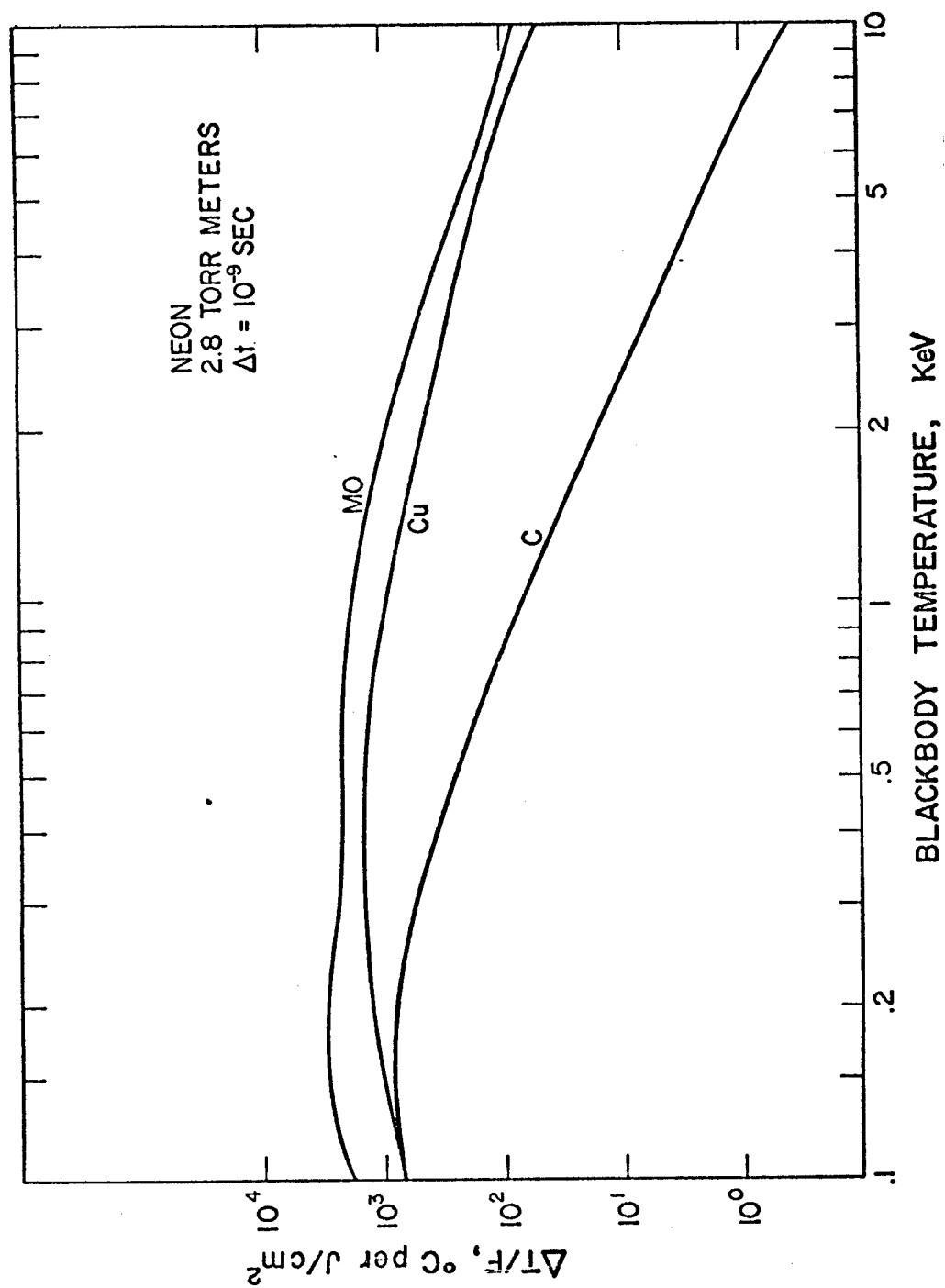BLACKBODY TEMPERATURE, KeV

$\Delta T/F$, °C per J/cm^2

Fig. VII. 4. X-Ray Temperature Response of Various Materials

of the lighter gases will be required to achieve the same effect. Neon at 2.8 torr-meters reduces the temperature excursion by factors of 2-5 for black body spectra up to about 1 keV. Xenon essentially eliminates the X-ray temperature response for these spectra while helium gives only a small (10-30%) reduction for spectra at 0.1 to 0.3 keV. For black body spectra of 5 keV and above, all gases tend to lose their effectiveness as the cross sections become smaller.

Figure VII.2 shows the effect of various areal densities of gas for copper and neon as a function of source temperature at a 1 nanosecond source duration. These data demonstrate the exponential behavior of response on the torr-meters of gas present. The irregularities in the curves at higher gas densities are due to the combination of absorption edges in the gas and those of the matter in which the temperature is calculated. A maximum develops in the curves as gas density is increased as the gas tends to preferentially absorb lower energy X-rays. The higher energy X-rays are allowed to pass into the copper and can still produce significant temperature response.

The effect of source duration is shown in figure VII.3 for copper and neon at 2.8 torr-meters. A substantial reduction from the adiabatic response is noted due to the conductivity of the material. The effect is most significant for lower source temperatures where gradients near the surface are the highest and the maximum reduction due to longer source times is observed in copper due to its high thermal diffusivity. These data are compatible with the estimates made in section V.C which predicted the time scales for which the

adiabatic assumption was valid.

Figure VII.4 shows variation in the material on response with neon at 2.8 torr-meters and a source duration of 1 nanosecond. These data show the difference in both X-ray absorption properties and thermal properties of the material. In general the temperature response is shown to be greater with materials of higher atomic number. This effect is especially evident for higher energy spectra in which carbon (Z=6) shows a marked lower response than either copper or molybdenum.

VII.B.2.   Ion Response

In this analysis the response of a copper was studied to variations in ion spectra. Helium ions were chosen for the study since they are a reaction product and therefore a species which has a wide potential range of energy spectra. Characteristic spectra were chosen as Gaussian distributions in which both the mean energy and the standard deviation were varied. These spectra range from the most energetic distributions simulating essentially uncollided alpha particles from the D,T reaction to much lower energy distributions with wide standard deviations characteristic of spectra downscattered in the pellet or by gaseous layers.

The calculations were performed for five cavity radii ranging from 5 meters to 10 meters. Response was determined in terms of the maximum ion energy yield for which the temperature excursion would not exceed 2/3 of the melting temperature. Ion spectra were chosen whose mean ranged from 500 keV to 3500 keV and for each case calculations were performed for standard deviations which ranged from 35 to

40% of the mean value.

The results for 5, 7 and 10 meters are presented in figures VII.5, .6, and .7, respectively. These data indicate the maximum fraction which can be allowed at a given radius. The response variation shown represents a trade-off between (a) "narrow" spectra and "wide" spectra in which the times of deposition are correspondingly increased as the spectral widths increase and (b) high energy distributions and low energy distributions in which the ion penetration is reduced as ion energy is decreased causing variations in volumetric energy depositions and near surface temperature gradients.

If the helium ions are assumed to be due to a D,T reaction which produced a total energy of 17.6 MeV, these data can be converted from maximum ion energy fraction to maximum thermonuclear energy allowed. These data are shown in figures VII.5, .6, and .7. The lower ion energy allows higher total energy yield since the total number of particles is higher. It should be pointed out here however that these data represent the temperature response to one ion species only and the total energy lost by reducing the mean ion energy, in fact, may be deposited in the first wall in another form.

VII.C. Response to Complete Spectra

In this section the response of selected materials to a complete spectra from "typical" laser fusion pellet yields is calculated. Three sets of spectra are considered: (a) a bare pellet spectrum with photon and light ions only and (b) a structured pellet spectrum which is characterized by a dominant heavy ion component, and (c) a modified
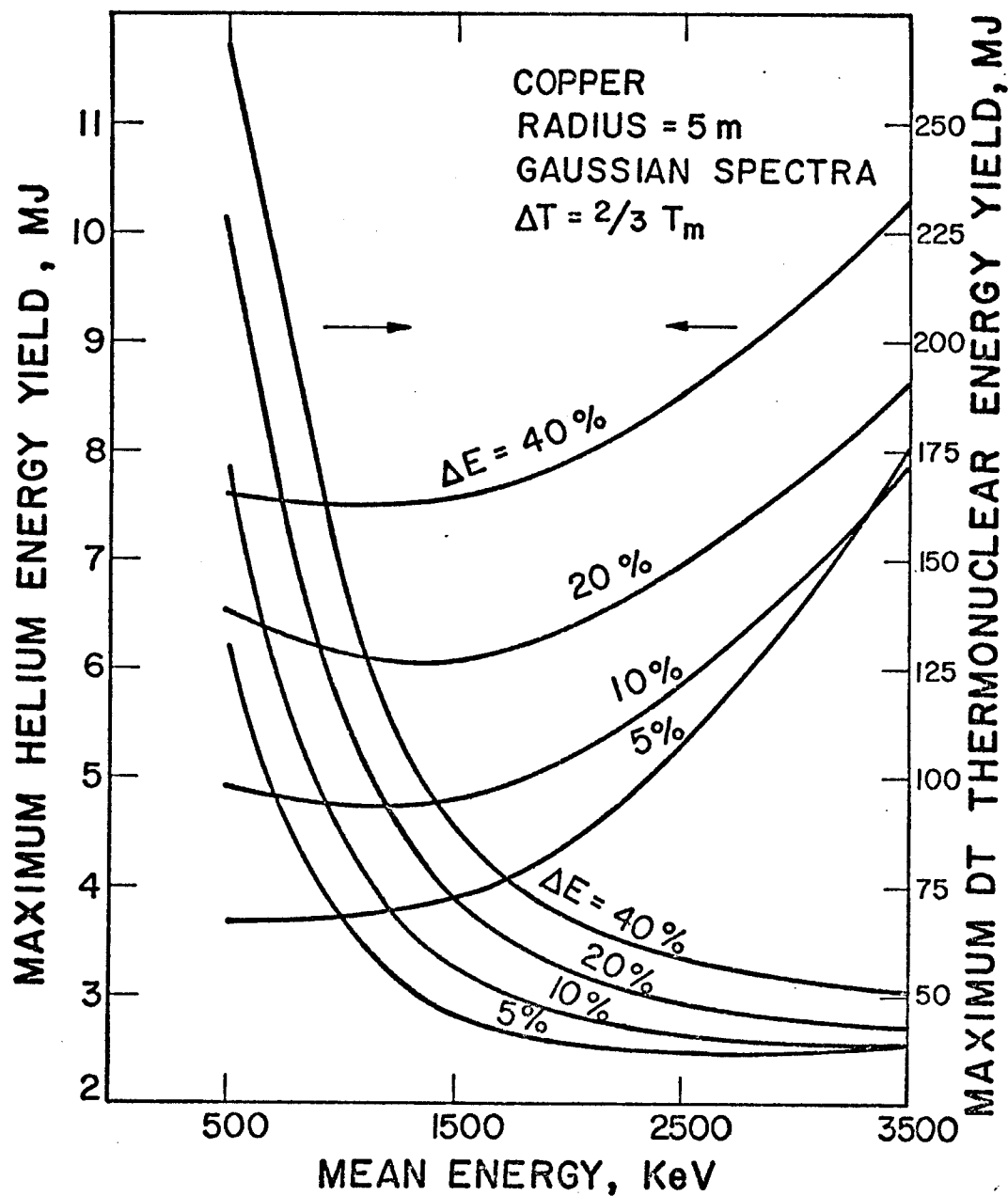
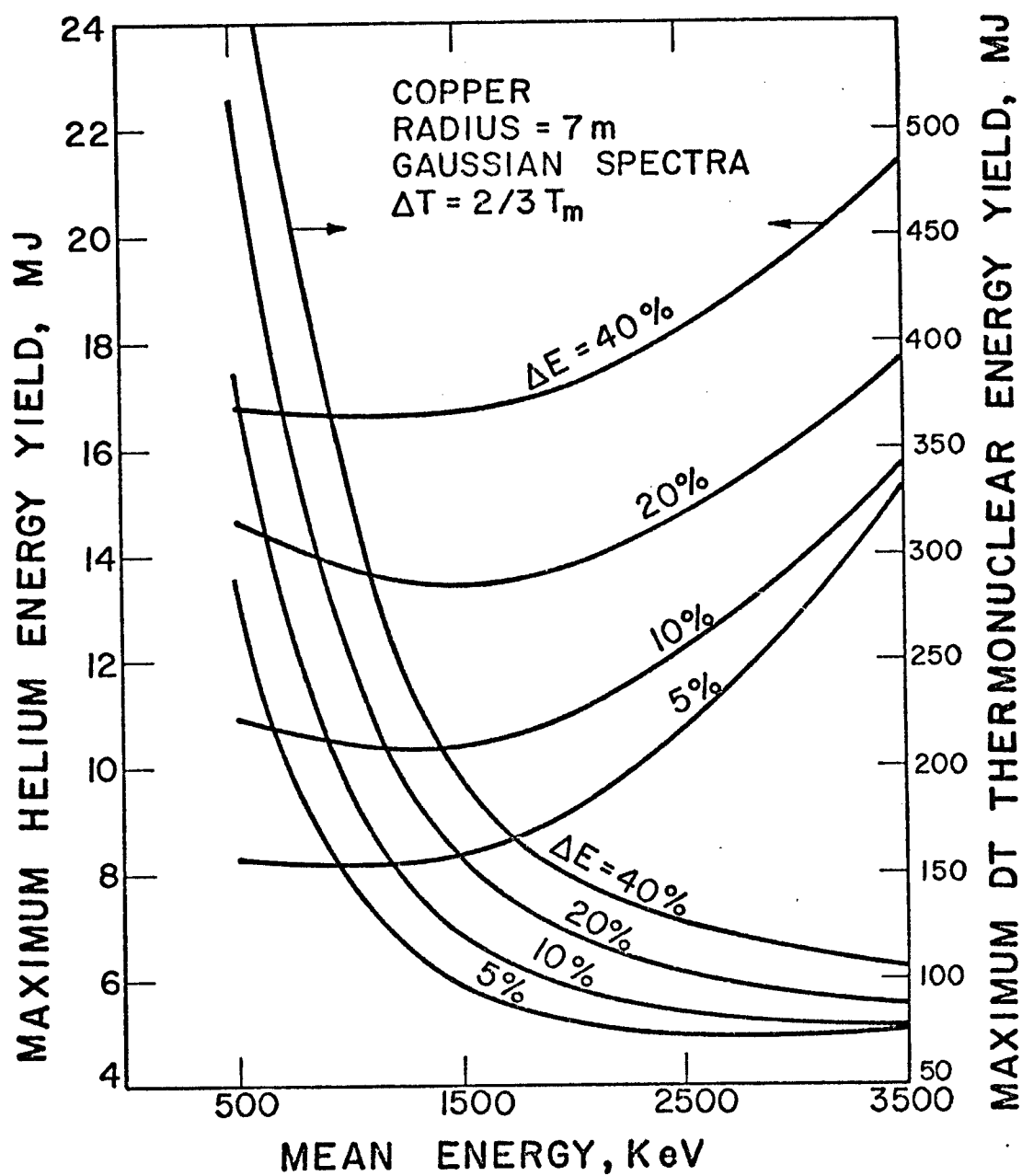Fig. VII. 5.   Maximum Allowable TN Yield for Copper at 5 Meters

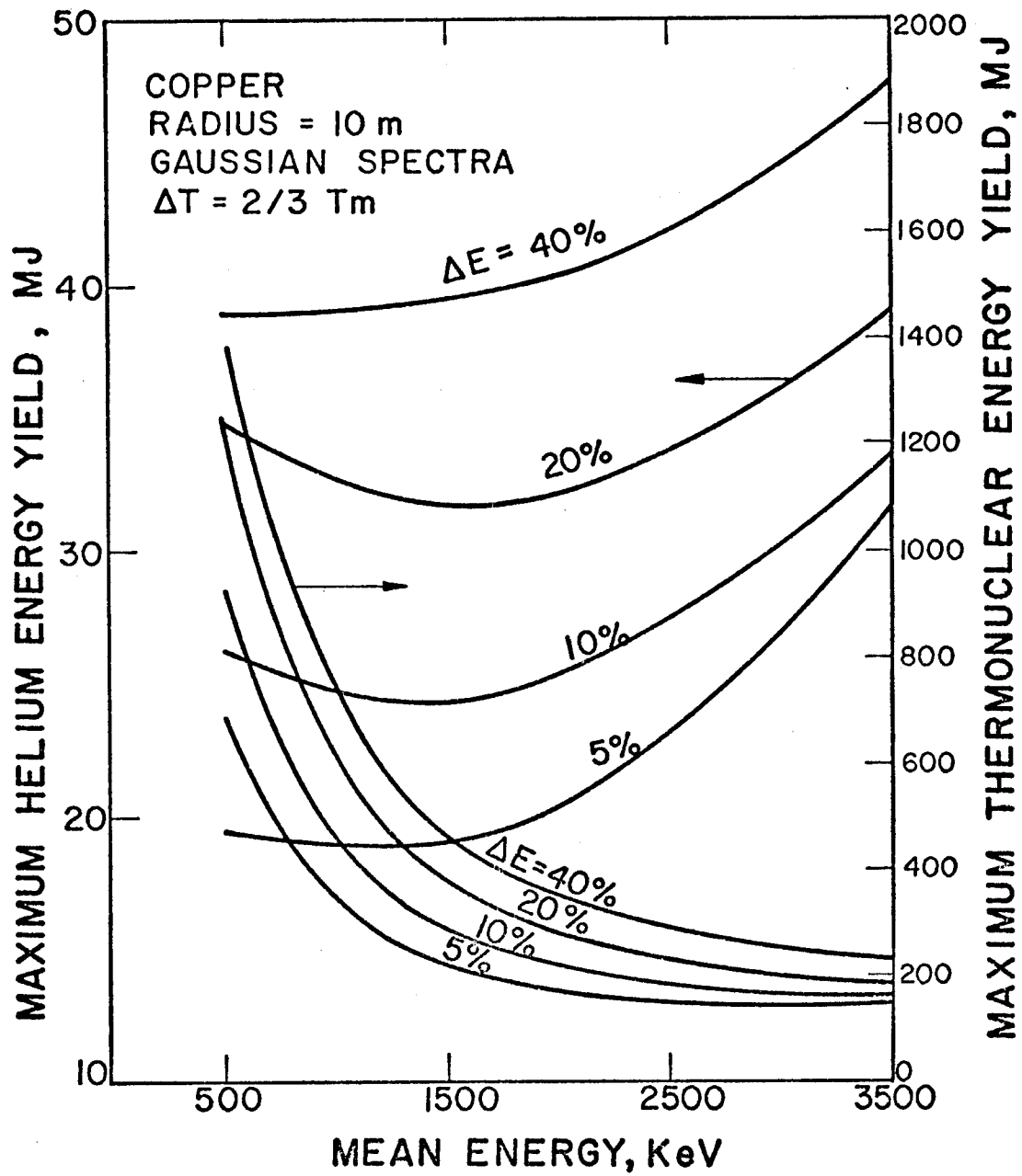Fig. VII. 6.   Maximum Allowable TN Yield for Copper at 7 Meters

Fig. VII. 7.   Maximum Allowable TN Yield for Copper at 10 Meters

bare pellet spectrum with both heavy and light ions.

VII.C.1. Comparison of Bare Pellet and Structural Pellet Response

This section will demonstrate the use of the T-DAMEN code by comparing the response of both molybdenum and carbon to the spectra which were outlined in table II.5. The spectra represent pellet hydrodynamic calculations using the PHD-IV code[112] for a characteristic "bare" pellet, containing fuel only, and a "structured" pellet which was surrounded by a heavy liner (mercury).

Calculations were performed for the response of carbon and molybdenum at a radius of 6 meters for each of these spectra. Selected data will be presented which compare the energy deposition, temperature, and displacement production for bare wall exposure. These data do not represent all the information obtained during the calculation but rather a few of the more important comparative responses which demonstrate the analytical method.

In both of these spectra the temperature response is dominated by the ions since the X-ray spectra are composed of high energy photons which have relatively low absorption coefficients. A spectrum with lower energy photons is considered in the next section where the influence of gas protection is also analyzed.

The particle flux and corresponding time of arrival from these spectra are shown in figure VII.8. The photons from the source are not shown but arrive about 20 ns after thermonuclear burn followed by the neutrons and finally the ions. The ions from the bare pellet arrive considerably earlier than those of the structured pellet and
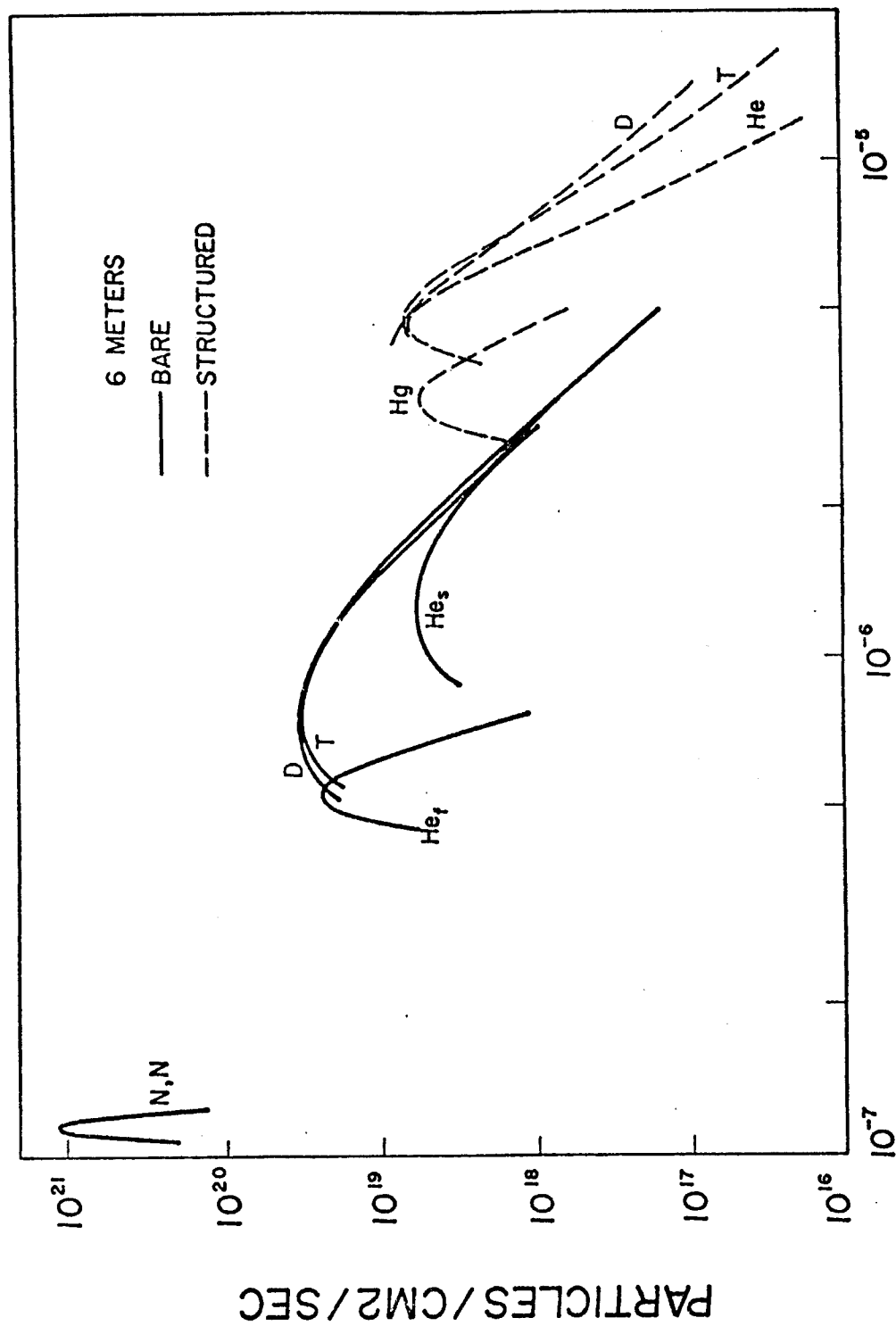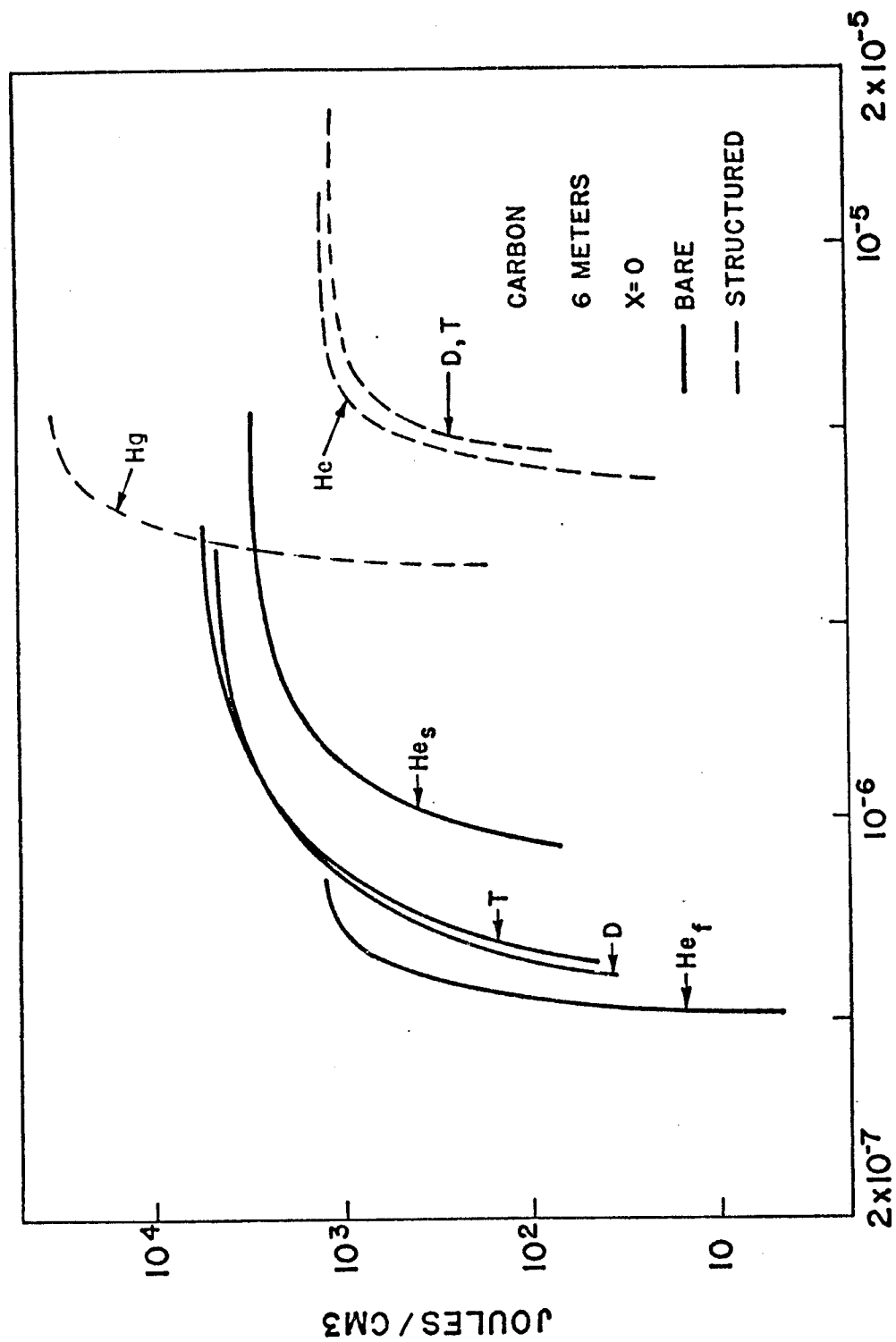
TIME FROM TN BURN–SEC

Fig. VII. 8. Particle Flux from Bare and Structured Pellet Spectra

their pulse durations are shorter.

The energy deposition at the front surface is shown in figure VII.9 for carbon. The total energy deposited by the ions from the structured pellet is higher due to the short range of the heavy ions. This energy is however deposited over a much longer period of time and a considerable amount of the energy is conducted away from the deposition region. The difference between the energy deposition profiles at the end of the respective pulses is shown in figure VII.10 which indicates that the deposition from the Hg ions is about 6 times larger than any component of the bare pellet. The neutron energy deposition is always quite low and is on the order of 1 J/cm^3 even though it is essentially uniformly deposited through the first wall.

The temperature increase over the ambient value for carbon is displayed in figure VII.11 for each of the components in each spectrum. The initial excursion for the laser light is based on a uniform deposition duration of 1 ns while the X-ray absorption is assumed to occur as an impulse in time. Each component of the bare pellet produces a significant ΔT (except the X-rays) occurring at slightly different times while the structured pellet response is dominated by the heavy Hg ions. The time at which the temperature is elevated at the front surface is longer for the bare pellet due to the larger deposition region and commensurate smaller temperature gradients.

The total temperature increase from all components in each spectrum is shown in figure VII.12 for both carbon and molybdenum. In both cases the bare pellet temperature excursion exceeds that of

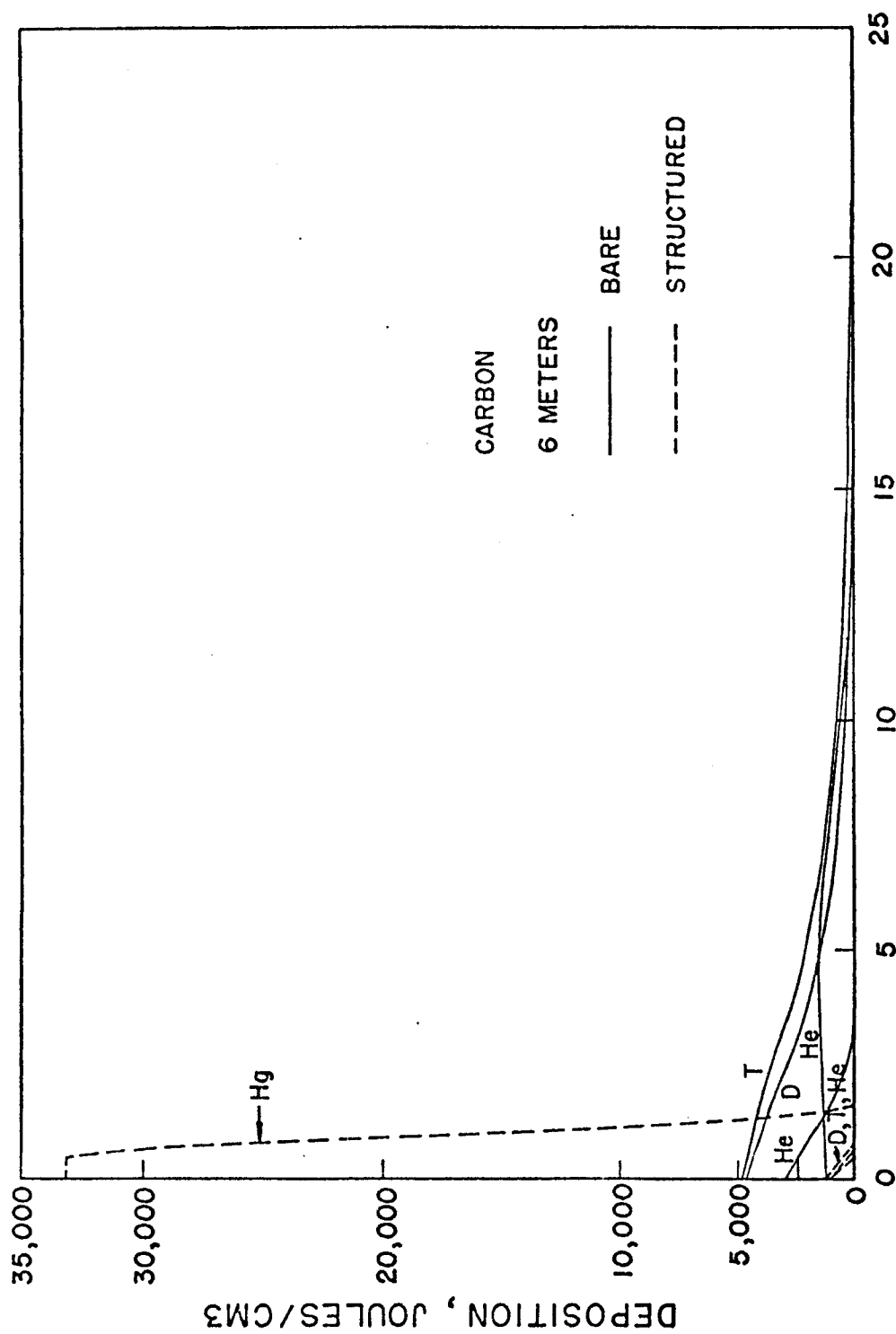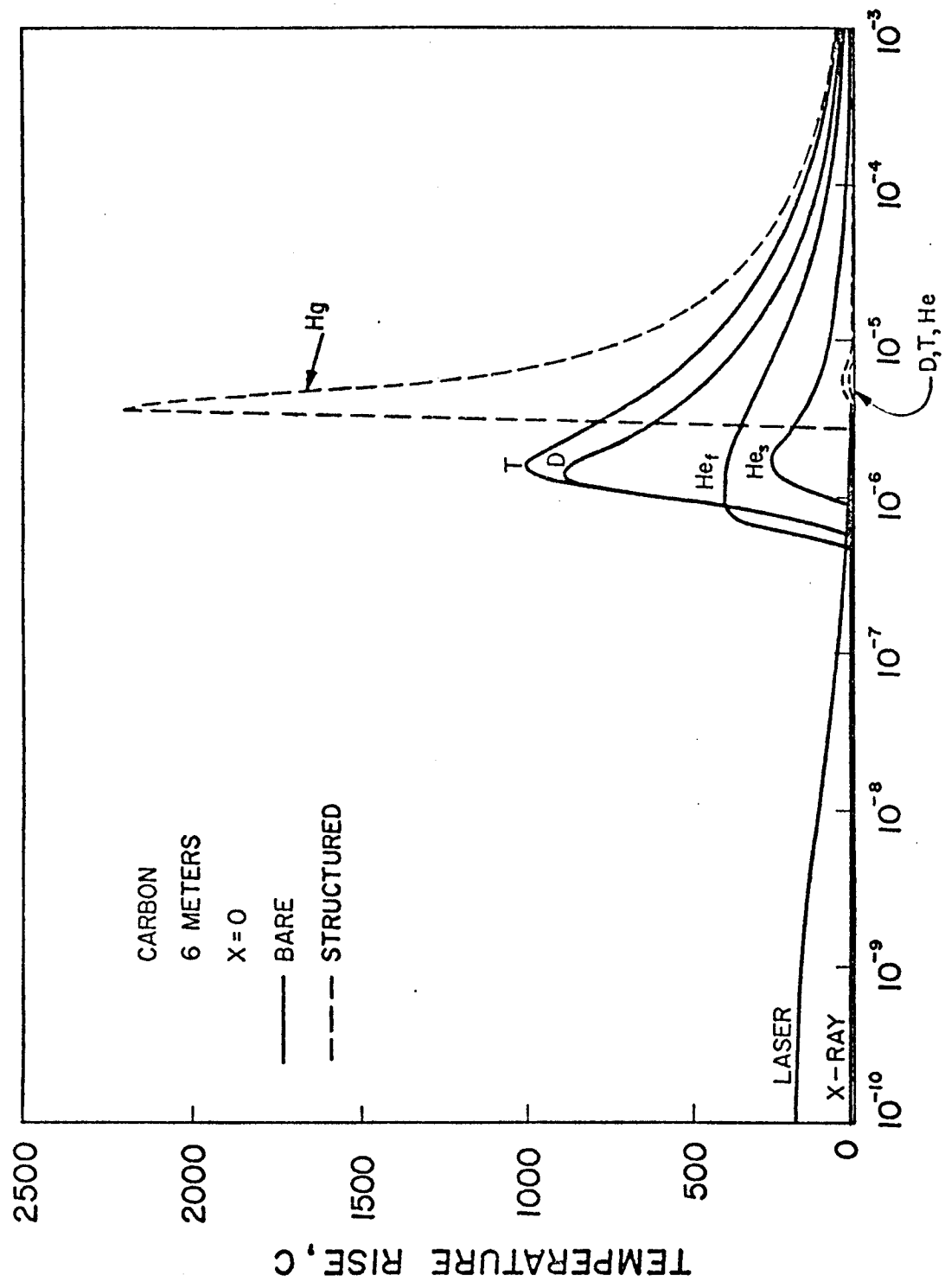Fig. VII. 9.   Ion Energy Deposition for Bare and Structured Pellet
Spectra

Fig. VII. 10. Total Ion Energy Deposition for Bare and Structured Pellet Spectra

TIME FROM X-RAY ARRIVAL, SEC

Fig. VII. 11.   Component Temperature Increase for Bare and Structured
Pellet Spectra

Fig. VII. 12. Total Temperature Increase for Carbon and Molybdenum

the structured pellet due to the longer time interval over which the deposition took place and the larger gradients associated with the heavy ions. The comparison of molybdenum and carbon indicates that Mo and C show essentially equivalent responses for the bare pellet but a smaller excursion is noted for the former with the structured pellet due to the higher thermal diffusivity of the Mo. This effect is noted to be even more significant in materials of higher thermal conductivity such as copper.

The displacement production for light ions like those of the bare pellet is determined by the local energy of the ion as it slows down in the material. The displacement cross section in general is inversely proportional to the ion energy. Consequently the dpa rate increases with distance into the material. The displacement rate for each ion species at the front surface is shown in figure VII.13. The dpa rate for neutrons were developed from neutron fluxes determined from time dependent neutronics calculations[7] and are noted to be an order of magnitude lower than any of the ion species.

The total displacement rate and the commensurate temperature excursion in molybdenum for the bare pellet is shown in figure VII.14. The maximum dpa rate exceeds 30 dpa/sec which is a factor of 10^7 higher than that observed in fission reactors and 100 times larger than ion simulation facilities. The displacement rate at a position 1 micron from the surface is a factor of 5 higher than the front surface values.

Figure VII. 15 shows the effect of introducing gas into the reac-
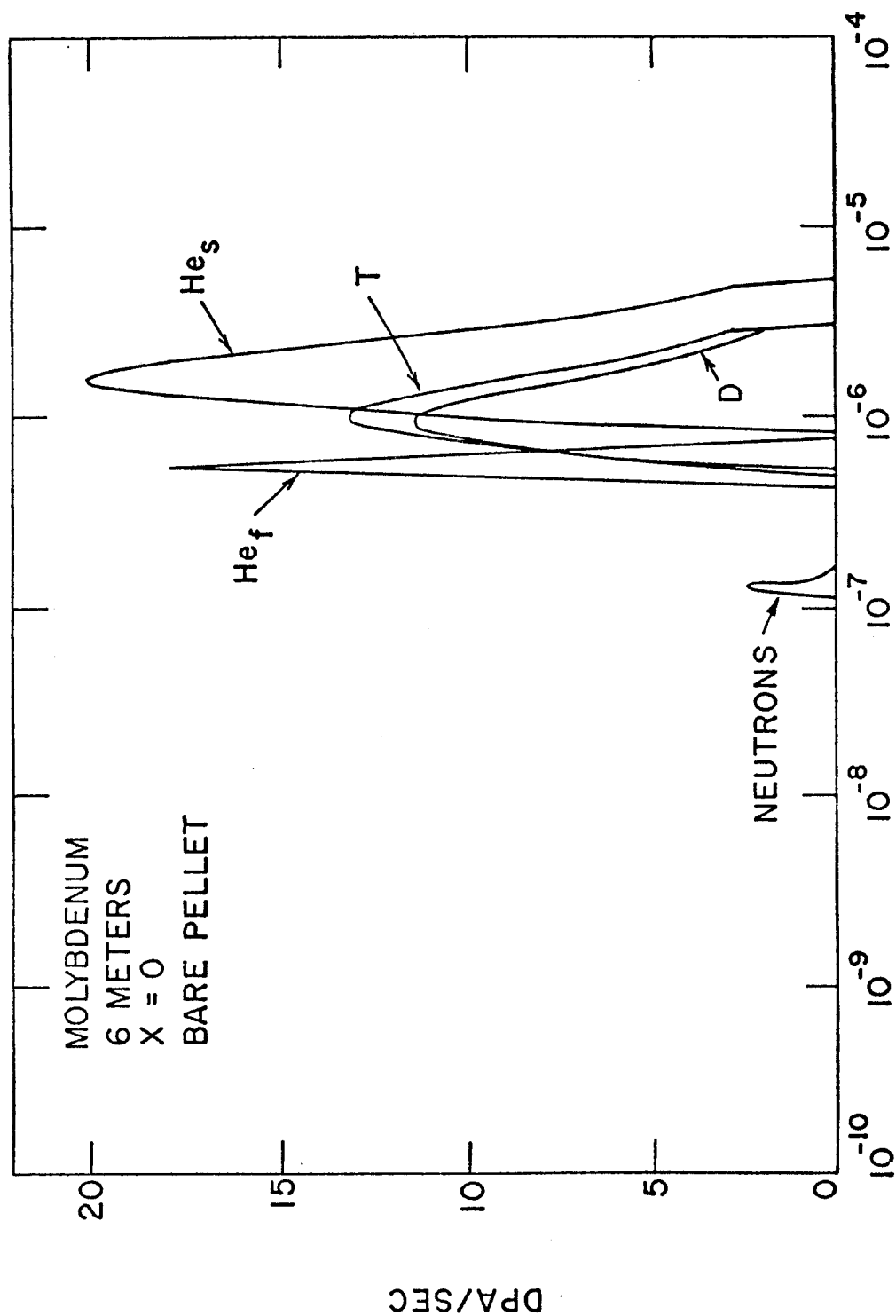
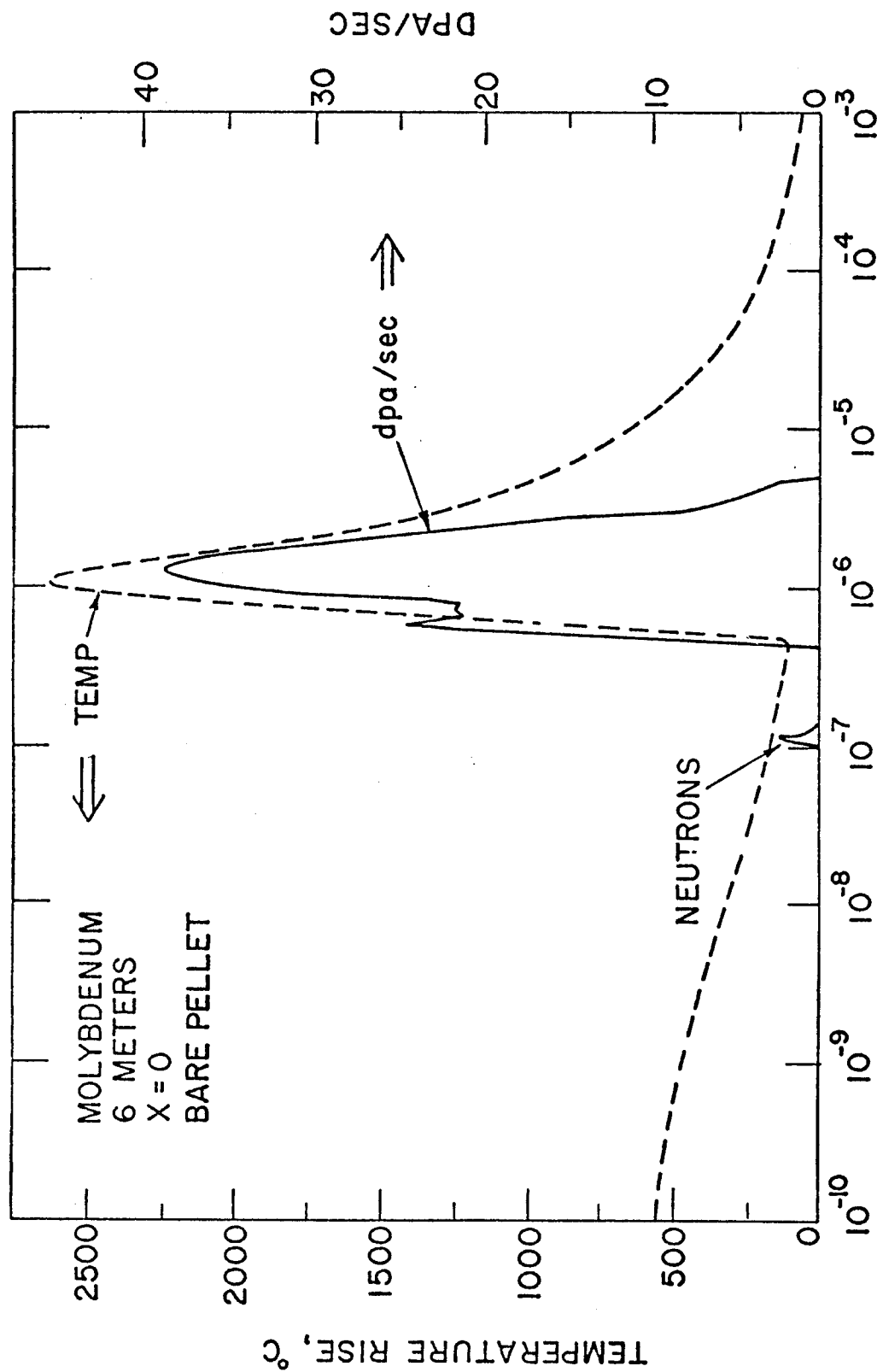Fig. VII. 13. Component Displacement Rate in Molybdenum

Fig. VII. 14. Temperature and Displacement Rate in MO
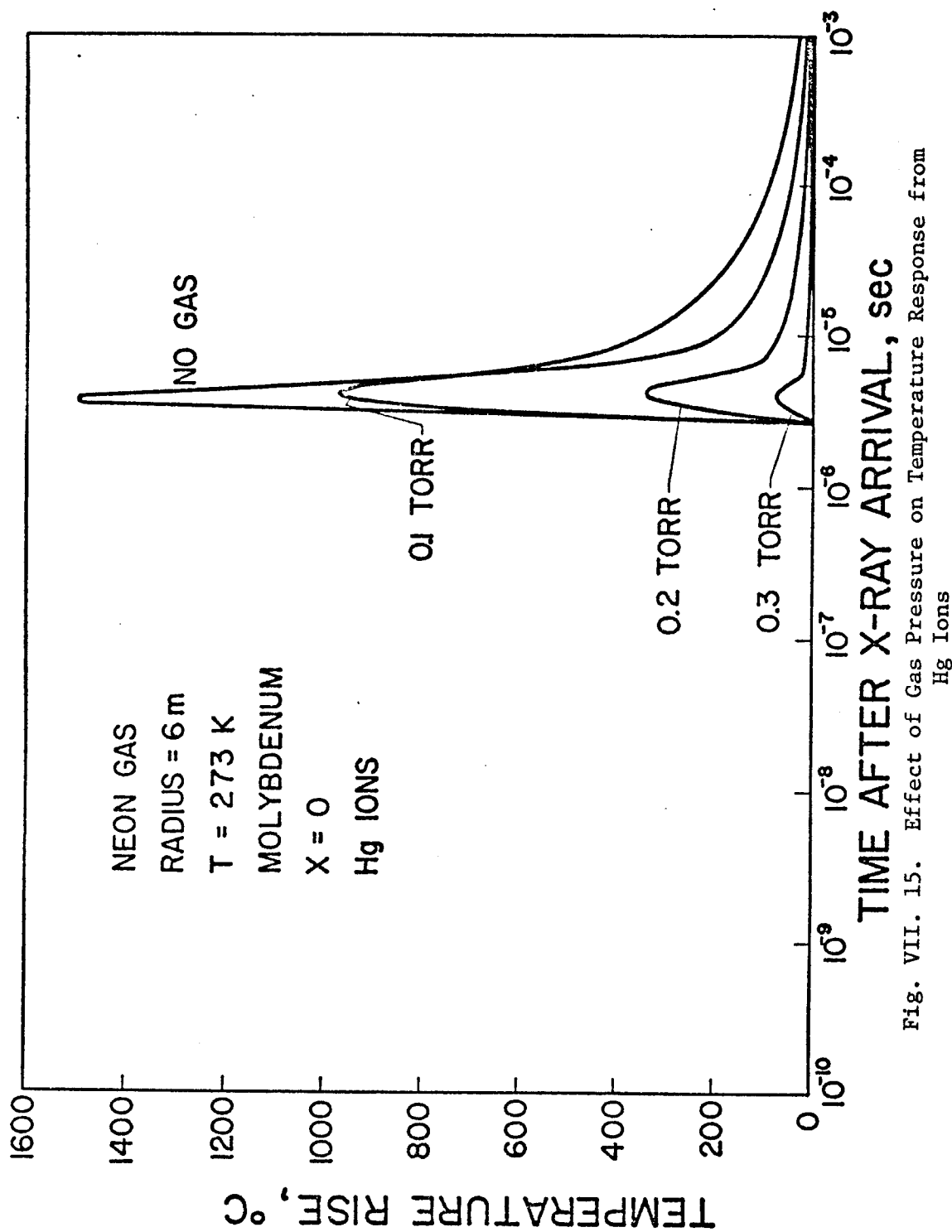
Fig. VII. 15. Effect of Gas Pressure on Temperature Response from Hg Ions

tor chamber.   The mercury ion induced temperature excursion of

the molybdenum is displayed for various pressure of neon gas. These

data indicate that pressures as low as a few tenths of a torr (0.6 -

2.0 torr-meters) are sufficient to reduce the temperature rise con-

siderably. The thermal response is reduced until by 0.4 torr of Ne,the

gas absorbs essentially all the ion energy and no mercury ions reach

the wall. A more comprehensive example of gas protection will be

given in the next section.

VII.C.2. Response to a Genetic Set of Spectra

This section will consider the response of copper to a reference

set of spectra which consists of both light and heavy ion components.

The calculation performed will demonstrate not only the use of the

T-DAMEN code for such spectra but,in addition,will emphasize the

effect of a gaseous protective layer on the response of the exposed

material.

The spectra chosen consists of a modification of bare pellet
spectra[113] with the addition of high Z component, Si, to simulate the

pellet coating and to demonstrate the effect of higher mass in the

damage process. The components of these spectra are given in table

VII.11. A total energy of 100 MJ is chosen with most of the energy in

neutrons with a few percent X-rays and the balance distributed between

reaction products, unburnt fuel, pellet material and reflected laser

light. The helium distribution is chosen to be bimodal with a high

energy component and a thermalized component even though in practice

there is likely to be a more complex coupling between the down

TABLE VII.11

Reference Spectra (100 MJ)

	Energy (MJ)	Spectrum
Laser	.2	10.6 μ
X-ray	2	1.0 keV - BB
D	4.6	160 keV - M
T	6.9	240 keV - M
He (Slow)	1.2	320 keV - M
He (Fast)	5.4	$2 \pm .5$ MeV - G
Silicon	2.7	800 keV - M
Neutrons	77.	14 ± 1 MeV - G

BB = Black Body   M = Maxwellian   G = Gaussian

scattered spectra.

The spectra are shown in figure VII.16 in terms of the energy content per unit area at a 7 meter radius. The effect of 0.5 torr of neon on each of the components is also demonstrated in figure VII.16. Each component is shifted down in energy and the spectra is broadened as the ions energy is reduced. The most notable shift is in the silicon ions in which many of the lower energy ions do not penetrate the gas. The modification of the X-ray spectrum shows the high absorption near the K-edge of neon.

The flux and arrival times associated with each species is depicted in figure VII.17. Each pulse is lowered in peak amplitude and spread in time by the gas. The silicon component, however, is noted to not only be reduced in magnitude but shortened in time since the ions which would normally arrive at late times do not reach the exposed surface. The deuterium and tritium flux were originally the same without gas protection; yet, because of the different stopping powers in neon, the deuterium was more radically modified than the tritium. The photons are not shown but arrive in about 23 ns after thermonuclear burn. It is assumed that the time of X-ray production is very short compared to the cavity transit time, hence an impulse model is used for deposition and response. The laser light is assumed to be deposited over a period of 10 ns. The neutrons are assumed to be unaffected by the gas.

An example of the deposition profile generation by the code is given in figure VII.18 in which the energy deposition profile for the
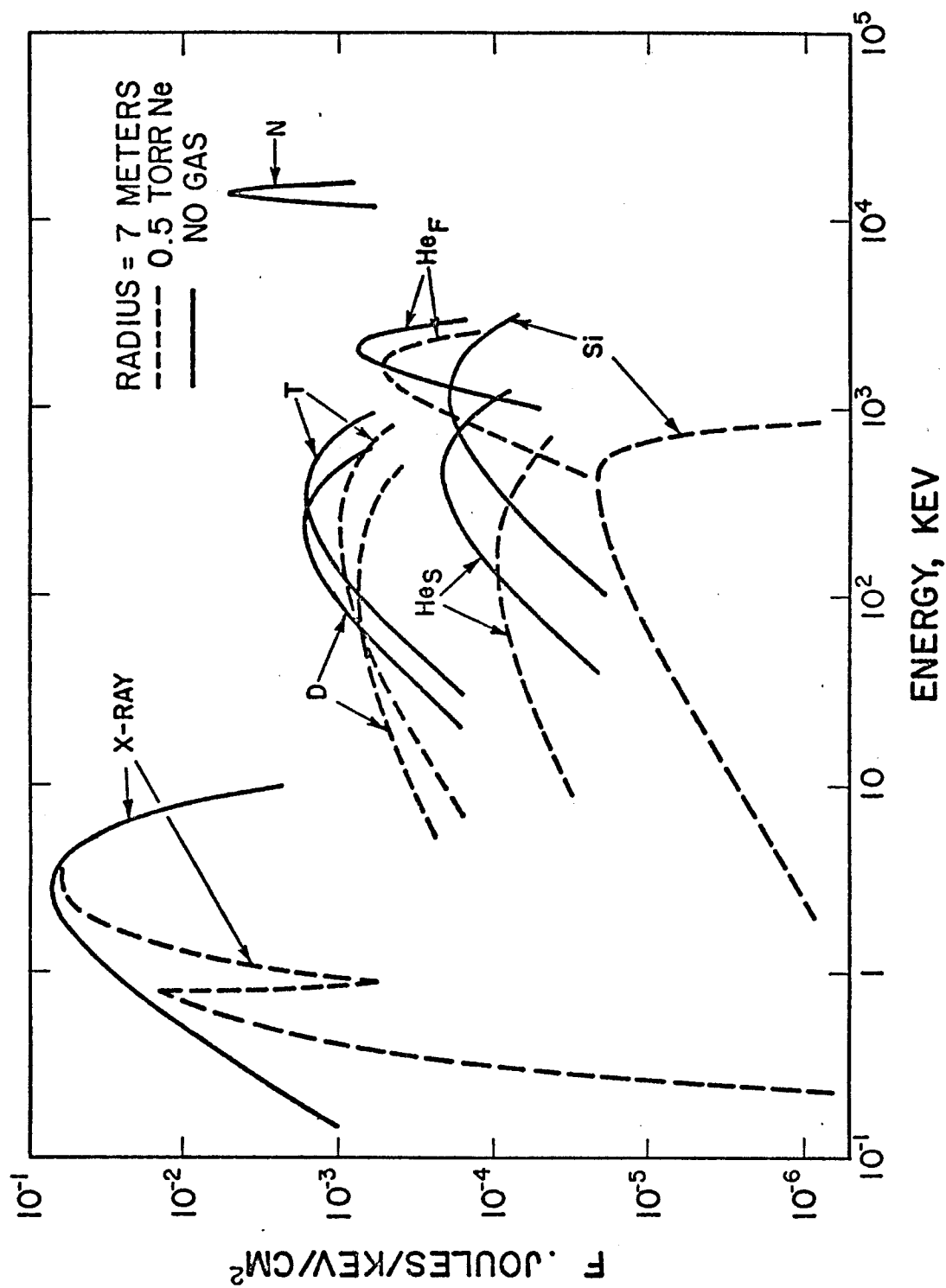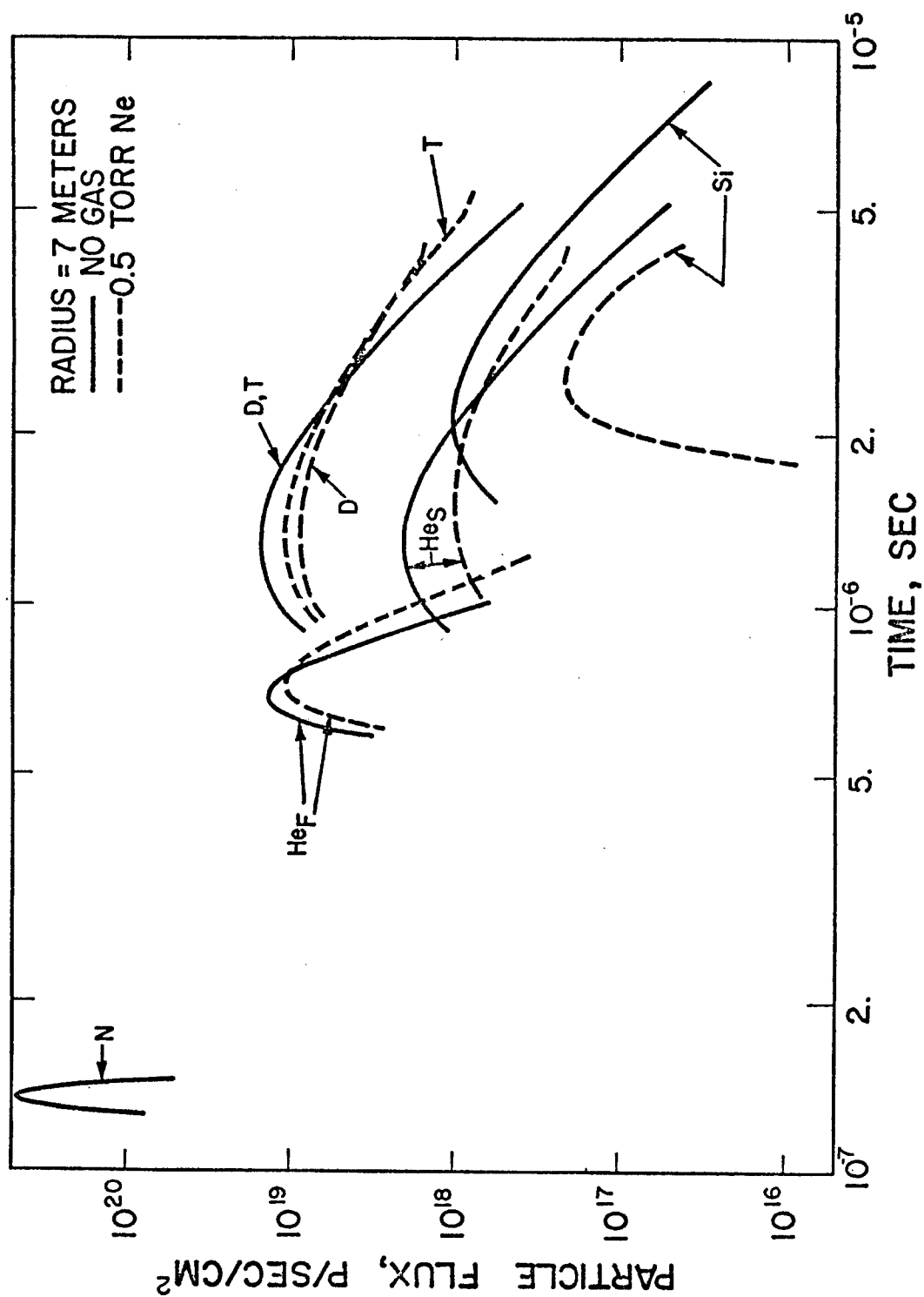
Fig. VII. 16. Energy Spectra – Ion and X-Rays

Fig. VII. 17. Ion Particle Flux

COPPER
7 METERS

Si (3200 keV)

He_F (3000 keV)

T (960 keV)

D(640 keV)

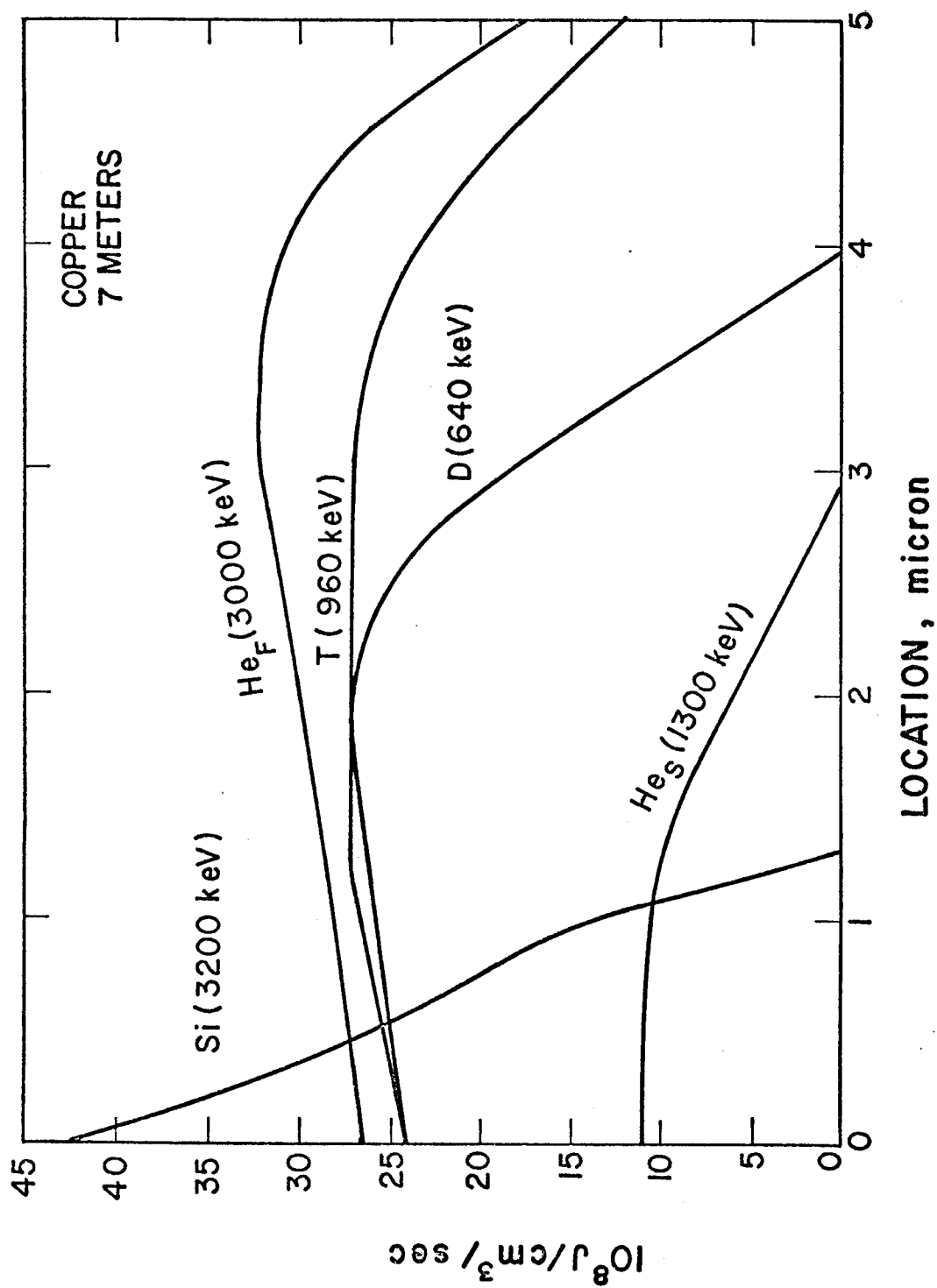He_S (1300 keV)

LOCATION, micron

10^8 J/cm^3/ sec

Fig. VII. 18.   Component Energy Deposition Rate First Ion

first ion energy group of each component in the spectrum is displayed. The data are given in terms of the power deposited by that ion energy group hence the amplitude of each curve is determined by the product of the flux and the energy loss rate. The energetic light ions (He^{++}, D, T) show deposition profiles which increase with depth until the peak in the stopping power is reached. The silicon ions shown the result of the deposition functions for electronic and nuclear energy deposition. The initial negative slope is characteristic of the electronic loss while the change in slope near the edge of range is due to the nuclear contribution.

The modified spatial energy deposition profiles at the end of each ion pulse are shown in figure VII.19. These data represent the depositions from all of the ions in a spectrum. The silicon is observed to give the largest surface deposition, yet because it is deposited over a longer time, it will not produce the largest temperature excursion. The gas is observed to actually increase the surface deposition from the high energy helium since the ion energies are moved closer to the peak in the stopping power curves. These less energetic ions, however, do not penetrate as deeply as the original spectrum and the extent of the deposition is reduced. The silicon deposition is the most radically affected due to the large loss of energy in the gas. These energy depositions are modified by the gas and are coupled with the reduced fluxes of figure VII.17 to produce a lower temperature rise in the copper.

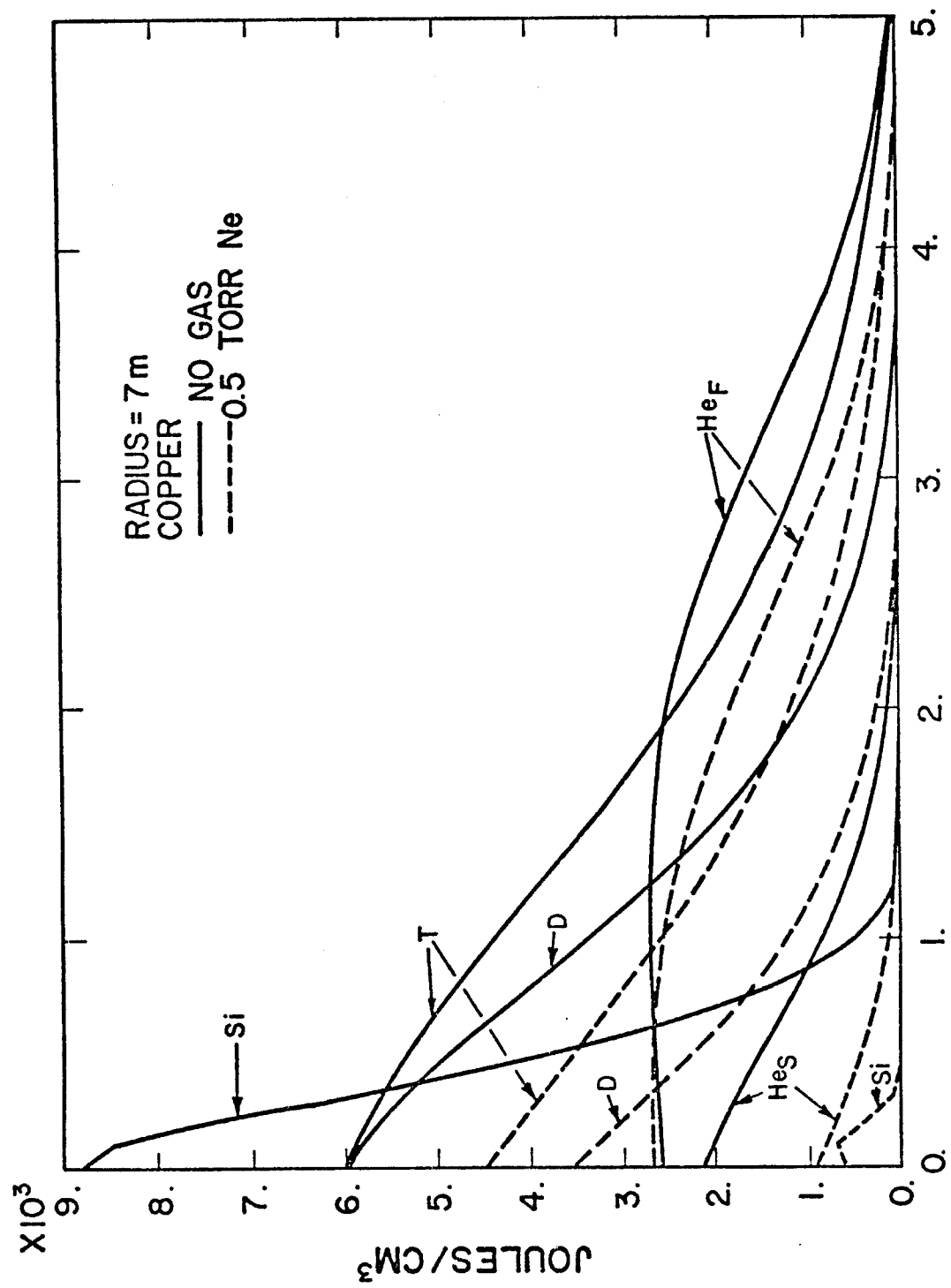The temperature response from each of the components is displayed

Fig. VII. 19. Total Deposited Energy

in figure VII.20 for the case in which no gas is present. The maximum response is due to the X-rays, but surface is observed to cool considerably before the ions arrive. The maximum temperature contribution from the ions is due to the fast helium, followed by the tritium at a slightly later time. The silicon ions produce a smaller temperature excursion than all the ions except the slow helium even though their surface energy deposition was the largest. The surface temperature rise due to all components is observed to be very small after 1 millisecond which is considerably sooner than subsequent pulses might occur.

A comparison of the total temperature excursions due to all the components for bare and gas protected surfaces is displayed at the surface and at a depth of 1 micron in figures VII.21 and VII.22, respectively. The summation of the ion responses is observed to give a net response which is essentially equivalent to that of the photons. The ion temperature pulse is however much longer in duration. At the 1 micron depth the bare wall response due to the ions is only slightly smaller than the surface response. The photon response is however considerably smaller since it consists primarily of energy which has "diffused" from a position nearer the surface.

A reduction in maximum temperature of 50% due to the gas protection is noted in the temperature transient at the surface with a similar reduction at a depth of 1 micron. The same type of reduction to both ions and photons is found at the front surface. At the 1 micron position the temperature excursion is only slightly reduced because the initial transient is due to higher energy photons that
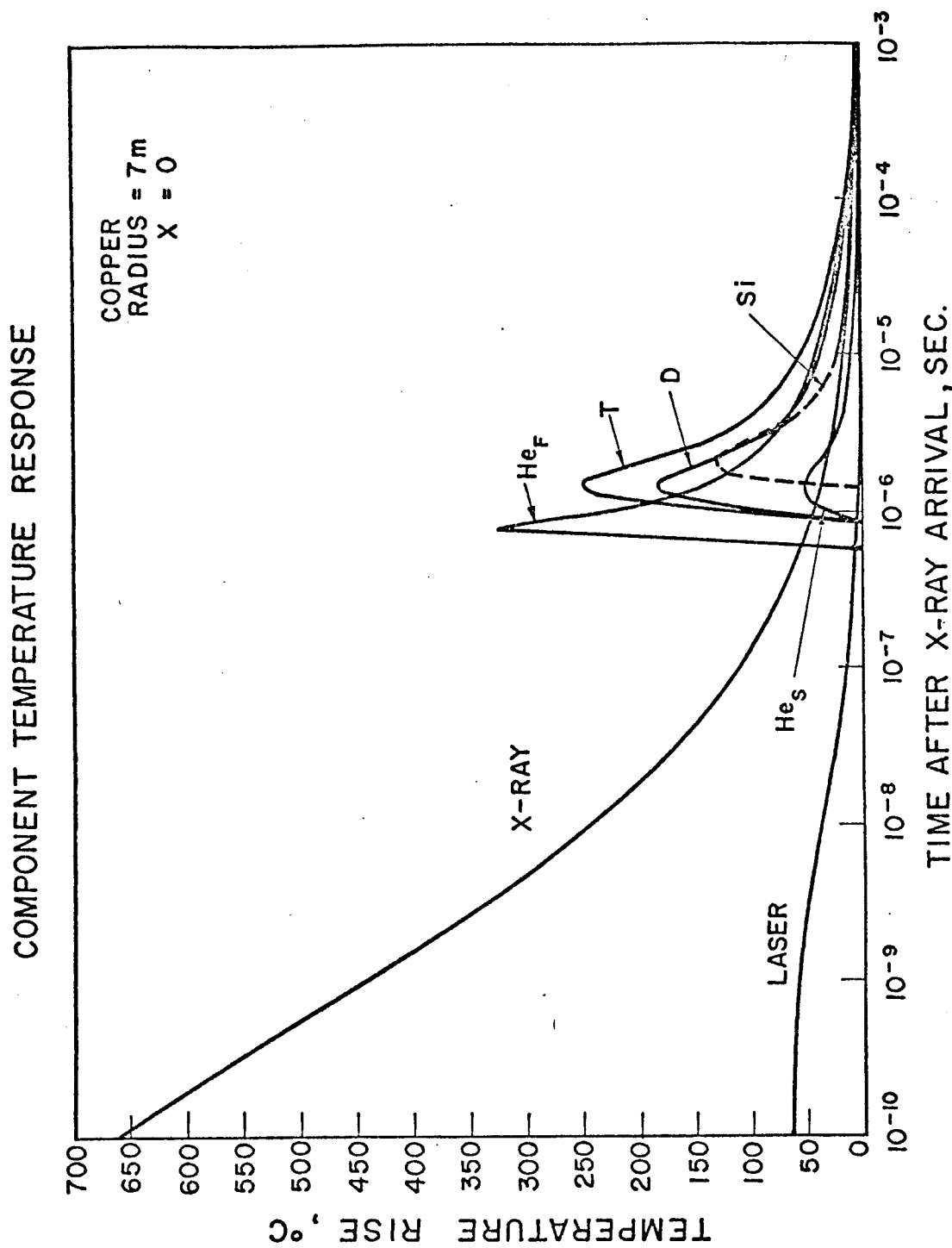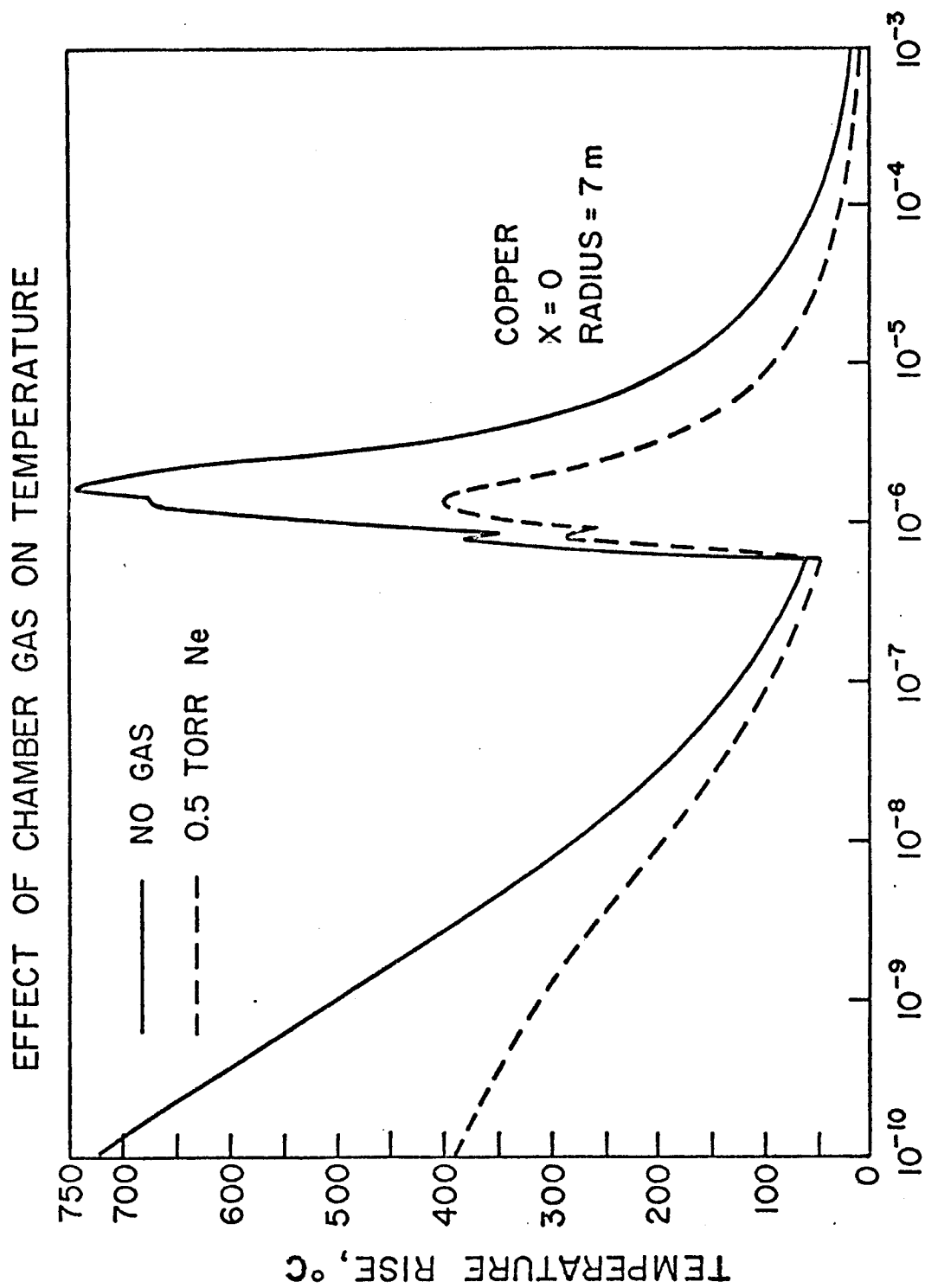
COMPONENT TEMPERATURE RESPONSE

Fig. VII. 20.   Component Surface Temperature Response

Fig. VII. 21. Effect of Chamber Gas on Total Surface Temperature
Response

TOTAL TEMPERATURE RESPONSE

RADIUS = 7m
COPPER
X = 1 MICRON
——— NO GAS
– – – 0.5 TORR Ne
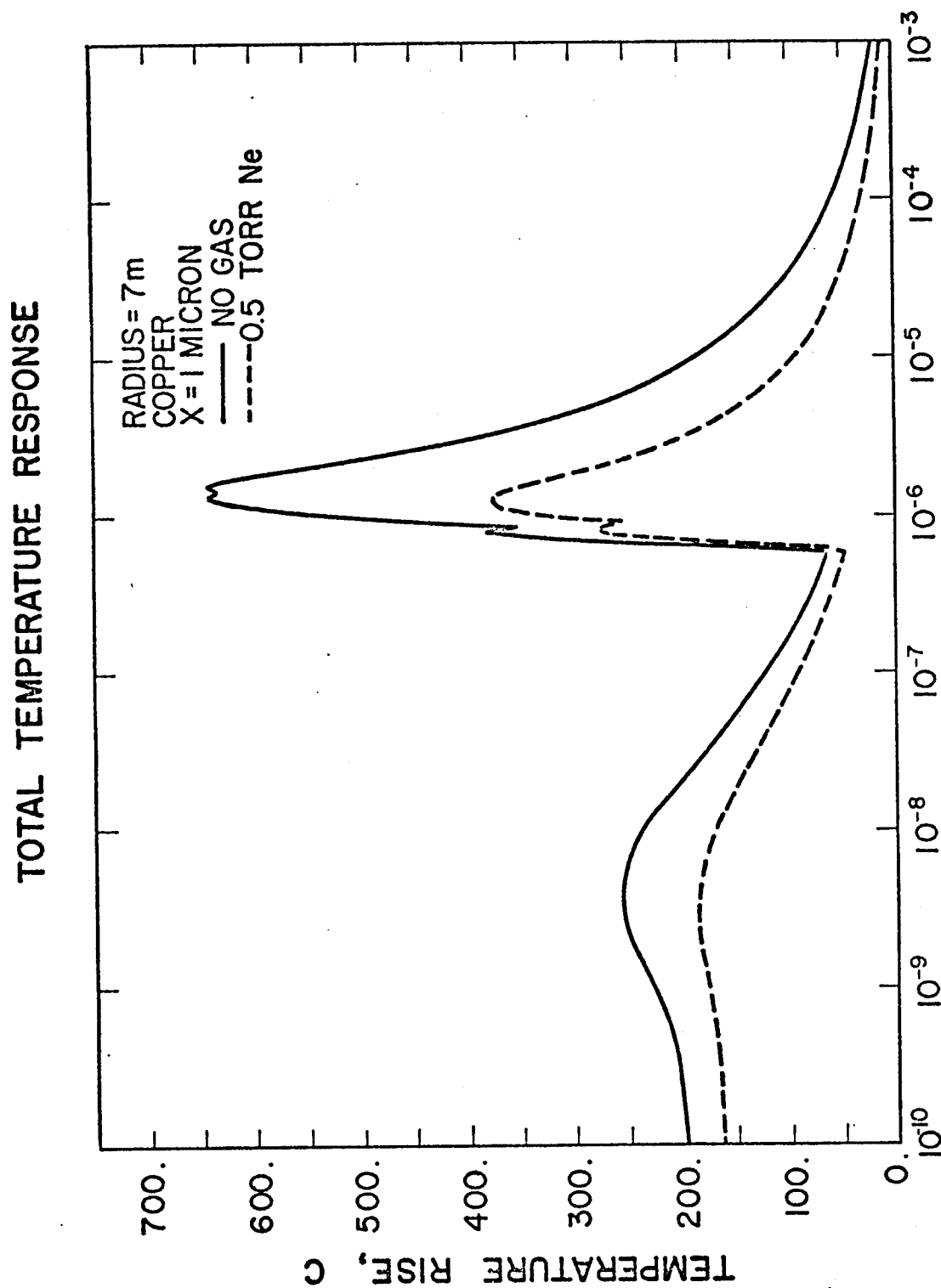
Fig. VII. 22. Effect of Chamber Gas on Temperature Response at
1 Micron

pass through the gas more easily. The reduction in temperature increase noted here not only lowers the probability of approaching the melting temperature, but it also can substantially reduce the severity of other effects such as generation of stress waves, sputtering, and evaporation. The temperature dependence of the latter two of these effects will be discussed in section VII.D.

The displacement response due to each component in the spectrum is shown in figure VII.23 for the unprotected case. The dominant contributor to displacement production is the heaviest ion component, silicon. The other components produce considerably lower dpa rates, as well as lower total displacements per pulse due to the lower effective displacement cross sections. The neutron displacement rates are taken from neutronics calculations by Beranek[7] after making appropriate adjustments for the dpa cross section.

At the 1 micron depth (figure VII.24) the displacement production is larger for all components except the neutrons due to the increasing damage production with decreasing ion energy. The silicon dpa rate is 5 times the surface value but the duration is considerably shorter since all the ions did not penetrate that deep into the solid.

The effect of gas protection on the total displacement production at the front surface shows only about a 30% reduction at 0.5 torr of neon (figure VII.25). This is primarily due to the fact, that although the energy and number of silicon ions are reduced, the lower ion energies are characterized by a significantly higher effective displacement cross section. Figure VII. 26 shows the displacement rate

TIME AFTER X-RAY ARRIVAL, SEC.

Figure VII. 23. Component Displacement Rate at X = 0
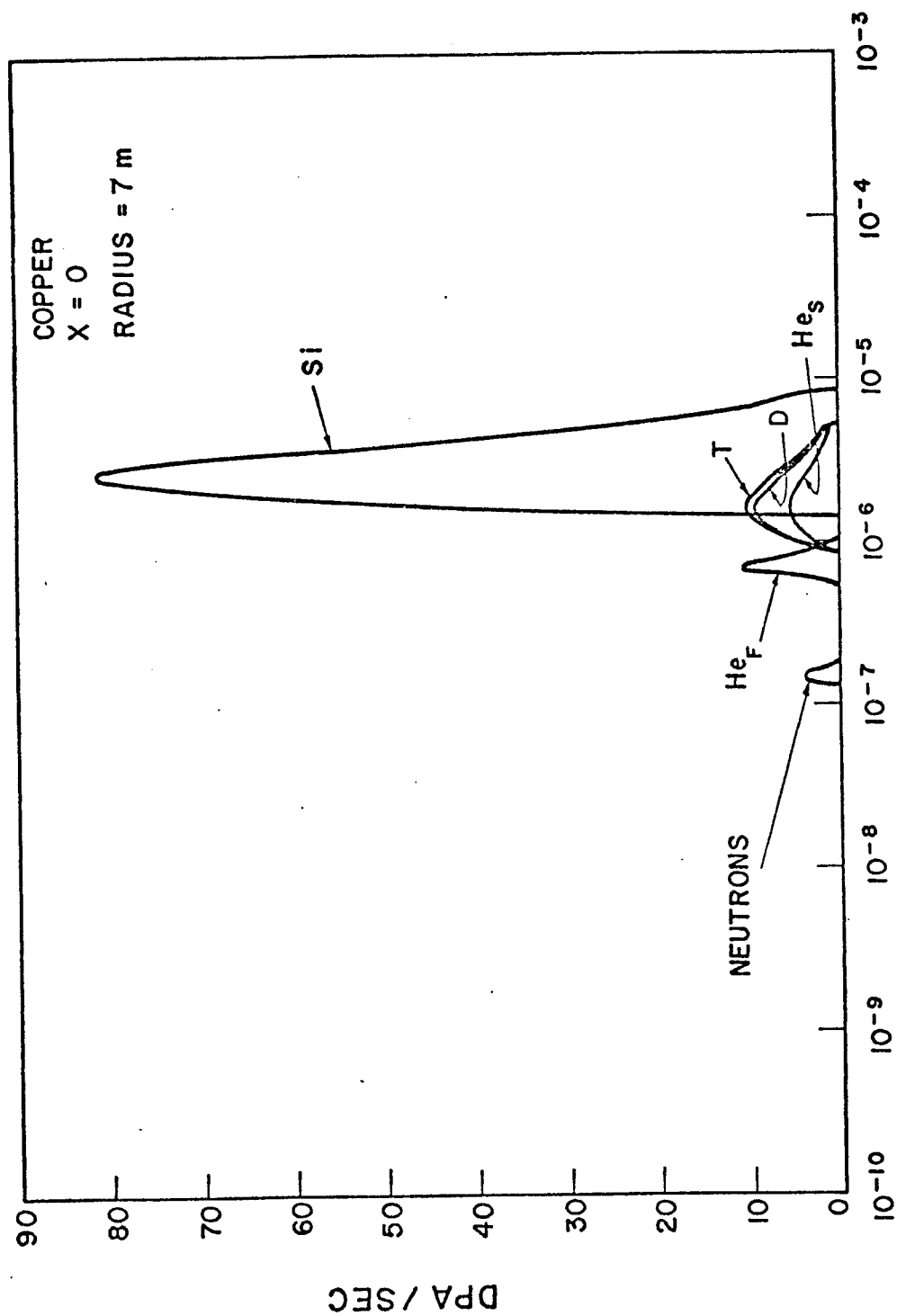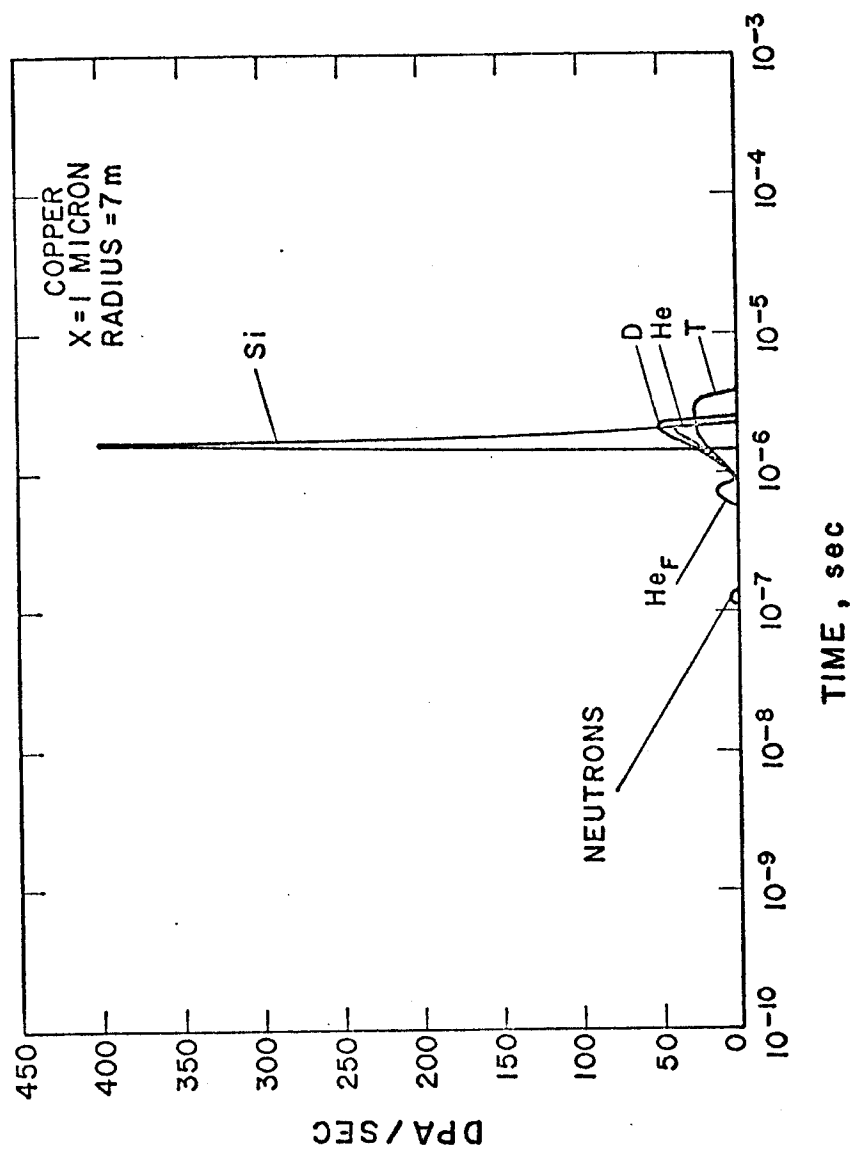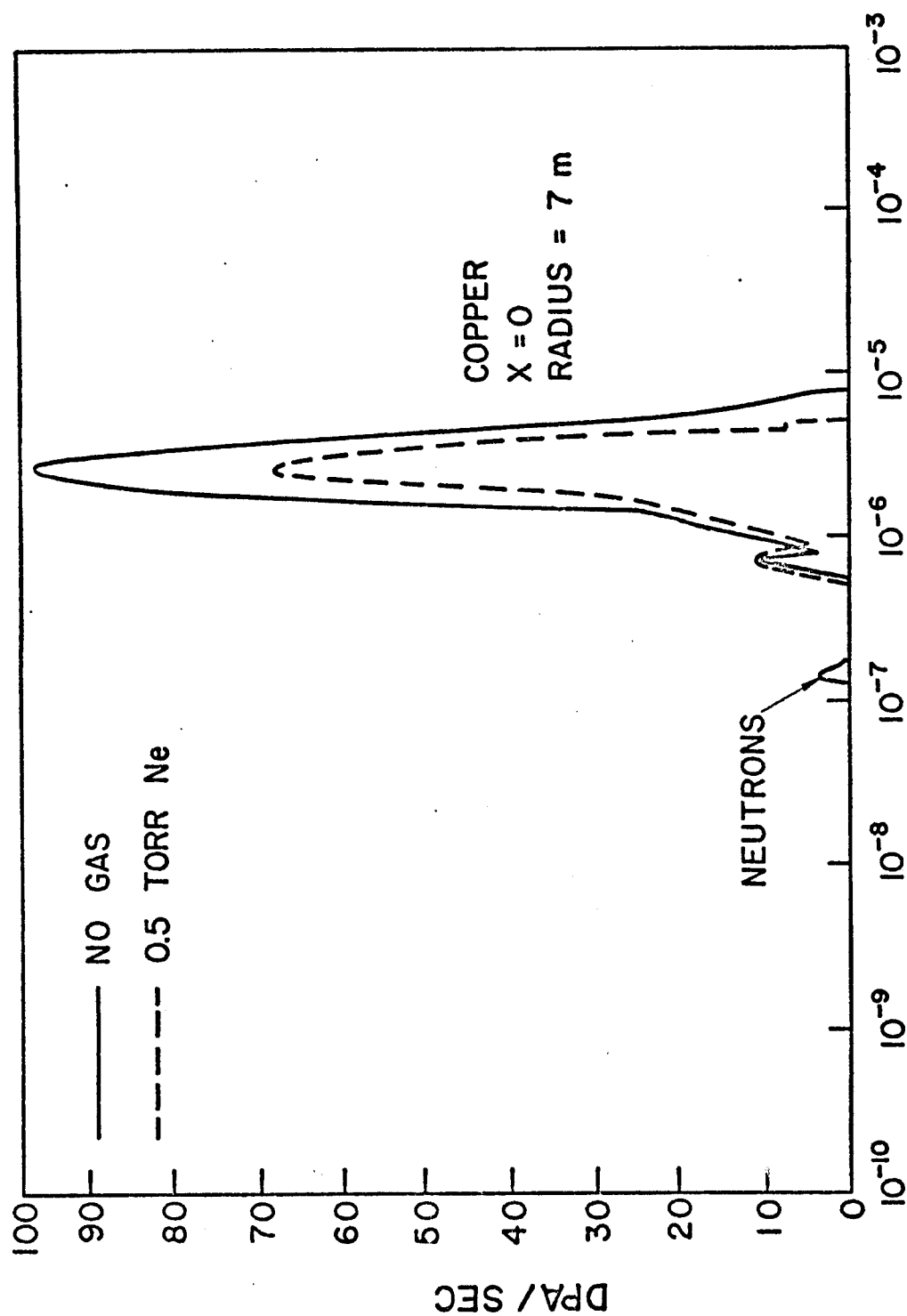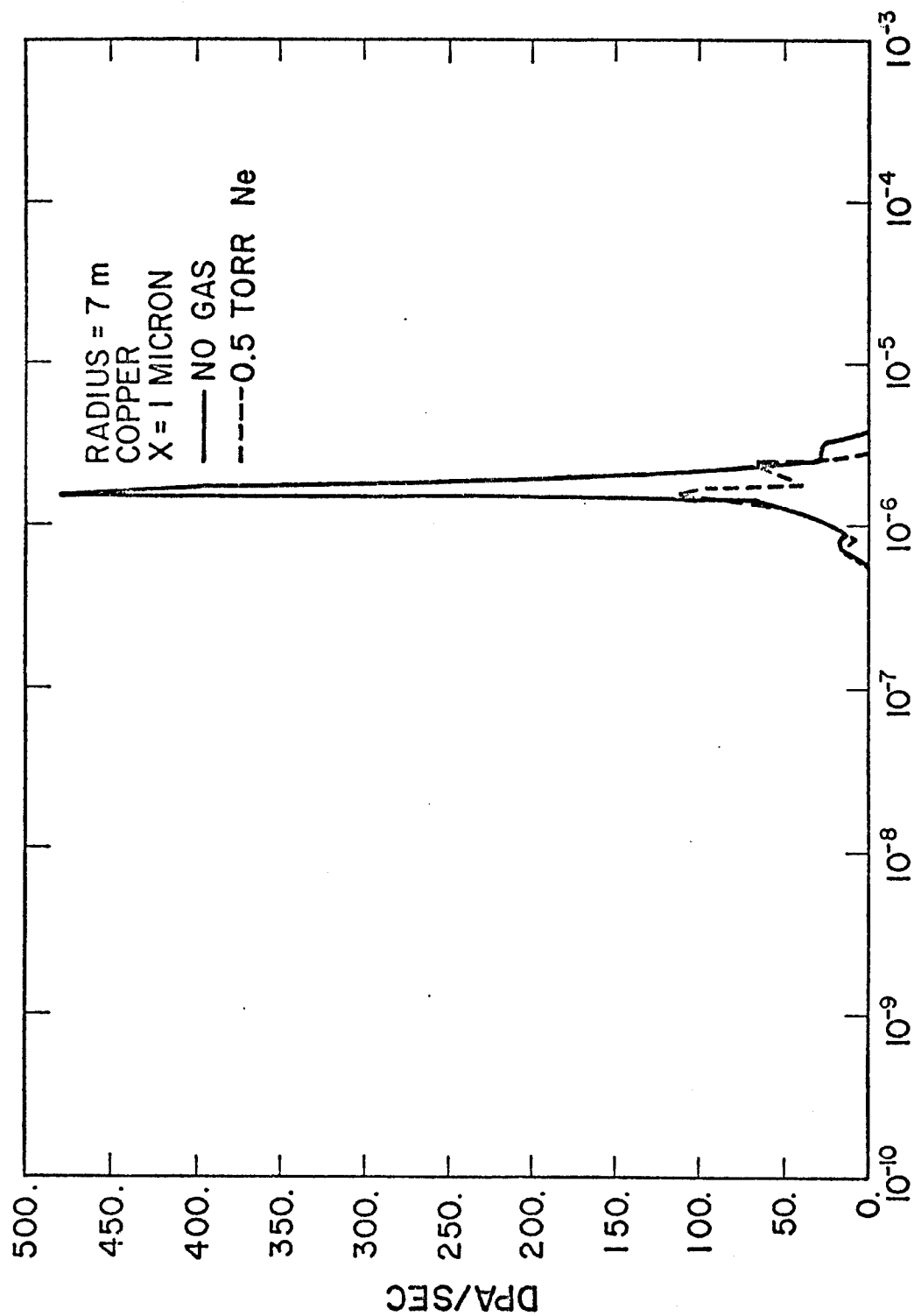
Fig. VII. 24. Component Displacement Rate at X = 1 Micron

Fig. VII. 25. Effect of Chamber Gas on Total Surface DPA Rate

TIME AFTER X – RAY ARRIVAL, sec

Fig. VII. 26. Effect of Chamber Gas on Total DPA Rate at X = 1 Micron

RADIUS = 7 m
COPPER
X = 1 MICRON
—— NO GAS
----0.5 TORR Ne

at one micron. The significant reduction of damage is apparent since the silicon ions are less energetic after passing through the gas and do not penetrate to this position. The displacement production by the neutrons is essentially uniform throughout the material and at greater depths (>10 microns) is the only contributor to the displacement rate. The damage at positions deeper than 1 micron is almost entirely produced by the light components. The most revealing comparison of the effect of gas protection on displacement productions given in fig. VII. 27 which shows the composite spatial distribution of all the ion components after the deposition pulse. The peak damage is reduced from 1.2 x 10^{-3} dpa per pulse to about 3.6 x 10^{-4} dpa per pulse by the addition of gas.

The relationship of temperature rise and displacement modification at the surface is displayed in figure VII.28. Most of the displacements are produced while the material is at an elevated temperature. These temperatures will affect the disposition and lifetime of point defects which are produced; the effective supersaturation concentration will be reduced and existing clustered defects will be annealed.

VII.D. Effect of Irradiation of Subsequent Effects

V.D.1. Introductory Remarks

The last few sections have shown how the ion fluxes, energy deposition, temperature, and displacement production can be simultaneously analyzed for any set of pulsed thermonuclear spectra. This section will address the use of data generated by the methods of this study
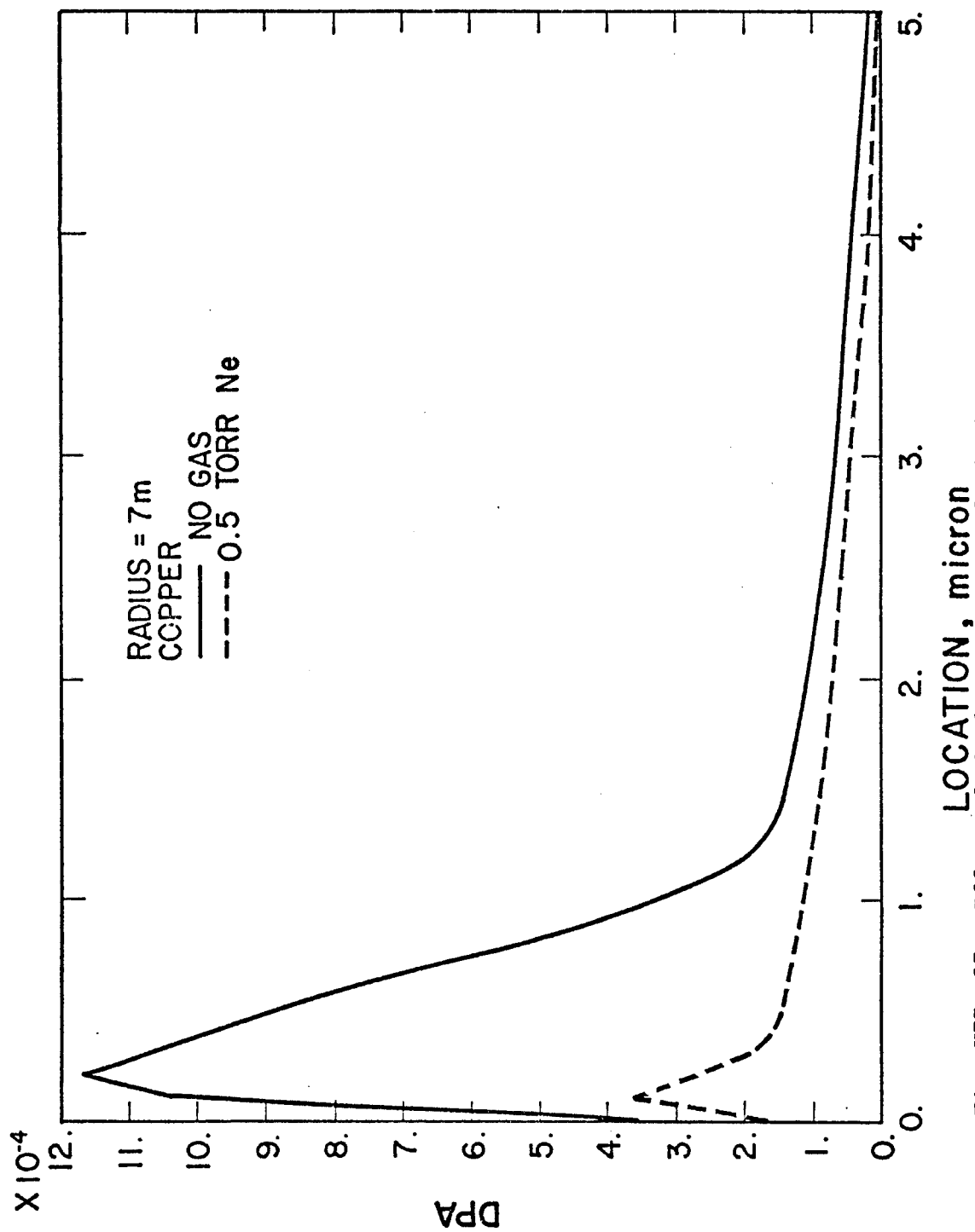
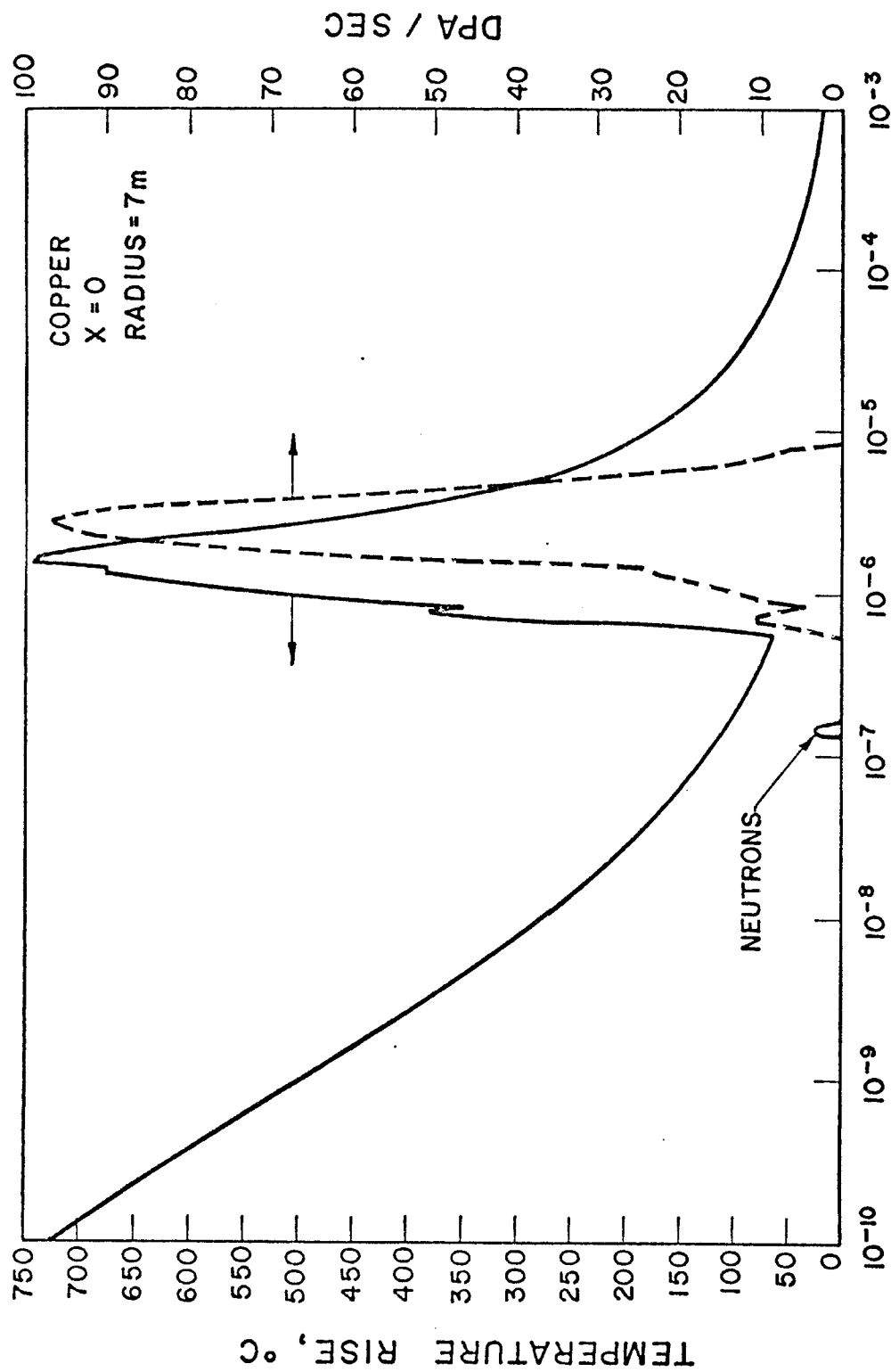Fig. VII. 27. Effect of Chamber Gas on Total Displacement

Fig. VII. 28. Comparison of Surface Temperature and Displacement Rate

for assessing the effect of these combined responses on subsequent effects. Three specific topics will be addressed: transient analysis of sputtering, blistering, and surface evaporation. Models will be reviewed which can estimate these effects and results will be shown for the reference spectrum of the last section upon incorporating these effects into the T-DAMEN code.

VII.D.2. Transient Sputtering Analysis

Ion bombardment of solids can produce erosion of the target surface by sputtering. This sputtering process is the result of near surface atoms which acquire sufficient momentum normal to the surface to escape the binding potential. Theories to explain the magnitude and spectra of sputtered ions have been developed which account for such mechanisms as random collision, cascades, focused collision sequences, ion or atom channeling, and thermal spikes. These theories have been summarized in review articles by many authors including McCracken [114] and therefore will not be reviewed here. The emphasis here will be on models which have been used to predict the energy and temperature dependence of the sputtering yield.

VII.D.2.a. Energy Dependence

Experimental studies indicate that the sputtering ratio, i.e., the number of atoms sputtered per incident ion, shows an energy dependence which is proportional to energy at low ion energy, reaches a maximum value, and is then inversely proportional to energy at higher ion energies. This behavior is demonstrated for niobium in

figure VII.29 for various incident ions. In general, this dependence on ion energy is in agreement with the theory of Sigmund[115] which directly correlates the sputtering yield with the energy transferred into nuclear processes at the surface. This relationship also explains why ions of higher mass have much higher sputtering ratios than light ions and why neutron sputtering values are several orders of magnitude less than most ions. In addition, this model supports the existence of a threshold energy for sputtering since the ion energy must be sufficient to transfer the binding energy to an atom in a binary collision.

Although theoretical models have been formulated, including numerical studies such as the Monte Carlo calculation of Haggmark[116] and discrete ordinance methods of Hoffman, et al,[40] no unified theory can reproduce all the experimental observations to date. Consequently, empirical models have been developed which are useful in estimating sputtering yield.

One model is that of Bohachevsky[117] which determines the energy dependence of sputtering yield and the dependence of sputtering ratio on the impact angle of the incoming ion. The energy dependence is given by:

$$161) \quad S(\varepsilon) = \frac{S_o \; (\ln \varepsilon)^{1+C/\varepsilon}}{\varepsilon \; 1 + b/e}$$

where: $\varepsilon = E/E_o$ which is ≥ 1

S_o, b, C are empirically determined constants

E_o is the threshold energy.

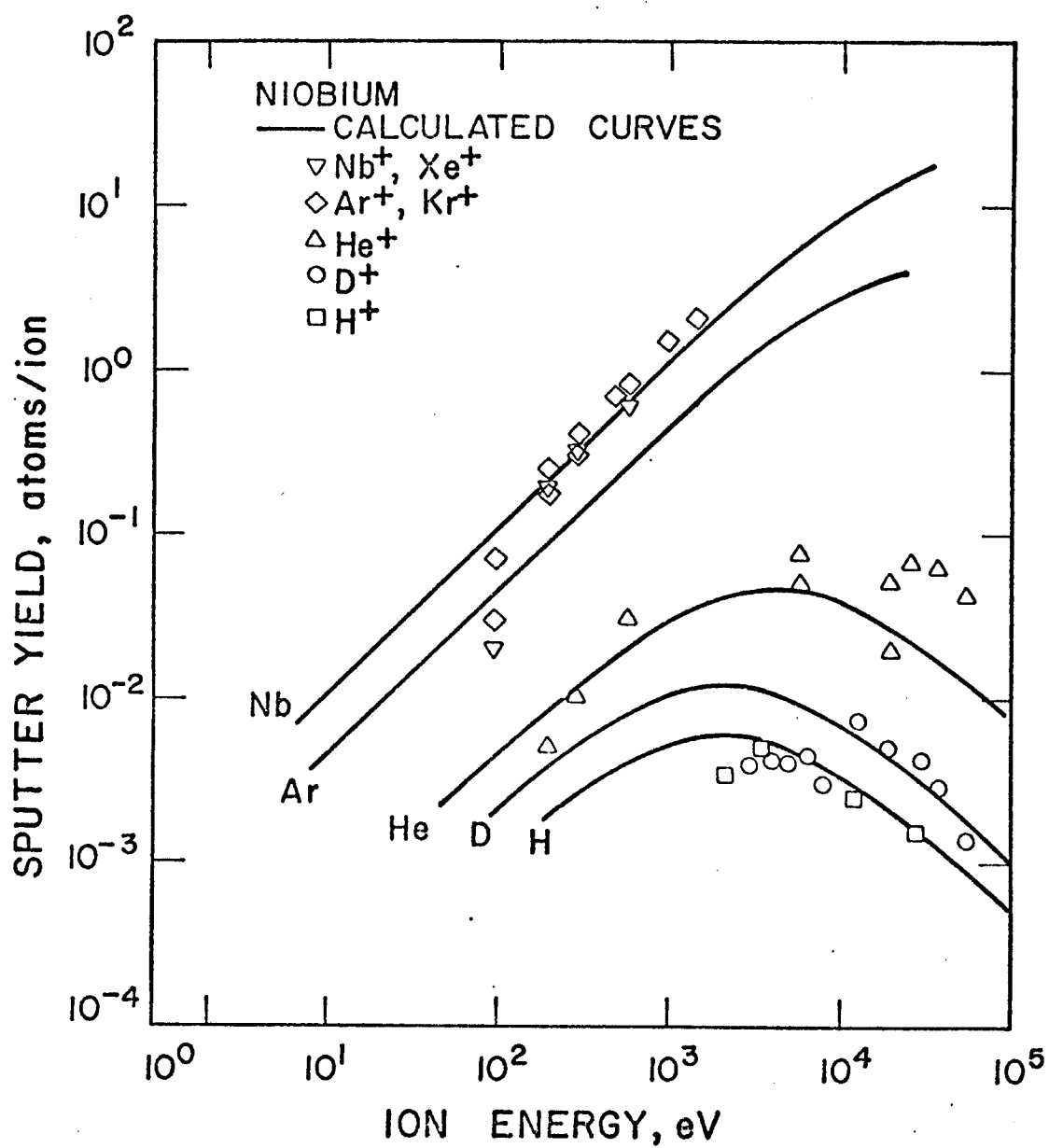A similar empirical expression for the angular dependence was also

Fig. VII. 29.   Ion Sputtering in Niobium

determined by Bohachevsky but will not be repeated here since this discussion will be limited to normally incident ions.

The net sputtering ratio is obtained from the product of equations for energy and angular dependence. Bohachevsky has used these functional forms and an interactive computer analysis technique to reproduce sputtering data for various ion-target combinations.[117-118] Although equation 1 gives a good representation of the energy dependence, it is awkward to develop the empirical parameters, S_0, b, c unless the software of the Bohachevsky codes is used.

An alternative energy dependence is given in the work of Smith[119] who develops a simpler formula which basically shows proportionally to E at low and 1/E at higher energies. Smith presents the formula so that it can account for all ion-target combinations by introducing a factor which depends on ion-target mass and atomic number and a factor which contains the energy dependency as:

2)
$$S = \frac{C}{V_0} \; f_1(Z,M)f_2(E,Z)$$

where: C is an empirical constant

V_0 is the surface binding energy

f_1 is the mass factor

f_2 is the energy factor

The mass factor is a simplification of the relationship for the atomic number and mass dependence of the nuclear cross section which Smith gives as:

3) $$f_1(Z,M) - Z_1 Z_2 \frac{M_1}{M_2}$$

where: Z_1 = ion atomic number

Z_2 = target atomic number

M_1 = ion atomic mass

M_2 = target atomic mass

the energy dependent factor is given as:

4) $$f_2(E,Z) = \frac{Z_1 Z_2 E}{(E + 50\ Z_1 Z_2)^2}$$

where: E is the ion energy in electron volts and the factor 50 was empirically determined from the data at the energy peak.

Equation 3 and 4 were combined into equation 2 and the empirical constant, C, was determined by assessing data from numerous ion-target combinations. The result was:

5) $$S = \frac{20}{U_0}\ Z_1^2 Z_2^2 \frac{M_1}{2M_2}\ \frac{E}{(E + 50\ Z_1 Z_2)^2}$$

Although equation 5 gives the proper general function dependence of sputtering ratio on energy it was found in this study to be inadequate for all ion-target combinations, consequently, its use was limited to cases where the constants were determined from available data.

Specific information on sputtering yield of copper can be estimated from the work of Sigmund[115] in which data for neon and argon bombardment were compared with theory. Approximate sputtering values for silicon bombardment of copper are a peak value of 5 atoms/ion at

50 keV and 1.5 atoms/ions at 800 keV. These data can be put in the form

of equation 5 as:

6) $$S_e(E) = 19.4 \ z_1^2 z_2^2 \ \frac{M_1}{M_2} \ \frac{E}{(E + 166.8 \ z_1 z_2)^2} \ 2$$

where: E = ion energy in eV

$S_e(e)$ = sputtered atoms/ion

Similar expressions are easily devised for other ion-target combina-

tions. Equation 6 is assumed to be valid for small perturbations in

z_1, M_1, and z_2,M_2 around silicon and copper, respectively.

VII.D.2.b. Surface Temperature Dependence

Sputtering yield has been found to be dependent not only on the

ion energy and angle but on the temperature of the surface as well.

This effect was noted by Nelson[120] in which experiments were per-

formed at various temperatures for Au, Ag, Cu, Zn, Bi, and Ge.

Sputtering yield was measured in excess of evaporation and in general

found to range from values near 1 at room temperature to ~30 at 90%

of the melting temperature. This enhancement of sputtering yield at

high temperature is attributed to thermal spikes and was also investi-

gated in the work of Chapman, et al.,[121] in which sputtered ion

spectra were observed for Au and found to increase in the range of

0.1 to 1.0 eV as surface temperature is increased.

In the analysis here it was assumed that this temperature effect

could be incorporated in the form of equation 167.

7) $$S(E,T) = S_e(E)S_t(T)$$

where: $S_e(E)$ has the form of equation 6 and $S_t(T)$ has the form:

8) $$S_t(T) = 1 + K\ e^{-E_0/kT}$$

where E_0 is an empirically determined activation energy and

K is an empirical constant.

The original data of Nelson were for 45 keV bombardment of copper with Xe ions. These data were normalized to silicon irradiation at 800 keV using relations for the relative mass dependence data of Anderson and Bay[122] and the energy dependent data of Sigmund.[115]   The result of this estimated temperature effect is shown in figure VII.30 and the constants in equation 8 were determined as:

$$K = 3.219 \times 10^7$$

$$E_0 = 1.476\ eV$$

VII.D.2.c.   Application to General Spectrum

The energy and temperature formulation for sputtering can be coupled with the surface ion arrival flux and spectrum and the temperature response models of previous sections to determine the enhancement of sputtering due to the thermal effects. This coupling was done in the T-DAMEN code and the response to the spectra in table VII.11 was analyzed. The sputtering rate due to the silicon ions was calculated using the temperature response due to the entire spectrum. The results of this analysis are shown in figure VII.31 in terms of sputtering rate during the irradiation for various ambient temperatures. At higher ambient temperatures an order of magnitude
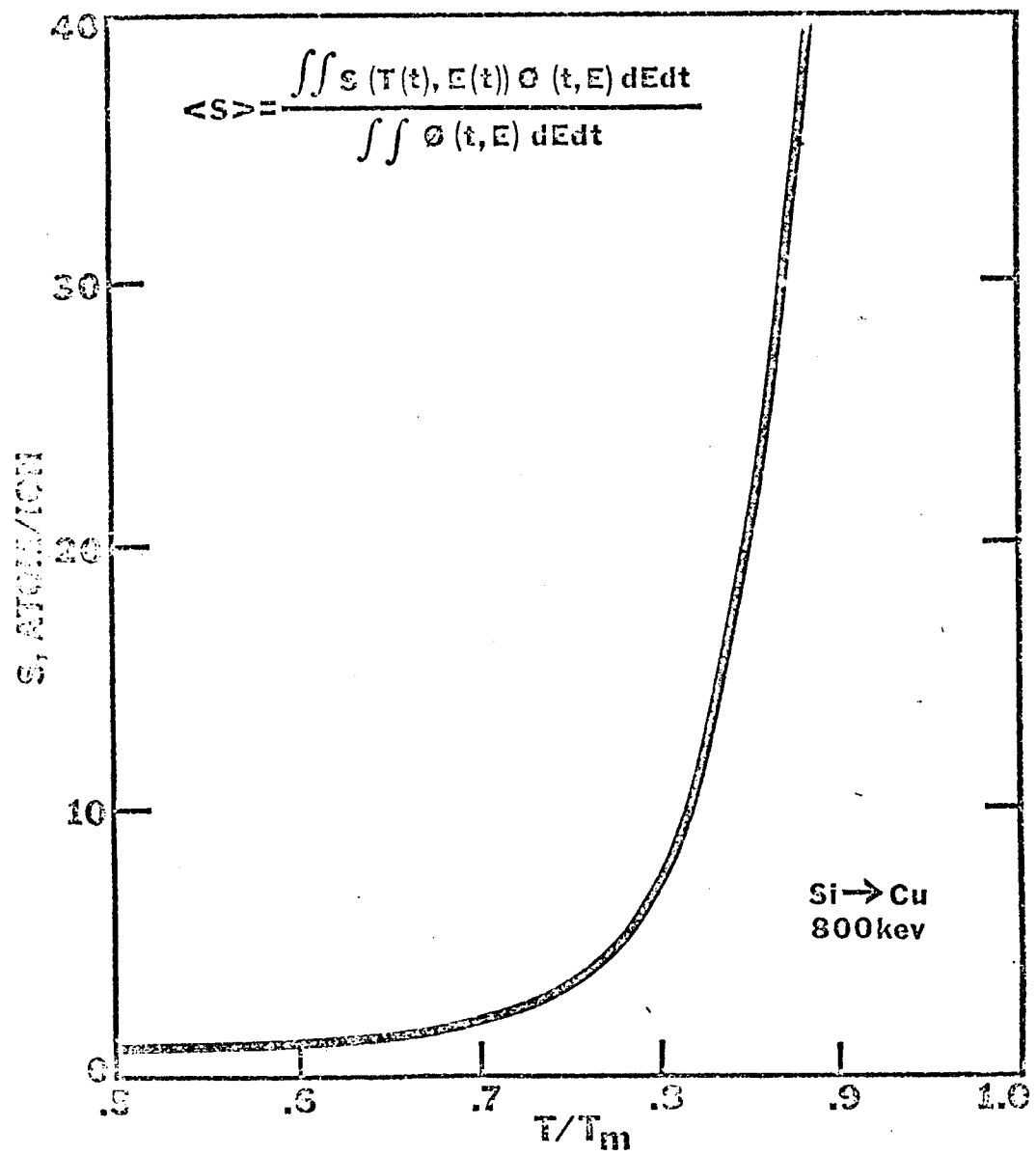
$$<S> = \frac{\iint S\,(T(t),\,E(t))\,\emptyset\,(t,E)\,dEdt}{\iint \emptyset\,(t,E)\,dEdt}$$

Si → Cu
800 kev

Figure VII. 30.   Temperature Dependence of Sputtering in Copper
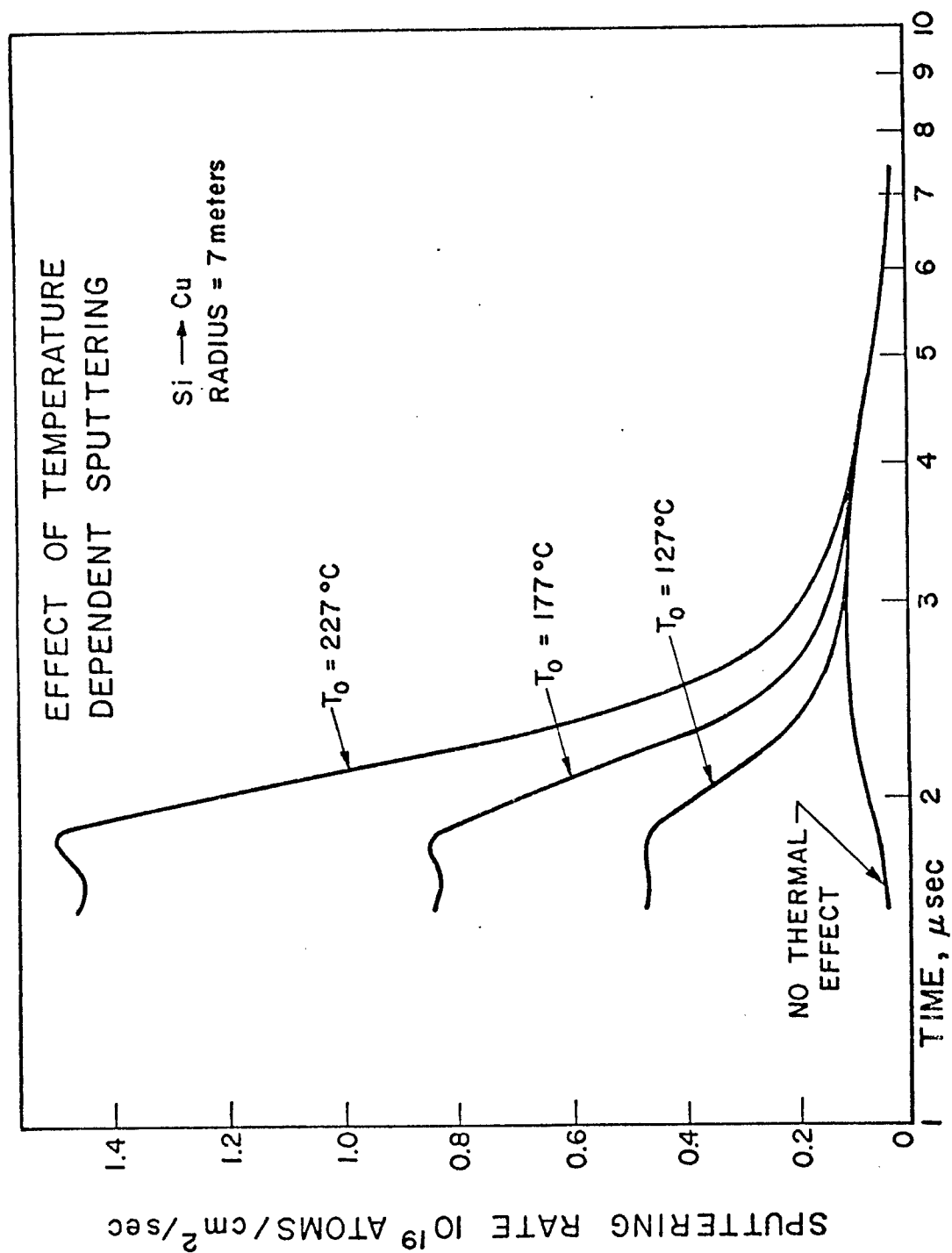
297

Figure VII. 31. Effect of Temperature Dependent Sputtering

increase in sputtering rates is observed. The synergism between ion energy, flux and surface temperature can be understood by comparing figure VII.31 with the surface temperature response data of section VII.C. This comparison reveals that while the peak sputtering ratios are higher, the thermal effect amplifies the initial higher energy part of the silicon spectrum, because temperatures are still elevated due to deposition of the other ion components. The later, lower energy silicon bombardment occurs after the surface has cooled and the rates are not enhanced significantly by the temperature.

The total ions sputtered per pulse is shown in figure VII.32 as a function of ambient temperature. These data indicate that if the ambient surface temperature is low enough, the enhancement of sputtered will be negligible.

At an ambient temperature of 227°C the total sputtering yield due to the silicon ions was 1.5×10^{13} atoms per pulse or a 0.0174 $\overset{\circ}{A}$ per pulse erosion when the surface temperature effect is considered. For a 1000 MW_t reactor operating at an 80% plant factor, this would correspond to surface erosion rates of 0.439 mm per year. This is in contrast to about 0.00481 $\overset{\circ}{A}$ per pulse and a wall erosion rate of 0.121 mm per year when the sputtering is based on ambient temperature only. This comparison indicates that previous calculations which do not consider the surface temperature may have seriously underestimated the wall erosion rates in inertial confinement systems.

VII.D.3. Surface Evaporation for Transient Pulses

One possible mechanism for the deterioration of first walls in
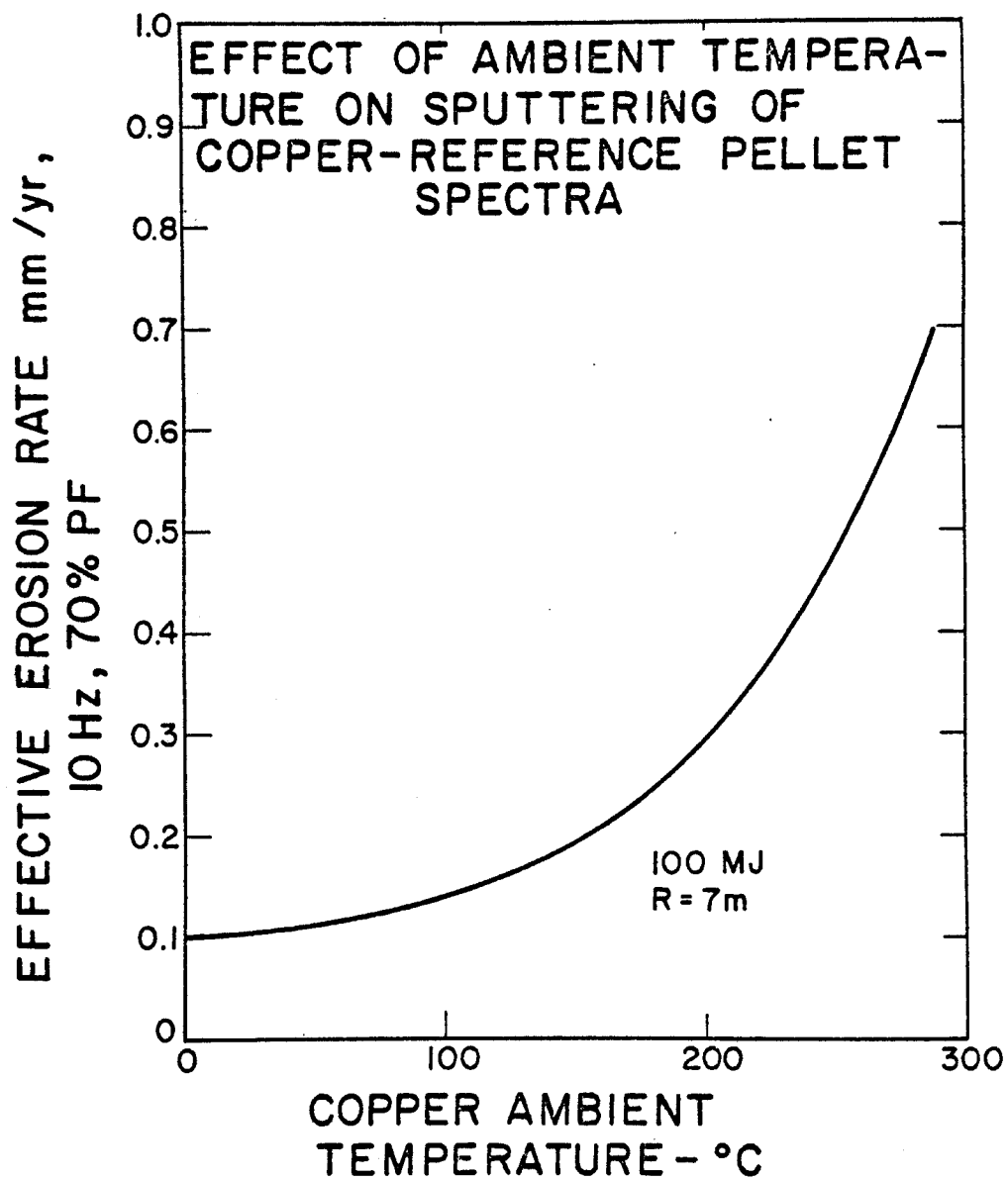
Fig. VII. 32. Effect of Ambient Temperature on Sputtering
of Copper

fusion devices is erosion by evaporation. The high temperature transients associated with inertial confinement fusion reactors can be associated with high evaporation rates. The analysis of the time history of surface temperature using the methods of this study allow an estimate to be made of the severity of this effect.

A simple model to estimate evaporation rate from the equilibrium vapor pressure of a solid material is given by Behrish[81] as:

9) $$\overset{\circ}{n}(T) = \alpha \frac{3.5 \times 10^{22}}{\sqrt{m}} \frac{P(T)}{\sqrt{T}}$$

where: α is the sticking probability (normally = 1)

m is atomic mass, amu

P is the vapor pressure, Torr

T is surface temperature, K

$\overset{\circ}{n}$ is evaporation rate, atoms/sec/cm^2

The vapor pressure for metal are well-known and can in general be described by:

10) $$P = P_0 \exp \left(\frac{-\Delta H}{kT}\right)$$

where: ΔH is the heat of sublimation

k is Boltzmann's constant

P_0 is a derived constant

This equilibrium model is assumed to be appropriate for temperature excursions experienced in inertial confinement systems. The response to X-rays, because of its short duration may require modification for non equilibrium effects. The temperature excursion due to

ions are sufficiently long (microseconds) compared with atomic vibrational periods that the above models are reasonable estimates and it is the ion response that is the dominant contributor to surface evaporation.

The above models can be applied to the previous analyses for surface temperature history to determine the evaporation rate in a similar manner as that done for carbon due to X-ray and heat flux responses reported in reference 80.

The evaporation rate of copper at an ambient temperature of 200°C exposed to the reference spectrum of table VII.2 using data for the vapor pressure of copper from reference 123 is shown in figure VII. 33. The time integral of the rate data is given in figure VII.34 which indicates that the ion contribution to the total evaporation is four orders of magnitude greater than that due to the photons.

A comparison with the sputtering data of section VII.D.2 indicate that for copper (and this spectrum) the evaporation rate is about a factor of 10^5 lower than the sputtering rate hence rendering it insignificant for this case.

Additional calculations were performed for the same reference spectrum and a carbon surface at 7 meters radius. These data (figures VII.35 and 36) indicate that significantly more carbon atoms will be lost due to evaporation for a surface initially at 1200°C. This is an expected effect due to carbon's higher evaporation rate. The peak temperature rise during the ion deposition in carbon was ~ 1550°C, which on a homologous basis is similar to that of the copper.
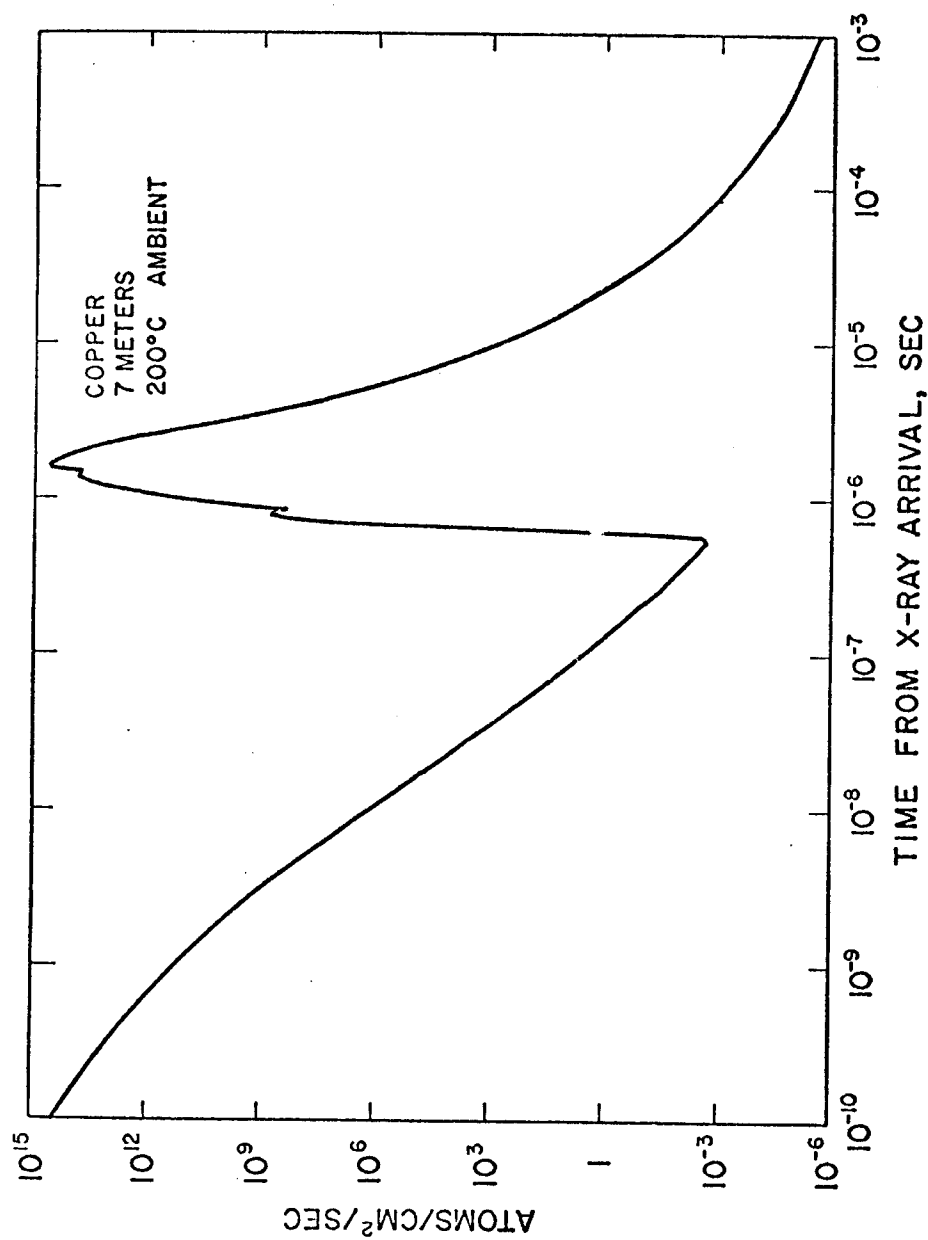
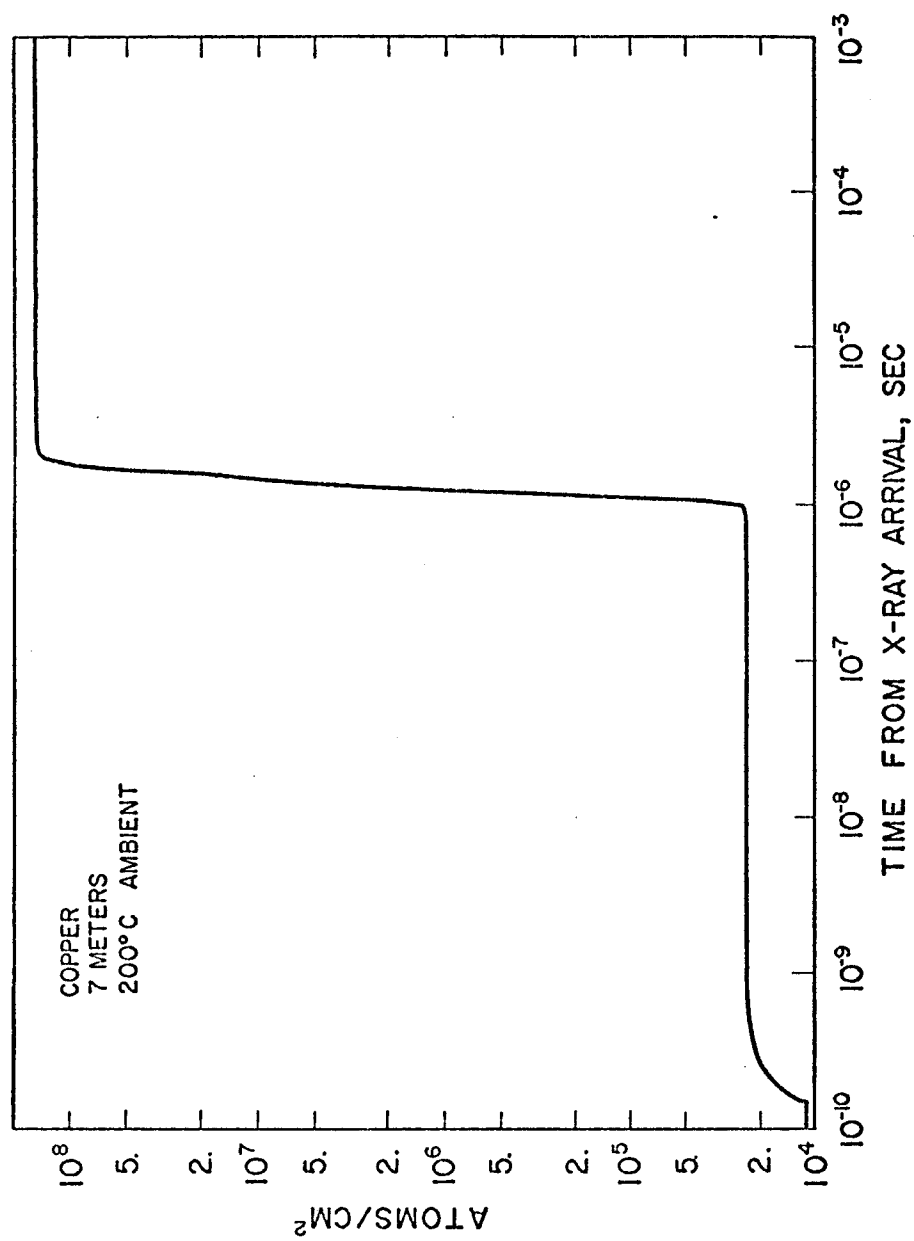Fig. VII. 33. Surface Evaporation Rate of Copper
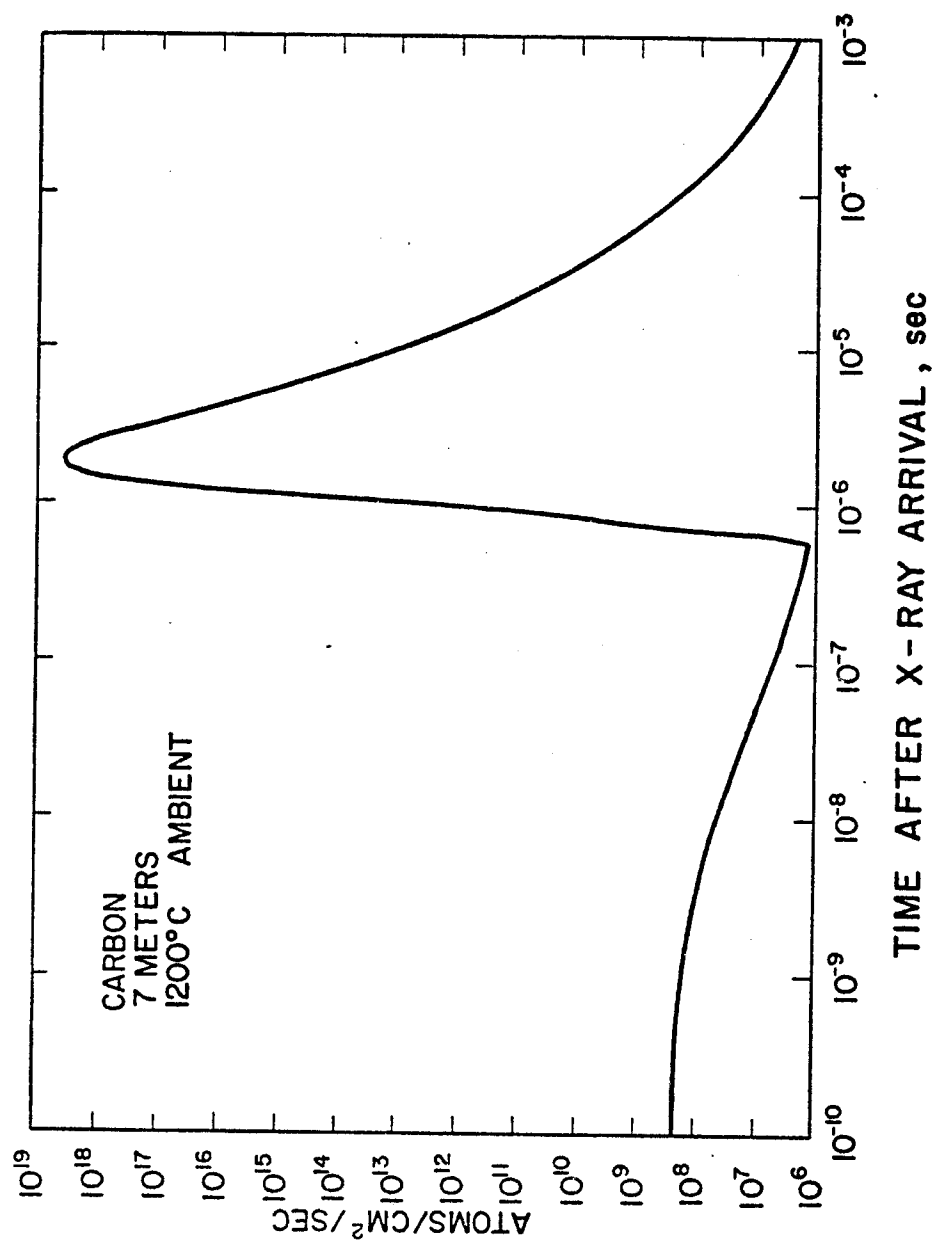
Fig. VII. 34.   Surface Evaporation of Copper

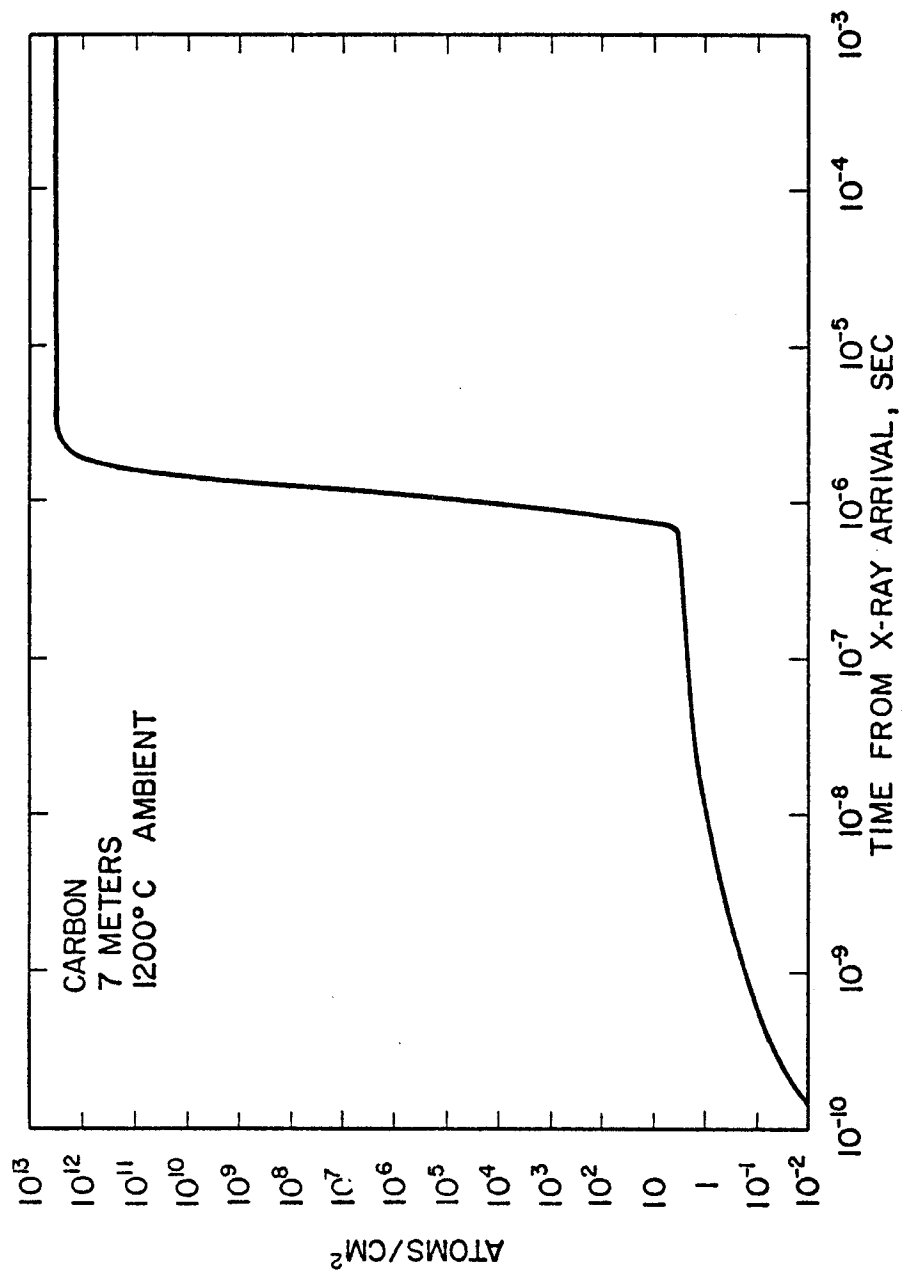Fig. VII. 35. Surface Evaporation Rate of Carbon

Fig. VII. 36.   Surface Evaporation of Carbon per Pulse

VII. D.4. Implications for Blistering

The deposition of light ions in the walls of fusion devices can cause additional deterioration by blistering of the surfaces. This phenomena has been attributed to a build up of gas atom concentration in small bubbles which coalesce when a critical concentration is reached.[124] The resulting agglomeration of bubbles exerts a pressure on the surface sufficient to cause plastic deformation and eventually fracture of the blister. The formation and fracture of blistering are associated with the re-emission of the gas species which is observed experimentally to occur in ion doses of $\sim 10^{18}$ ions/cm^2.[125]

It was not the intent of this study to present the various mechanisms associated with the blistering phenomenon nor to analyze in detail its effects, but rather to use the analyses of the previous sections to demonstrate aspects of potential importance in inertial confinement devices.

Information on the radiation damage environment in terms of temperature, displacement production, and ion implantation distributions can be derived from the T-DAMEN code. An example of this data from the reference spectrum of table VII.2 is given in figure VII.37 in which the helium concentration for both fast and thermal components is displayed.

In contrast to typical blistering experiments in which the implanted helium distributions are due to monoenergetic ions, the helium atom distributions in inertial confinement systems are determined by all the energies of the ion spectra arriving at the front surface.

In addition, the helium atoms come to rest in regions of high lattice distortion which are subject to high temperature fluctuations for about 10 microseconds.

The relation of these effects are shown in figure VII.37 in which the total displacement profile at the end of the pulse and temperature profiles at various times during the pulse are also given. The implantation distributions were found to have peak concentrations of 2×10^{16} atoms/cm^3 located approximately 1 micron into the copper for each pulse.

The severity of blistering in these environments can be estimated from the data of Bauer and Thomas[125] who have reported significant increases in the re-emission of niobium at fluences of approximately 10^{18} He ions/cm^2 at 300 keV. Ignoring the difference between copper and niobium and assuming their data are indicative of spallation thresholds, these calculations indicate that equivalent peak concentrations will be achieved in a laser fusion device after about 80 hours at 1000 MW$_t$. This concentration is achieved, however, after a fluence which is about 10 times greater than required for a mono-energetic spectrum due to the width of the He spectra.

In addition to the spectral differences on the fluence-critical concentration relationship, the temperature excursions will also influence the history of gas atoms. An indication of this effect can be seen in the work of Wilson,[126] who, by observation of gas re-emission characteristics, identified three temperature regions which exhibited different response:
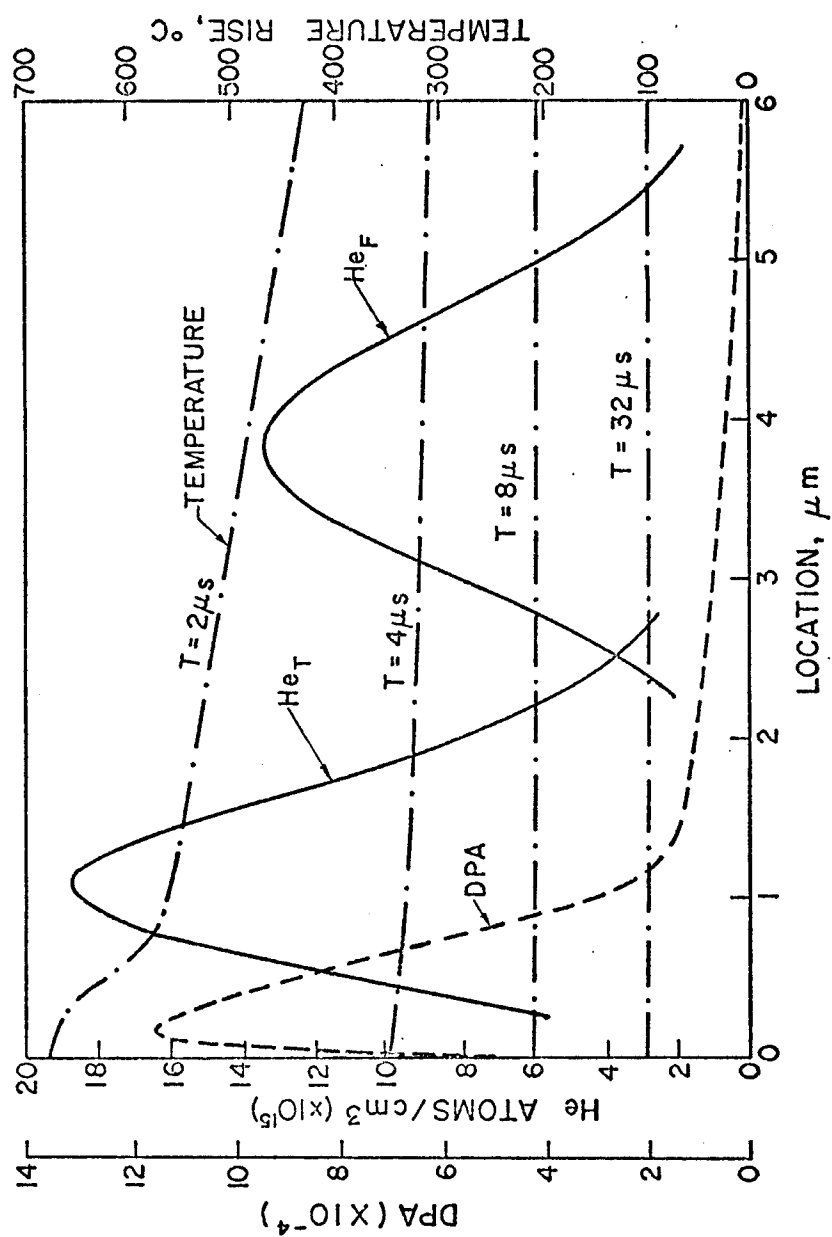
Fig. VII.37 • Implanted Helium Distribution and Associated Damage and Temperature Profiles

1. Low temperature blistering (~ 0.1 T_m)

2. Intermediate temperature flaking (~ 0.3 T_m)

3. High temperature blistering and pore formation (~ 0.5 T_m)

An interesting consequence pertinent to high temperature environments was that although surface deformation occured in all regions, erosion was only observed in region 2. Hence, at high temperature the helium can escape via pores after which the surface becomes stable to subsequent He bombardment, since the gas is released at the same rate as it is implanted.

An additional consequence is the high damage produced near the surface by the heavy ions. This region can intersect the low energy implantation zone. The synergism of this high damage and high damage rate will effect the migration of the helium atoms. An example of such a complex environment is in the work of McDonnell[127] in which whisker growth was observed in containers for short-lived transuranium nuclides. Platinum - 10% Rh capsules containing ^{252}Cf experienced surface exposure to both alpha particles and fission fragments. The damage produced by the fission fragments overlapped the helium implantation and elongated blisters in the form of "whiskers" were observed at helium concentrations of 3 atom % instead of the 20 atom % required at low temperature for helium bombardment alone.

The surface damage environment in inertial confinement systems is even more complex than observed by McDonnell due to its transient nature. The methods of this study, however, provide methods to assess the conditions on which a more detailed analysis can be performed.

CHAPTER VIII

SUMMARY AND CONCLUSIONS

VIII.A. Summary of Results from the Development of Analytical Methods

This document provides the basis for a general, comprehensive set of analytical models which can be used to determine the response of materials to transient thermonuclear radiation. The phenomena which are associated with the interaction of radiation with materials have been organized and incorporated into an analysis methodology which will allow determination of the radiation damage environment for an arbitrary set of photon or ion spectra.

This technique has proven to be useful in the assessment of the response of first walls and other components in inertial confinement fusion reactor (ICRF) designs. The numerical efficiency of the methods developed coupled with the linearity of these models allow a self consistent analysis of numerous effects from many different radiation species. This coupling and multiple response assessment were considered impractical by previously employed methods which were developed for a single response or interaction process.

The models developed provide for determination of the energy deposition, temperature, and displacement production as functions of time and space in the exposed material. In addition, methods were shown to assess the conditions for formation of thermoelastic stress waves. These responses were coupled to determine the synergistic effect on such subsequent phenomena as sputtering, surface evaporation, and blistering.

In addition to models for calculating response of exposed surfaces, a method was developed in this study to provide for the alteration of ion spectra in gases which might be used to protect first walls in ICFR's. This model which is based on a diffusion approximation to the transport of ions in continuous media allows determination of ion distributions at intermediate energies between impact and rest. This method was shown to generally agree with more complex numerical methods and due to its simplicity could be used to predict ion flux and spectra at various positions in the gas for initial spectra exhibiting wide energy distributions.

Another development which allowed formulation of the response into models which were sufficiently efficient to accomodate multi-group spectra was the concept of deposition. functions for ion irradiation. These functions were general polynomials whose co-efficients are energy dependent and can therefore be used to repro-duce the electronic or nuclear energy deposition for an ion of any energy. These functions, which become analogous to cross sections for neutronics calculations, were created by processing the results of implantation codes for monoenergetic ions.

These deposition functions not only allow assessment of the energy deposition profiles for general spectra but can also be used to develop the displacement response via incorporation of a secondary defect production model into the nuclear deposition functions.

General temperature response models were developed compatible with both photon and ion depositions. Photon cross sections were

incorporated into a general library covering all elements. The ion depositions were all processed into the spatial form of the polynomials discussed above and the temperature model was developed based on a general Green's function formulation in which the spatial dependence was eliminated by deriving on closed form solutions which only required a time integration to accomodate arbitrary spectra.

In summary, the specific achievements of this model development phase of this work were:

THE SYNTHESIS OF ANALYTICAL TECHNIQUES INTO A SELF-CONSISTENT METHOD FOR TRANSIENT RADIATION DAMAGE ANALYSIS INCLUDING THE FOLLOWING UNIQUE FEATURES:

a) Development of general deposition functions for energy distributions.

b) A stopping power formulation for light ions which provided energy distributions analytically.

c) A solution to the heat conduction equation incorporating energy dependent polynomial coefficients.

d) General solutions for exponential photon energy deposition for slabs and semi-infinite media.

e) Displacement production calculations for general ion spectra based on deposition functions.

f) A diffusion approximation for modification of ion
    flux and spectra in gases.

g) A Green's function formulation for stress waves from
    general ion depositions.

VIII. B. Summary and Conclusions from Application of Models to
Inertial Confinement Systems Output Spectra

All the models for transient responses of materials were incor-
porated into a general computer code, T-DAMEN. This code was used to
assess the radiation damage environment for various materials to
reference spectra typical of inertial confinement fusion systems.

Spectra were chosen which represent "bare" pellets, and consis-
ting primarily of light ion components, structured pellets, con-
sisting of heavy ion components, and a combination which had com-
ponents of both. Data were presented for the response of copper,
molybdenum, and carbon. In addition parametric studies were per-
formed for characteristic photon and ion spectra. The following
general conclusions can be made from these analyses:

a) Temperature excursions will exceed $2/3\ T_m$ for unprotected
    surfaces in inertial confinement fusion devices at x-ray
    fluences of 1 J/cm^2 for spectra which are colder than .3
    keV (Black body) in the case of carbon and 2 keV for
    copper and molybdenum.

b) The temperature response of surfaces is sensitive to
    the source time for X-ray production. A reduction in the
    ΔT of 50% is noted for high conductivity materials such
    as copper as the source time is increased from an impulse
    assumption to 1 nanosecond for a .5 keV blackbody tem-
    perature.

c) For the materials analyzed in this study, the exposed
    surfaces had time to cool to near ambient values in the
    time interval between X-ray and ion arrival.

d) Pulsed ion irradiation produced large volumetric depo-
    sitions; yet, temperature excursions were much lower than
    estimated by adiabatic assumption since most of the
    energy escaped the deposition region by conduction during
    the time of deposition.

e) Although photon depositions may be short enough to induce
    thermoelastic stress waves, ion pulse durations are
    typically too long to produce waves of any significant
    amplitude.

f) The displacement rates associated with the ions of inertial
    confinement spectra exceed those of all current fission
    systems, envisioned fusion designs, and simulation methods
    (figure VIII. 1). These damage rates can exceed 500 dpa
    second at end of range of heavy ions.[128] These high defect

production rates can have a significant effect on both point and clustered defect behavior.

g) Gas protection can significantly reduce the temperature excursions in materials from both soft X-rays and ions. These reductions can be achieved even at pressures which do not stop all the ions from the pellet. Displacement rates from ions can also be reduced especially at greater depths in the material.

h) Sputtering due to ions can produce significant erosion of exposed surfaces. In addition, the associated temperature excursion during ion deposition can enhance, by factors of 4-6, the amount of material removed per pulse.

i) Evaporation can also produce erosion of exposed surfaces although most metallic surfaces will experience several orders of magnitude less evaporation than low Z materials such as carbon for the same homologous temperature excursion.

j) Conditions for blistering in inertial confinement fusion devices will be different than in most experimental systems since implanted helium is due to spectra composed of a wide range of energies and since high damage rates and large temperature excursions will be experienced in the helium implantation zone.

Finally, the methods in this study allow assessment of the temporal and spatial dependence of the radiation damage environment produced by most photon and ion spectra encountered in pulsed fusion devices. These methods of analysis can provide the basis for numerous investigations of the effect of transients on subsequent responses of materials.
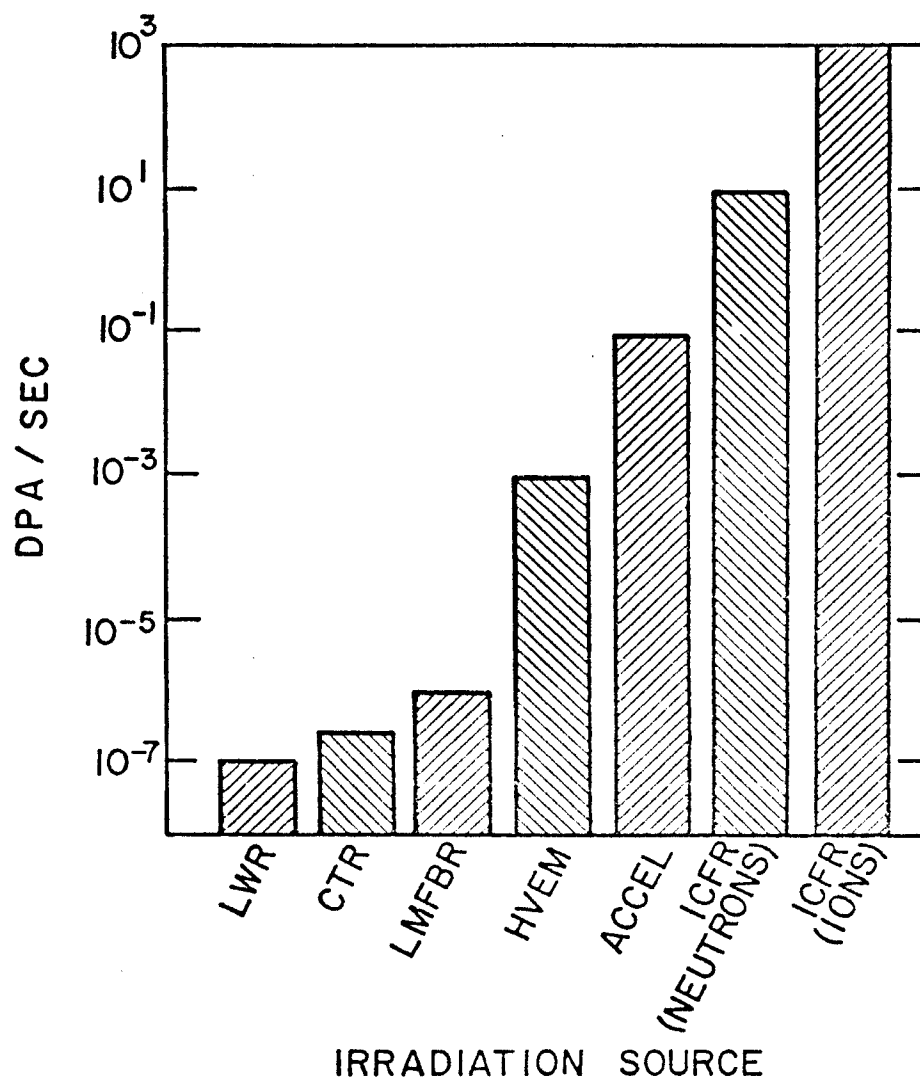
Figure VIII. 1. Comparison of Peak Damage Rates

REFERENCES

1. J. O. Neff; "Perspective on Fusion Power Commercialization,"
    Trans. Am. Nucl. Soc. 27, 10 (1977).

2. J. F. Decker; "A Status Report on the Current DMFE Review of
    Alternative Magnetic Confinement Systems," Trans. Am Nucl
    Soc. 27, 41 (1977).

3. B. Badger, et al.;"UWMAK-III, A Non Circular Tokamak Power
    Reactor Design,"Nuclear Engineering Dept. Report UWFDM-
    150, (Univ. of Wisconsin), July 1976.

4. An Engineering Design Study of a Reference Theta-Pinch Reactor
    (RTPR), Prepared for US. AEC by Argonne National Labora-
    tory and Los Alamos Scientific Laboratory, LA-5336 ANL-
    8019, March 1974.

5. L. A. Booth;"Central Station Power Generation by Laser-Driven
    Fusion,"LA-4858, Vol. 1, Los Alamos Scientific Laboratory,
    February 1972.

6. S. G. Varnado, et al.;"Preliminary Systems Considerations for an
    Electron Beam Induced Fusion Power Plant," Sandia Labora-
    tories, SAND-74-0160, 10/74.

7. F. Beranek; "Time Dependent Neutronics Studies," Ph.D. Thesis,
    Dept. of Nucl. Eng., Univ. of Wisconsin-Madison (1978).

8. F. L. Vook, et al.; Reviews of Modern Physics, Vol. 47, Supplement
    No. 3 (1975).

9. J. E. Westmoreland, et al.; "Dose Rate Effects in Nickel-Ion-
    Irradiated Nickel," Radiation Effects 26, 1 (1975).

10. G. L. Kulcinski;"Radiation Damage by Neutrons to Materials in
    DT Fusion Reactors,"IAEA-CN-33/S 3-1; Reprint from Plasma
    Physics and Controlled Nuclear Fusion Research, 1974, Vol.
    II, International Atomic Energy Agency, Vienna, 1975.

11. G. L. Kulcinski, et al.;"Comparison of Displacement and Gas
    Production Rates in Current Fission and Future Fusion
    Reactors";Special Technical Production 570, American
    Society for Testing and Materials, 1976.

12. W. G. Johnston, et al.; "Nickel Ion Bombardment of Type 304
    Stainless Steel; Comparison with Fast Reactor Swelling
    Data," Journal of Nuclear Materials, No. 47, 1973, pp.
    155-167.

13. J. B. Whitley; Ph.D. Thesis, Dept. of Nucl. Eng., University of Wisconsin-Madison, to be published.

14. M.W. Thompson; Defects and Radiation Damage in Metals; Cambridge University Press, 1969.

15. N. M. Ghoniem; "A Dynamic Rate Theory for the Response of Metals During Steady State and Pulsed Irradiation," Ph.D. Thesis, University of Wisconsin-Madison, September 1977.

16. T. Frank; "Summary of Proceedings of Inertial Confinement Fusion Working Group," IAEA Conference and Workshop on Fusion Reactor Design, Madison, Wisconsin, October 1977.

17. R. W. Conn, et al.; "Solase-A Conceptual Laser Fusion Reactor Design," UWFDM-220, Nuclear Engineering Dept., University of Wisconsin-Madison, December 1977.

17a. J. Maniscalco; "The Civilian Applications of Laser Fusion," Lawrence Livermore Laboratory, April 1977.

18. L. A. Booth and T. G. Frank; "A Characterization of Laser Fusion Reactor Concepts," Trans. Am. Nucl. Soc, 27, 32 (1977).

19. Assessment of Laser-Driven Fusion; EPRI ER-203 (Research Project 470-1), Prepared by K. A. Brueckner and Assoc., Inc.; Electric Power Research Institute, Palo Alto, Ca.; September 1976.

20. J. Williams et al.;"A Conceptual Laser Controlled Thermonuclear Reactor Power Plant";Proc. of 1st. Topical Mtg. on Technology of Controlled Nuclear Fusion, San Diego, Ca., 4/74, p. 70.

21. T. Frank, et al.; "A Laser Fusion Reactor Concept Utilizing Magnetic Fields for Cavity Wall Protection"; Proc. of 1st. Topical Mtg. on Technology of Controlled Nuclear Fusion, San Diego, Ca., 4/74, p. 83.

22. M. J. Tobin and A. P. Fraas; "Fusion by Laser", Scientific American, 224, No. 6 (June 1971).

23. H. Hovingh, et al.;"The Preliminary Design of a Suppressed Ablation Laser-Induced Fusion Reactor"; Proc. of 1st Topical Mtg. on Technology of Controlled Nuclear Fusion, San Diego, Ca., 4/74, p. 96.

24. J. A. Maniscalco;"A Conceptual Design Study for a Laser Fusion Hybrid"; Proc. of 2nd Topical Mtg. on Technology of Controlled Nuclear Fusion, Richland, Washington, 1976.

25. J. Hovingh;"First Wall Studies of a Laser-Fusion Hybrid Reactor
        Design"; Proc. of 2nd Topical Mtg. on the Technology of
        Controlled Nuclear Fusion; Richland, Washington, 1976.

26. J. A. Maniscalco, W. R. Mier and M. J. Monsler; "Conceptual
        Design of a Laser Fusion Power Plant," Trans Am. Nucl.
        Soc., 27, 34 (1977).

27. J. A. Blink, P. E. Walker and H. W. Meldner; "Energy Partition
        and Neutron Spectra from Laser Fusion Reactor Targets,"
        Trans. Am Nucl. Soc., 27, 70 (1977).

28. T. O. Hunter, S. I. Abdel-Khalik, G. L. Kulcinski; "Response of
        First Walls in Inertial Confinement Reactors to Thermo-
        nuclear Radiation," UWFDM-221, Nuc. Eng. Dept., University
        of Wisconsin, October 1977.

29. Samuel G. Varnado and Gary A. Carlson;"Considerations in the
        Design of Electron-Beam-Induced Fusion Reactor Systems";
        Nuclear Technology, Vol. 29, 415, June 1976.

30. Electron-Beam-Fusion Progress Report, Directorate of Physical
        Research 5200, Sandia Labs, Albuquerque, N. Mex., SAND76-
        0148, 1975.

31. W. W. Engle, Jr.;"A Users Manual for ANISN," K-1693, Oak Ridge
        Gaseous Diffusion Plant, March 1967.

32. Randall K. Cole, Jr.;"A Program for Rapid Calculation of X-ray
        Deposition", SC-RR-69-855, Sandia Labs, Albuquerque, N.
        Mex., July 1970.

33. S. L. Thompson; "Improvements in the CHART-D Energy Flow Hydro-
        dynamic Code V", Sandia Laboratories, SLA-73-0477, October
        1973.

34. P. Holzhauser and R. J. Lawrence;"WONDY III--An Improved Program
        for Calculating Problems of Motion in One Dimension", Sandia
        Laboratories, SC-DR-68-217, June 1968.

35. J. Hovingh; "First Wall Response to Energy Deposition in Con-
        ceptual Laser Fusion Reactors," UCRL-77588, Lawrence
        Livermore Laboratory (1976).

36. I. Manning and G. P. Mueller; Depth Distribution of Energy
        Deposition by Ion Bombardment, Computer Physics Communica-
        tion, 6, 1973.

37. D. K. Brice;"Ion Implantation Range and Energy Reposition Codes
        COREL, RASE 4, AND DAMG2, SAND75-0622",Sandia Laboratories,

Albuquerque, New Mexico, July 1977.

38. K. B. Winterbon; "Heavy-Ion Range Profiles and Associated Damage Distributions," Radiation Effects, 13, 215 (1972).

39. O. S. Oen and M. T. Robinson; "Monte Carlo Range Calculations for a Thomas Fermi Potential," Journal of Applied Physics, Vol. 35, No. 8 (August 1961).

40. T. J. Hoffman; "Sputtering Calculations with the Discrete Ordinance Method," Trans. Am Nucl. Soc., 27, 266 (1977).

41. J. F. Gibbons, W. S. Johnson and S. W. Mylroie, "Projected Range Statistics," Halstad Press, 2nd Ed. (1975).

42. David K. Brice; "Three-Parameter Formula for the Electronic Stopping Cross Section at Non-realivistic Velocities," Physical Review A, Vol. 6, No. 5, 1791, November 1972.

43. D. K. Brice; "Spatial Distribution of Ions Incident on a Solid Target as a Function of Instantaneous Energy"; Radiation Effects, Vol. 11, 227 (1971).

44. K.B. Winterbon; "Ion Implantation Range and Energy Deposition Distribution", Vol. 2, IFI/Plenum, New York, 1975.

45. D. K. Brice; "Ion Implantation Range and Energy Deposition Distribution," Vol. 1, IFI/Plenum, New York, 1975.

46. Frank Biggs and Ruth Lighthill; "Analytical Approximations for X-ray Cross Sections II", SC-PR-71 0507, Sandia Labs., Albuquerque, N.M. December 1971.

47. T. O. Hunter and G. L. Kulcinski; "T-DAMEN, a Computer Code for Analysis of Transient Radiation Damage," UWFDM-247, Nuclear Engineering Dept., University of Wisconsin-Madison, May 1978.

48. W. H. McMaster, et al.; "Compilation of X-ray Cross Sections. Section I"; UCRL-50174, California Univ., Livermore; Lawrence Radiation Lab., January 1970.

49. Frank Biggs and Ruth Lighthill; "Analytical Approximations for X-ray Cross Sections II", SC-PR-71 0507, Sandia Labs., Albuquerque, N.M. December 1971.

50. J. W. Robinson; Handbook of Spectroscopy, Vol. I; CRC Press, Cleveland, Ohio.

51. R. E. Evans; The Atomic Nucleus; McGraw-Hill, 1955, pp. 672-745.

52. K. G. Adams and F. Biggs;"Efficient Computer Access to the Sandia Photon Cross Sections,"SC-PR-72-0683, Sandia Labs., Albuquerque, N. Mex., December 1973.

53. F. Biggs and R. Lighthill;"Analytical Approximations for Total and Energy Absorption Cross Sections for Photon-Atom Scattering"; SC-PR-720685; Sandia Labs., Albuquerque, N. Mex., December 1972.

54. J. D. Jackson; Classical Electrodynamics; 2nd Ed. John Wiley and Sons, 1975, pp. 284-292.

55. Max Born and Emil Wolf; Principles of Optics; 5th Ed. Pergamon Press, 1975.

56. G. L. Simmons and J. H. Hubbell;"Comparison of Photon Interaction Cross Section Data Sets II." Biggs-Lighthill and ENDF/B; NBS-10818, National Bureau of Standards, Washington, D. C., March 1972.

57. G. L. Simmons and J. H. Hubbell;"Comparison of Photon Interaction Cross Section Data Sets VII." Biggs-Lighthill (Rev.) and ENDF/B; NBSIR 73-241, National Bureau of Standards, Washington, D. C., July 1973.

58. Handbook of Chemistry and Physics; CRC Press, Cleveland, Ohio.

59. Lewis T. Chadderton; Radiation Damage in Crystals; John Wiley and Sons, Inc.; New York.

60. J. Lindhard, et al.; "Range Concepts and Heavy Ion Ranges"; Mat. Fys. Medd. Dan. Vid. Selsk. 33, No. 14, 3, (1963).

61. J. M. Chesire, G. Dearnaley and Jim Poate; Phys. Letters 27A, 318, 1968.

62. J. G. Ziegler, W. K. Chu;"The Stopping of ^{4}He Ions in Elemental Matter,"Thin Solid Films, 19 (1973), 281-287.

63. L. C. Northcliffe and R. F. Schilling; Range and Stopping-Power Tables for Heavy Ions; Nuclear Data Sec. Vol. 7, No. 3-4, 1970.

64. J. F. Ziegler and H. H. Anderson; The Stopping and Ranges of Ions in Matter, Vol. 1-5, Pergamon Press, New York (1977).

65. Ordean S. Oen and Mark T. Robinson; "Slowing-Down Time of Energetic Ions in Solids," Journal of Applied Physics, Vol. 46, No. 12, 5069, December 1975.

66. M. A. Abdou, C. W. Maynard and R. Q. Wright; "MACK: A Program to Calculate Neutron Energy Release Parameters (Fluence-to-Kerma Factors) and Multigroup Neutron Reaction Cross Sections from Nuclear Data in ENDF Format"; ORNL-TM-3994, Oak Ridge National Laboratories.

67. B. Badger, et al.; "UWMAK-1, A Wisconsin Foroidal Fusion Reactor Design," USFDM-68, Nuclear Eng. Dept., University of Wisconsin-Madison (November 1973), Vol. 1.

68. F. Beranek and R. W. Conn; "Time Dependent Neutronics for Laser Fusion Blanket and Materials Analysis," UWFDM-210, Nuc. Eng. Dept., University of Wisconsin, June 1977.

69. G. L. Kulcinski, et al.; "Radiation Damage Limitations in the Design of the Wisconsin Tokamak Fusion Reactor," Nuclear Technology, Vol. 22, April 1974.

70. G. J. Zimmerman; "Numerical Simulation of Laser-Initiated Fusion," Comments on Plasma Physics and Controlled Fusion, Vol. II (1976).

71. E. U. Condon and H. Odishaw, eds.; Handbook of Physics, 2nd Ed. McGraw-Hill, 1967, pp. 7-126, 7-138.

72. J. M. Williams and T. G. Frank; Laser-Controlled Thermonuclear-Reactor Materials Requirements; Nuclear Technology, Vol. 22; June 1974, p. 350.

73. W. G. Wolfer; Personal Notes of Slowing Down time of the PKA's in NI Produced by 14 MeV Neutrons; 7/15/76.

74. D. L. Lessor; "Neutron and Alpha Particle Energy Spectrum and Angular Distribution Effects from Plasma D-T Fusions," BNWL-B-409, NTIS, 4/1975.

75. G. Shuy; Calculations of Neutron Pulse Spreading from D-T Pellet, Personal Communication, 9/1976.

76. F. Kreth; Principle of Heat Transfer; International, 1965.

77. J. Matthews and R. L. Walker; Mathematical Methods of Physics, W. A. Benjamin, Inc. New York (1970).

78. H. S. Carslaw and J. C. Jaeger; Conduction of Heat in Solids; 2nd Ed., Oxford, 1959.

79. M. Abramouritz and I. A. Stegon, eds.; Handbook of Mathematical
       Functions, U. S. Dept. of Commerce AMS 55, June 1964.

80. S. I. Abdel-Khalik and T. O. Hunter; "Assessment of Surface
       Heating Problems in Laser Fusion Reactions"' UWFDM-197,
       Dept. of Nucl. Eng., University of Wisconsin-Madison
       (January 1977).

81. R. Behrisch;"First-Wall Erosion in Fusion Reactors"; Nuclear
       Fusion, No. 12, 1972, p. 695.

82. John F. Ready; Effects of High-Power Laser Radiation; Academic
       Press, New York, 1971.

83. J. Howard and T. O. Hunter; "Mirror Damage Thresholds for Laser
       Fusion Pulse Shapes"; UWFDM-230, Dept. of Nucl. Eng.,
       University of Wisconsin-Madison (January 1978).

84. T. G. Frank;"Heat Transfer Problems Associated with Laser Fusion";
       16th National Heat Transfer Conference, St. Louis, Mo.,
       August 1976.

85. R. A. Axford;"Direct Evaluation of Transient Surface Temperatures
       and Heat Fluxes"; LA-6051, Los Alamos Scientific Lab., N.
       Mex., August 1975, p. 8.

86. T. O. Hunter and G. L. Kulcinski; "Description of the Response
       of Reactor First Walls to Pulsed Thermonuclear Radiation,"
       (Part I), UWFDM-196, Nuc. Eng. Dept., University of Wiscon-
       sin-Madison (March 1977).

87. Y. C. Fung; Foundations of Solid Mechanics; Prentice-Hall, Inc.,
       1965.

88. Eli Sternberg and J. G. Chaknavorty;"On Inertia Effects in a
       Transient Thermoelastic Problem"; Journal of Applied
       Mechanics, Vol. 26, No. 4, December 1959.

89. Masashi Daimaruya and Masachika Naito;"A Transient Coupled
       Thermoelastic Problem in the Semi-Infinite Medium"; Bulle-
       tin of the Japanese Society of Mechanical Engineers.
       539.3.7.01 (1972).

90. R.M. White; "Generation of Elastic Waves by Transient Surface
       Heating"; Journal of Applied Physics; Vol. 34, No. 12,
       December 1963.

91. B. A. Boley and I. S. Tolens; "Transient Coupled Thermoelastic
       Boundary Value Problems in the Half-Space", J. of App.
       Mech. 29 (December 1962).

92. L. W. Morland;"Generation of Thermoelastic Stress Waves by Impulsive Electromagnetic Radiation"; AIAA Journal, Vol. 6, No. 6., June 1968.

93. G. A. Hegemier and L. W. Morland;"Stress Waves in a Temperature Dependent Viscoelastic Half-Space Subjected to Impulsive Electromagnetic Radiation"; AIAA Journal, Vol. 7, No. 1, January 1969.

94. S. S. Penner and O. P. Sharma;"Interaction of Laser Radiation with an Absorbing Semi-Infinite Solid Bar"; Journal of Applied Physics, Vol. 37, No. 6, May 1966.

95. T. A. Zaker;"Stress Waves Generated by Heat Addition in an Elastic Solid"; Journal of Applied Mechanics, 32, 143, March 1965.

96. F. C. Perry; "Thermoelastic Response of Polycrystalline Metals to Relativistic Electron Beam Absorption"; J. of App. Physics, Vol. 41, No. 12 (November 1970).

97. Fusion Reactor Studies: Potential of Low Z Materials for the First Wall; EPRI 115-2, Prepared by General Atomic Co., Electric Power Research Institute, Palo Alto, CA., September 1975.

98. J. Weertman;"Potential Fatigue Problems in First-Wall Laser-Controlled Fusion Reactors"; LA-5664-MS; Los Alamos Scientific Laboratory, November 1974.

99. G. A. Korn and T. M. Korn; Mathematical Handbook for Scientists and Engineers, McGraw-Hill, 1961.

100. T. O. Hunter and G. L. Kulcinski, "Description of the Response of Materials to Pulsed Thermonuclear Radiation (Part 2)", UWFDM-217, Dept. of Nuc. Eng., University of Wisconsin, Madison (Oct. 1977).

101. D. R. Olander; Fundamental Aspects of Nuclear Reactor Fuel Elements, TID-26711-P1, USERDA, 1976.

102. D. G. Doran, et al.; Report of the Working Group on Displacement Models and Procedures for Damage Calculations, HEDL-TME 73-76, Hanford Engineering Development Laboratory, December 1973.

103. H. Bichsel; "Passage of Charged Particles Through Matter," American Institute of Physics Handbook, 3rd Ed., 1972, pp. 8-142.

104. J. W. Corbett and L. C. Ianniello, eds.; Radiation-Induced Voids in Metals, National Technical Information Service, CONF-710601, p. 397, April 1972.

105. K. B. Winterbon, P. Sigmund and J. B. Sanders;"Spatial Distribution of Energy Deposited by Atomic Particles in Elastic Collisions," Kgl. Danske Videnskab, Selscab, Mat-Jup. Medd. 37, No. 14 (1970).

106. O. S. Oen, et al.;"Ion Radiation Damage,"In Applications of Ion Beams to Metals, ed. by S. T. Picraux, E. P., 1974, pp. 641-650.

107. T. O. Hunter and G. L. Kulcinski; "Description of the Response of Materials to Pulsed Thermonuclear Radiation (Part 3)" UWFDM-232, Nuc. Eng. Dept., University of Wisconsin-Madison (April 1978).

108. T. Tsurushima and ii. Tanoue; "Spatial Distribution of Energy Deposited by Energetic Heavy Ions in Semi-Conductors," J. of Phy. Soc. of Japan, Vol. 3., No. 6 (December 1971).

109. G. Moses and D. Smatlak; Nucl. Eng. Dept., University of Wisconsin-Madison, to be published.

110. MACC Computing Handbook, Academic Computing Center, University of Wisconsin-Madison (November 1973).

111. Approximation & Interpolation - Reference Manual for the 1108. Mathematical Routine Series A I, Academic Computing Center, Uuniversity of Wisconsin-Madison, 1972.

112. G. Moses and G. Magelssen; "PHD-IV, A Laser-Plasma Simulation Code," Trans. Am. Nucl. Soc. 27, 39 (1977).

113. T. O. Hunter and G. L. Kulcinski; "Surface Damage and Thermal Effects from Transient Thermonuclear Radiation in Inertial Confinement Fusion Reactors," UWFDM-233, Dept. of Nucl. Eng., University of Wisconsin-Madison (April 1978).

114. G. M. McCracken; "Behavior of Surfaces under Ion Bombardment," Rep. Prog. Phys. 38 (1975).

115. P. Sigmund; "Theory of Sputtering I. Sputtering Yield of of Amorphous and Polycrystalline Targets," Phys. Rev., 184, No. 2 (August 1969).

116. L. G. Haggmark and W. D. Wilson; "Monte Carlo Studies of Sputtering," 3rd Int. Conf. on Plasma Surface Interaction in Controlled Fusion Devices, Culham Laboratory, UK,

April 1978.

117. I. O. Bohachevsky and J. F. Hafer; "Sputtering Erosion of Fusion Reactor Cavity Walls," LA-6633-MS, Los Alamos Sc. Lab (December 1976).

118. I. O. Bohachevsky and J. F. Hafer; "Dependence of Sputtering Erosion on Fuel-Pellet Characteristics," LA-6991-MS, Los Alamos Sc. Lab (November 1977).

119. D. L. Smith; "Physical Sputtering Model for Fusion Reactor First-Wall Materials," Trans. Am Nucl Soc., 27, 265 (1977).

120. R. S. Nelson; "Investigation of Thermal Spikes by Studying the High Energy Sputtering of Metals at Elevated Temperatures," Phil. Mag. Vol. 11, No. 110, 291 (February 1965).

121. G. E. Chapman, et al.; "The Energy Distribution of Sputtered Atoms from Gold," Radiation Effects, 13, 121 (1972).

122. H. Anderson and H. Bay; Radiation Effects, 19, 257 (1973).

123. Vacuum Engineering Tables and Diagrams; HERAEUS HOCHVAKUUM GMBH, 900.123E 6C (April 1966).

124. S. K. Erents and G. M. McCracken; "Blistering of Molybdenum under Helium Ion Bombardment," CLM-P323, Culham Laboratory, UK. (1972).

125. W. Bauer and G. J. Thomas; "Helium Re-Emission and Surface Deformation in Niobium During Multiple Temperature Helium Implantation," Proc. Int. Conf. on Ion Beam Surface Laser Analysis, Karlsrube, Germany (September 1975).

126. K. L. Wilson; "Gas Re-Emission from Ion-Implanted Solids," SAND 76-8692, Sandia Laboratories (September 1976).

127. W. R. McDonnell; "Whisker Growth--A New Mechanism for Helium Blistering of Surfaces in Complex Radiation Environments," 3rd Int. Conf. on Plasma Surface Interactions in Controlled Fusion Devices, Culham Laboratory, U.K. (April 1978).

128. T. O. Hunter and G. L. Kulcinski; "Temperature and Displacement Transients in Inertial Confinement Fusion First Walls", Trans. Am. Nucl. Soc. 27, 40 (1977).